SISSA
Scuola
Internazionale
Superiore di
Studi Avanzati

Physics Area - PhD course in
Statistical Physics

Synthetic quantum matter - from quantum simulation to quantum information

Candidate:
Poetri Sonya Tarabunga

Advisor:
Dr. Marcello Dalmonte

Academic Year 2023-2024

Abstract

In this thesis, we study two distinct, yet equally fascinating, aspects of many-body physics. Synthetic quantum matter – engineered many-body systems with high controllability and tunability – serves as a cornerstone for the research. The combination of these features makes them incredibly suited for research at the crossroads of traditional statistical physics, new concepts coming from field theory (particularly gauge theories), and quantum information.

In the first part, we delve into the quantum simulation of novel quantum phenomena with analog quantum simulators. In particular, recent advances in the synthetic platforms based on Rydberg atoms, i.e., neutral atoms trapped in optical tweezers, have opened up new avenues to explore exotic topological phases like quantum spin liquids, which hold potential applications in quantum computing. We employ a combination of numerical and analytical tools to address open questions regarding the realization of these phases in experiments. Our results show that the recently observed spin liquids can be directly connected to a Higgs-Ising lattice gauge theory, providing a clear-cut theoretical argument for its origin. Moreover, different setups with chiral interacting Hamiltonians offer new avenues to realize chiral spin liquids - a lattice version of the celebrated quantum Hall effect.

In the second part, we explore the role of a quantum information quantity known as nonstabilizerness in quantum many-body systems. By now, the study of quantum information concepts in the realm of many-body theory represents a very active research effort, with a prominent example being entanglement, which has revolutionized our understanding of quantum systems. Similar to entanglement, nonstabilizerness has emerged as a crucial resource for achieving quantum advantage, although in a fundamentally different way. While entanglement is well-studied, the exploration of nonstabilizerness in many-body contexts is still in its very early stages. Its ongoing investigation holds significant promise for deepening our understanding of many-body systems and their complexity. We develop new methods based on tensor networks and Monte Carlo methods to enable the quantification of nonstabilizerness at large scales. We subsequently apply them to uncover the role of nonstabilizerness in various many-body settings, particularly in critical phenomena, gauge theory, and quantum circuits.

List of publications

Publications discussed in this thesis:

[1] **Poetri Sonya Tarabunga**, Federica Maria Surace, Riccardo Andreoni, Adriano Angelone, and Marcello Dalmonte
Gauge-theoretic origin of Rydberg spin liquids
Physical Review Letter **129**, 195301 (2022)

[2] **Poetri Sonya Tarabunga**, Giuliano Giudici, Titas Chanda, and Marcello Dalmonte
Classification and emergence of quantum spin liquids in chiral Rydberg models
Physical Review B **108**, 075118 (2023)

[3] Emanuele Tirrito, **Poetri Sonya Tarabunga**, Guglielmo Lami, Titas Chanda, Lorenzo Leone, Salvatore F.E. Oliviero, Marcello Dalmonte, Mario Collura, and Alioscia Hamma
Quantifying nonstabilizerness through entanglement spectrum flatness
Physical Review A **109**, L040401 (2024)

[4] **Poetri Sonya Tarabunga**, Emanuele Tirrito, Titas Chanda, and Marcello Dalmonte
Many-body magic via Pauli-Markov chains - from criticality to gauge theories
PRX Quantum **4**, 040317 (2023)

[5] **Poetri Sonya Tarabunga**
Critical behaviors of non-stabilizerness in quantum spin chains
Quantum 8, 1413 (2024)

[6] **Poetri Sonya Tarabunga** and Claudio Castelnovo
Magic in generalized Rokhsar-Kivelson wavefunctions
Quantum **8**, 1347 (2024).

[7] **Poetri Sonya Tarabunga**, Emanuele Tirrito, Mari Carmen Bañuls, and Marcello Dalmonte
Nonstabilizerness via Matrix Product States in the Pauli basis
Physical Review Letter **133**, 010601 (2024)

[8] Martina Frau, **Poetri Sonya Tarabunga**, Mario Collura, Marcello Dalmonte, Emanuele Tirrito
Nonstabilizerness versus entanglement in matrix product states
Physical Review B **110**, 045101 (2024)

[9] **Poetri Sonya Tarabunga** and Emanuele Tirrito
Magic transition in measurement-only circuits
arxiv:2407.15939

[10] Hernan B. Xavier, **Poetri Sonya Tarabunga**, Marcello Dalmonte, and Rodrigo Pereira

Emergent dipole field theory in atomic ladders
arxiv:2407.21019

Other publications not discussed in this thesis:

[11] **Poetri Sonya Tarabunga**, Tiago Mendes-Santos, Fabrizio Illuminati, and Marcello Dalmonte
Finite-temperature quantum discordant criticality
Physical Review B **105**, 075104 (2022)

[12] Pedro R. Nicácio Falcão, **Poetri Sonya Tarabunga**, Martina Frau, Emanuele Tirrito, Jakub Zakrzewski, and Marcello Dalmonte
Non-stabilizerness in U(1) lattice gauge theory
arxiv:2409.01789

Introduction

Our universe, from the subatomic realm to the vast expanse of galaxies, is governed by the laws of quantum mechanics. This captivating theory underpins the behavior of everything, from the tiniest particle to the collective behavior of millions of stars in a galaxy. However, when we turn our attention to quantum many-body systems, namely, systems composed of many interacting quantum particles, these very laws present us with a formidable challenge [13–15]. Their immense complexity arises due to the exponential scaling of the size of the Hilbert space with the number of interacting particles. These particles strongly interact with each other, which lead to emergent behavior: a collective behavior that transcends the properties of the individual particles. For instance, the different phases and transitions observed in water, magnetism, and superconductors, all stem from correlations within systems of electrons and ions.

A notable example of a rich phenomenology in strongly correlated systems is the emergence of novel phases of matter that go beyond the classical Landau spontaneous symmetry breaking paradigm [16, 17]. These phases exhibit exotic properties, such as non-local order, and properties that depend on the topology in which the system is defined. Moreover, they host “fractionalized excitations", namely, emergent particles that can be seen as equivalent to a fraction of an elementary charge, such as an electron or magnetic monopoles. This new type of order is called topological order, which has already been experimentally demonstrated in fractional quantum Hall (FQH) effect [18].

Beyond the realm of theoretical curiosity, quantum many-body systems hold immense potential for technological breakthroughs in areas like quantum computing and the design of novel materials. As such, their investigations have been at the forefront of condensed matter physics research for the past several decades, and it remains a vibrant and exciting area of research to date. Scientists are not only striving to deepen our fundamental understanding of these phenomena but also actively seeking to harness their novel properties for technological applications.

However, directly simulating these complex systems using classical computers quickly becomes intractable due to the large number of interacting qubits. To overcome this hurdle, physicists have developed a range of powerful simulation techniques. One promising approach utilizes specially designed quantum systems to mimic the behavior of the target many-body system. These “quantum simulators" essentially act as miniature quantum computers, capable of solving problems beyond the reach of classical computers. In particular, recent advances in the synthetic platforms based on Rydberg atoms [19, 20], i.e., neutral atoms trapped in optical tweezers, have opened up unprecedented possibilities to explore exotic phases like quantum spin liquids, which hold potential applications in quantum information technologies. At the same time, they are offering a new platform to probe many-body dynamics, with unique features in terms of controllability and probing that go well beyond what is available in solid state experiments.

In Chapter 3, we investigate the recently discovered spin liquids in Rydberg atom arrays with strongly repulsive van der Waals interactions. While the emergence of

QSLs in physically realizable parameter regimes has been verified both numerically and experimentally, the specific mechanism stabilizing such a phase remained unclear. We elucidate the origin of the previously observed QSLs by directly linking it to a Ising-Higgs lattice gauge theory. Furthermore, we show numerically that the topological phases extend in a broad region of the parameter space. Finally, we propose an experimental protocol to realize the extended Rydberg model using Rydberg dressing.

In Chapter 4, we focus on the emergence of a chiral spin liquids (CSL) - lattice analogue of FQH Laughlin state - in a very different regime of Rydberg systems. Specifically, the dynamics solely takes place within the Rydberg subspace, with the atoms interacting through dipolar exchange interactions. Such a setup has been experimentally demonstrated in a system of three sites. To understand what classes of CSLs these models can stabilize, we classify all possible CSLs with $U(1)$ global symmetry using parton construction on the honeycomb lattice. The resulting classification includes six distinct classes of gapped CSLs: the corresponding variational wavefunctions obtained from two of these classes accurately describe the Rydberg many-body ground state at $1/2$ and $1/4$ particle density.

While the first two chapters concern topological spin liquids, in Chapter 5 we instead focus on exotic dipole symmetry that emerges in atomic ladders. We study the dynamics of a model of hard-core bosons on ladders, in the presence of strong kinetic constrains akin to those of the Bariev model. The model displays a paired Tomonaga-Luttinger liquid phase featuring an emergent dipole symmetry, which encodes the local pairing constraint into a global, non-local quantity. We scrutinize the effect of such emergent low-energy symmetry during quench dynamics including single particle defects. We observe that, despite being approximate, the dipole symmetry still leads to very slow relaxation dynamics, which we model via an effective field theory. The model is amenable to realization in both cold atoms in optical lattices and Rydberg atom arrays with dynamics taking place solely in the Rydberg manifold. We present a blueprint protocol to observe the effect of emergent dipole symmetry in such experimental platforms, combining adiabatic state preparation with quench dynamics.

In a distinct development, remarkable advancements in our understanding of many-body physics have been achieved through the exploration of concepts originally developed in the context of quantum information theory and their subsequent application to quantum many-body systems [21, 22]. The first and most prominent example is a concept known as entanglement [23]. In quantum mechanics, entanglement describes a phenomenon where the quantum states of two or more particles become inextricably linked, such that a measurement on one particle instantaneously influences the state of the other, regardless of their physical distance. From the quantum information point of view, entanglement has been known to be a key resource for performing several quantum information protocols, such as quantum teleportation [24] and quantum cryptography [25].

In the realm of many-body physics, entanglement plays an important role as a tool to characterize and classify phases of matter and their transitions. Building on its early understanding in few-body systems, its importance for the many-body problem has been uncovered [26–28]. It has found applications over a wide range of phenomena, from real-time dynamics [29], to topological order [30, 31] and classification of states [32, 33]. Moreover, a particularly useful perspective has pivoted on the role of bipartite entanglement in representing quantum wave functions, leading to the formulation of several classes of tensor network states [34–38]. These tensor network states have found immense success in numerical applications, exploiting

the well-known fact that ground states of quantum systems with local interactions possesses lower amount of entanglement than generic states, known as the area law. Finally, advancements in experimental platforms have enabled to probe and measure entanglement in quantum systems of few qubits [39–42].

The significant impact achieved through the application of entanglement in many-body theory underscores the need to investigate additional quantum information quantities that could serve as powerful tools for understanding complex quantum systems. In a recent development, another key quantity in quantum information - magic, also known as nonstabilizerness [43] - has received a lot of attention within the domain of many-body physics [44]. As the name suggests, nonstabilizerness is related to the complexity of simulating states that are not in the class of *stabilizer states*. These are quantum states with a rich structure, and while they can exhibit a large amount of entanglement, they can be efficiently simulated by classical computers according to the Gottesmann-Knill theorem [45–47]. Interestingly, this efficient simulability has proven valuable in studying entanglement dynamics in quantum circuits, including both unitary dynamics [48] and measurement-induced phenomena [49, 50].

In the context of quantum computing, magic plays a pivotal role in achieving universal quantum computation through a specific scheme known as *magic state injection* [43]. Thus, similarly to entanglement, magic is a fundamental resource essential for achieving quantum advantage, although in a fundamentally distinct way. It is worth noting a recent breakthrough experiment conducted by the Harvard group [42], which realizes a quantum circuit designed to exhibit a high degree of both entanglement and magic in order to demonstrate possible quantum advantage. However, in contrast to entanglement, to date little is known about the properties and behavior of magic in many body quantum systems.

The main challenge is the difficulty in quantifying magic compared to entanglement. In the case of entanglement, the von–Neumann entanglement entropy is widely accepted as a good measure for bipartite entanglement in pure states, and efficient theoretical and numerical methods to explore it in many-body systems have been developed. In contrast, the choice of a "good measure" for magic is still under discussion in current literature. Of particular interest is the recently introduced measure of magic, known as the stabilizer Rényi entropy (SRE) [51], which was subsequently shown to be a good magic monotone [52]. The key advantage of the SRE lies in its computability, making it particularly attractive for studying magic in many-body systems.

In Chapter 7, we introduce a method to compute the SRE based on a statistical exploration of Pauli strings via Markov chains. By sampling the Pauli strings, this obviates the need to compute the exponentially many terms in the definition of SRE, enabling to estimate the SRE in many-body settings. We also formulate an equivalent of mutual information for magic, dubbed mutual magic, which can be computed efficiently within our formalism as well. While the formalism is rather general, we focus on a class of tensor network state called Tree Tensor Network (TTN), where the sampling procedure can be done efficiently by exploiting its hierarchical structure. We showcase the applicability and efficiency of this method in various many-body models, demonstrating the importance of magic in criticality and gauge theories. Additionally, we discuss the corresponding experimental protocol relying on the same technique.

In Chapter 8, we applied the Pauli-Markov method to calculate a measure of magic known as mana, which has strong advantages compared to the SRE. To this end, we introduce Rényi generalizations of mana, which are also measures of magic

for pure states, and show how this allows to adapt previous methods for SREs to compute mana in large quantum systems. We provide numerical evidence that mutual mana exhibits universal logarithmic scaling with distance in critical spin chains governed by (1+1)D conformal field theories, analogous to entanglement.

We propose another tensor network method in Chapter 10, which is based on writing a matrix product state (MPS) in the Pauli basis, dubbed Pauli-MPS. The coefficients of a state in the Pauli basis are exactly the Pauli spectrum, i.e., the set of expectation values of all possible Pauli strings. Similarly to entanglement spectrum, Pauli spectrum captures the magic properties of a state, and many measures of magic are defined in terms of the Pauli spectrum. We discuss how this method allows us to express the SRE as the contraction of replicas of Pauli-MPS, enabling its efficient calculation. While the use of replica trick to compute the SRE has been known previously [53], the replica trick based on Pauli-MPS stands out as it facilitates the use of controlled approximation scheme, offering a significant practical advantage. In addition, the method is easily generalized to compute other measures of magic, such as Bell magic [54] and stabilizer nullity [55].

In Chapter 9, we focus on a class of wavefunction called the (generalized) Rokhsar-Kivelson (RK) wavefunctions. The amplitudes of this class of wavefunctions are associated to classical statistical mechanics models, thereby admitting a simplification when it comes to computing quantities of interest, including the SRE. This allows powerful analytical and numerical approaches that are not usually available in conventional quantum many body settings. We exploit this property to express the SRE as a free energy difference of related classical problems, that can be evaluated using classical Monte Carlo techniques. We apply this to a range of quantum RK Hamiltonians, which affords us to obtain analytical and numerical results of the SRE in large high-dimensional systems.

In Chapter 11, we introduce and study the magic in a measurement-only circuit consisting of Clifford and non-Clifford measurements. The investigation of magic in quantum circuits has been an outstanding challenge, due to the inherent difficulty of evaluating measures of magic in large quantum systems. We overcome this challenge by showing that the magic in our circuit model can be efficiently quantified by any measure of magic which is additive for tensor product of single-qubit states. This allows us to perform large-scale simulations to study the magic transition in this circuit, which can be viewed as a result of the competition between Clifford and non-Clifford measurements. Furthermore, we explore the intriguing behavior of specifically constructed linear combinations of magic, analogous to those used for entanglement.

In Chapter 12, we uncover an intriguing relation between magic and entanglement. From the structure of stabilizer states, it is straightforward to show that the entanglement spectrum of stabilizer states for any bipartition is “flat", namely, all entanglement spectrum are equal. The converse is not true, however: a state with flat entanglement spectrum is not necessarily a stabilizer state. Our key finding is that the SRE is directly related to the entanglement spectrum flatness averaged over Clifford orbit. This establishes a deep connection between the two fundamental resource quantities. Leveraging this connection, we developed an experimental protocol to efficiently probe nonstabilizerness in cold atom and solid-state platforms.

Finally, in Chapter 13, we study the dependence of magic with bond dimension of MPS representing ground states. The results indicate that obtaining converged results for nonstabilizerness is typically considerably easier than entanglement. Specifically, we observed that the magic converges with $1/\chi^2$, where χ is the

MPS bond dimension. Moreover, mutual magic also consistently shows a fast convergence with bond dimension. As a byproduct of our study, we show how Pauli-Markov chains (originally formulated to evaluate magic) resets the state of the art in terms of computing mutual information for MPS.

Bibliography

1. Tarabunga, P. S., Surace, F. M., Andreoni, R., Angelone, A. & Dalmonte, M. Gauge-Theoretic Origin of Rydberg Quantum Spin Liquids. *Phys. Rev. Lett.* **129,** 195301. https://link.aps.org/doi/10.1103/PhysRevLett.129.195301 (19 Nov. 2022).
2. Tarabunga, P. S., Giudici, G., Chanda, T. & Dalmonte, M. Classification and emergence of quantum spin liquids in chiral Rydberg models. *Physical Review B* **108.** ISSN: 2469-9969. http://dx.doi.org/10.1103/PhysRevB.108.075118 (Aug. 2023).
3. Tirrito, E. *et al.* Quantifying nonstabilizerness through entanglement spectrum flatness. *Physical Review A* **109.** ISSN: 2469-9934. http://dx.doi.org/10.1103/PhysRevA.109.L040401 (Apr. 2024).
4. Tarabunga, P. S., Tirrito, E., Chanda, T. & Dalmonte, M. Many-Body Magic Via Pauli-Markov Chains—From Criticality to Gauge Theories. *PRX Quantum* **4,** 040317. https://link.aps.org/doi/10.1103/PRXQuantum.4.040317 (4 Oct. 2023).
5. Tarabunga, P. S. Critical behaviors of non-stabilizerness in quantum spin chains. *Quantum* **8,** 1413. ISSN: 2521-327X. http://dx.doi.org/10.22331/q-2024-07-17-1413 (July 2024).
6. Tarabunga, P. S. & Castelnovo, C. Magic in generalized Rokhsar-Kivelson wavefunctions. *Quantum* **8,** 1347. ISSN: 2521-327X. http://dx.doi.org/10.22331/q-2024-05-14-1347 (May 2024).
7. Tarabunga, P. S., Tirrito, E., Bañuls, M. C. & Dalmonte, M. Nonstabilizerness via Matrix Product States in the Pauli Basis. *Physical Review Letters* **133.** ISSN: 1079-7114. http://dx.doi.org/10.1103/PhysRevLett.133.010601 (July 2024).
8. Frau, M., Tarabunga, P. S., Collura, M., Dalmonte, M. & Tirrito, E. Nonstabilizerness versus entanglement in matrix product states. *Physical Review B* **110.** ISSN: 2469-9969. http://dx.doi.org/10.1103/PhysRevB.110.045101 (July 2024).
9. Tarabunga, P. S. & Tirrito, E. *Magic transition in measurement-only circuits* 2024. arXiv: 2407.15939 [quant-ph]. https://arxiv.org/abs/2407.15939.
10. Xavier, H. B., Tarabunga, P. S., Dalmonte, M. & Pereira, R. G. *Emergent dipole field theory in atomic ladders* 2024. arXiv: 2407.21019 [cond-mat.quant-gas]. https://arxiv.org/abs/2407.21019.
11. Tarabunga, P. S., Mendes-Santos, T., Illuminati, F. & Dalmonte, M. Finite-temperature quantum discordant criticality. *Phys. Rev. B* **105,** 075104. https://link.aps.org/doi/10.1103/PhysRevB.105.075104 (7 Feb. 2022).
12. Falcão, P. R. N. *et al. Non-stabilizerness in U(1) lattice gauge theory* 2024. arXiv: 2409.01789 [quant-ph]. https://arxiv.org/abs/2409.01789.

13. Wen, X.-G. *Quantum Field Theory of Many-Body Systems* https://doi.org/10.1093/acprof:oso/9780199227259.001.0001 (Oxford University Press, Sept. 2007).
14. Fradkin, E. *Field theories of condensed matter physics* (Cambridge University Press, 2013).
15. Lacroix, C., Mendels, P. & Mila, F. *Introduction to frustrated magnetism: materials, experiments, theory* (Springer Science & Business Media, 2011).
16. Savary, L. & Balents, L. Quantum spin liquids: a review. *Reports on Progress in Physics* **80,** 016502. ISSN: 1361-6633. http://dx.doi.org/10.1088/0034-4885/80/1/016502 (Nov. 2016).
17. Wen, X.-G. Colloquium : Zoo of quantum-topological phases of matter. *Reviews of Modern Physics* **89.** ISSN: 1539-0756. http://dx.doi.org/10.1103/RevModPhys.89.041004 (Dec. 2017).
18. Tsui, D. C., Stormer, H. L. & Gossard, A. C. Two-Dimensional Magnetotransport in the Extreme Quantum Limit. *Physical Review Letters* **48,** 1559–1562. ISSN: 0031-9007. http://dx.doi.org/10.1103/PhysRevLett.48.1559 (May 1982).
19. Browaeys, A. & Lahaye, T. Many-body physics with individually controlled Rydberg atoms. *Nature Physics* **16,** 132–142. ISSN: 1745-2481. http://dx.doi.org/10.1038/s41567-019-0733-z (Jan. 2020).
20. Kaufman, A. M. & Ni, K.-K. Quantum science with optical tweezer arrays of ultracold atoms and molecules. *Nature Physics* **17,** 1324–1333. ISSN: 1745-2481. http://dx.doi.org/10.1038/s41567-021-01357-2 (Nov. 2021).
21. Nielsen, M. A. & Chuang, I. L. *Quantum Computation and Quantum Information* https://doi.org/10.1017/cbo9780511976667 (Cambridge University Press, June 2012).
22. Zeng, B., Chen, X., Zhou, D.-L. & Wen, X.-G. *Quantum Information Meets Quantum Matter: From Quantum Entanglement to Topological Phases of Many-Body Systems* ISBN: 9781493990849. http://dx.doi.org/10.1007/978-1-4939-9084-9 (Springer New York, 2019).
23. Horodecki, R., Horodecki, P., Horodecki, M. & Horodecki, K. Quantum entanglement. *Reviews of Modern Physics* **81,** 865–942. ISSN: 1539-0756. http://dx.doi.org/10.1103/RevModPhys.81.865 (June 2009).
24. Bennett, C. H. *et al.* Teleporting an unknown quantum state via dual classical and Einstein-Podolsky-Rosen channels. *Physical Review Letters* **70,** 1895–1899. ISSN: 0031-9007. http://dx.doi.org/10.1103/physrevlett.70.1895 (Mar. 1993).
25. Ekert, A. K. Quantum cryptography based on Bell's theorem. *Physical Review Letters* **67,** 661–663. ISSN: 0031-9007. http://dx.doi.org/10.1103/PhysRevLett.67.661 (Aug. 1991).
26. Plenio, M. B. & Virmani, S. S. in *Quantum Information and Coherence* 173–209 (Springer International Publishing, 2014). https://doi.org/10.1007/978-3-319-04063-9_8.
27. Amico, L., Fazio, R., Osterloh, A. & Vedral, V. Entanglement in many-body systems. *Rev. Mod. Phys.* **80,** 517–576. https://link.aps.org/doi/10.1103/RevModPhys.80.517 (2 May 2008).

28. Eisert, J., Cramer, M. & Plenio, M. B. Colloquium: Area laws for the entanglement entropy. *Rev. Mod. Phys.* **82,** 277–306. https://link.aps.org/doi/10.1103/RevModPhys.82.277 (1 Feb. 2010).
29. Calabrese, P. & Cardy, J. Evolution of entanglement entropy in one-dimensional systems. *Journal of Statistical Mechanics: Theory and Experiment* **2005,** P04010. ISSN: 1742-5468. http://dx.doi.org/10.1088/1742-5468/2005/04/P04010 (Apr. 2005).
30. Kitaev, A. & Preskill, J. Topological Entanglement Entropy. *Phys. Rev. Lett.* **96,** 110404. https://link.aps.org/doi/10.1103/PhysRevLett.96.110404 (11 Mar. 2006).
31. Levin, M. & Wen, X.-G. Detecting Topological Order in a Ground State Wave Function. *Phys. Rev. Lett.* **96,** 110405. https://link.aps.org/doi/10.1103/PhysRevLett.96.110405 (11 Mar. 2006).
32. Chen, X., Gu, Z.-C. & Wen, X.-G. Classification of gapped symmetric phases in one-dimensional spin systems. *Phys. Rev. B* **83,** 035107. https://link.aps.org/doi/10.1103/PhysRevB.83.035107 (3 Jan. 2011).
33. Schuch, N., Pérez-García, D. & Cirac, I. Classifying quantum phases using matrix product states and projected entangled pair states. *Phys. Rev. B* **84,** 165139. https://link.aps.org/doi/10.1103/PhysRevB.84.165139 (16 Oct. 2011).
34. Schollwöck, U. The density-matrix renormalization group in the age of matrix product states. *Ann. Phys* **326,** 96–192. ISSN: 0003-4916. https://www.sciencedirect.com/science/article/pii/S0003491610001752 (2011).
35. Orús, R. A practical introduction to tensor networks: Matrix product states and projected entangled pair states. *Annals Phys.* **349,** 117–158. ISSN: 0003-4916. https://www.sciencedirect.com/science/article/pii/S0003491614001596 (2014).
36. Verstraete, F., Murg, V. & Cirac, J. Matrix product states, projected entangled pair states, and variational renormalization group methods for quantum spin systems. *Adv. Phys* **57,** 143–224. https://doi.org/10.1080/14789940801912366 (2008).
37. Bañuls, M. C. Tensor Network Algorithms: A Route Map. *Annu. Rev. Condens. Matter Phys* **14,** null. https://doi.org/10.1146/annurev-conmatphys-040721-022705 (2023).
38. Silvi, P. *et al.* The Tensor Networks Anthology: Simulation techniques for many-body quantum lattice systems. *SciPost Phys. Lect. Notes,* 8. https://scipost.org/10.21468/SciPostPhysLectNotes.8 (2019).
39. Elben, A., Vermersch, B., Dalmonte, M., Cirac, J. I. & Zoller, P. Rényi Entropies from Random Quenches in Atomic Hubbard and Spin Models. *Phys. Rev. Lett.* **120,** 050406. https://link.aps.org/doi/10.1103/PhysRevLett.120.050406 (5 Feb. 2018).
40. Brydges, T. *et al.* Probing Rényi entanglement entropy via randomized measurements. *Science* **364,** 260–263. ISSN: 1095-9203. http://dx.doi.org/10.1126/science.aau4963 (Apr. 2019).
41. Huang, H.-Y., Kueng, R. & Preskill, J. Predicting many properties of a quantum system from very few measurements. *Nature Physics* **16,** 1050–1057. ISSN: 1745-2481. http://dx.doi.org/10.1038/s41567-020-0932-7 (June 2020).

42. Bluvstein, D. *et al.* Logical quantum processor based on reconfigurable atom arrays. *Nature.* ISSN: 1476-4687. http://dx.doi.org/10.1038/s41586-023-06927-3 (Dec. 2023).
43. Bravyi, S. & Kitaev, A. Universal quantum computation with ideal Clifford gates and noisy ancillas. *Phys. Rev. A* **71,** 022316. https://link.aps.org/doi/10.1103/PhysRevA.71.022316 (2 Feb. 2005).
44. Liu, Z.-W. & Winter, A. Many-body quantum magic. *PRX Quantum* **3,** 020333. https://link.aps.org/doi/10.1103/PRXQuantum.3.020333 (2022).
45. Gottesman, D. *Stabilizer codes and quantum error correction* (California Institute of Technology, 1997).
46. Gottesman, D. *The Heisenberg representation of quantum computers* 1998. eprint: arXiv:quant-ph/9807006. https://doi.org/10.48550/arXiv.quant-ph/9807006.
47. Aaronson, S. & Gottesman, D. Improved simulation of stabilizer circuits. *Phys. Rev. A* **70,** 052328. https://link.aps.org/doi/10.1103/PhysRevA.70.052328 (5 Nov. 2004).
48. Nahum, A., Ruhman, J., Vijay, S. & Haah, J. Quantum Entanglement Growth under Random Unitary Dynamics. *Physical Review X* **7.** ISSN: 2160-3308. http://dx.doi.org/10.1103/PhysRevX.7.031016 (July 2017).
49. Li, Y., Chen, X. & Fisher, M. P. A. Measurement-driven entanglement transition in hybrid quantum circuits. *Physical Review B* **100.** ISSN: 2469-9969. http://dx.doi.org/10.1103/PhysRevB.100.134306 (Oct. 2019).
50. Skinner, B., Ruhman, J. & Nahum, A. Measurement-Induced Phase Transitions in the Dynamics of Entanglement. *Physical Review X* **9.** ISSN: 2160-3308. http://dx.doi.org/10.1103/PhysRevX.9.031009 (July 2019).
51. Leone, L., Oliviero, S. F. E. & Hamma, A. Stabilizer Rényi Entropy. *Phys. Rev. Lett.* **128,** 050402. https://link.aps.org/doi/10.1103/PhysRevLett.128.050402 (5 Feb. 2022).
52. Leone, L. & Bittel, L. *Stabilizer entropies are monotones for magic-state resource theory* 2024. arXiv: 2404.11652 [quant-ph].
53. Haug, T. & Piroli, L. Quantifying nonstabilizerness of matrix product states. *Phys. Rev. B* **107,** 035148. https://link.aps.org/doi/10.1103/PhysRevB.107.035148 (3 Jan. 2023).
54. Haug, T. & Kim, M. Scalable Measures of Magic Resource for Quantum Computers. *PRX Quantum* **4,** 010301. https://link.aps.org/doi/10.1103/PRXQuantum.4.010301 (1 Jan. 2023).
55. Beverland, M., Campbell, E., Howard, M. & Kliuchnikov, V. Lower bounds on the non-Clifford resources for quantum computations. *Quantum Science and Technology* **5,** 035009. ISSN: 2058-9565. http://dx.doi.org/10.1088/2058-9565/ab8963 (June 2020).

Contents

Part I

Quantum simulation of many-body physics

Chapter 1

Quick overview of tensor networks

Quantum many-body systems, with their intricate interactions between a large number particles, hold the key to unraveling fundamental phenomena in quantum physics. Understanding these systems is thus crucial for both theoretical advancements and novel technological applications. However, investigating complex quantum systems presents a formidable challenge, which lies in the fact that the Hilbert space dimension grows exponentially with system size. Simulating such systems using classical computers requires resources that increase exponentially as well, quickly becoming intractable even for moderately sized systems.

Over the last decades, Tensor Network (TN) methods have emerged as a reliable tool to solve quantum many-body problems on a classical computer. They offer a compact description of quantum many-body states which possess limited entanglement, by exploiting the underlying entanglement structure. They have shown massive success in simulating one-dimensional (1D) systems and are increasingly being applied to higher dimensions. Beyond numerical simulations, Tensor Networks have also become valuable tools for theoretical investigations, such as in the classification of 1D gapped phases of matter [1–5].

This chapter provides a general overview on Tensor Networks, a tool which we have employed extensively throughout this thesis. Our focus here is not an exhaustive review – for that, we refer to established references such as [6–10]. Instead, we aim to introduce the core concepts behind Tensor Networks and how they are used in practice, while omitting technical details.

1.1 Tensor Networks in a nutshell

We will consider a quantum many-body system consisting of N qubits (or spin-1/2). Each qubit has a Hilbert space $\mathcal{H} \simeq \mathbb{C}^2$ spanned by the two basis states $|0\rangle, |1\rangle$. The total Hilbert space of N qubits is obtained as the tensor product of the local Hilbert spaces $\mathcal{H} \simeq \mathbb{C}^{\otimes 2n}$.

The most general (pure) quantum state can be written as

$$|\psi\rangle = c_{s_1 s_2 \ldots s_N} |s_1 s_2 \ldots s_N\rangle \tag{1.1}$$

where $s_i \in \{0, 1\}$ and $c_{s_1 s_2 \ldots s_N} = \langle s_1 s_2 \ldots s_N | \psi \rangle$ are the wavefunction coefficients. This representation captures the complete information about the wavefunction. However, the number of such coefficients that we need to specify is 2^N, that grows exponentially with the number of qubits. This makes it computationally impractical to describe quantum systems with many qubits in classical computers. As we shall see in the next sections, Tensor Networks offer a solution to this challenge. In a nutshell,

Tensor Networks represent quantum many-body systems by leveraging the underlying entanglement structure within the system. As such, Tensor Networks are extremely powerful at representing and simulating states with low entanglement. In such cases, Tensor Networks achieve a significant reduction in the number of parameters needed to describe the state, bringing it down from an exponential dependence on the number of qubits to a much more manageable polynomial dependence.

Tensor Network representation came about by viewing the coefficients $c_{s_1 s_2 \ldots s_N}$ as a tensor with N indices, each corresponding to each spin. Each indices thus has dimension 2 (for qubits). The key idea is to decompose the tensor $c_{s_1 s_2 \ldots s_N}$ as a network of smaller, interconnected tensors. These smaller tensors are connected through auxiliary indices which encode information about the correlations of the system. The dimension of these auxiliary indices are called the bond dimensions, usually denoted by χ, which represent its representation power. In essence, the bond dimension acts as a control parameter for the accuracy of the tensor network representation. If the bond dimension required to faithfully represent a state is finite (or at most polynomially growing), the Tensor Network representation is said to be efficient. This efficiency hinges on the entanglement structure of the state itself – states with lower entanglement require lower bond dimensions for faithful representation.

Depending on the way the tensors are connected, several Tensor Network geometries have been established over the last decades. The geometry of the Tensor Network plays a crucial role for the efficiency of Tensor Network algorithm as well as the capability to capture the entanglement scaling properties of the state. The most widely employed structures are the Matrix Product States (MPS), the Tree Tensor Networks (TTN) and the Projected Entangled Pair States (PEPS). They will be discussed in more details in Sec. 1.3.

1.2 Main concepts in Tensor Networks

In this section, we will review the fundamental concepts in Tensor Networks. We will begin from the mathematical foundation, which is rooted in linear algebra. This framework translates into concrete physical consequences in terms of quantum correlations within the wavefunction, which is reflected in the structure of Tensor Networks.

1.2.1 Singular Value Decomposition and QR decomposition

Singular Value Decomposition (SVD) is a linear algebra tool that is extensively used in tensor network. Here, we briefly recall its definition.

The SVD of an $m \times n$ complex matrix M is given by

$$M = USV^{\dagger}, \tag{1.2}$$

where $U(V)$ is an $m \times r$ ($r \times n$) complex matrix with orthonormal columns (rows) and S is an $r \times r$ diagonal matrix with non-negative real numbers elements. Here, $r = \min(m, n)$ is the rank of M, and the diagonal elements of S are called the singular values of M. The SVD is not unique, but the singular values are uniquely determined by M. Moreover, it is always possible to choose the decomposition such that the singular values are in descending order. Note that If M is real, then U and V are real orthogonal matrices. The computational complexity of the numerical algorithms for SVD is $O(mn^2)$, if $m \geq n$.

The power of SVD lies in its ability to provide the most efficient low-rank approximation of any matrix. Specifically, for a matrix M (rank r), we can construct a matrix $M' = US'V$ (with rank $r' \leq r$) that provides the optimal approximation of M in the Frobenius norm $\|M\| = \sqrt{\mathrm{Tr}(MM^\dagger)}$. Here, S' is obtained from S by keeping only the largest r' singular values.

In Tensor Network applications, it is often the case that one needs only the matrix U and the product $SV^\dagger$. In this case, the QR decomposition, which is given by

$$M = QR, \tag{1.3}$$

offers a computationally cheaper way. Here, Q is a matrix of dimension $m \times r$ with orthonormal columns, $Q^\dagger Q = 1$, and R is upper-triangular.

1.2.2 Entanglement and area law

For a pure state with two complementary partitions A and B, the entanglement with respect to the bipartition can be assessed by the Schmidt decomposition. For any pure state $|\psi\rangle$, there exists orthonormal bases $\{|\psi_A\rangle_i\}$ and $\{|\psi_B\rangle_i\}$ of A and B, such that $|\psi\rangle$ can be written as

$$|\psi\rangle = \sum_i \lambda_{i=1}^r |\psi_A\rangle_i |\psi_B\rangle_i , \tag{1.4}$$

where $\lambda_i > 0$ are the Schmidt coefficients. Such a decomposition can be obtained using SVD where the state is first rewritten as $|\psi\rangle = c_{(s_1 \ldots s_k),(s_{k+1} \ldots s_N)} |s_1 \ldots s_k\rangle_A |s_{k+1} \ldots s_N\rangle_B$. We can then perform SVD on the matrix $c_{(s_1 \ldots s_k),(s_{k+1} \ldots s_N)}$, obtaining $c_{(s_1 \ldots s_k),(s_{k+1} \ldots s_N)} = USV^\dagger$. Here, the columns of U correspond to the orthonormal bases of A, while the rows of V correspond to the orthonormal bases of B. Moreover, the singular values in S are precisely the Schmidt coefficients.

The amount of entanglement can be quantified using a suitable function of λ_i. The standard measure of entanglement is the von Neumann entanglement entropy, defined as

$$\begin{aligned} S &= -\mathrm{Tr}\, \rho_A \log \rho_A \\ &= -\sum_i \lambda_i^2 \log \lambda_i^2, \end{aligned} \tag{1.5}$$

where ρ_A is the reduced density matrix of the subsystem A, $\rho_A = \mathrm{Tr}_B[|\psi\rangle\langle\psi|]$. The entanglement entropy S is zero if and only if the state is a product state of A and B, and it is greater than zero otherwise. Moreover, it does not increase on average under local operation and classical communications (LOCC). It is upper bounded by $N_A \log 2$, where N_A is the number of qubits in the subsystem A.

Consider a D-dimensional system with linear system sizes L. Most states in the Hilbert space have entanglement entropy that scales extensively $S \sim L^D$, the so-called volume-law. However, if we consider ground states of local gapped Hamiltonians, they instead follow an area law, $S \sim aL^{D-1}$. Physically, the area law points out that entanglement is localized around the boundary between two subsystems. In 1D systems, where the area law implies the entanglement approaches a constant value in the thermodynamic limit, this has been rigorously proved to hold when the system is gapped [11]. For a 1D critical system described by conformal field theory (CFT), the entanglement entropy acquires a logarithmic correction to the area law [12]. In higher dimensions, there are fewer rigorous results on the area law. For free bosonic systems, the area law is shown to hold in any dimension [13]. The area

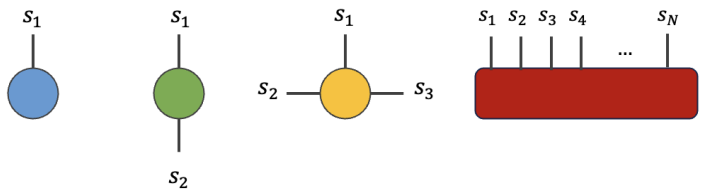

FIGURE 1.1: Graphical representation of (a) an order-1 tensor (i.e. a vector), (b) an order-2 tensor (i.e. a matrix) , (c) an order-3 tensor, and (d) an order-N tensor.

law also holds for non-critical free fermionic systems, while in critical fermionic systems, the area law is violated if the system exhibits a finite Fermi surface, in which case the entropy scales as $L^{D-1} \log L$ [14, 15]. However, in a fermionic model with zero-dimensional Fermi surface, numerical analysis showed that the corrections are sub-logarithmic [16]. In any case, it is expected that all ground states of lattice models satisfy such entanglement scaling governed by the area law, possibly with some corrections.

The area law signifies that relevant physical states occupy a tiny fraction of the entire Hilbert space. This result is extremely crucial as the family of Tensor Network states precisely targets these relevant area-law states.

1.2.3 Tensors

The fundamental building block of a Tensor Network is a tensor. From a mathematical point of view, an order-n tensor T is a multidimensional array with n indices. Each tensor element $T_{i_1,\ldots,i_n}$ is a scalar. For example, an order-1 tensor is a vector, while an order-2 tensor is a matrix. In Tensor Network applications, tensors are often visualized graphically, as illustrated in Fig. 1.1. Here, the tensors are represented by circles (or similarly closed shapess), while the indices are represented by outgoing legs. The contraction of two indices is obtained by connecting the legs representing the indices that are summed over. This graphical approach allows for a compact visual representation of complex tensor algebra equations using diagrams.

1.3 Tensor Network states

There are different ways to represent the coefficient $c_{s_1 s_2 \ldots s_N}$ as a Tensor Network, depending on the geometry of the network. This leads to different classes of Tensor Network states. Here, we review some of the prevalent Tensor Network states.

1.3.1 Matrix Product States (MPS)

Matrix Product States (MPS) are the first and the most commonly used Tensor Network states [6, 17]. The MPS representation is given by

$$c_{s_1 s_2 \ldots s_N} = \sum_{a_1,\ldots,a_{N-1}} A^{s_1}_{a_1} A^{s_2}_{a_1,a_2} \ldots A^{s_N}_{a_{L-1}}, \tag{1.6}$$

where $A^{s_i}_{a_{i-1},a_i}$ are order-3 tensors (except at the left and right boundaries where they are order-2 tensors). The index s_i corresponds to the physical index, while the other two are auxiliary indices. Its graphical representation is shown in Fig. 1.2(a). The

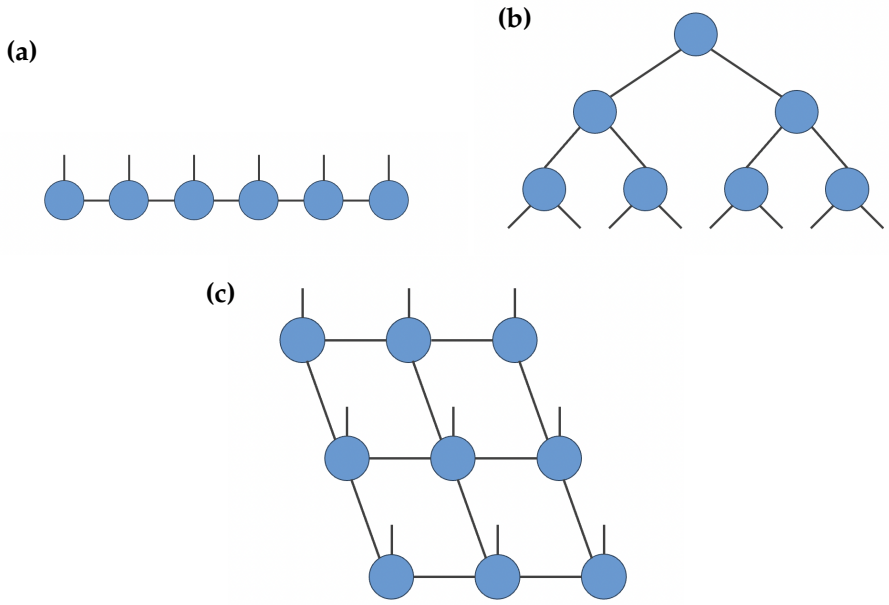

FIGURE 1.2: Various Tensor Network geometries: (a) MPS and (b) TTN for 1D systems, (c) PEPS for 2D systems.

dimension of each auxiliary index, $\chi_i = \dim(a_i)$, determines the amount of entanglement that the MPS captures. We denote the maximum value of χ_i across all links as χ, which is known as the bond dimension of the MPS.

Any quantum state $|\psi\rangle$ can be decomposed as an MPS by performing repeated SVD decomposition. The important question is: when is it useful to work with MPS representation? The answer to this question lies in the entanglement properties of the state. Indeed, one can show that the von Neumann entanglement entropy of an MPS is bounded by

$$S \leq \log \chi \tag{1.7}$$

Thus, a state with bounded entanglement can be expressed as an MPS with $\chi \sim \exp(S)$. When χ is finite (or grows at most polynomially with N), the MPS representation is efficient. Namely, the total number of parameters is reduced from an exponential $O(e^N)$ to a polynomial $O(poly(N))$ with respect to system size N, thus the simulation requires only polynomial resources. This points to the main reason of the success of MPS in the investigation of 1D systems in equilibrium: in 1D, it is well-known that all gapped phases obey the area law with $S \sim O(1)$, while critical states governed by conformal field theory may exhibit a logarithmic scaling $S \sim \log N$. In both cases, the MPS representation is efficient. In out-of-equilibirum dynamics or higher-dimensional systems, the entanglement is expected to grow with the system size and time (with known exceptions), thus the bond dimension required to faithfully represent the state as an MPS must grow exponentially. Nevertheless, MPS has proven valuable in their investigations, by making use of the established MPS algorithms and pushing the bond dimension to a large value [18, 19].

The tensor contractions and manipulations in MPS can be done efficiently with cost $O(\chi^3)$. More generally, any Tensor Network state which contains no loop in its structure can be contracted efficiently. Such Tensor Network state is called loopless tensor network, of which MPS is the simplest example.

1.3.2 Tree Tensor Networks (TTN)

Tree Tensor Network (TTN) is another example of loopless tensor network [7, 20]. In TTN, the tensors are arranged in a tree structure as shown in Fig. 1.2(b). The complexity of TTN contraction is $O(\chi^4)$, that is slightly more expensive than MPS. The advantage of TTN lies in its strongly connected structure: the distance between two tensors are at most $O(\log N)$ in the TTN structure, as opposed to $O(N)$ in MPS. Consequently, TTN is able to represent states with polynomally decaying correlations, such as 1D critical systems. Moreover, with its flexible geometry, it is particularly suited to handle systems with periodic boundary conditions and higher dimensional systems, while maintaining efficient manipulation.

1.3.3 Projected Pair Entangled State (PEPS)

Projected Pair Entangled State (PEPS) is a natural extension of MPS to two-dimensional (and higher) systems [9, 17], as depicted in Fig. 1.2(c). The structure of PEPS inherently capture states that obey the area law of entanglement in any dimension. However, unlike MPS, PEPS contains many loops within their structure, hindering efficient contraction. This makes PEPS considerably more challenging to handle, both analytically and numerically.

1.4 Tensor Network algorithms

Tensor Networks have various algorithms for a broad range of applications. Below, we describe two of the most prominent algorithms using Tensor Networks.

1.4.1 Ground state search

The most common application of Tensor Networks is to solve a given many-body Hamiltonian H for its ground state, i.e., an eigenstate with the lowest energy. For this purpose, the Tensor Network is treated as a variational ansatz with some chosen bond dimension, and the algorithm is designed to optimize the variational parameters of the Tensor Network ansatz $|\psi\rangle$ by minimizing the energy

$$E = \frac{\langle\psi| H |\psi\rangle}{\langle\psi|\psi\rangle}. \tag{1.8}$$

For MPS and TTN, such minimization problem can be formulated as an eigenvalue problem in terms of the local tensors, which can then be solved one at a time. This is the core idea of the well-known density matrix renormalization group (DMRG) for MPS, and a similar algorithm for TTN [7, 20].

1.4.2 Time evolution

Another important Tensor Network algorithm is the simulation of time evolution under a unitary dynamics. There are two established methods for performing such a time evolution. The first, and the most intuitive, algorithm is Time-Evolving Block Decimation (TEBD) [21], which is based on decomposing the unitary evolution by means of a Suzuki-Trotter decomposition into a set of local operators to be applied to the network. The second method is the Time-Dependent Variational Principle (TDVP) [22, 23], which exploits mathematical concepts of differential calculus to compute a time evolution based on the geometry of the network. Despite of these

well-established algorithms, it is important to note that simulations of time evolution are typically limited to small system sizes in 1D or short time-scales. This is because the entanglement in non-equilibrium dynamics typically scales as volume-law, thus it is not efficiently simulable with Tensor Networks.

1.5 Final remarks

The tools and concepts introduced in this chapter have been applied extensively in much of the work presented in this thesis. Our simulations are done using the C++ iTensor library [24], in which MPS algorithms like the DMRG and TDVP are readily available. Additionally, we have implemented TTN codes in iTensor, which were utilized in Chapter. 7.

Chapter 2

Quantum simulation of spin liquids

Quantum spin liquids (QSLs) are a fascinating phases of matter which have captivated the attention of physicists for decades. These phases exhibit exotic quantum properties, such as long-range entanglement, topological degeneracy, and fractionalized excitations.

Due to their exotic properties, QSLs hold potential applications in quantum computing technologies, and therefore, the experimental realization of QSLs is of considerable interest. This remains a major challenge in the field despite intense theoretical efforts. The main obstacle lies in the fact that most theoretically established models that support QSLs involve interactions that encompass multi-body (more than two) interactions. This differs from the interactions that naturally occur in experimental setups, which typically involve only two-body interactions. However, recent advances in the synthetic platforms based on Rydberg atoms, i.e., neutral atoms trapped in optical tweezers, have opened up new avenues for exploring novel quantum phases in these platforms. In recent years, several numerical studies have predicted the appearance of QSLs in two distinct experimental setups of Rydberg atom arrays [25–28], with pioneering experiments already reporting evidence for realization of QSL in the "toric code" phase [29].

In this chapter, we will introduce some of the key concepts on this topic that will be relevant throughout Part I. In Section 2.1, we describe the experimental platform of Rydberg atom arrays. In Section 2.2, we discuss how $\mathbb{Z}_2$ QSLs emerge in the framework of $\mathbb{Z}_2$ gauge theory. Finally, in Section 2.3, we review the parton construction and projective symmetry group (PSG) classification of spin liquids, which could be used as a tool to identify QSLs in experimentally relevant models.

2.1 Rydberg atom arrays

Quantum simulation has emerged as a powerful tool for understanding quantum many-body systems. It involves building a synthetic quantum system in the lab, implementing a theoretical model of interest which is inaccessible using classical simulations. This idea dates back to Richard Feynmann [30], but only in the last two decades that significant advancements in experimental techniques have finally made quantum simulation becomes a reality. State-of-the-art quantum simulators have been able to simulate systems reaching hundreds of qubits.

Among all the platforms being developed, Rydberg atom arrays have come to the forefront of synthetic quantum systems [31]. These consist of ensembles of individual neutral atoms trapped in optical lattices or optical tweezers, that are almost fully

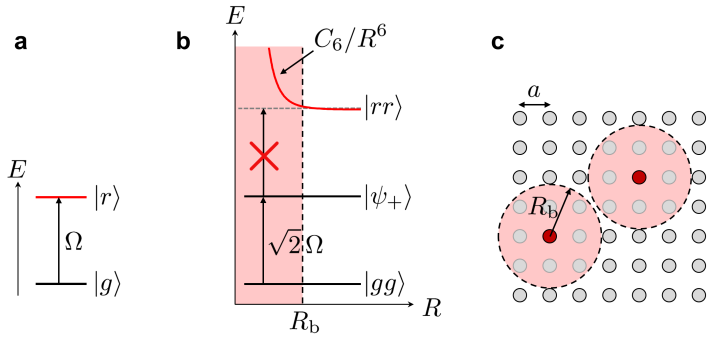

FIGURE 2.1: **a:** The ground and Rydberg states $|g\rangle$ and $|r\rangle$ are coupled by a resonant laser with Rabi frequency Ω. **b:** For two atoms separated by a distance $R < R_b$, the collective ground state $|gg\rangle$ is coupled only to $|\psi_+\rangle = (|gr\rangle + |rg\rangle)/\sqrt{2}$, but not to $|rr\rangle$, as this is forbidden by the strong van der Waals interaction. **c:** In an array of atoms with lattice spacing a, an atom in the Rydberg state $|r\rangle$ (denoted by red circle) prevents the excitation of all the atoms contained in a sphere of radius R_b. Figures taken from Ref. [31].

controllable and tunable. The atomic states are coupled via a laser excitation to a Rydberg state, i.e., a state with large principal quantum number n.

The large electric dipole moment of atoms excited to Rydberg states leads to strong dipole-dipole interactions between them. There are two types of interaction naturally occur between two Rydberg atoms, which leads to a mapping onto Ising and XY Hamiltonians, respectively.

2.1.1 Blockade interactions

The Rydberg excitations are modeled as hard-core bosons with the mapping $|0\rangle = |g\rangle$ and $|1\rangle = |r\rangle$, where $|g\rangle, |r\rangle$ are the ground and Rydberg state, respectively. We introduce the creation and annihilation operators $b_j, b_j^\dagger$, with the operator $n_j = b_j^\dagger b_j$ signals the presence of a Rydberg excitation at site j. The Hamiltonian is given by [32]

$$H_{\text{Ryd}} = -\Omega \sum_j (b_j + b_j^\dagger) - \delta \sum_j n_j + \sum_{i \neq j} V_{i,j} n_i n_j, \tag{2.1}$$

which is equivalent to the Ising Hamiltonian with transverse and longitudinal field in the spin language. Here, Ω is the Rabi frequency, δ is the detuning of the laser, and $V_{i,j}$ is the strength of the van der Waals-type interactions between two Rydberg atoms at sites i and j. The latter is strongly repulsive at short distances and decays as $1/r^6$ at large distances, where $r = |i - j|$ is the distance between the two atoms. This interaction profile is very well approximated by 'blockade interaction', namely

$$V_{i,j} = \begin{cases} \infty, & \text{if } |i-j| \leq R_b \\ 0, & \text{otherwise}, \end{cases} \tag{2.2}$$

where R_b is the blockade radius defined from $V(R_b) = \Omega$. This induces an effective constraint $n_i n_j = 0$ at low energies, known as *Rydberg blockade* [33]: simultaneous excitation of two atoms within the blockade radius to the Rydberg state is forbidden. This Rydberg blockade interaction is schematically illustrated in Fig. 2.1.

In 1D, when the blockade extends only to nearest-neighbors, the resulting effective model is equivalent to the model first introduced by Fendley, Sengupta, Sachdev (FSS) [34], that can be directly related to exactly soluble classical statistical mechanics systems in some parameter regimes. In recent years, it is also known as the PXP model. Such a constrained dynamics could lead to a plethora of interesting phenomena, such as quantum many-body scars [35, 36]. The dynamics described by H_{Ryd} has already been realized in several experiments utilizing either optical lattices or optical tweezers [37–42]. More recently, Ref. [29] implemented the blockade which extends to third nearest neighbors on the Ruby lattice, discovering signatures of quantum spin liquids in some parameter regimes.

2.1.2 Dipolar exchange interactions

In a different scenario, the atoms belong to the same Rydberg manifold and differ, e.g., by their total angular momentum, such as $|nS\rangle$ and $|nP\rangle$. The mapping to hard-core bosons is then given by $|0\rangle = |nS\rangle$ and $|1\rangle = |nP\rangle$. Here, the dipole-dipole interaction leads to a coherent exchange of photons, thus flipping the internal states of the atoms. This results in an effective interaction potential that scales as $1/r^3$. The Hamiltonian reads

$$H = -\Omega \sum_j (b_j + b_j^\dagger) - \delta \sum_j n_j + \sum_{i \neq j} \frac{C_3}{|i-j|^3} (b_i b_j^\dagger + b_j b_i^\dagger), \tag{2.3}$$

which is equivalent to the XY Hamiltonian with transverse and longitudinal field. The model has been realized in [43] in a two-dimensional square lattice, which demonstrated true long-range ferromagnetic order in 2D for the first time.

2.2 $\mathbb{Z}_2$ lattice gauge theory

As mentioned above, Rydberg atom arrays have emerged as a powerful platform for exploring exotic phases of matter in the lab, including QSLs. In this section, we discuss how the emergence of QSLs can be understood within the framework of $\mathbb{Z}_2$ lattice gauge theory (LGT).

2.2.1 Toric code

Before embarking on the discussion of $\mathbb{Z}_2$ LGT, we will first review the toric code model introduced by Kitaev [44] as a simplest LGT.

We consider a $L \times L$ square lattice on the torus, and we put the spins at the edges of the lattice. There are thus $N = 2L^2$ qubits. We define the star operators S_s and plaquette operators P_p on the vertices and plaquettes, respectively, as (see Fig. 2.2(a)):

$$S_s = \prod_{i \in s} \sigma_i^x, \qquad P_p = \prod_{i \in p} \sigma_i^z, \tag{2.4}$$

where $\sigma^{x,z}$ are the Pauli operators. The toric code Hamiltonian has the form

$$H_{\text{TC}} = -J \sum_s S_s - J' \sum_p P_p. \tag{2.5}$$

It is easy to check that S_s and P_p form a mutually commuting set. Therefore, a ground state of H_{TC} minimizes each individual term in Eq. (2.5), i.e, $S_s = 1$ and $P_p = 1$ for all vertices and plaquettes. A Hamiltonian with this property is also known as a

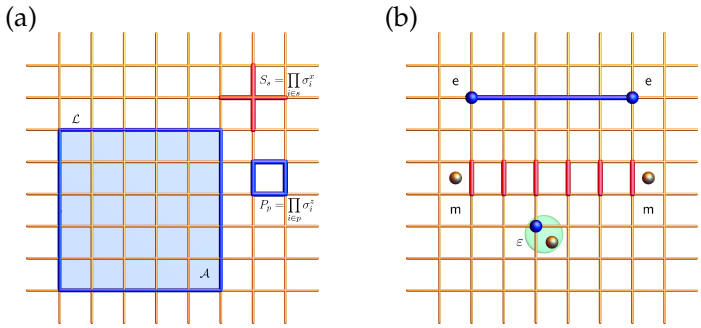

FIGURE 2.2: (a) Operators in the toric code on the square lattice. Blue and red links denote σ_i^x and σ_i^z operators, respectively. A star S_s and plaquette P_p are shown, as is a loop operator on the contour $\mathcal{L}$ enclosing the area $\mathcal{A}$. (b) Anyons in the toric code. A pair of e particles is created at the ends of a string of σ_i^x operators as shown. Similarly, a pair of m anyons is created at the ends of a string of σ_i^z operators, as indicated. The ε anyon is defined as the composite particle of an e and m particle. Figures taken from Ref. [45].

frustration-free Hamiltonian. Note that the ground state is not unique; there is fourfold degeneracy if the system is placed on a torus. These degenerate groundstates are characterized by topological string operators, which we will discuss in more detail below. More generally, the groundstate degeneracy is 4^g if the system is placed on an orientable manifold with boundaries with genus g.

The groundstates can be intuitively understood using a graphical representation. Let us consider the σ^x basis, and we represent the $\sigma^x = -1$ by a string. Due to the constraint $S_s = 1$, an even number of strings must emanate from each vertex, implying that these strings form closed loops. Furthermore, the constraint $P_p = 1$ effectively generates a superposition of loop configurations. More specifically, the state with $P_p = 1$ is the equal-weight superposition of all possible loop configurations that are related to one another by the flip of square plaquettes.

The groundstates can be characterized by the t'Hooft loop operators

$$T_{x,y} = \prod_{i\in c_{x,y}} \sigma_i^x \tag{2.6}$$

and the Wilson loop operators

$$W_{x,y} = \prod_{i\in c'_{x,y}} \sigma_i^z. \tag{2.7}$$

Here, $c_{x,y}$ is a loop (closed path) that winds around the torus in the $x(y)$ direction, whereas $c'_{x,y}$ is a cut, i.e. a loop on the dual lattice defined analogously. The string operators $T_{x,y}, W_{x,y}$ have the same commutation relations as $\sigma^z_{1,2}, \sigma^x_{1,2}$, and thus the ground state space corresponds to a state of two qubits, i.e., the degeneracy is fourfold.

The low-energy excitations can also be described in a rather simple way. An elementary excitation occurs if one has $S_s = -1$ or $P_p = -1$ at a given vertex or plaquette. These excitations are referred to as "electric" (e) and "magnetic" (m) excitations, respectively. Alternatively, they are also called spinon and vison in the literature. Because of the relations $\prod_s S_s = 1$ and $\prod_p P_p = 1$, there must be at least two vertices (plaquettes) such that $S_s = -1$ ($P_p = -1$). It follows that the elementary excitations cannot be created individually; they must be created in pairs. One can

create a pair of elementary excitations by applying a string of $\sigma^z(\sigma^x)$ to an arbitrary ground state, in which case the excitations would live at each end of the string (see Fig. 2.2(b)).

The nonlocal nature of the e and m excitations in the toric code manifests in their unusual braiding statistics. Consider an m particle placed at the origin and an e particle moved around it in a closed loop (see Fig. 2.2(b)). Moving the e particle one link at at a time by acting with σ_i^z operators, where i labels the connecting link, results in a final state related to the initial state by the action of a product of spins around the closed loop $\mathcal{L}$

$$|\psi_{\text{fin}}\rangle = \prod_{i\in\mathcal{L}} \sigma_i^z \, |\psi_{\text{init}}\rangle \, . \tag{2.8}$$

One can see that the product of σ_i^z can be written as a product of plaquette operators:

$$\prod_{i\in\mathcal{L}} \sigma_i^z = \prod_{p\in\mathcal{A}} P_p, \tag{2.9}$$

where $\mathcal{L} = \partial\mathcal{A}$ is the closed loop and $\mathcal{A}$ is the region enclosed by the loop. Since the initial state has an m particle inside $\mathcal{L}$, exactly one P_p in this product will be negative. This results in a negative sign in the final state:

$$|\psi_{\text{fin}}\rangle = - \, |\psi_{\text{init}}\rangle \, . \tag{2.10}$$

This phase factor of -1 (or a π phase shift) acquired by the state upon moving one particle around another (of different type) highlights their "mutual statistics". Particles exhibiting such behavior are called anyons. Due to this property, a composite particle formed by combining an e and an m particle would exhibit fermionic self-statistics.

The existence of anyons can be seen as a fundamental property of the toric code. For example, the ground state degeneracy on the torus can be directly attributed to the existence of anyonic excitations within the system [46].

2.2.2 Ising gauge theory

As we shall see below, the toric code in fact emerges in a particular limit of an Ising gauge theory. We again consider a $L \times L$ square lattice, with the spins at the edges of the lattice. Here, the spins represent $\mathbb{Z}_2$ gauge fields. The Hamiltonian of the Ising gauge theory has the form

$$H_{\text{Ising}-\text{GT}} = -J \sum_p P_p - g \sum_i \sigma_i^x. \tag{2.11}$$

The model is invariant under the Gauss' law operators

$$G_s = \prod_{i\in s} \sigma_i^x, \tag{2.12}$$

defined on each site s. Consequently, we can work in the sector with fixed values of G_s. Usually, one would consider the sector $G_s = 1$, i.e., the physical states are gauge-invariant, meaning that $G_s \, |\psi\rangle = |\psi\rangle \, , \forall s$ (Gauss' law). This sector is also called the "even" Ising gauge theory. Instead, the "odd" Ising gauge theory corresponds to the sector $G_s = -1, \forall s$.

It is instructive to consider the various limits of $H_{\text{Ising}-\text{GT}}$. Firstly, for $g/J \to 0$, the model reduces to the toric code discussed in the previous section, i.e., the

phase is topologically ordered. The phase hosts excitations that can be separated at any distance with finite energy cost; we say that the excitations are deconfined. Conversely, for $g/J \to \infty$, the phase is a trivial paramagnet. In this case, it takes a large energy cost (specifically, linear with distance) to separate two excitations; we say that the excitations are confined. We thus expect that there is a phase transition at some $(g/J)_c$ between the deconfined (toric code) and confined (paramagnetic) phase.

Interestingly, it is known that $H_{\text{Ising}-\text{GT}}$ can be transformed to the 2D transverse-field Ising model through a duality known as Wegner duality [47]. Therefore, the location of the transition is given exactly by the critical point of the 2D transverse-field Ising model.

2.2.3 Ising-Higgs gauge theory

One can couple the Ising gauge theory to matter; the resulting theory is called the Ising-Higgs gauge theory. The matters live on the vertices of the lattice, and we denote the matter operators by $\tau^{x,z}$. The Hamiltonian reads

$$H_{\text{Ising}-\text{Higgs}} = -J\sum_p P_p - h_x\sum_i \sigma_i^x - h_z\sum_i \sigma_i^z \prod_{\ell\in\partial i}\tau_\ell^z - m\sum_\ell \tau_\ell^x. \tag{2.13}$$

The Gauss' law operators become

$$G_s = \tau_s^x \prod_{i\in s}\sigma_i^x. \tag{2.14}$$

By integrating out the matter field, the model is transformed to the toric code in parallel magnetic field

$$H = -J\sum_p P_p - \prod_{i\in s}\sigma_i^s - h_z\sum_i \sigma_i^z - h_x\sum_i \sigma_i^x. \tag{2.15}$$

There exists a duality that interchanges h_x and h_z. The phase diagram of the model has been obtained with Quantum Monte Carlo in [48, 49]. There are three distinct phases: topological, e-condensed, and m-condensed phases (see Fig. 2.3). The transitions from the topological phase to the two condensed phases are both second-order. The second-order transition lines merge into a first-order line that lies on the self-dual line ($h_x = h_z$). The three transition lines have been conjectured to meet at a multicritical point, although numerical simulations have not been able to show this conclusively [48].

2.3 Parton construction of spin liquids

In this section, we review the parton construction for quantum spin liquids in spin $S = 1/2$ systems. Building upon this construction, we then discuss the PSG classification of spin liquids. We recall that quantum spin liquids are phases of matter that do not (spontaneously) break any symmetry, and yet they are distinct from a trivial phase. The PSG classification offers a systematic approach to classify all possible QSLs based on symmetry considerations and how these symmetries manifest in the parton representation of the spins.

Our focus here will be on the slave-boson (Abrikosov fermion) approach [50, 51]. While the slave-fermion (Schwinger boson) approach also exists, it is limited to describing gapped spin liquids.

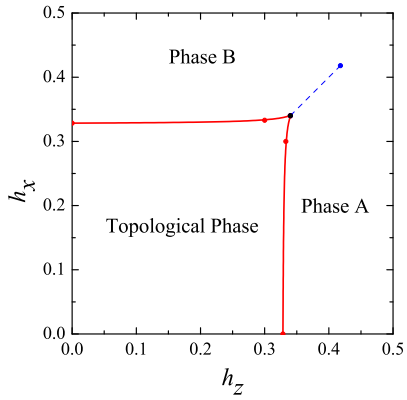

FIGURE 2.3: Phase diagram of the toric code model in magnetic field. The second-order transition lines are shown by full (red) lines and the first-order transition line is represented by dashed (blue) line. Phase A is the e-condensed phase and Phase B is the m-condensed phase. Figure taken from Ref. [48].

The core step of the construction is to write spin operators in terms of spinon operators. The latter are effective low-energy quasiparticles carrying a fractional spin quantum number. The spin operators are represented by

$$S^a = \frac{1}{2} f_i^\dagger \sigma_{ij}^a f_j \tag{2.16}$$

for $a \in \{x, y, z\}$. Here σ^a are Pauli matrices and f_i, $i \in \{\uparrow, \downarrow\}$, are the fermionic spinon operators. Notice that the local Hilbert space dimension is doubled as a result, since the fermionic Fock space is four-dimensional. The equivalence is thus only valid by imposing a constraint that there is exactly one spinon per site

$$f_i^\dagger f_i = 1, \tag{2.17}$$

while all the other fermionic states are unphysical.

In the following, it is convenient to introduce a two-component spinor

$$\Psi = (f_\uparrow \, f_\downarrow^\dagger)^T. \tag{2.18}$$

The f-fermion states and the Ψ-fermion states have the following relation

$$\begin{aligned} |0_f\rangle &= \Psi_2^\dagger |0_\Psi\rangle \\ f_\downarrow^\dagger |0_f\rangle &= |0_\Psi\rangle \\ f_\uparrow^\dagger f_\downarrow^\dagger |0_f\rangle &= \Psi_1^\dagger |0_\Psi\rangle \\ f_\uparrow^\dagger |0_f\rangle &= \Psi_1^\dagger \Psi_2^\dagger |0_\Psi\rangle \end{aligned} \tag{2.19}$$

Therefore, the constraint $f_i^\dagger f_i = 1$ is equivalent to the constraint that there are even Ψ-fermion, with the empty state corresponds to down-spin and the doubly-occupied state corresponds to the up-spin state.

One can verify that the representation in Eq. (2.16) is unchanged under $SU(2)$ transformations on Ψ, i.e., $\Psi \to g\Psi$, where g is an $SU(2)$ matrix. As this can be performed independently on each site of a lattice, this leads to $SU(2)$ gauge symmetry on the spinon representation. The additional gauge symmetry implies that there

is some flexibility in how physical (spin) symmetries manifest within the spinon Hilbert space. If the original spin model possesses a symmetry x, the corresponding symmetry in the spinon space can be realized with an additional $SU(2)$ gauge transformation g_x. In this case, we say that the symmetry group is (projectively) represented in the spinon Hilbert space.

For spin models which possess spin-spin interactions (e.g. quantum Heisenberg models), directly rewriting the spins in terms of spinons using Eq. (2.16) gives rise to quartic spinon interactions, which do not lead to a solvable model. Nevertheless, one can perform a mean-field approximation to transform it into a quadratic spinon Hamiltonian

$$H_{MF} = \sum_{ij} \Psi_i^\dagger u_{ij} \Psi_j + \text{h.c.} \sum_i \lambda_i^a \Psi_i^\dagger \sigma_a \Psi_i, \tag{2.20}$$

which is then solvable. Here, u_{ij} are the mean-field amplitudes which include hopping and pairing terms, and λ_i^a are the on-site potentials.

The matrices u_{ij} can be written as $u_{ij} = u_{ij}^\mu \tau^\mu$, where $(\tau^\mu) = (i\sigma^0, \sigma^a)$, u_{ij}^μ are complex parameters and σ^a are Pauli matrices. Real u_{ij}^μ correspond to singlet terms, while imaginary u_{ij}^μ correspond to triplet terms. Different mean-field ansätze are labeled by different $\left[u_{ij}, \lambda_i\right] = \left[u_{ij}^\mu \sigma^\mu, \lambda_j^a \sigma^a\right]$. The core of the PSG classification is to determine all possible $\left[u_{ij}, \lambda_i\right]$ which produces physical wavefunctions respecting certain symmetries of interest. For a given ansatz labeled by $\left[u_{ij}, \lambda_i\right]$, the corresponding physical spin state is obtained by applying Gutzwiller projection

$$|\psi\rangle = P_G |\psi_{MF}\rangle, \tag{2.21}$$

with $P_G = \prod_i n_i(2 - n_i)$, to the mean-field ground state $|\psi_{MF}\rangle$. Expectation values in such wavefunctions can be efficiently computed numerically using variational Monte Carlo (VMC) techniques [52].

In this section, we restrict ourselves to real u_{ij}^μ when the full $SU(2)$ spin rotation symmetry is preserved. In this case, the mean-field amplitudes u_{ij} can be written as $(u_{ij}^\mu) = (\chi_{ij}^1, \eta_{ij}^1, \eta_{ij}^2, \chi_{ij}^2)$ where $\chi_{ij} = \chi_{ij}^1 + i\chi_{ij}^2$ are complex hopping and $\eta_{ij} = \eta_{ij}^1 + i\eta_{ij}^2$ are singlet pairing terms. We can then write in a compact form

$$u_{ij} = \begin{pmatrix} \chi_{ij} & \eta_{ij} \\ \eta_{ij}^* & -\chi_{ij}^* \end{pmatrix} \tag{2.22}$$

One can verify that the spinon Hamiltonian in Eq. (2.20) is invariant under $SU(2)$ gauge transformation g_i

$$\begin{aligned} \Psi_i &\to g_i \Psi_i \\ u_{ij} &\to g_i u_{ij} g_j^\dagger \\ \lambda_j &\to g_j \lambda_j g_j^\dagger \end{aligned} \tag{2.23}$$

The presence of gauge symmetry in the spinon Hilbert space leads to a crucial implication: if two mean-field ansätze are related by a gauge transformation, they will lead to the same physical spin state using the Gutzwiller projection in Eq. (2.21). This implies that the invariance of a physical wavefunction under a symmetry transformation only requires the invariance of the corresponding mean-field ansatz up to a gauge transformation.

Consequently, we can classify mean-field ansatz using PSG, which distinguishes

between phases that have the same physical symmetries. More specifically, PSG contains all symmetry transformations x that leave the physical wavefunction invariant, along with the corresponding gauge transformation g_x. We will call the group of symmetry transformations SG. Then we can write $Q_x(u) = (g, x) \in \text{PSG}$, which action on the ansatz $u = \left[u_{ij}, \lambda_j\right]$ is

$$Q_x(u) = \left[g_i u_{x^{-1}(i,j)} g_j^\dagger, g_j \lambda_{x^{-1}(j)} g_j^\dagger\right]. \tag{2.24}$$

The multiplication law in this group is

$$Q_x Q_y = (g_x, x)(g_y, y)(g_x x g_y x^{-1}, xy), \tag{2.25}$$

and the inverse element is

$$Q_x^{-1} = (g_x)^{-1} = (x^{-1} g^{-1} x, x^{-1}). \tag{2.26}$$

The invariance of an ansatz under its PSG requires that $Q_x(u) = u$ for unitary transformations and $Q_x(u) = -u$ for anti-unitary transformations.

Every PSG contains an important subgroup of gauge transformations that leave the mean-field Hamiltonian invariant known as the invariant gauge group (IGG), i.e., $g(u) = u$ for all $g \in \text{IGG}$. It always contains $\mathbb{Z}_2$ as a subgroup since global transformations $g_j = \pm 1$ leave any ansatz invariant. Typically, it is either $SU(2), U(1)$, or $\mathbb{Z}_2$. The IGG characterizes the emergent low-energy gauge fluctuations in the effective theory. For example, if IGG $= \mathbb{Z}_2$, the emergent gauge bosons are gapped and expected to be irrelevant at low energy. However, if IGG $= U(1)$ or IGG $= SU(2)$, the gauge bosons ("photons" or "gluons") are gapless and may strongly affect the low-energy physics. Depending on the IGG of its ansatz, a spin liquid is said to have a $\mathbb{Z}_2, U(1)$, or $SU(2)$ gauge structure. The IGG is related to the PSG through the following relation

$$\text{SG} = \text{PSG}/\text{IGG}. \tag{2.27}$$

This relation tells us that a PSG is a projective representation or an extension of the symmetry group. Once we specify the PSG, we can subsequently construct the corresponding ansätze that respect those symmetries.

As a final remark, it is important to discuss the effect of fluctuations on the mean-field states. Some mean-field states are stable against fluctuations. For such stable states, the corresponding PSG accurately captures the underlying quantum order in the physical spin liquids. As mentioned above, this is for example the case when the IGG $= \mathbb{Z}_2$, where gauge fluctuations are gapped via the Anderson-Higgs mechanism. Alternatively, the Chern-Simons mechanism can also gap out gauge bosons, leading to chiral spin liquids. Conversely, there are mean-field states that are unstable against fluctuations. In these cases, the PSG may not accurately reflect any real quantum order within the spin liquid.

Chapter 3

Gauge-theoretic origin of Rydberg quantum spin liquids

Introduced by Kitaev as a model for fault-tolerant quantum computation, the toric code is one of the most renowned examples of topological order [44]. Its ground state, a $\mathbb{Z}_2$ quantum spin liquid (QSL) characterized by long-range entanglement, topological degeneracy and fractionalized excitations, has had a profound impact on both quantum information and condensed matter physics [45, 53]. In particular, it has shed considerable light onto the use of topological matter to encode quantum information in a robust manner. One of its key elements is its particularly clear connection to the gauge-theoretical origin of QSLs [54–57]: the presence of a $\mathbb{Z}_2$ gauge symmetry allows to interpret the latter as a deconfined phase of matter, where excitations (e.g., anyons) can be separated at arbitrary distance at finite energy cost, in sharp contrast to what happens in confined phases [58, 59].

Despite the aforementioned clear theoretical interpretation, experimentally observing such deconfined phases has proven challenging, mostly because directly engineering the toric code is highly non-trivial. A recent development has been the proposal that topological QSL can be realized in Rydberg atom arrays [31, 60, 61]: in these systems, constraints akin to Gauss laws (or, equivalently, dimer constraints [62]) are imposed by means of the phenomenon of Rydberg blockade [33, 63–67].

Recent numerical work has reported signatures of QSLs in a constrained model on the Ruby lattice, both at equilibrium [25] and at the level of diabatic state preparation [68]: in the following, we will refer to this state as a Rydberg quantum spin liquid (RQSL). In a similar model [29], strong signatures of deconfinement of a gauge theory have also been observed in experiments, albeit not yet in the ground state. Despite these remarkable results, the theoretical origin of such a deconfined phase remains so far unclear. While the similarity between the Rydberg blockade and a dimer constraint suggests that the RQSL phase can be understood as a resonant dimer state on the kagome lattice (which is known to be a $\mathbb{Z}_2$ QSL state [69, 70]), this interpretation is challenged by the fact that no QSL phase is found in the dimer-model limit. In fact, signatures of a QSL are observed only when a moderate density of *monomers* is present: if this density is too low or too high the system will be in a crystalline or in a trivial phase, respectively. It remains an open question what is the mechanism that can allow for the emergence of topological order in such a small range of densities, with the additional crux that, at odds with gauge-theoretical expectations [59, 71], such a QSL appears in the absence of plaquette terms.

Here we address this conundrum by proving an exact mapping between $\mathbb{Z}_2$ lattice gauge theories [72] on the kagome lattice and a class of constrained models on the ruby lattice. Using this connection, we find a regime where topological order can be analytically established, showing how a resonating valence bond (RVB) [55] state

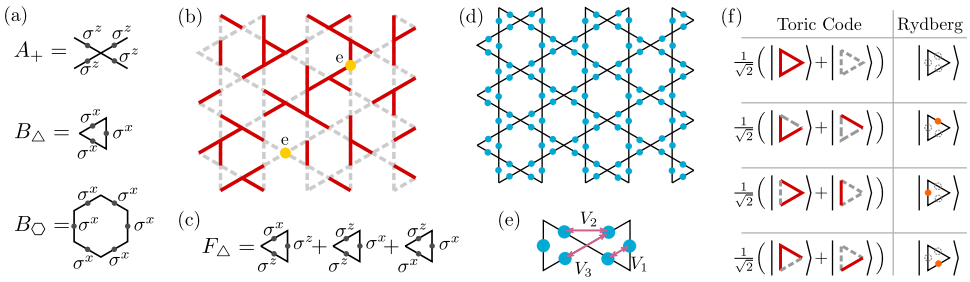

FIGURE 3.1: (a) Definition of vertex operators A_+ and plaquette operators $B_\triangle$, $B_\hexagon$. (b) Example of a configuration in the σ_z basis: links marked with red solid (grey dashed) lines correspond to $\sigma^z = +1$ ($\sigma^z = -1$). Electric excitations are located on vertices with $A_+ = 1$. (c) Definition of the operator $F_\triangle$. (d) Examples of atom positions on the ruby lattice, formed by the midpoints on the links of a kagome lattice. (e) Definition of the interaction terms: nearest, next-nearest, and next-next-nearest neighbor interactions are $V_1 = \infty$, $V_2 = 4W$ and $V_3 = 4W$, respectively. Longer-range interactions are neglected. (f) Local mapping between the Hilbert spaces of a triangle in the toric code (left) and Rydberg atom models (right). The toric code space is constrained by $B_\triangle = 1$. Solid red (grey dashed) lines indicate links with $\sigma^z = 1$ ($\sigma^z = -1$). The Rydberg atom Hilbert space is constrained by the Rydberg blockade phenomenon: a triangle can have either 0 or 1 Rydberg excitations (orange circles).

is the *exact* ground state wavefunction of a Hamiltonian featuring solely two-body interactions. We then study the phase diagram beyond this regime using numerical simulations. Our results suggest that the QSL phase reported in Ref. [25] is adiabatically connected to the exactly soluble point in an extended parameter space: importantly, according to our mapping, the experimentally relevant point is compatible with deconfinement, as its dual model features *strong* plaquette interactions - albeit, rather peculiarly, only on a certain sublattice. We then discuss how the type of models resulting from our mapping can be realized using Rydberg dressing techniques [1].

3.1 Lattice gauge theory

We are interested in the toric code Hamiltonian on the kagome lattice, where Pauli operators σ_j^α are assigned to each link j. We define the operators A_+, $B_\triangle$ and $B_\hexagon$ on vertices, triangular, and hexagonal plaquettes, respectively, as (see Fig. 3.1-a):

$$A_+ = \prod_{j\in+} \sigma_j^z, \qquad B_\triangle = \prod_{j\in\triangle} \sigma_j^x, \qquad B_\hexagon = \prod_{j\in\hexagon} \sigma_j^x. \tag{3.1}$$

$A_+, B_\triangle$ and $B_\hexagon$ form a mutually commuting set. Our Hamiltonian of interest has the form

$$H_0^{\mathrm{TC}} = W\sum_{+} A_+ - J_1 \sum_{\triangle} B_\triangle - J_2 \sum_{\hexagon} B_\hexagon - g\sum_j \sigma_j^x. \tag{3.2}$$

Let us first focus on the case $g = 0$. Here, the ground state is obtained for $A_+ = -1$ on every vertex and $B_{\triangle/\hexagon} = 1$ on every plaquette, and is a (odd) $\mathbb{Z}_2$ spin liquid,

[1] We note that our discussion specifically applies to the experimental setups inspired by Ref. [29], and is complementary to other approaches to spin liquids in Rydberg systems [28, 65, 73, 74]

with anyonic excitations. A vertex with $A_+ = 1$ represents an *electric* excitation or *charge* (see Fig. 3.1-b), with mass $2W$, while a plaquette with $B_\triangle = -1$ ($B_\hexagon = -1$) is a *magnetic* excitation or *vison*, with mass $2J_1$ ($2J_2$).

For $g \neq 0$ the Hamiltonian does still commute with $B_\triangle$ and $B_\hexagon$, but does not commute with the A_+ operators. The effect of the term proportional to g is to excite pairs of electric charges on neighbouring sites; the model is a Ising-Higgs lattice gauge theory [71, 75], as it describes a $\mathbb{Z}_2$ gauge field coupled to matter. Since the toric-code ground state is gapped, for sufficiently small g the system remains a $\mathbb{Z}_2$ spin liquid [57, 71]. For g/W larger than a critical value, the model has a phase transition to a confined phase (a condensate of electric charges). Utilizing Wegner duality [47], we quantitatively establish the extent of the topological phase until $g_c/W = \widetilde{g}_c \simeq 0.3387$. This argument and the location of the phase transition are valid for arbitrary J_1 and J_2, as long as the ground state is in the sector with no magnetic excitations. The model in Eq. (3.2) can equivalently be interpreted as a pure Ising gauge theory on the dual lattice (a *dice lattice*), where electric and magnetic charges are interchanged: the term proportional to g now excite pairs of magnetic excitations on neighboring plaquettes while the electric charge is static, the plaquette terms $B_{\triangle,\hexagon}$ become vertex terms, and Gauss' law is enforced on every vertex.

In our mapping to the Rydberg model below, we will consider $J_1 \to \infty$ and $J_2 = 0$: in this case, we are restricted to the sector with $B_\triangle = 1$ on every triangular plaquette, while hexagonal plaquettes have zero "mass" for $g = 0$. While the absence of a gap at $g = 0$ may be concerning, as it does not guarantee that the system is in a gapped spin liquid state in a finite range of g/W, we will show via both numerical simulations and perturbation theory that the ground state is always in the sector with no magnetic excitations and that a gapped spin liquid is present in a region with $0 < g/W < \widetilde{g}_c$. This is because the term proportional to g generates an effective mass for magnetic excitations, allowing for a gapped ground state with topological order even for $J_2 = 0$.

3.2 Rydberg model

We now map the toric code on the kagome lattice to a model of Rydberg atoms constrained by the Rydberg blockade. The atoms are located on the links of the lattice, forming a ruby lattice (see Fig. 3.1-d). The Rydberg excitations are modeled as hard-core bosons with operators $b_j, b_j^\dagger$. We assume that interactions between neighbouring atoms (i.e., belonging to the same triangle) are repulsive and very strong, inducing a nearest-neighbor blockade. Under this assumption, each triangle can have either 0 or 1 Rydberg excitation: each triangle has a Hilbert space spanned by the four basis states in Fig. 3.1-f (right column). Note that this assumption differs from the one of Ref. [25], where the blockade extends to next-nearest and next-next-nearest neighbours: this naturally leads to different gauge constraints.

In the model in Eq. (3.2), the constraint $B_\triangle = 1$ reduces the Hilbert space dimension of a triangle from 2^3 to 4. The constrained Hilbert space is spanned by the states in Fig. 3.1-f (left column), defining a local mapping between the Hilbert spaces of the two models. This correspondence allows a direct mapping between the Hamiltonian in Eq. (3.2) with $J_1 \to \infty$, $J_2 = 0$ and the following Hamiltonian for Rydberg

excitations (see Sec. 3.2.1):

$$\begin{aligned} H_0^{\mathrm{Ryd}} = &- g\sum_j (b_j + b_j^\dagger) - g\sum_{\langle i,j\rangle}(b_i^\dagger b_j + b_j^\dagger b_i) \\ &- 4W\sum_j n_j + 4W\sum_{\langle\langle i,j\rangle\rangle} n_i n_j + 4W\sum_{\langle\langle\langle i,j\rangle\rangle\rangle} n_i n_j. \end{aligned} \tag{3.3}$$

Here, the first term is the creation/annihilation of Rydberg excitations, the second term is the hopping of excitations between neighbouring atoms, the third term is a chemical potential for the excitations, and the fourth and fifth terms are Rydberg interactions between next-nearest neighbors and next-next-nearest neighbors respectively. Note that, while the nearest-neighbour interaction is $V_1 = \infty$, next-nearest-neighbor and next-next-nearest-neighbor interactions are $V_2 = V_3 = 4W$ (see Fig. 3.1-e). The experimental realization of this Hamiltonian will be discussed in Sec. 3.6.

A first result of the mapping above is that 't Hooft and Wilson lines in the toric code model are mapped onto the string operators proposed in Ref. [25] [2]: this suggests the QSL phase observed there has the same nature as the topological phase of the model in Eq. (3.2), that is, stemming from a genuine $\mathbb{Z}_2$ gauge theory. Moreover, the resonating valence bond (RVB) state of dimers in [25] is here mapped to the toric code ground state (equal weight superposition of the configurations with $A_+ = -1$ on each vertex): our mapping provides a local unitary transformation that relates the RVB dimer state and the toric code ground state; the existence of such a unitary was proven in [78].

3.2.1 Mapping

In this section, we show the mapping of H^{TC} to H^{Ryd}. First of all, since all triangular plaquettes are independent, the Hilbert space can be decomposed as $\mathscr{H} = \bigotimes_\triangle \mathscr{H}_\triangle$. Both the constraints $B_\triangle$ and $n_i n_j = 0$ (for nearest neighbors i, j) restrict the Hilbert space of a single triangle from 8 to 4 dimensions. We take a basis of 4 states of a triangle in the $\mathbb{Z}_2$ LGT model and map them to 4 states of a triangle in the Rydberg model, as shown in Fig. 3.1-f.

With this mapping, the Hamiltonian terms are transformed in the following way,

$$\begin{aligned} \sigma_i^x\left(\frac{1+\sigma_j^z\sigma_k^z}{2}\right) &\longmapsto (b_i^\dagger + b_i) \\ \sigma_k^x\left(\frac{1-\sigma_i^z\sigma_j^z}{2}\right) &\longmapsto (b_i b_j^\dagger + h.c.) \\ \prod_{i\in\times}\sigma_i^z &\longmapsto \prod_{i\in\times}(2n_i - 1) \\ \sum_{\langle ij\rangle\in\triangle}\sigma_i^z\sigma_j^z &\longmapsto -4\sum_{j\in\triangle} n_j + 3 \end{aligned} \tag{3.4}$$

[2] We nevertheless stress that utilizing such operators as order parameters for deconfinement should be done with great care: the correct order parameter [76] is defined by correlations in real space and imaginary time, and it is not necessarily matching real space correlations in lattice models with very small correlation length (for a spectacular failure, see Ref. [77]). While our work suggests a very strong correspondence between those and deconfinement even in real space, a quantitative verification of their regime of applicability is an interesting, open question.

where i, j and k are the three links belonging to a single triangle. We note that terms of the form $b_i^\dagger b_j^\dagger$ are not present in the model (and, in the implementation discussed in the main text, can be systematically avoided as discussed in Ref. [65]).

To simplify the term $\prod_{j\in\times}(2n_j-1)$, consider the links $i,j,k,l\in\times$ with i,j belonging to the same triangle and k,l belonging to a different triangle. Then,

$$\begin{aligned}\prod_{j\in\times}(2n_j-1) &= (2n_i-1)(2n_j-1)(2n_k-1)(2n_l-1)\\ &= (4n_in_j-2n_i-2n_j+1)(4n_kn_l-2n_k-2n_l+1)\\ &= (-2n_i-2n_j+1)(-2n_k-2n_l+1)\\ &= 4n_in_k+4n_in_l+4n_jn_k+4n_l-2(n_i+n_j+n_k+n_l)+1.\end{aligned} \tag{3.5}$$

Hence, we obtain

$$\prod_{j\in\times}\sigma_j^z \longmapsto 1-2\sum_{j\in\times}n_j+4\sum_{i\in>}\sum_{j\in<}n_in_j \tag{3.6}$$

Note that each link belongs to two vertices, hence

$$\sum_{\times}\sum_{j\in\times}n_j = 2\sum_j n_j \tag{3.7}$$

Moreover, $\sum_{i\in>}\sum_{j\in<}n_in_j$ contains four pairs: two at distance r_2 and two at distance r_3, i.e., they are respectively second and third nearest neighbors, $\langle\langle i,j\rangle\rangle$ and $\langle\langle\langle i,j\rangle\rangle\rangle$. Finally, summing over all triangles and vertices, the mappings in Eq. (3.4) and (3.6) define a mapping (up to constants) of H^{TC} to H^{Ryd}.

3.3 Wegner duality and Ising model

In this section, we show the mapping of the Hamiltonian H_0^{TC} for $J_1\to\infty$ and $J_2=0$ to the quantum Ising model on the kagome lattice. This mapping follows the general approach of Wegner dualities [47]. Although the hexagonal plaquette operators $B_{\hexagon}$ do not appear in the Hamiltonian, they do commute with the Hamiltonian. Therefore, we can study the model separately in each sector of fixed eigenvalues of $B_{\hexagon}$ and the Wilson loops $W_{x,y}$. Each sector can be mapped to a transverse-field Ising model on the kagome lattice with appropriate nearest-neighbor coupling signs. To see this, we define an Ising variable on each vertex r of a kagome lattice

$$\begin{aligned}\tau_r^z &= \prod_{j\in\times}\sigma_j^z\\ \tau_r^x &= \prod_{j\in\gamma_r}s_j\sigma_j^x,\end{aligned} \tag{3.8}$$

where the signs $s_{r,r'}=\pm1$ are chosen such that $\prod_{j\in\triangle,\hexagon}s_j = B_{\triangle,\hexagon}$ and $\prod_{j\in\gamma_{x,y}}s_j = W_{x,y}$, and γ_r is a path between a specific vertex and r (see Fig. 3.2-a). Note that the variables τ_r^x are defined independently of the choice of the path γ_r because $\prod_{j\in\Gamma}s_j\sigma_j^x=1$ for every closed loop Γ. The variable τ_r^z indicates the presence of/absence of an electric charge in r.

With the mapping in Eq. (3.8), the toric code Hamiltonian is mapped to

$$H=-g\sum_{\langle r,r'\rangle}s_{r,r'}\tau_r^x\tau_{r'}^x+W\sum_r\tau_r^z. \tag{3.9}$$

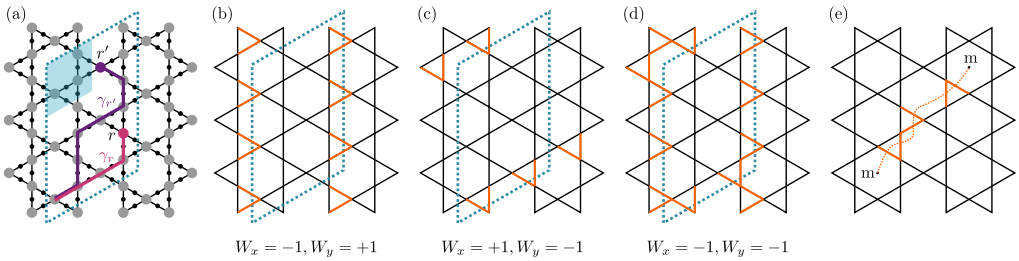

FIGURE 3.2: (a) The LGT variables σ_j^α are located on the links of the kagome lattice (black dots). The Ising variables are defined on the vertices of the kagome (grey circles). A unit cell (blue shaded area) contains 6 LGT sites, 3 Ising sites, 2 triangular plaquettes, 1 hexagonal plaquette. The dashed blue line delimits a system with $N_c = 6$ cells. Periodic boundary conditions are imposed. The paths $\gamma_r, \gamma_{r'}$ connect a designated vertex (here on the left-bottom corner) with sites r and r'. (b-d) Sectors with different values of the Wilson loops are obtained by setting $s_j = -1$ on the links crossing the horizontal/vertical boundaries. The links in orange are the ones with $s_j = -1$. (e) A sector with a pair of magnetic excitations can be obtained with an appropriate choice of signs of s_j: a line is drawn that connects the two magnetic excitations; for all the links crossed by the line we set $s_j = -1$. This choice ensures that $B_{\hexagon} = -1$ for the two plaquettes with the excitations, and $B_{\triangle} = 1$, $B_{\hexagon} = 1$ for all the other plaquettes.

A few comments are in order. In the original lattice gauge theory, the number of degrees of freedom once the plaquettes and the Wilson loops are fixed is $6N_c - N_p - N_W + 1 = 3N_c - 1$, where N_c is the number of unit cells in the system (each unit cell has 6 spins, see Fig. 3.2-a), $N_p = 3N_c$ is the number of plaquettes, $N_W = 2$ is the number of independent Wilson loops, and we also take into account the fact that not all plaquettes are independent, because the product of all plaquettes is 1. In the corresponding Ising model, each unit cell contains 3 Ising variables, so the total number of degrees of freedom is $3N_c$. To obtain the correct counting, we have to further fix the value of the parity $P = \prod_r \tau_r^z$ to $P = 1$ (this is easily found by rewriting P in terms of the original σ_j^z operators).

We now comment on the physical interpretation of the mapping to the Ising model outlined in this section. The Ising variables correspond to the vertex operators A_+ defined in the main text: $\tau_r^z = +1$ indicates the presence of an electric charge on site r, while no charge is present for $\tau_r^z = -1$. The (fixed) plaquettes represent a static background of magnetic fluxes, while the Wilson loops represent the fluxes around the two directions of the torus. The Hamiltonian in Eq. (3.9) describes the dynamics of the charges in the static background of magnetic fluxes.

The lowest energy is obtained when no flux is present, i.e., when all the plaquettes are fixed to $B_{\triangle,\hexagon} = 1$, and $W_x = W_y = 1$. For $g > 0$, this sector is mapped to the ferromagnetic Ising model on the kagome lattice, with $s_j = 1$ for every j. The QSL phase in this sector is mapped to the paramagnetic phase in the ferromagnetic Ising model, which is known to exist up until $g_c/W = 0.338678(4)$ [79]. The correlation length of the ground state in this sector is associated with the mass of the electric excitation and vanishes for $g \to g_c$. On the other hand, for $g < 0$, the no-flux sector is mapped to the antiferromagnetic Ising model on the kagome lattice. In this model, it is known that the paramagnetic phase extends along the whole $g < 0$ line (as long as $W \neq 0$) [54, 80]. This shows that the QSL phase exists in our model for $h = 0, \lambda = 0$ for any value of $g/W < 0$.

In the QSL phase, the lowest energy states in the sectors with $B_{\triangle,\hexagon} = 1$ for every plaquette but different signs of Wilson loop operators have a gap $\propto \exp(-cL)$ (where L is the shortest linear size of the system) with respect to the case $W_x = W_y = 1$. Possible configurations of s_j corresponding to these sectors are shown in Fig. 3.2-b,c,d.

Another interesting quantity that we can compute exploiting this mapping is the mass of magnetic excitations. Because the product of all plaquettes is equal to 1, we can only have an even number of magnetic excitations. Therefore, to measure the mass of a single excitation, we consider a sector with two excitations at very long distance (see Fig. 3.2-e): we expect that their interaction energy becomes small for sufficiently long distance, such that the energy difference between the lowest-energy state in this sector and the ground state is equal to twice the mass of a magnetic excitation.

3.3.1 Effective magnetic mass from perturbation theory

Each sector of the toric code Hamiltonian H_0^{TC} can be mapped to a quantum Ising model on the kagome lattice with appropriate nearest-neighbor couplings, as shown above. We can apply perturbation theory to these Ising models in the small g/W limit to estimate the ground-state energy for each sector. We note that perturbation theory is carried out within the regime of validity of the mapping we discussed above, and it is only needed to estimate energy splittings within allowed states in the spectrum.

At $g = 0$, the ground state is the paramagnetic state with all $\tau_r^z = -1$ and the energy is $E_0 = -6WN_c$ in each sector. The first perturbative correction that depends on the sector is at sixth order, $E_6 \propto -g^6 \sum_{\hexagon} B_{\hexagon}$, corresponding to flipping 6 Ising variables around a hexagonal plaquette. We see that, for both $g < 0$ and $g > 0$, the lowest ground state energy belongs to the sector with all $B_{\hexagon} = 1$, and there is a finite gap (mass of magnetic excitations) separating this state from all the other sectors. Note that this mass is zero for $g = 0$ and it is generated "dynamically" by the charge fluctuations, resulting in a gapped spin liquid ground state even in the absence of hexagonal plaquette terms.

3.4 Additional terms

In order to emphasize the wide applicability of our reasoning in terms of experimental platforms, we now consider a broader class of dynamics, introducing additional Hamiltonian terms:

$$H_1^{\mathrm{Ryd}} = -h \sum_j (b_j + b_j^\dagger) + h \sum_{\langle ij \rangle} (b_i^\dagger b_j + b_j^\dagger b_i) - 4\lambda \sum_j n_j, \tag{3.10}$$

which, under the local mapping in 3.1-f become

$$H_1^{TC} = -h \sum_{\triangle} F_{\triangle} + \lambda \sum_{\langle i,j \rangle} \sigma_i^z \sigma_j^z, \tag{3.11}$$

where $F_{\triangle}$ is the operator in Fig. 3.1-c. Note that H_1^{TC} commutes with the triangular plaquette operators $B_{\triangle}$, but does not commute with the hexagonal plaquette operators $B_{\hexagon}$. In particular, the term proportional to h creates a pair of electric charges and a pair of visons (on hexagonal plaquettes) on the toric code ground state, while

the term proportional to λ creates pairs of visons on neighboring hexagons (i.e., hexagons that share a vertex).

We remark that, by using the mapping defined for the states in Fig. 3.1-f, *any* Hamiltonian term of the Rydberg-atom model that is compatible with nearest-neighbor blockade (e.g., longer-range interactions) can be mapped to a Hamiltonian term of the toric code model. The blockade is the fundamental ingredient to enforce Gauss law [63].

3.4.1 Self-duality

We show here that the Hamiltonian $H_0^{\mathrm{TC}} + H_1^{TC}$ with $J_2 = 0$ has a self-duality that maps $g \to -h, h \to -g$. The transformation we consider is induced by the following unitary mapping:

$$U = \exp\left[-i\frac{\pi}{4}\sum_{\triangle}\left(\sum_{j\in\triangle}\sigma_j^z + \prod_{j\in\triangle}\sigma_j^z\right)\right] = \prod_{\triangle}\left[\frac{1}{2}\left(1 - \sum_{\langle i,j\rangle\in\triangle}\sigma_i^z\sigma_j^z\right)\right] \tag{3.12}$$

We remark that, in contrast with other dualities of the theory, this transformation has a completely local nature. The action of this transformation on the Pauli operators of the link j is

$$U\sigma_j^z U^\dagger = \sigma_j^z, \tag{3.13}$$

$$U\sigma_j^x U^\dagger = -\sigma_j^x\sigma_i^z\sigma_k^z, \tag{3.14}$$

where i and k are the two links that belong to the same triangle as j. It can be easily checked that $UB_\triangle U^\dagger = B_\triangle$ and $UA_+U^\dagger = A_+$, while

$$U\left(\sum_{j\in\triangle}\sigma_j^x\right)U^\dagger = -F_\triangle, \tag{3.15}$$

$$UF_\triangle U^\dagger = -\sum_{j\in\triangle}\sigma_j^x. \tag{3.16}$$

Therefore, the transformation sends $g \to -h$, $h \to -g$ while leaving W, J_1 and λ invariant. Note that, while $B_\triangle$ and A_+ are invariant under the transformation, the hexagonal plaquette $B_\hexagon$ is not, as it gets decorated by σ^z operators.

Under the mapping to the Rydberg model, the unitary U in Eq. (3.12) takes the form

$$U = \prod_j (-1)^{n_j}, \tag{3.17}$$

and therefore induces the transformations $Ub_jU^\dagger = -b_j$, $Ub_j^\dagger U^\dagger = -b_j^\dagger$, $Un_jU^\dagger = n_j$.

A consequence of the self-duality illustrated here is that the phase diagram in the $g - h$ plane is symmetric under reflection with respect to the axis $h = -g$, and that the line $g = 0$ for $\lambda = 0$ can also be solved analytically with a mapping to the Ising model, similarly to the $h = 0$, $\lambda = 0$ case. On the self-dual line $h = -g$ the quantity $\sum_{\langle i,j\rangle}\sigma_i^z\sigma_j^z$ (and, equivalently, the total number of Rydberg excitations $\sum_j n_j$) is conserved.

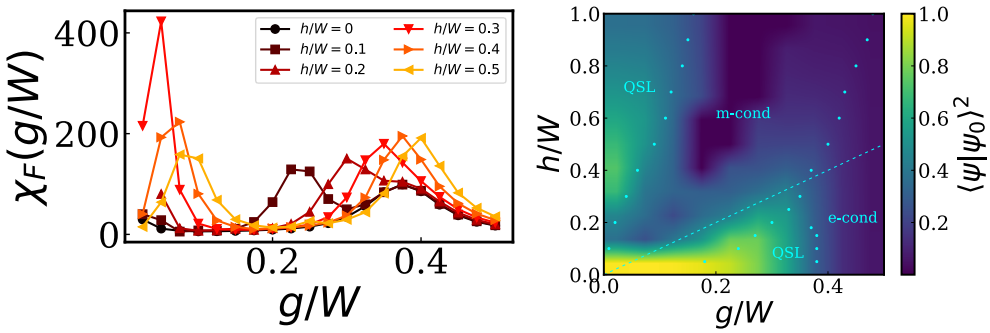

FIGURE 3.3: (a) Fidelity susceptibility of the Hamiltonian H^{TC} for $\lambda = 0$ as a function of the parameter g. (b) Phase diagram of H^{TC} for $\lambda = 0$. The heatmap indicates the overlap of the ground state with $|\psi_0\rangle$. The dots indicate the peaks of the fidelity susceptibility.

3.5 Phase diagram

We now study the phase diagram of the Hamiltonian $H^{\mathrm{TC}} = H_0^{\mathrm{TC}} + H_1^{\mathrm{TC}}$ by means of exact diagonalization, imposing the constraint $J_1 \to \infty$ by directly restricting the Hilbert space to the states with $B_\triangle = 1$ on every triangular plaquette. All results shown are for a 3×2 cluster containing 36 spins. Our goal here is not to precisely determine transition points, but rather, to discuss the generic structure of the phase diagram against theory.

We first focus on the case $\lambda = 0$. For $g = 0$ or $h = 0$, the model can be mapped to the quantum Ising model on the kagome lattice (see Sec. 3.3), whose phase diagram has been obtained in previous studies [54, 79, 80]. To detect the transition points and obtain the phase diagram for arbitrary g, h, we compute the fidelity susceptibility χ_F defined as

$$\chi_F(\eta) = \lim_{\delta\eta \to 0} \frac{-2 \ln F(\eta, \delta\eta)}{(\delta\eta)^2} \tag{3.18}$$

where the fidelity F is defined as $F(\eta, \delta\eta) = |\langle\psi(\eta)|\psi(\eta + \delta\eta)\rangle|$, with η being any parameter of the Hamiltonian. In systems with finite volume L^d, χ_F/L^d is known to exhibit peaks, whose amplitudes diverge in the thermodynamic limit and whose positions converge towards the critical point; the position of the latter can be derived via finite-size scaling techniques [81].

Fig. 3.3-a shows the fidelity susceptibility as a function of g for $\lambda = 0$. The marked dots in Fig. 3.3-b indicate the phase boundary, estimated as the position of the maximum of the fidelity susceptibility.

In addition, we compute the overlap of the ground state $|\psi\rangle$ with the state $|\psi_0\rangle$, defined as the ground state of the model for $h = 0$, $\lambda = 0$, $g/W = 0.1$. Since we know that the ground state of the model with $h = 0$, $\lambda = 0$ and small g/W is a QSL, the overlap of $|\psi_0\rangle$ with the ground state of the other points in the parameter space may tell us if those ground states have the same correlation structure. Fig. 3.3-b shows that, as expected, the overlaps are large in the QSL phases, and are close to 0 for the electric and magnetic condensates.

3.5.1 Adiabatic path from exactly soluble point to the Rydberg line

A key question is, whether the exactly soluble point is adiabatically connected to the regime studied in Ref. [25]. To reproduce the parameter ranges considered

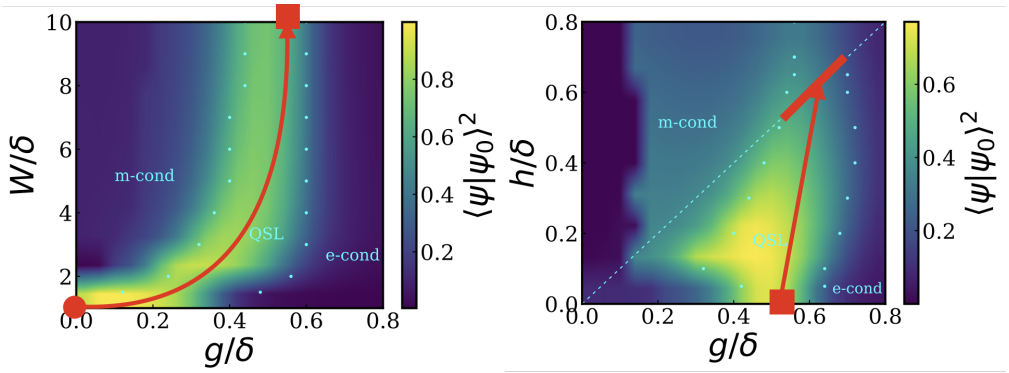

FIGURE 3.4: Adiabatic path from exactly soluble point (red dots) to the Rydberg line (thick red line): the square dot is common to both parts of the path. The overlap of the ground state of H^{TC} with $|\psi_0\rangle$ at (a) $h = 0$ and (b) $W/\delta = 10$.

there, we first define $\delta = W + \lambda$, and set it to be finite, while W is taken to be large ($W = 10\delta$). We proceed in two steps: (i) on the $h = 0$ hyperplane, we ramp W/δ from 1 to 10, and (ii) on the hyperplane $W = 10\delta$, we ramp h from 0 to the Rydberg line, $g = h$ [25].

Fig. 3.4 shows the overlap with the exact RVB wave function in these parameter regimes; the various phases are separated by local peaks of the fidelity susceptibility, indicated by dots. The red line is a sample of an adiabatic path entirely in the QSL phase: starting from the exactly soluble point (red circle), to the Rydberg line (thick red line in the right panel). As a non-trivial check on the latter line, we find two transitions at $g/\delta \approx 0.525$ and $g/\delta \approx 0.7$, corresponding to $\delta/\Omega = 1.4$ and $\delta/\Omega = 1.9$ in the notation of Ref. [25], and compatible with the transitions found there. Overall, these results show that the QSL phase observed in Ref. [25] is connected with the QSL phase that we demonstrated for $W/\delta = 1$.

3.5.2 Quantum Monte Carlo spectroscopy

It is expected that, within the entire topological phase, the ground state is approximately four-fold degenerate on torus geometries. An important question is how large is the energy gap separating the ground state manifold from excited states. This question is particularly relevant in this case, as there is no "bare mass" for the magnetic excitations on hexagonal plaquettes (i.e., $J_2 = 0$). Along the line $h = 0$, we have devised a spectroscopy based on simulating, via unbiased Quantum Monte Carlo approaches [82, 83], a dual Ising model description of low-lying states.

To this end, we exploit the mapping between the superselection sectors of the toric code Hamiltonian in Eq. (3.2) and inhomogeneous transverse-field Ising models, each characterized by the change in sign of a different subset of the nearest-neighbor couplings, as discussed in Sec. 3.3. Subsequently, we simulate the resulting quantum Ising models via Stochastic Series Expansion Monte Carlo [82, 83], a state-of-the-art, unbiased method for the calculation of equilibrium properties of bosonic and unfrustrated quantum spin systems.

We compute the energies, on a cluster containing $N_{\mathrm{cells}} = 8 \times 8$ elementary cells,

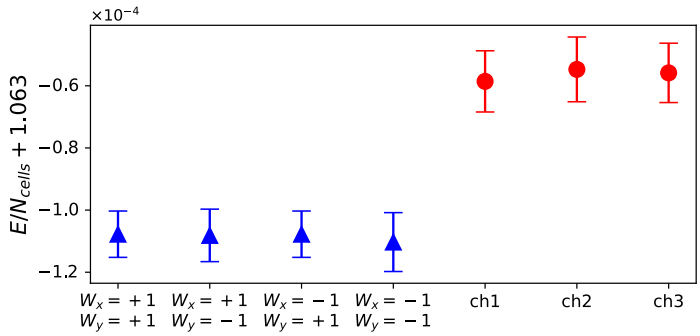

FIGURE 3.5: Rescaled energy per elementary cell of the quasi-degenerate ground states (blue triangles) and of the charged states (red circles) for the model H^{TC} on a $N_{\mathrm{cell}} = 8 \times 8$ cluster and $g/W = 0.32$. All charged states displayed here are characterized by the Wilson loop signs $W_x = W_y = +1$. Errorbars correspond to a 95% confidence interval.

of the four quasi-degenerate ground states and of three charged states with increasing charge separation. Each of these calculations corresponds to a ground-state analysis of a different quantum Ising model as discussed above. A sample of the corresponding results are presented in Fig. 3.5 for $g/W = 0.32$. The four-fold degeneracy of the ground state manifold is clear: the (expected) small splitting between those states is within our error bars. The gaps to the first excited states with magnetic excitations (labelled as "ch1,2,3") are finite; their relatively small magnitude we attribute to the strong anisotropy of magnetic and electric excitations. Convergence to the ground-state regime has been verified in all cases by the compatibility within error of the results for inverse temperatures $\beta = 16, 32$.

3.6 Experimental realization with Rydberg dressing

The class of models in H^{Ryd} considerably extends the range of target Hamiltonians that can realize a QSL. The salient features of Eq. (3.3) and Eq. (3.10) are naturally realized in arrays of atoms weakly laser-coupled to Rydberg states [39, 65, 84–98], and trapped into very deep potentials (e.g., optical lattices or tweezers), so that tunneling is suppressed over the time scales of the experiment. We discuss here two distinct experimental implementation for the $h \neq g$ regime and for $h = g$, respectively.

For $h \neq g$, we consider two states of an atom with different m_F, both belonging to the ground state manifold. They are laser-coupled to a Rydberg manifold with Rabi frequency Ω, and detuning δ, with $|\Omega| \ll \delta$. Within perturbation theory, the most relevant terms are: (a) a soft-shoulder potential that decays quickly to 0 after a cut-off distance that can be tuned by changing Ω and δ: this realizes our potentials in the limit $g/W \ll 1$; and (b) a hopping term, induced by the off-diagonal part of the Rydberg interaction. The range of the latter can be tuned independently of the previous one [65]. The linear terms in $b, b^\dagger$ as well as the λ term can be realized, e.g., utilizing a resonant microwave coupling.

The regime $h = g$ as realized in Ref. [29], often referred to as frozen Rydberg gas, features interparticle interactions decaying as power law potentials: this induces substantial differences between V_2, V_3, and possibly next-neighbor interactions. This is because the native interactions between Rydberg atoms are induced dipole dipole

ones, and only differ from that functional form at very short distances (where, however, a precise modelling of the dynamics as spin-1/2 model is not necessarily valid).

We propose here an alternative, double-dressing scheme that allows to independently tune V_1/V_2, and realize $V_2 \simeq V_3$. We consider alkaline-earth like atoms trapped into deep optical potentials [99–102], so that atomic motion can be neglected. Within the low-energy manifold, we consider the electronic ground state $|g\rangle$ and the $^3P_0$ (or $^3P_2$) metastable state $|e\rangle$ [3][103]. These two states represent the $n_j = 0, 1$ states, and are coupled by a clock laser, with Rabi frequency Ω_C and detuning δ_C: these two quantities will determine $(h + g)$ and λ, respectively.

The metastable state is then off-resonantly coupled to two Rydberg states (see, e.g., Ref. [104] for another proposal utilizing related settings), $|r_{1,2}\rangle$, with Rabi frequencies $\Omega_{1,2}$ and detunings $\delta_{1,2}$, such that $\delta_{1,2} \gg \Omega_{1,2}$, and $\Omega_1/\delta_1 \gg \Omega_2/\delta_2$. Note that both of those couplings can be single-photon couplings to s-states, so that the resulting potentials are spatially isotropic. For both $^3P_0$ and $^3P_2$, they have already been experimentally engineered in Sr [101] and Yb bosonic isotopes [105].

The resulting dressed potential is dominated by two contributions in perturbation theory:

$$V(r) = \frac{V^{(1)}}{1 + (r/r_1)^6} + \frac{V^{(12)}}{1 + (r/r_{12})^6} \tag{3.19}$$

with $V^{(1)} = \Omega_1^4/8\delta_1^3$, $r_1 = (C_6[11]/2\delta_1)^{1/6}$, $V^{(12)} \propto \Omega_1^2\Omega_2^2/\delta_1\delta_2^2$, $r_{12} \propto (C_6[12]/\delta_1)^{1/6}$, where $C_6[ij]$ are the van der Waals coefficients capturing the interactions between two atoms in the states i, j. Under the condition that $(C_6[11]/C_6[12])^{1/6} \simeq 2$, Eq. (3.19) describes a potential that is very strong at short distances, with ratio $V_2/V_1 \simeq (\frac{\Omega_2\delta_1}{\Omega_1\delta_2})^2$, and then features a plateau that realizes approximately equal interactions for V_2 and V_3.

3.6.1 State preparation protocols

In both implementations discussed, coupling to Rydberg states will necessarily lead to some amount of noise. In order to minimize the role of the latter, fast state preparation protocols are desirable.

For the case of quantum spin liquids, the corresponding (diabatic) state preparation can take advantage of the relatively fast timescales that have been proven effective in preparing spin liquid states. In particular, in Ref. [68], it has been shown that, even for moderate sizes of up to 70 spins, state preparation times of order of few tunneling processes shall suffice to realize very large overlaps with the target state. Since we do have access to an exactly soluble point, state preparation may further be shortened by starting from exact dimer coverings, following ideas already discussed in the context of strongly correlated fermions [106].

An interesting, alternative path is to explore Floquet driving within the Rydberg manifold [107], that has already been demonstrated as a powerful tool to engineer long-ranged Heisenberg-like models [108].

3.7 Conclusions

In this work, we showed that a $\mathbb{Z}_2$ lattice gauge theory with matter on a kagome lattice can be exactly mapped to a blockaded model of atoms on the ruby lattice, realizable with Rydberg-dressed potentials. Building on this analytical finding, we

[3] The hyperfine structure can be handled in different ways, depending on the laser polarizations.

proved the existence of a $\mathbb{Z}_2$ QSL and precisely located the transition to a trivial phase. By including additional perturbations, we extended our model to comprise, as a specific case, the Hamiltonian studied in Ref.[25, 29]: our numerical results suggest that the QSL observed therein belongs to the same phase of our solvable case. By elucidating the origin of QSL phases in blockaded systems, our work opens interesting directions for future experiments: more robust QSL states could be realized in an enlarged class of models, and the gauge-theoretical interpretation can help to identify useful perturbations that stabilize QSL phases, as well as suitable observables to detect and characterize their topological properties.

Chapter 4

Classification and emergence of quantum spin liquids in chiral Rydberg models

There is presently considerable interest in studying strongly correlated phases of matter in synthetic quantum systems based on Rydberg atom arrays [31, 109]. Stimulated by early experiments realizing symmetry-protected topological phases in one dimension [40], these platforms are now able to realize frustrated Hamiltonian dynamics in two dimensions [29, 41, 42], thus providing unparalleled opportunities to realize quantum spin liquids (QSLs) – elusive, exotic states of matter which have captivated the attention of physicists for decades [45, 53, 55, 57]. One route to access QSLs is based on the realization of frustrated Ising models in the so-called frozen gas regime [31, 33, 110]: several theoretical works have proposed different realistic scenarios for both gapped and gapless phases of matter [25, 61, 67, 68], with pioneering experiments already reporting evidence for deconfinement [29]. These models resemble closely situations investigated in the context of quantum dimer models [54], providing direct link between gauge theories and experimental settings [63, 111–113].

Over the last two years, a new route has been paved in a very different experimental regime, where the dynamics solely takes place within the Rydberg subspace. The resulting Hamiltonians naturally feature various forms of chiral multibody interactions [28, 74, 114, 115], which have already been experimentally demonstrated [116]. These classes of dynamics differ fundamentally from traditional Ising- and Heisenberg-type frustrated magnets and, while very promising since they display chiral terms, it is presently not even clear what classes of quantum spin liquids these can stabilize, and in which parameter regimes they might be observed.

In this work, we provide a general framework to describe chiral spin liquids (CSLs) in Rydberg atom honeycomb arrays. This framework is based on a systematic CSLs classification [117–119] using a fermionic spinon construction [50, 51] that yields Gutzwiller-projected parton wavefunction *ansätze* for the many-body ground state. The resulting classification differs substantially from those of Heisenberg-type regimes: it rules out the possibility of gapless Dirac spectrum, while predicting several, distinct topological phases.

Combining variational wavefunctions obtained from the classification with exact diagonalization (ED) methods, we demonstrate that the former capture the intermediate liquid regime of the chiral Rydberg model at both $1/2$ [74] and $1/4$ density [28], which - surprisingly - encode the same form of topological order: a twofold ground state degeneracy and a fractionalized Chern number $C = 1/2$ per state. These two CSLs represent two distinct phases characterized by different projective

representations of the lattice symmetries in the underlying fermionic spinon space. Remarkably, the CSL at 1/2 density is a new phase which corresponds to integer filling of the single-particle band, thereby representing an interaction-driven topological phase generated from a trivial band insulator [1], setting an open quest recently put forward in Ref. [74]. We then corroborate the topological character of this phase by computing the topological correction to the area-law scaling of entanglement entropy [121, 122], which is consistent with a CSL ground state, and by analyzing the pattern of currents at the edges of a cylinder using the density-matrix-renormalization-group (DMRG) [6, 9, 123, 124], which shows substantial counter-propagating nearest-neighbor edge currents, offering a simple mean for experimental detection. In the 1/4-density case, our results allow to frame the recent observation of CSL [28] within a rigorous classification, as well as providing a genuine understanding of the system wavefunction.

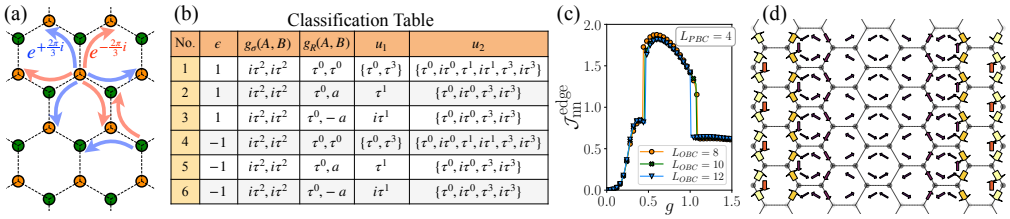

No.	ϵ	$g_\sigma(A,B)$	$g_R(A,B)$	u_1	u_2
1	1	$i\tau^2, i\tau^2$	τ^0, τ^0	$\{\tau^0, \tau^3\}$	$\{\tau^0, i\tau^0, \tau^1, i\tau^1, \tau^3, i\tau^3\}$
2	1	$i\tau^2, i\tau^2$	τ^0, a	τ^1	$\{\tau^0, i\tau^0, \tau^3, i\tau^3\}$
3	1	$i\tau^2, i\tau^2$	$\tau^0, -a$	$i\tau^1$	$\{\tau^0, i\tau^0, \tau^3, i\tau^3\}$
4	−1	$i\tau^2, i\tau^2$	τ^0, τ^0	$\{\tau^0, \tau^3\}$	$\{\tau^0, i\tau^0, \tau^1, i\tau^1, \tau^3, i\tau^3\}$
5	−1	$i\tau^2, i\tau^2$	τ^0, a	τ^1	$\{\tau^0, i\tau^0, \tau^3, i\tau^3\}$
6	−1	$i\tau^2, i\tau^2$	$\tau^0, -a$	$i\tau^1$	$\{\tau^0, i\tau^0, \tau^3, i\tau^3\}$

FIGURE 4.1: (a) Schematics of the model on the honeycomb lattice. The signs of the complex phase in the next-nearest-neightbor (NNN) hoppings are indicated by the colored arrows. (b) Mean-field ansätze of chiral spin liquids on the honeycomb lattice with broken time-reversal and reflection symmetries. ϵ indicates whether the unit-cell is doubled in the spinon space. $g_\sigma(A/B)$ and $g_R(A/B)$ are projective representations of reflection and rotation symmetries, respectively, with $a = e^{i2\pi/3\tau^3}$. u_1 and u_2 are mean-field amplitudes at NN and NNN links, respectively. The CSL phase at 1/2 and 1/4-density are captured by ansatz no. 1 and 4, respectively. (c) NN edge currents for cylinders with periodic width $L_{\mathrm{PBC}} = 4$ (i.e., 8 lattice sites). The edge currents are substantially larger in the intermediate phase compared to the neighboring phases. (d) The current profile at $g = 0.74$ for a cylinder with periodic width $L_{\mathrm{PBC}} = 4$ and length $L_{\mathrm{OBC}} = 8$. Widths of the arrows are proportional to the current values and directions denote the current directions. Large counter-propagating NN currents are observed only at the edges, while they vanish in the bulk.

4.1 Model Hamiltonian and phase diagram

We consider a system with atoms arranged on a honeycomb lattice. We assume optical control on the three Rydberg states $|0\rangle$, $|+\rangle = a^\dagger|0\rangle$, and $|-\rangle = b^\dagger|0\rangle$, where the state $|0\rangle$ has no excitations, and the states $|+\rangle$ and $|-\rangle$ (which belong to the same Rydberg manifold and differ, e.g., by their total angular momentum) encode two species of hard-core bosons created by the operators $a^\dagger$ and $b^\dagger$, respectively. Atomic motion is irrelevant on typical experimental timescales: below, we focus on the dynamics of the Rydberg excitations. The model Hamiltonian is [114, 115]:

[1] In a different context, another example of such occurrence on a Kagome lattice is reported in Ref. [120].

$$H_0 = \sum_{i\neq j} \begin{pmatrix} a_i \\ b_i \end{pmatrix}^\dagger \begin{pmatrix} -t^a_{ij} & w_{ij}e^{-i2\phi_{ij}} \\ w_{ij}e^{i2\phi_{ij}} & -t^b_{ij} \end{pmatrix} \begin{pmatrix} a_j \\ b_j \end{pmatrix} + \frac{\mu}{2}\sum_i (n^a_i - n^b_i). \tag{4.1}$$

The first term represents hopping processes (of excitations) between different sites, with the real hopping conserving the internal state, and the complex hopping resulting in a change of the internal state. The amplitudes for real and complex hoppings are given by t^a_{ij}, t^b_{ij}, and $w_{ij}e^{\pm i2\phi_{ij}}$ respectively, with ϕ_{ij} being the polar angle between the two Rydberg atoms on the sites i and j. All the amplitudes scale as $1/r^3_{ij}$. The second term represents the energy difference between the two internal states, with n^a_i and n^b_i being the particle number operators for the $|+\rangle$ and $|-\rangle$ states, respectively.

Here, we focus on the regime $\mu \gg t^a_{ij}, t^b_{ij}, w$, in which case the internal state $|+\rangle$ can be adiabatically eliminated. We further make an approximation by considering only nearest-neighbor (NN) interactions in Eq. (4.1), with NN hopping amplitudes t^a, t^b, and $we^{\pm i2\phi_{ij}}$. At leading order, the effective Hamiltonian is given by [116]

$$H = -J\sum_{\langle ij\rangle} b^\dagger_j b_i - 2gJ \sum_{\langle\langle ij\rangle\rangle} b^\dagger_j b_i e^{\pm 2\pi i/3}(1-n_{ij}) + \text{h.c.} + 4gJ\sum_{\langle ij\rangle} n_i n_j, \tag{4.2}$$

where $J = t^b$ and $g = w^2/(2\mu)$. The complex phases $e^{\pm 2\pi i/3}$ in the next-nearest-neighbor (NNN) hopping are illustrated in Fig. 4.1a. The NNN hoppings explicitly break time-reversal and reflection symmetries, but preserves their combination. The Hamiltonian has U(1) symmetry related to particle-number conservation. Note that, in the language of spins, the U(1) symmetry corresponds to spin-rotation symmetry around the z-axis. Hereafter, we set the energy scale to $J = 1$.

The phase diagram of the model at 1/2-density has been studied in Ref. [74], where three different phases were found for $g \geq 0$. For $g \lesssim 0.4$, the phase is a Bose-Einstein condensate (BEC) [2], while for $g \gtrsim 0.9$ the phase exhibits spiral or 120° spin order. The intermediate phase between $0.4 \lesssim g \lesssim 0.9$, shows no clear order, and it is believed to be a candidate for a spin liquid. However, its true nature remains unclear, also due to hard-to-interpret spectral properties.

At 1/4-density, Ref. [28] investigated the full model in Eq. (4.1) and provided clear numerical evidence for a fractional Chern insulating state: that included ground state degeneracy and Chern number compatible with a $\nu = 1/2$ bosonic Fractional Quantum Hall (FQH) state. Building on such numerical understanding, we will show below how that reflects into a very clear ansatz for the system wavefunction, informed by our classification.

[2] As we report in Sec. 4.7, an extra intermediate phase occurs for $0.25 \lesssim g \lesssim 0.4$.

4.2 Classification and variational wavefunctions from parton construction

In order to construct a spin liquid wavefunction, a method based on fermionic representation of spins have been introduced in [50, 51]. The main idea is to fractionalize the spin-1/2 operators into fermionic spinon operators as $S^a = \frac{1}{2} f_i^\dagger \sigma_{ij}^a f_j$, where σ^a are Pauli matrices, with the constraint of one spinon per site. It is convenient to introduce a two-component spinor $\Psi = (f_\uparrow \; f_\downarrow^\dagger)^T$. Directly rewriting the spins in terms of spinons gives rise to quartic spinon interactions, which after performing mean-field approximation, leads to a quadratic spinon Hamiltonian

$$H_{MF} = \sum_{ij} \Psi_i^\dagger u_{ij} \Psi_j + \text{h.c.}, \tag{4.3}$$

where u_{ij} are the mean-field amplitudes. The spinon interactions include hopping and pairing terms. The mean-field Hamiltonian is invariant under global spin rotation around the z-axis [125, 126]. The matrices u_{ij} can be written as $u_{ij} = u_{ij}^\mu \sigma^\mu$, where $(\sigma^\mu) = (i\tau^0, \tau^a)$, u_{ij}^μ are complex parameters and τ^a are Pauli matrices. Real u_{ij}^μ correspond to singlet terms, while imaginary u_{ij}^μ correspond to triplet terms [3]. Different mean-field ansätze are described by different (gauge-inequivalent) $\{u_{ij}\}$ on the links of the lattice. Finally, a physical spin state is obtained by applying Gutzwiller projection $|\psi\rangle = P_G |\psi_{MF}\rangle$, with $P_G = \prod_i n_i(2 - n_i)$, to the mean-field ground state $|\psi_{MF}\rangle$.

A method to systematically classify all possible spin liquids within this parton construction has been introduced by Wen [117, 118], based on projective symmetry groups (PSG). It has subsequently been extended to classify spin liquid phases in the absence of time-reversal (i.e., CSL) [119] and SU(2) spin-rotation [125, 126] symmetries. Here, we are interested in a CSL which breaks time-reversal and reflection symmetries but preserve their combination, and which preserves U(1) spin-rotation symmetry. Such chiral mean-field states are stable beyond mean-field treatment, as the mean-field gauge fluctuations are gapped out by the Chern-Simons mechanism [127].

The PSG classification of symmetric spin liquids on the honeycomb lattice has been worked out in [128], where 160 different algebraic PSG's are found. In the absence of time-reversal symmetry, we do not need to specify the SU(2) representation of the time-reversal operation [119]. Below, we provide the details on the PSG classification

The symmetry group on the honeycomb lattice that we are interested in is generated by translations along x and y, reflection accompanied by time-reversal $\mathbf{T}\sigma$, and $\pi/3$ rotation centered on a hexagonal plaquette R. Each algebraic PSG class is characterized by the SU(2) representation of each symmetry generator: $g_x(x, y, s)$,

[3] The "singlet" and "triplet" terminology is derived from the discussion of SU(2) spin-rotation symmetric Hamiltonians, which have been extensively studied in the literature. If the state does not spontaneously break the spin-rotation symmetry, only singlet terms are present. However, in the presence of spin-rotation symmetry-breaking perturbations, both terms may be present, and more generally the mean-field Hamiltonian has to be written in terms of a four-component spinor $\Psi = (f_\uparrow \; f_\downarrow^\dagger \; f_\downarrow \; -f_\uparrow^\dagger)^T$. If the spin-rotation is only broken down to U(1), it is still possible to use a two-component spinor representation as in Eq. (4.3), where the singlet and triplet terms can be present without mixing.

No.	$g_\sigma(A/B)$	$g_R(A/B)$	ϵ_σ	$\epsilon\epsilon_R$	$\epsilon_{\sigma R}$
1	τ^0/τ^0	τ^0/τ^0	+	+	+
2	$-\tau^0/-\tau^0$	$\tau^0/-\tau^0$	+	-	+
3	$\tau^0/-\tau^0$	τ^0/τ^0	-	+	+
4	$-\tau^0/\tau^0$	$\tau^0/-\tau^0$	-	-	+
5	$-i\tau^2/i\tau^0$	τ^0/τ^0	+	+	-
6	$-i\tau^2/i\tau^0$	$\tau^0/-\tau^0$	+	-	-
7	$i\tau^2/i\tau^0$	τ^0/τ^0	-	+	-
8	$i\tau^2/i\tau^0$	$\tau^0/-\tau^0$	-	-	-
9	$-i\tau^2/i\tau^0$	τ^0/a	+	+	-
10	$-i\tau^2/i\tau^0$	$\tau^0/-a$	+	-	-
11	$i\tau^2/i\tau^0$	τ^0/a	-	+	-
12	$i\tau^2/i\tau^0$	$\tau^0/-a$	-	-	-

TABLE 4.1: PSG representations of point-group symmetries on the honeycomb lattice.Taking into account the two possible signs $\epsilon = \pm 1$ gives 24 distint algebraic PSG's in total.

$g_y(x,y,s)$, $g_\sigma(x,y,s)$, $g_R(x,y,s)$, respectively. This can be further simplified by working in a specific gauge. Here, we choose a gauge defined as [128]

$$g_x(x,y,s) = \tau^0 \tag{4.4}$$
$$g_y(x,y,s) = \epsilon^x \tau^0 \tag{4.5}$$
$$g_\sigma(x,y,s) = \epsilon^{x+y(y+1)/2} g_\sigma(s) \tag{4.6}$$
$$g_R(x,y,s) = \epsilon^{xy+x(x-1)/2} g_R(s), \tag{4.7}$$

where $\epsilon = \pm 1$, with $\epsilon = -1$ indicates that the unit-cell is doubled in the spinon space. Within this gauge choice, each PSG is characterized by the representations of reflection, $g_\sigma(A,B)$, and $\pi/3$ rotation, $g_R(A,B)$, for each sublattice A and B. The representation matrices satisfy the equations (for a detailed derivation, see [128])

$$g_\sigma(A)g_\sigma(B) = g_\sigma(B)g_\sigma(A) = \epsilon_\sigma \tau^0 \tag{4.8}$$
$$(g_\sigma(A)g_R(B))^2 = (g_\sigma(B)g_R(A))^2 = \epsilon_{\sigma R}\tau^0 \tag{4.9}$$
$$(g_R(A)g_R(B))^3 = (g_R(B)g_R(A))^3 = \epsilon\epsilon_R \tau^0. \tag{4.10}$$

We find 24 different classes of algebraic PSG, which are listed in table 4.1.

Given the model that we study, we focus on those ansätze that have nonzero mean-field amplitudes on the NN and NNN links. For each algebraic PSG, we now determine the mean-field amplitudes u_{ij} allowed by symmetry up to NNN links. The consistency conditions for u_1 and u_2 are

$$\begin{aligned} u_1^\dagger &= -(-1)^\chi g_\sigma(A) u_1 g_\sigma(B)^\dagger \\ u_1^\dagger &= g_R(A)g_R(B)g_R(A)u_1 g_R(B)^\dagger g_R(A)^\dagger g_R(B)^\dagger \\ u_2^= &- (-1)^\chi g_R(B)g_\sigma(A)u_2 g_\sigma(B)^\dagger g_R(A)^\dagger, \end{aligned} \tag{4.11}$$

where $\chi = 0$ for singlet terms and $\chi = 1$ for triplet terms. This leaves 6 distinct

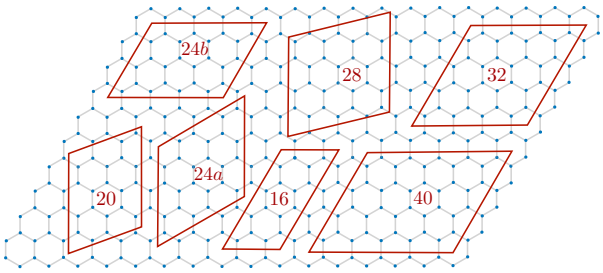

FIGURE 4.2: Periodic clusters used for the exact diagonalization calculations.

ansätze, which are listed in the Fig. 4.1b. The last 2 columns indicate the symmetry-allowed terms in the mean-field Hamiltonian on the NN and NNN links [4]. Each u_{ij} can be propagated to the entire lattice using rotations, which act as

$$u_{ij} = g_R(i) u_{R^{-1}(i)R^{-1}(j)} g_R(j)^\dagger, \tag{4.12}$$

followed by translations, which act similarly with $g_{x,y}$. Their amplitudes are taken as variational parameters in the following section.

Note that if the ansätze are restricted to NN interactions, the mean-field states are gapless with Dirac spectrum (in particular, ansatz no. 1 corresponds to the SU(2) algebraic spin liquid (ASL) state discussed in [129], or equivalently the u-RVB state discussed in [128]). Thus, the resulting states after Gutzwiller projection describe a Dirac spin liquid (DSL). However, this DSL ansatz submanifold preserves time-reversal, which is explicitly broken by our Hamiltonian. This excludes the possibility of a DSL being stabilized in chiral systems such as our model.

4.3 Overlaps with Gutzwiller-projected parton wavefunctions

To determine whether the intermediate phase of the model in Eq. (4.2) is described by one of the ansätze above, we optimize the variational parameters by maximizing the overlap of the exact ground state of the Hamiltonian with the wavefunction ansatz, for each of the 6 ansätze. The optimization of the overlap is performed using the Nelder-Mead optimization method, implemented in MATLAB. The optimization is performed on a 16-site cluster at $g = 0.7$. We find that the ansatz with the largest overlap with the ground state at 1/2-density is ansatz no. 1, characterized by non-zero real triplet NN hopping parameter τ^0, imaginary singlet NNN hopping parameter $i\tau^0$, and imaginary triplet NNN hopping parameter $i\tau^3$. The corresponding amplitudes are $u_2^{i\tau^0}/u_1^{\tau^0} = -0.31$ and $u_2^{i\tau^3}/u_1^{\tau^0} = -0.1$. We have also checked that the optimal parameters do not differ much from the optimal parameters on the smaller clusters.

The spinon band structure with the optimal parameters are shown in Fig. 4.3a. Note that each band is spin-degenerate. With one fermion per site, the mean-field ground state is obtained by filling all single-particle orbitals in the lower band, for both spin-up and spin-down orbitals. There is a finite energy gap to the valence

[4] We include all terms that are allowed by symmetry for each link, which in principle can be present in a mean-field state. However, if the mean-field Hamiltonian is restricted in the range of interactions (such as up to NNN interactions in our case), some of the terms can be removed by a gauge transformation.

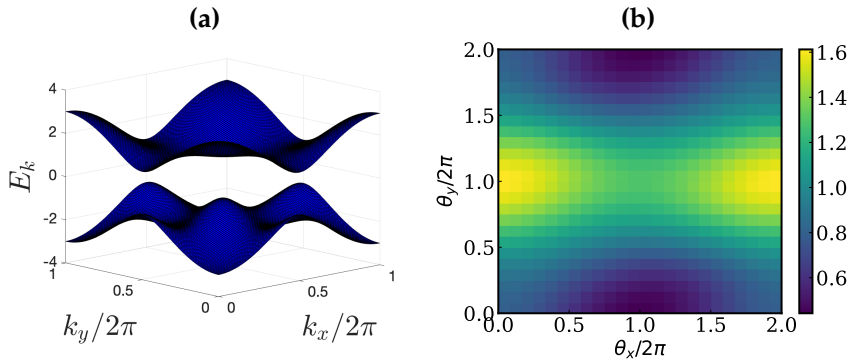

FIGURE 4.3: (a) Spinon bandstructure and (b) Berry curvature on the cluster 24b (normalized with the average) of the optimal ansatz at $g = 0.7$ for $n = 1/2$. The parameters are $u_2^{i\tau^0}/u_1^{\tau^0} = -0.31$ and $u_2^{i\tau^3}/u_1^{\tau^0} = -0.1$.

band, resulting in a fully gapped state. The Gutzwiller projection of such an ansatz has been shown to yield a topological CSL [127, 130, 131], which is a lattice analogue of $\nu = 1/2$ FQH Laughlin state [132]. The topological nature of such CSL is manifested by the two-fold topological degeneracy of states on a torus. These degenerate states can be constructed by threading fluxes along the non-contractible loops on a torus [133], which can be implemented by twisting the boundary conditions of the spinons, $\Psi \to e^{i\theta/2}\Psi$. Although there are four states that can be constructed with $\theta_x, \theta_y \in \{0, \pi\}$, they only span a 2-dimensional space, resulting in two topological states. We verify this numerically by computing the overlap matrix for the four states, defined as $O_{ij} = \langle\psi_j|\psi_i\rangle$. We find that the rank of the overlap matrix is 2, within a numerical accuracy on the order of 10^{-2}. The two independent states are then constructed from the eigenvectors of the overlap matrix with non-zero eigenvalues.

Furthermore, we computed the many-body Chern number, a topological invariant that characterizes the topologically nontrivial phases of matter [134]. It can be computed by twisting the boundary condition by angles $\theta_{x,y}$ in the x, y direction, and is given by the integral of the Berry curvature over the twist space:

$$C = \frac{1}{2\pi i}\int_0^{2\pi}\int_0^{2\pi} d\theta_x d\theta_y (\langle\partial_{\theta_x}\Psi(\theta)^*|\partial_{\theta_y}\Psi(\theta)\rangle - \langle\partial_{\theta_y}\Psi(\theta)^*|\partial_{\theta_x}\Psi(\theta)\rangle), \tag{4.13}$$

where $|\Psi(\theta)\rangle = |\Psi(\theta_x, \theta_y)\rangle$ is the ground state wavefunction with twist angles θ_x and θ_y. To compute Eq. (4.13) numerically, we discretize the twist space into $D \times D$ mesh and sum the discretized Berry curvature. We have obtained $C = 2$, with the Berry curvature for $D = 24$ is shown in Fig. 4.3b. Note that the twist $0 \leq \theta_{x,y} \leq 2\pi$ for the fermionic spinon operators corresponds to 0 to 4π twist for the spin operators, and therefore, the result must be divided by 4. Thus, the Chern number of the spin wavefunction is fractionalized $C = 1/2$ per state. The Chern number, along with the two-fold degeneracy, are consistent with the properties of $\nu = 1/2$ bosonic Laughlin state.

Having established the FQH nature of the ansatz, we next compute the overlap of the ground state of the Hamiltonian with the two topological states [135, 136],

$$\mathcal{O}_{GW}^{ED} = \sqrt{|\langle\psi_{ED}|\psi_{GW}^1\rangle|^2 + |\langle\psi_{ED}|\psi_{GW}^2\rangle|^2}. \tag{4.14}$$

where $|\psi_{ED}\rangle$ is the ground state obtained with ED and $|\psi^1_{GW}\rangle$ and $|\psi^2_{GW}\rangle$ are the two topological states. All the ED clusters that are considered are depicted in Fig.4.2. We impose periodic boundary conditions, and the ED calculations are performed exploiting translational symmetry. The cluster 24a and the 32-site cluster has sixfold rotational symmetry, which we also exploit.

The results are shown in Fig. 4.4a for different system sizes. It can be seen that the overlap remains large in the middle phase with increasing system size, indicating that the ground state is strongly related to the topological states. Interestingly, on a 32-site cluster, we find that the ground state in the intermediate phase is not in the rotation-neutral sector. Specifically, if we take the operator $R_{\pi/3}$ which generates a $\pi/3$ rotation around the center of a honeycomb plaquette, then $R_{\pi/3}|\psi_{ED}\rangle = e^{-2\pi i/3}|\psi_{ED}\rangle$. This can be seen in Fig. 4.4a as a discontinuous jump in the overlap at $g \approx 0.45$, as the transition from the BEC phase becomes a level crossing between different rotation sectors. Remarkably, one of the two topological states is in the same nontrivial rotation sector as the ground state of the Hamiltonian, i.e., the eigenvalue of $R_{\pi/3}$ is $e^{-2\pi i/3}$. This nontrivial observation strongly supports the hypothesis that the intermediate phase is described by the wavefunction ansatz.

At this point, it is worth emphasizing that the CSL phase found at 1/2-density represents a novel phase that has not been previously identified. Notably, this CSL has a dispersive band (see Fig. 4.3a), distinguishing it from the previously observed CSLs at 1/4-density [28, 137] and 1/8-density [137], that possesses topological flat bands. As such, this CSL is inevitably missed by previous approaches relying on the identification of flat bands [28, 137]. Moreover, its dispersive band significantly affects the physical properties on finite-size clusters, thus hindering the identification of the true CSL nature in previous study [74]. Our hybrid approach, combining theoretical PSG classification and numerical optimization, thus showcases its effectiveness by successfully identifying the CSL phase even in the presence of strong finite-size effects.

To compare with the 1/2-density case, we performed the same parameter optimization procedure for the 1/4-density case. In [28], it was shown that a CSL emerges at 1/4-density for the full model in Eq. (4.1). For the effective model in Eq. (4.2), we found that the CSL phase emerges in a narrow range around $g = 0.2$. For 1/4-density, a gapped phase can be obtained within the parton construction when the mean-field ansatz has a doubled unit-cell. We obtain large overlaps with the ansatz no. 4 at small-size clusters in the CSL phase. Fig. 4.4b shows the overlaps for 1/4-density with the optimized parameter for different system sizes. We found that the overlap remains huge in the CSL phase, reaching 0.96 at the largest system size we considered, $L = 40$.

In Fig. 4.5, we present the excitation spectrum in the momentum sector $k = (0, 0)$ at $g = 0.1$ and $g = 0.7$, along with the overlaps $\mathcal{O}^{ED}_{GW}$ for each eigenstate. Note that, since the two topological states $|\psi^1_{GW}\rangle$ and $|\psi^2_{GW}\rangle$ lie in the momentum sector $k = (0, 0)$, only the eigenstates in this sector can have non-zero overlap. In agreement with [74], we observe no approximate two-fold degeneracy in the ED spectra, which would have been expected in a CSL. Nevertheless, this can be attributed to finite-size effects, which may significantly modify the spectra on small-size clusters. It is therefore possible that one of the low-lying states corresponds to another topological ground state, which becomes degenerate with the true ground state in the thermodynamic limit. To test this hypothesis, it is useful to examine the overlaps of the low-lying levels. If an eigenstate describes the topological ground state of the CSL, it would have a sizable overlap with the wavefunction ansatz. Indeed, at $g = 0.7$, we observe that the overlap is highest for the ground state, and that there is a low-lying

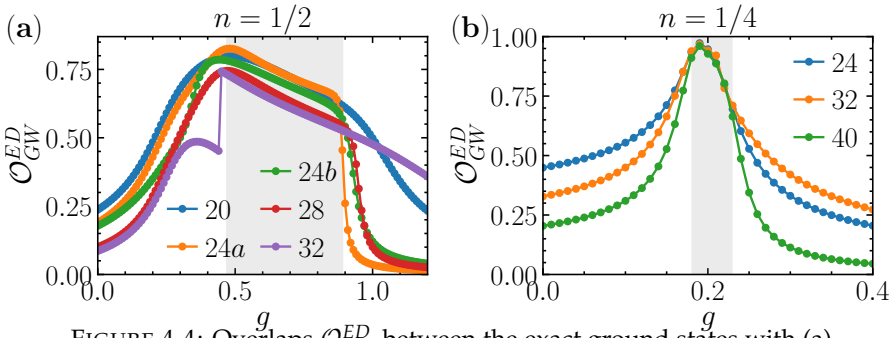

FIGURE 4.4: Overlaps $\mathcal{O}_{GW}^{ED}$ between the exact ground states with (a) ansatz no. 1 at 1/2-density and (b) ansatz no. 4 at 1/4-density. The shaded region denotes the intermediate phase which we show to be a CSL.

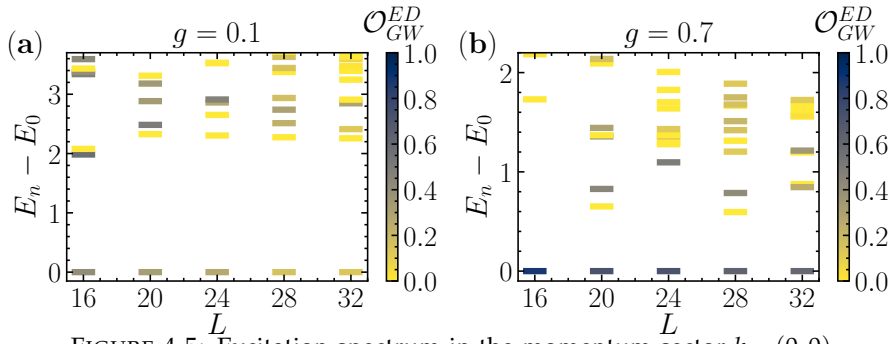

FIGURE 4.5: Excitation spectrum in the momentum sector $k = (0, 0)$ up to the 10th excited state for (a) $g = 0.1$ and (b) $g = 0.7$ at 1/2-density. The markers are colored according to the overlap $\mathcal{O}_{GW}^{ED}$.

state with a modest overlap. In contrast, at $g = 0.1$, the overlaps do not exhibit any clear pattern for each system size.

4.4 Excitation spectra

In Ref. [74], a DSL was proposed as one of possible scenarios, based on the observation that the gap to the first excited state varies significantly with twist angle when imposing twisted boundary conditions. In light of this, we analyze the excitation gaps as a function of twist angles $\theta_{1,2}$ along the lattice vectors $\vec{a}_{1,2}$. In Fig. 4.6a, we show the gap to the first excited state obtained with ED on a 24-site cluster, while the gap to the second excited state and the (symmetrized) charge gap are shown in Fig. 4.6b and 4.6c, respectively. We observe that while the first gap may become very small at some isolated points in twist space, the second gap and charge gap remain wide open. This contrasts with the expected behavior of a DSL, where all gaps would exhibit a vanishing behavior with respect to twist angles [138–140]. This is consistent with our results that DSL is unstable against time-reversal symmetry breaking perturbations (see Sec. 4.2).

We note that the drastic variation of the first gap with respect to the twist angles becomes even more pronounced at larger sizes, as can be seen in the cluster of $L = 32$ sites shown in Fig. 4.6d. Based on our findings, we are able to offer an interpretation of the curious vanishing of the gap to the first excited state as observed in [74]. Indeed, for a CSL two topological ground states will flow into each other

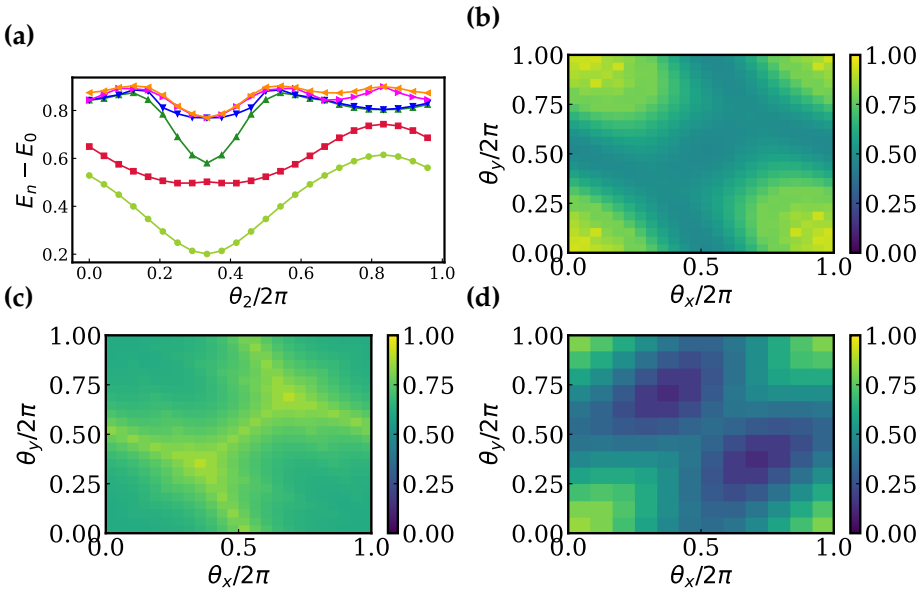

FIGURE 4.6: (a) Excitation spectrum on the cluster 24a at $g = 0.7$ with twist $\theta_1 = 2\pi/3$ and varying θ_2. (b) Gap to the second excited state $E_2 - E_0$ and (c) (symmetrized) charge gap $\Delta^c(N) = \frac{1}{2}(E(N+1) + E(N-1) - 2E(N))$ with $N = L/2$ as a function of the twist angles $\{\theta_1, \theta_2\}$ on the cluster 24a. (d) Gap to the first excited state $E_1 - E_0$ in the $k = (0,0)$ momentum sector on the 32-site cluster as a function of the twist angles $\{\theta_1, \theta_2\}$.

upon inserting flux (see, e.g., [137]). In the case of CSL at $n = 1/2$ density, the two ground states live in the same $k = (0,0)$ momentum sector. Consequently, the flow between these ground states manifests as an avoided crossing. As a result, the gap appears to vanish at some isolated points, corresponding precisely to the locations where the avoided crossing occurs. This behavior is specific to the first gap and not observed in higher gaps or the charge gap, as the CSL is gapped to all excitations. This is consistent with our results on excitation spectra discussed above.

4.5 Topological entanglement entropy

A topological phase can be characterized by the scaling of the entanglement entropy. The entanglement entropy for a region with perimeter L is known to scale as $S(L) = \alpha L - \gamma$, where the subleading term γ is a universal constant called the topological entanglement entropy which characterizes the topological order in a ground state wavefunction [121, 122]. Here, we employ the Kitaev-Preskill scheme [121] to compute γ:

$$\gamma = S_{AB} + S_{BC} + S_{AC} - S_A - S_B - S_C + S_{ABC}, \tag{4.15}$$

where the partitioning is depicted in Fig. 4.7a. In Fig. 4.7b, we show the behavior of γ in the exact ground state obtained with ED for $n = 1/2$ density. In the CSL phase, even in small systems, the computed γ is finite, and close to the expected value $\gamma = \frac{1}{2}\log(2)$ for a $\nu = 1/2$ FQH state [5].

[5] We note however that the finite volume effects prevent a clear interpretation of this data as a striking signature of topological order: such effects are expected given the observed strong finite-size effects in the numerical simulations.

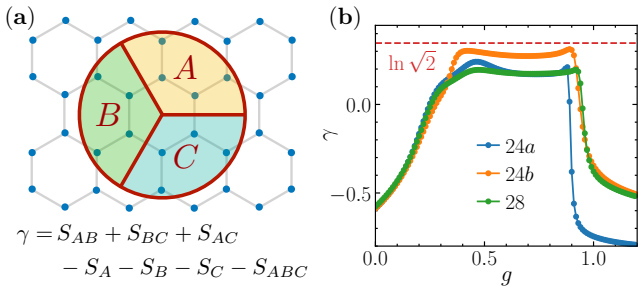

FIGURE 4.7: (a) Partitions used for the topological entanglement entropy calculation. (b) Topological entanglement entropy γ as a function of g at 1/2-density, obtained from the exact ground state on different periodic clusters (see Fig. 4.2). The dashed red line is the value of γ expected for a $\nu = 1/2$ FQH state.

4.6 Chiral currents

Quantum Hall states can be identified through the pattern of the currents in the system. With a finite gap in the bulk and gapless edge excitations on the boundary, it is expected that the currents are large at the edges and vanish in the bulk. Furthermore, the current can be readily measured in experiments, making it a convenient tool for diagnosing the phase in experimental setups. The NN and NNN currents can be derived using the continuity equation, resulting in

$$\begin{aligned} \mathcal{J}_{\text{nn}} &= i\langle b_j^\dagger b_i - b_j b_i^\dagger \rangle, \\ \mathcal{J}_{\text{nnn}} &= 2gie^{\pm 2\pi/3i}\langle (1-n_{ij})(b_j^\dagger b_i - b_j b_i^\dagger)\rangle, \end{aligned} \tag{4.16}$$

where i and j are nearest-neighbors or next to nearest-neighbors respectively.

We perform DMRG simulations on a finite cylinder to compute the edge currents as a function of g, as shown in Fig. 4.1c [6]. It can be seen that the NN edge currents, computed across two rungs in one of the edges, in the intermediate phase are significantly larger compared to those in the neighboring phases. The transition points are in good agreement with those found in [74]. Furthermore, we show the full current profile in the intermediate phase ($g = 0.74$) in Fig. 4.1d. It is clear that, in the CSL phase, large NN currents are only observed at the edges, while they vanish in the bulk. The full current profile is shown for each phases in Fig. 4.8. Clearly, substantial counter-propagating NN edge currents manifests only in the CSL phase that vanish in the bulk. On the other hand, most dominant currents in the other phases are of the NNN nature that originate from the NNN term in the Hamiltonian.

4.7 Another intermediate phase

Notice that Fig. 4.1c also exhibits signatures of another intermediate phase with non-zero edge currents for $0.25 \lesssim g \lesssim 0.4$. While its full characterization is beyond the scope of this work, we report here our preliminary findings on this possible new phase.

[6] We consider two different cylinder geometries for our calculations, namely the geometries I and II, as demarcated in [141].

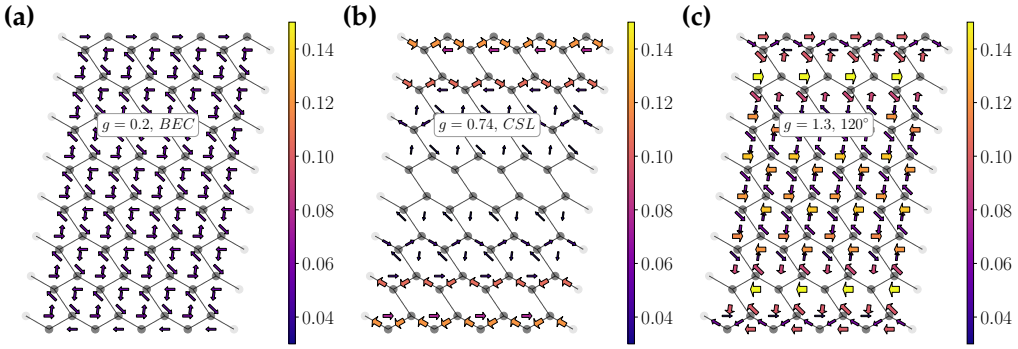

FIGURE 4.8: Full current profiles at $n = 1/2$ filling for the cylinders with geometry I and with periodic width $L_{\text{PBC}} = 4$ and length $L_{\text{OBC}} = 8$ for three representative values of g inside three phases, namely BEC (top), CSL (middle), and the 120° (bottom) phases. The widths of the arrows are proportional to the magnitudes of the current, while their direction indicates the directions of respective currents.

To detect transition points and obtain the phase diagram as a function of g, we compute the fidelity-susceptibility χ_F defined as

$$\chi_F(g) = \frac{2}{L} \lim_{\delta g \to 0} \frac{-\ln F(g, \delta g)}{(\delta g)^2} \tag{4.17}$$

where the fidelity F is defined as $F(g, \delta g) = |\langle \psi(g) | \psi(g + \delta g) \rangle|$. The fidelity susceptibility χ_F is known to be a good indicator for quantum phase transition, whose critical point can be derived via finite-size scaling techniques [81]. In case of iDMRG simulations, however, we have

$$F(g, \delta g) = \lim_{L \to \infty} |\eta|^L, \tag{4.18}$$

where η is the dominant eigenvalue of the transfer matrix constructed from the iMPS ansatze of $|\psi(g)\rangle$ and $|\psi(g + \delta g)\rangle$. Since, for two normalized iMPS $|\psi(g)\rangle$ and $|\psi(g + \delta g)\rangle$, $|\eta| < 1$ for $\delta g \neq 0$, we get $F(g, \delta g) \to 0$ as $L \to \infty$. The fidelity-susceptibility can be expressed as

$$\chi_F(g) = -2 \ln |\eta|, \tag{4.19}$$

which remains finite.

We show the fidelity-susceptibility obtained using iDMRG for two different types of cylinders in Fig. 4.9(a). The emergence of the CSL phase can be identified in the parameter range $0.4 \lesssim g \lesssim 1$. Interestingly, there appears to be an additional phase emerging between the BEC phase and the CSL. Since, the system is invariant under the joint operation of time-reversal and reflection, total nearest-neighbor edge current $\mathcal{J}_{\text{nn}}^{\text{edge 1}} + \mathcal{J}_{\text{nn}}^{\text{edge 2}}$, odd under this joint operation, must vanish for the ground states that respects reflection $\times$ time-reversal symmetry. By performing finite DMRG on finite-cylinders, we find that this reflection $\times$ time-reversal symmetry gets spontaneously broken in this parameter regime, and the total nearest-neighbor edge current $\mathcal{J}_{\text{nn}}^{\text{edge 1}} + \mathcal{J}_{\text{nn}}^{\text{edge 2}}$ attains a finite (positive or negative) value (see Fig. 4.9(b)). The profile of the total edge current in Fig. 4.9(b) clearly indicates two-fold degenerate ground-state manifold in this new unknown phase.

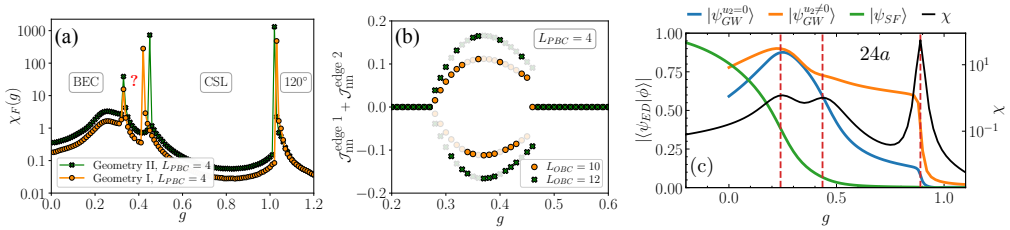

FIGURE 4.9: (a) The fidelity susceptibility $\chi_F(g)$ as a function of g for infinite cylinders with two different geometries and with periodic width $L_{\text{PBC}} = 4$ in the $n = 1/2$ density regime. The $\chi_F(g)$ shows the existence of a new phase sandwiched between the BEC and the CSL phases. (b) The total nearest-neighbor edge current $\mathcal{J}_{\text{nn}}^{\text{edge 1}} + \mathcal{J}_{\text{nn}}^{\text{edge 2}}$ computed for finite cylinders of geometry I and with periodic width $L_{\text{PBC}} = 4$ for $n = 1/2$ density. In the new intermediate phase, reflection $\times$ time-reversal symmetry gets spontaneously broken, and the total edge current becomes finite (positive or negative). Since, the DMRG simulations breaks this $\mathbb{Z}_2$ symmetry somewhat randomly, there is a arbitrariness in the sign of the edge current. That is why transparent symbols are added that represent the currents with opposite signs of the actual DMRG data. (c) Fidelity susceptibility and overlaps of the exact ground state with various ansatz on the cluster 24a for $n = 1/2$. Orange line: overlap with ansatz no. 1 optimized at each point. Blue line: Overlap with DSL wavefunction with uniform spin-dependent NN hopping τ^0. Green line: Overlap with superfluid ansatz, defined as the equal-weight superposition of all states at fixed density. The emergence of the additional phase can already be observed, between the two nearby peaks of fidelity susceptibility at $g = 0.24$ and $g = 0.43$, which are denoted by the vertical red lines. The overlap with DSL wavefunction peaks close to the transition between the BEC phase and the additional phase.

We note that the emergence of this additional phase can already be seen in small size clusters, as observed from ED calculations. In Fig. 4.9(c), we show the fidelity susceptibility as well as the overlap of the exact ground state with various ansatz on the cluster 24a. We find that the additional phase also have a large overlap with ansatz no. 1, where now we optimize the ansatz at each point (orange line). We find that the optimal ansatz in this phase is in the vicinity of the DSL wavefunction. Indeed, the overlap with the DSL wavefunction (blue line), which is obtained by setting the NNN interactions to zero, is remarkably close with the optimal overlap. One possible scenario to explain this observation is that the DSL wavefunction describes the critical wavefunction at the transition from the BEC phase to the unknown phase. A similar scenario was put forward in [136]. Finally, the optimal overlap becomes smaller in the BEC phase, as expected. Instead, in this regime, large overlaps are obtained with the superfluid ansatz, which is defined as the equal-weight superposition of all states at fixed density [142].

4.8 Conclusions

In this work, we systematically classify CSLs on the honeycomb lattice relevant to Rydberg atom experiments using the PSG analysis. We show that the CSL wavefunctions constructed from the Gutzwiller-projected parton wavefunctions are able

to capture the intermediate disordered phase in chiral Rydberg atom arrays. In particular, our results resolve the previously unclear nature of the intermediate phase found in Ref. [74]. In the context of Rydberg atom experiments, our work provides a general framework which can be utilized to search for CSLs in other lattice models. Given the fast experimantal progress in the field, it would be interesting to extend our approach to other lattices, which are immediately available in tweezer arrays [31, 38].

Chapter 5

Emergent dipole field theory in atomic ladders

Sparked by a series of remarkable atomic physics experiments [37, 143–145], constrained dynamics in quantum many-body systems have attracted a great deal of attention in recent years [146–154]. From a fundamental viewpoint, these systems offer a rich playground for studying complex non-equilibrium properties, where the interplay of correlations and dynamical frustration can result in a variety of elusive phenomena, such as Hilbert space fragmentation [155–158], slow relaxation dynamics [159–161], as well as intriguing links to lattice gauge theories [66, 162–164] and fracton models [165–167]. Such phenomena are inherently related to strong correlations and lack a counterpart in the context of non-interacting particles.

The imposition of higher, multipole conservation laws in the many-body theory [147, 163] represents a new opportunity to generate nontrivial dynamics. This has been recently demonstrated in experiments with ultracold atom gases [143–145], where a tilted optical lattice is used to enforce a dipole (center-of-mass) preserving dynamics. In view of that, a number of works have not only established the ground state phase diagram of dipole-conserving lattice models of fermions or bosons [152], but have also considered the nonequilibrium dynamics of such models [153]. The core idea about this research line is to enforce as well as possible the dipole symmetry as a Hamiltonian property (regardless of energy scale).

In this work we pursue a different approach, where the symmetry constraint emerges as a low-energy property of the ground state. We draw inspiration from a Bariev-like model [168–172], whose phase diagram features a Tomonaga-Luttinger liquid (TLL) state formed by bound pairs. We use field theory arguments and exact diagonalization (ED) to link this ground state to an emergent dipole-type symmetry, which constrains the local dynamics of single-particle excitations that need to find partners in order to move. Having in mind atomic physics realizations (Fig. 5.1), we propose a quasi-adiabatic protocol [68] to prepare the dipole TLL state from biased optical ladders, as well as Rydberg atom arrays. We benchmark the state preparation by using a time-dependent variational principle (TDVP) algorithm to dynamically evolve an initial product state. Finally we consider the quench dynamics of isolated defects placed on top of the dipole TLL state. We use a combination of density matrix renormalization group (DMRG) and time-evolving block-decimation (TEBD) algorithms to prepare and evolve the single-defect states, contrasting our numerical results to field theory predictions. Figure 5.1 gives a general perspective onto a protocol that prepares and observes the time evolution of defects.

The rest of the chapter is organized as follows. We set our notation and introduce the model Hamiltonian as a hardcore boson ladder in Sec. 5.1. We inspect analytically specific parameter regimes, and then focus on the regime where the model exhibits strictly confined excitations. We utilize a duality map to reveal a connection

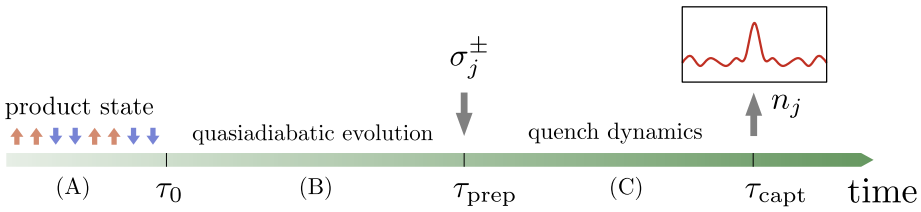

FIGURE 5.1: Schematic of the protocol to observe fragmentation dynamics in the presence of an emergent dipole symmetry. (A) Initially, a product state is prepared in the first time interval. (B) This is followed by a quasi-adiabatic state preparation over a time frame $T = \tau_{\text{prep}} - \tau_0$. (C) Once the target state is prepared, a single-particle defect is created by the action of the local operator $\sigma_j^{\pm}$, and the resulting state is left to undergo unitary evolution during the time interval. At the final time the density n_j is measured.

to a PXP-type model featuring Hilbert space fragmentation, providing an alternative viewpoint on dipole symmetry at one of the exactly solvable points the model features. We discuss experimental implementations of the microscopic dynamics in Sec. 5.2: we derive the effective Hamiltonian from physically sensible Rydberg- and cold-atom models, discussing pertinent perturbations to each platform. A low-energy field theory description for the lattice model is presented in Sec. 5.3, which we use to assess the stability of the dipole TLL state and devise the mobile impurity model. This analysis is complemented by numerical simulations in Sec. 5.4. We give particular focus to benchmark the state preparation protocol and test the nontrivial dynamics of isolated defects. We offer a summary and point out open perspectives in Sec. 5.5.

5.1 Effective hard-core boson model

We consider hard-core bosons on a two-leg zigzag ladder (shown in Fig. 5.2), where the number of particles is preserved separately in each sub-lattice. The system dynamics is described by a Bariev-like [168, 172] Hamiltonian:

$$H = -J\sum_i(\sigma_i^+\sigma_{i+2}^- + \text{H.c.}) - W\sum_i(\sigma_i^+\sigma_{i+1}^z\sigma_{i+2}^- + \text{H.c.}) + V\sum_i \sigma_i^z\sigma_{i+1}^z, \tag{5.1}$$

where $i = 1, 2, \ldots, L$ are sites in the zigzag geometry, and σ_i^+ is the hard-core boson creation operator. The hard-core boson occupation number $n_i = \sigma_i^+\sigma_i^-$ is related to the Pauli matrix σ_i^z by $n_i = (1+\sigma_i^z)/2$. The lattice model depends on three coupling parameters. The intra-leg hopping amplitude J, the correlated hopping term W, and the Ising-like interaction V. Note that single-particle tunneling among different legs is not allowed as it violates the number conservations.

The two global U(1) symmetries of the model can be expressed as the conservation of the total number of excitations and the so called inter-leg *magnetization*:

$$N = \sum_i n_i, \qquad M = \frac{1}{2}\sum_i (-1)^i n_i. \tag{5.2}$$

We call N and M the *charge* and *spin* quantum numbers, given the similarity to electronic systems. We use these two conserved charges to fix a subspace of interest. Hereafter, we concentrate on the scenario where both legs are half-filled, meaning

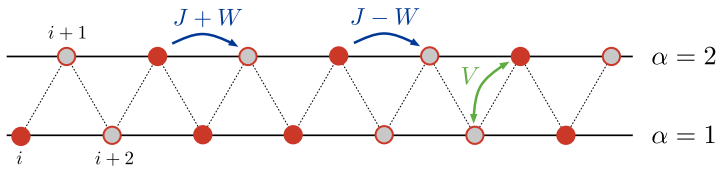

FIGURE 5.2: Illustration of the hard-core boson model. The two-leg ladder has the geometry of a zigzag chain where odd and even sublattices enjoy their own number conservation. Correlated hopping W modulates tunneling amplitudes according to the presence or absence of bosons in the other leg. Additional nearest-neighbor interactions V favor attraction or repulsion among neighboring bosons.

we shall consider chains whose thermodynamic limit is defined by $N/L \to 1/2$, with vanishing magnetization $M/L \to 0$. We use $J = 1$ to set the energy scale, and study the model as a function of W and V. We only consider positive values of W, given that we can flip its sign via a global particle-hole transformation, $\sigma_i^z \to -\sigma_i^z$.

5.1.1 Phase diagram overview

Bariev-like models and their corresponding phase diagrams have been discussed in the literature [168–172]. Below, we exploit some of these earlier results to clarify the phase diagram of the hard-core boson ladder, referring the reader to Refs. [171, 172] for more details. We will complement those with a field theory approach we describe below.

The phase diagram is schematically depicted in Fig. 5.3. At $V = W = 0$, we find the 2TLL phase, a critical state with power-law decaying correlation functions described by two independent TLL theories (as for decoupled chains). The TLLs govern the low-energy spectrum of collective excitations of charge and spin that are generated from the hybridization of the original excitations in the legs. This phase arises from the competition among the correlated hopping W and the antiferromagnetic V interaction that prevents excitations from pairing up.

If we keep V small and move towards dominant W coupling, spin excitations are gapped out and we enter the dipole TLL phase. The dipole TLL phase can be viewed as a quantum liquid of *molecular* dimers [168], where each dimer is formed by binding two single-particle excitations that live in distinct legs together. The associated pairing strength depends mostly on the correlated hopping W [169], which drives a BKT type transition at $V = 0$ into the dipole TLL phase. The underlying liquid ground state can be identified by a den Nijs-Rommelse type string order parameter as showed by Chhajlany *et al.* [172].

Alternatively, we identify here an emergent dipole-like symmetry that constrains the dynamics of single-particle excitations in the dipole TLL state. At $W = J$ the binding strength reaches its maximum [169]. At this special point, excitations are strictly confined (see Fig. 5.4) and the dipole symmetry becomes exact as the lattice model Eq. (5.1) commutes with

$$D = \sum_i i\tilde{n}_i, \qquad \tilde{n}_i = n_i \exp\left(\mathrm{i}\pi \sum_{j<i} n_j\right), \tag{5.3}$$

which encodes the local constraint in a nonlocal global operator. We point out that, although clearly grounded in the fixed points provided by the Bariev chain obtained

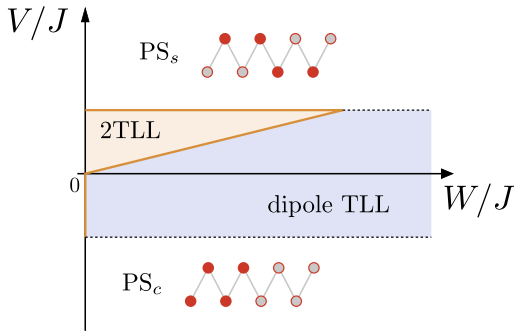

FIGURE 5.3: Simplified sketch of the phase diagram as obtained from the weak-coupling theory. Near the origin we find the 2TLL and dipole TLL phases. For large V these give room to phase separation PS_c and PS_s.

for $V = 0$ [168], the dipole TLL phase is quite robust to a great sort of perturbations, cf. Sec. 5.2, surviving up to finite values of V [172].

Finally, for dominant V coupling we find the phase separated (PS) states PS_c and PS_s. The phases PS_c and PS_s correspond to phase separation of charge and ladder spin [171, 173]. We note these are particularly sensitive to boundary conditions (as well as form of interactions, e.g., replacing Ising-like to density-density interactions). For simplicity we only comment on open chains with a double even number of sites, so each sub-lattice is at exact half-filling.

Ferromagnetic interactions favor clustering, giving rise to the PS_c phase at large enough $V < 0$. The two degenerate classical ground states of the Ising-like interaction take the domain-wall form

$$|\phi_1\rangle = |\bullet\bullet\bullet\bullet\bullet\bullet\circ\circ\circ\circ\circ\circ\rangle\,, \qquad |\phi_2\rangle = |\circ\circ\circ\circ\circ\circ\bullet\bullet\bullet\bullet\bullet\bullet\rangle\,, \tag{5.4}$$

breaking $\mathbb{Z}_2$ mirror reflection across the center link of the chain. The gapped spectrum is composed from the creation of additional domain-walls, obtained by either the full displacement of the cluster or its separation in smaller pieces. The addition of the couplings J and W do not lift the twofold degeneracy of the PS_c ground state, but give kinetic energy to domain-wall excitations renormalizing energy gaps.

On the other hand, strong antiferromagnetic interactions lead to the so-called PS_s phase, which can be thought of as a Néel state with a domain-wall excitation stuck in the center of the chain [171]. As in the ferromagnetic case, the antiferromagnetic Ising-like interaction has two classical ground states:

$$|\psi_1\rangle = |\circ\bullet\circ\bullet\circ\bullet\bullet\circ\bullet\circ\bullet\circ\rangle\,, \qquad |\psi_2\rangle = |\bullet\circ\bullet\circ\bullet\circ\circ\bullet\circ\bullet\circ\bullet\rangle\,. \tag{5.5}$$

However, while the addition of J is still innocuous, a nonzero W lifts the ground state degeneracy. The favored configuration can be deduced from the sign of W and the nature of the pair excitation in the center of the state. For positive W the state containing a particle dimer $|\psi_1\rangle$ is favored, while $|\psi_2\rangle$ is selected for negative W.

5.1.2 Duality and exotic dipole constraint

The behavior of the dipole TLL state is reminiscent of the so-called fractonic liquids that have been studied recently in literature [153, 166]. To clarify this link, we

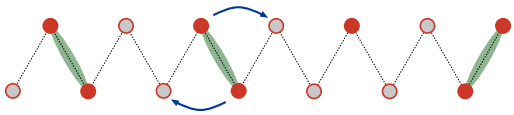

FIGURE 5.4: Cartoon of the strictly constrained point $W = J$. Dimers are depicted as bound pairs of bosons, which move by playing a *leapfrog* game. Isolated particles are unable to move by their own.

inspect more closely the point $W = J$ where the dipole-type operator D becomes an exact symmetry of the lattice model.

The operator D has been discussed before in the context of constrained quantum dynamics in one dimension [166, 174]. In particular, Ref. [166] introduced D as an ingredient to restrain spinless fermions to move in pairs and produce fractonic dynamics in one-dimensional polaronic systems. The hard-core boson ladder Eq. (5.1) has a similar behavior when $W = J$. As illustrated in Fig. 5.4, bosons in one leg only move when assisted by a boson partner in the neighboring chain, binding them into a two-site molecule.

The nonlocal character of D makes it hard to recognize its meaning. We thus move to a dual picture, by performing a Kramers-Wannier-like transformation, defined as

$$\tau_i^x = (-1)^i \prod_{j \leq i} \sigma_j^z, \qquad \tau_i^z = (-1)^i \sigma_i^x \sigma_{i+1}^x, \tag{5.6}$$

where we introduce oscillatory factors for convenience. Then, by replacing $n_i = \frac{1}{2}(1 + \sigma_i^z)$ into the formula for $\tilde{n}_i$ in Eq. (5.3), we learn $\tilde{n}_i$ is given by the difference $\tilde{n}_i = \frac{1}{2}(\tau_{i-1}^x - \tau_i^x)$. This implies that the dipole operator D becomes the dual magnetization along the x axis:

$$D = \frac{1}{2} \sum_i \tau_i^x, \tag{5.7}$$

where we assume an infinite system and drop boundary terms. Translating the hard-core boson model in Eq. (5.1) as well, we arrive at

$$H_{\mathrm{KW}} = \sum_i \left[W \tau_i^y \tau_{i+1}^y + J \tau_i^z \tau_{i+1}^z + \tau_{i-1}^x (J \tau_i^y \tau_{i+1}^y + W \tau_i^z \tau_{i+1}^z) \tau_{i+2}^x + V \tau_{i-1}^x \tau_{i+1}^x \right]. \tag{5.8}$$

The model H_{KW} has a quite intriguing form. First, we readily recognize it commutes with D when $W = J$, as H_{KW} becomes manifestly invariant under rotations along the x axis. The PXP-type constraint is perfectly implemented at the point $W = J$, where it becomes the folded XXZ model studied by Zadnik and Fagotti [160], who showed the existence of exponentially many jammed states. The $W = J$ model has also been considered by Yang et al. [157], who demonstrated that the Hamiltonian features Hilbert-space fragmentation and unusal thermalization properties even for nonzero V, away from the integrable point.

For $W \neq J$ the constraint is no longer perfectly implemented and the Hamiltonian H_{KW} loses its invariance under U(1) rotations along the x-axis. The model still features a pair of U(1) conservation laws, inherited from the N and M numbers, given by the numbers of ferromagnetic and antiferromagnetic domain walls $\sum_i \tau_i^x \tau_{i+1}^x$ and $\sum_i (-1)^i \tau_i^x \tau_{i+1}^x$, which are conserved for all W. We note that Eq. (5.8) highlights the existence of a strong-weak W coupling duality around $W = J$, implementing the exchange of $\tau^y \leftrightarrow \tau^z$ terms in the Hamiltonian.

5.2 Microscopic realizations of constrained dynamics

In this section we discuss potential realizations of our target Bariev-like model in atomic arrays. We use perturbation theory to examine two scenarios, one with Rydbergs in a linear chain and other where cold atoms move through the sites of an optical lattice. In both cases the central idea is the use of a strong potential bias to split the system into two sublattices, so that the slow, non-equilibrium dynamics preserves the relative number of excitations in each sublattice. Before continuing, let us note that some of the parameter regimes we are interested in can also be achieved following earlier proposals, in particular, Refs. [170–172].

5.2.1 Rydberg-atom chain

We first illustrate a proposal utilizing Rydberg atoms trapped into optical potentials in the frozen regime, where atomic motion can be neglected [31]. We assume atoms, prepared in two different Rydberg states, e.g., $|\circ\rangle = |nS\rangle$ and $|\bullet\rangle = |nP\rangle$, are placed in the sites of a linear chain. Dipolar coupling between Rydbergs produce a flip-flop (dipolar) exchange interaction t_{ij} between pairs of atoms that decays approximately as $t_{ij} = t_{|i-j|} = t/|i-j|^3$. We also assume the two atomic states are coupled by an external (microwave) drive. The Rydberg model Hamiltonian then reads

$$H_{\text{Ryd}} = \frac{\Omega}{2}\sum_i \sigma_i^x + \frac{\delta}{2}\sum_i (-1)^i \sigma_i^z + \sum_{i<j} t_{ij}(\sigma_i^+\sigma_j^- + \sigma_i^-\sigma_j^+), \tag{5.9}$$

where Ω is the Rabi frequency, and δ is the staggered detuning corresponding to the drive. The staggering can be realized, e.g., by locally changing the Stark shift generated by the optical potential. To engineer the model in Eq. (5.1), we work in the regime where $\Omega \to 0$ and $\delta \gg t$. We take the zero Rabi frequency limit $\Omega \to 0$ so the total number of excitations is preserved, while the large δ limit allow us to freeze the magnetization M and study hopping processes perturbatively.

Perturbative treatment.— We separate hopping terms in two groups. The first group does not change the number M, and comprises the hopping processes within the same sublattice. These tunneling amplitudes are hence not quenched by the detuning bias, popping out directly into the projected effective Hamiltonian. The second group on the other hand includes tunneling processes where an excitation moves from one sublattice to the other. These processes are associated with a change $\Delta M = \pm 1$, and their leading contribution comes from second-order perturbation theory. Finally, given the rapid decay of the tunneling amplitudes, we truncate long-range hoppings beyond second-neighbors and make use of a Schrieffer-Wolff transformation to find

$$H_{\text{Ryd,eff}} = J\sum_i (\sigma_i^+\sigma_{i+2}^- + \text{H.c.}) - W\sum_i (-1)^i (\sigma_i^+\sigma_{i+1}^z\sigma_{i+2}^- + \text{H.c.}), \tag{5.10}$$

where $J = t/8$, and $W = t^2/2\delta$. The effective model looks much like the Bariev chain [168], but the correlated exchange term acquires a staggering factor. The oscillatory phase is innocuous to our goal and favors pairing in the antisymmetric channel, giving rise to a dipole TLL made of particle-hole molecules. In fact the staggering phase in W can be easily removed by performing a particle-hole transformation in

just one of the legs, say

$$\mathcal{C}_1 : \quad \sigma^+_{2l+1} \leftrightarrow \sigma^-_{2l+1}, \qquad \sigma^z_{2l+1} \to -\sigma^z_{2l+1}. \tag{5.11}$$

The resulting model, although with dominant antiferromagnetic correlations, is thus equivalent to Eq. (5.1) exhibiting a dipole TLL phase.

The Hamiltonian in Eq. (5.10) can only be taken as the dominant contribution in the more general case once longer-range terms are included. We however anticipate that those perturbations should not be harmful to the dipole TLL liquid. For instance, two perturbations that could arise are

$$\delta H_{\text{Ryd,eff}} \approx t_4 \sum_i \sigma^+_i \sigma^-_{i+4} + w_4 \sum_i (-1)^i \sigma^+_i (\sigma^z_{i+1} + \sigma^z_{i+3}) \sigma^-_{i+4} + \text{H.c.} + \cdots, \tag{5.12}$$

where the estimated size of these couplings are $t_4 = t/64$ and $w_4 \sim t_1 t_3/\delta = t^2/27\delta$. These two terms break the integrability of the Bariev model, but are not enough to drive us away from the dipole TLL phase (as can be seen, at weak coupling, by analyzing their bosonized form). We thus argue Rydbergs are a promising platform to observe and study the dipole TLL state in quasi-adiabatic state preparations.

5.2.2 Cold atoms with laser driven hopping

We now consider an alternative implementation, based on ultracold atoms trapped in the sites of an optical lattice [175]. We assume atoms are allowed to hop among first and second neighbors sites of a zigzag chain, and repel whenever two or more of them occupy the same site. The microscopic Hamiltonian then takes the form of a Bose-Hubbard (BH) model, with an additional chemical potential bias μ between even and odd sublattices:

$$H_{\text{BH}} = -t \sum_i (a^\dagger_i a_{i+1} + \text{H.c.}) - t' \sum_i (a^\dagger_i a_{i+2} + \text{H.c.}) + \frac{U}{2} \sum_i n^a_i (n^a_i - 1) + \frac{\mu}{2} \sum_i (-1)^i n^a_i, \tag{5.13}$$

where a_i removes an atom sitting at i, t and t' are the hopping amplitudes, and U is the onsite Coulomb repulsion. The number of atoms is denoted as $n^a_i = a^\dagger_i a_i$ to discern it from the hard-core boson number introduced before.

We utilize here laser-assisted tunneling [176–178] to induce hopping of atoms with a site-dependent phase. In particular, we consider a nearest-neighbor hopping $t \to t e^{i\varphi_{i,i+1}}$ with staggered flux pattern, depicted in Fig. 5.5. We choose the phase so its sole effect is to flip the sign of t every two sites:

$$H_t \to H_t = -t \sum_l (-1)^l \left(a^\dagger_{2l-1} a_{2l} + a^\dagger_{2l} a_{2l+1} + \text{H.c.} \right), \tag{5.14}$$

where the l sum is taken over half the system size. This phase dressing helps us to cancel out the oscillatory factor that arises in the perturbation theory, as we argue below.

Perturbative treatment.— The perturbative treatment is reminiscent of that in the previous subsection. We consider the large-μ limit to effectively enforce spin symmetry, and assume U is strong enough so that every site contains at most one boson. It is worth noting that such strong couplings are not detrimental to a treatment in the single-band Hubbard regime, as the dynamics of single particles along the wires is not affected by those (in fact, similar regimes have been investigated in Ref. [90]).

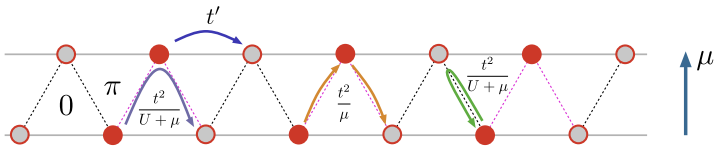

FIGURE 5.5: Illustration of the cold-atom ladder with second-order perturbative processes that arise in the quasi-adiabatic preparation. We assume t' is small enough that we can neglect its corrections. The ladder has an artificial staggered flux configuration: triangles pointing up and down enclose zero and π flux respectively.

We then take into account hopping processes perturbatively. As a further simplification, we consider the regime $t' \ll t$, so the second-neighbor hopping only contributes at first-order in perturbation theory (this assumption is not necessary, but makes computations easier to interpret). Taking into account second-order virtual processes generated by the first neighbor hopping, as seen in Fig. 5.5, we find the effective Hamiltonian governing the slow dynamics of the system takes the form

$$H_{\text{BH,eff}} = -\sum_{l\alpha}\left(J_\alpha \sigma^+_{2l-2+\alpha}\sigma^-_{2l+\alpha} + W_\alpha \sigma^+_{2l-2+\alpha}\sigma^z_{2l-1+\alpha}\sigma^-_{2l+\alpha} + \text{H.c.}\right) + V\sum_i \sigma^z_i\sigma^z_{i+1}, \tag{5.15}$$

where we use $\alpha = 1, 2$ to denote odd and even sub-lattices. The effective Hamiltonian features the desired $\text{U}(1)_c \times \text{U}(1)_s$ symmetry, but lacks leg permutation symmetry. From the Schrieffer-Wolff transformation, we estimate the couplings to be

$$J_{1,2} = t' \pm \frac{t^2}{U \pm \mu}, \qquad W_{1,2} = \frac{t^2}{\mu} \pm \frac{t^2}{U \pm \mu}, \qquad V = -\frac{t^2}{2}\left(\frac{1}{U+\mu} + \frac{1}{U-\mu}\right), \tag{5.16}$$

where we take the upper sign for $\alpha = 1$ and the lower sign otherwise. There are two different ways to restore $\mathbb{Z}_2$ leg symmetry.[1] The first involves adjusting the relative filling in the legs, changing the free Fermi velocity so that they match at some nonzero magnetization $M \neq 0$. Another, less fine-tuned possibility, amounts to considering an extra separation of energy scales in the lattice parameters. Either considering $U \gg \mu$ or $U \ll \mu$ will do the job. In the first case, for instance, by taking the limit $U \ll \mu$, with $t' \sim t^2/\mu$, we can approximate the couplings to $J_{1,2} \to J = t' + \frac{t^2}{\mu}$ and $W_{1,2} \to W = \frac{2t^2}{\mu}$, while V goes to $V \to t^2 U/\mu^2$, and is then assumed to be much smaller than J and W. In this limit, we thus arrive at precisely the model Hamiltonian in Eq. (5.1).

5.3 Effective field theory approach

In this section we present a long-distance, low-energy description for the hard-core boson ladder model. We use bosonization to analyze the effects of interactions starting from the limit of weakly coupled XY chains. As usual for TLLs, we can explore the predictions of the effective theory beyond the perturbative regime by treating the velocities and Luttinger parameters as phenomenological parameters. We shall see that this approach captures the transitions to the dipole TLL phase as

[1] We note the lack of this $\mathbb{Z}_2$ symmetry is not necessarily incompatible with the dipole conservation. As a simple check one may consider the dipole-preserving, but still leg-anisotropic case where $W_1 = J_1 = J + \eta$ and $W_2 = J_2 = J - \eta$, which realizes an alternating hopping pattern for dimers, in a similar fashion to the so called Su-Schrieffer-Heeger model [179].

well as to the classically ordered phases, providing a field theory framework for the entire phase diagram sketched in Fig. 5.3. In addition, we examine the representation of the dipole moment operator in the low-energy theory. We argue that the violation of the dipole symmetry is associated with the creation of gapped spin excitations that behave as mobile defects interacting with the gapless charge modes.

5.3.1 Tomonaga-Luttinger liquid theory

Let us write the hardcore boson ladder model in the limit of decoupled legs, obtained by setting $W = V = 0$ in Eq. (5.1). It is convenient to introduce a leg index $\alpha = 1, 2$ corresponding to odd and even sites, respectively, and denote the spin operators by $\sigma^{\pm}_{\alpha}(l) \equiv \sigma^{\pm}_{2l-2+\alpha}$, with $l \in \mathbb{Z}$. In this notation, the Hamiltonian for decoupled legs reads

$$H_0 = -J \sum_{l\alpha} [\sigma^{+}_{\alpha}(l)\sigma^{-}_{\alpha}(l+1) + \text{H.c.}]. \tag{5.17}$$

We can then bosonize the low-energy excitations of each XY chain separately [180]. The effective Hamiltonian is that of two independent free bosons:

$$H_0 \approx \sum_{\alpha} \frac{v_0}{2} \int \mathrm{d}x \left[(\partial_x \theta_\alpha)^2 + (\partial_x \phi_\alpha)^2 \right], \tag{5.18}$$

where $v_0 = 2J$ is the velocity of the bosonic modes in each leg and the bosonic fields obey the commutation relation $[\theta_{\alpha'}(x'), \partial_x \phi_\alpha(x)] = \mathrm{i}\delta_{\alpha\alpha'}\delta(x - x')$. The fields ϕ_α are associated with fluctuations of the hard-core boson occupation number by

$$\delta n_\alpha(l) = \frac{1}{2}\sigma^{z}_{\alpha}(l) \approx -\frac{1}{\sqrt{\pi}}\partial_x \phi_\alpha(x) + (-1)^x \text{const} \times \sin[\sqrt{4\pi}\phi_\alpha(x)]. \tag{5.19}$$

The staggered part has a nonuniversal prefactor and oscillates with momentum $\pi = \pi(1 + \langle \sigma^{z}_{i} \rangle)$ for a pair of half-filled chains, described by $N/L \to 1/2$ and $M/L \to 0$. Note that if we allow the numbers N and M to change, the value of the momentum is not fixed and may be even different in each sub-lattice. The continuum expansion of the spin raising and lowering operators reads

$$\sigma^{\pm}_{\alpha}(x) \propto \mathrm{e}^{\pm \mathrm{i}\sqrt{\pi}\theta_\alpha(x)} \left\{ 1 + (-1)^x \text{const} \times \cos[\sqrt{4\pi}\phi_\alpha(x)] \right\}. \tag{5.20}$$

We note that the lattice model is invariant under discrete translations $i \to i + 2$, corresponding to a rigid displacement of one site on each leg. In the low-energy theory, this lattice translation amounts to $x \mapsto x + 1$ translations, under which the bosonic fields transform according to

$$\mathcal{L}: \qquad \phi_\alpha \mapsto \phi_\alpha + \frac{\sqrt{\pi}}{2}, \qquad \theta_\alpha \mapsto \theta_\alpha + \sqrt{\pi}. \tag{5.21}$$

In addition, the zigzag chain is invariant under a reflection about a site, which acts as site parity for the leg that contains that site but link parity for the other leg. For instance, the reflection about an odd site acts in the low-energy theory as:

$$\mathcal{P}: \qquad x \mapsto -x, \quad \phi_1 \mapsto -\phi_1, \quad \phi_2 \mapsto \frac{\sqrt{\pi}}{2} - \phi_2, \quad \theta_1 \mapsto \theta_1, \quad \theta_2 \mapsto \theta_2 + \sqrt{\pi}. \tag{5.22}$$

We can also define time reversal as the anti-unitary transformation that takes $\boldsymbol{\sigma}_j \mapsto -\boldsymbol{\sigma}_j$. In the low-energy theory:

$$\mathcal{T}: \qquad \mathrm{i} \mapsto -\mathrm{i}, \quad \phi_\alpha \mapsto -\phi_\alpha, \quad \theta_\alpha \mapsto \theta_\alpha. \tag{5.23}$$

Next, we add interchain interactions perturbatively. We have $H = H_0 + H_W + H_V$, where

$$H_W = -W \sum_l \left[\sigma_1^+(l)\sigma_2^z(l)\sigma_1^-(l+1) + \sigma_2^+(l)\sigma_1^z(l+1)\sigma_2^-(l+1) + \mathrm{H.c.}\right], \tag{5.24}$$

$$H_V = V \sum_l \sigma_2^z(l)[\sigma_1^z(l) + \sigma_1^z(l+1)]. \tag{5.25}$$

The three-spin interaction H_W preserves $\mathcal{L}$ and $\mathcal{P}$ symmetries, but breaks $\mathcal{T}$. Using the continuum expansion of the spin operators, we can combine oscillatory terms from both legs to produce the operator $\delta H_W \approx -\frac{2W}{\pi^2}\int \mathrm{d}x\, \sin[\sqrt{4\pi}(\phi_1 - \phi_2)]$ as the most relevant contribution. The Ising-like interchain interaction H_V contributes with a marginal operator that couples the uniform magnetization in the two legs: $\delta H_V \approx \frac{8V}{\pi}\int \mathrm{d}x\, \partial_x\phi_1\partial_x\phi_2$. We define the charge and spin fields as the linear combinations

$$\phi_{c,s} = \frac{\phi_1 \pm \phi_2}{\sqrt{2}}, \qquad \theta_{c,s} = \frac{\theta_1 \pm \theta_2}{\sqrt{2}}. \tag{5.26}$$

Adding the leading perturbations to Eq. (5.18), we obtain a spin-charge-separated Hamiltonian in the form $H = H_c + H_s$, where

$$\begin{aligned} H_c &= \frac{v_c}{2}\int \mathrm{d}x \left[K_c(\partial_x\theta_c)^2 + \frac{1}{K_c}(\partial_x\phi_c)^2\right], \\ H_s &= \frac{v_s}{2}\int \mathrm{d}x \left[K_s(\partial_x\theta_s)^2 + \frac{1}{K_s}(\partial_x\phi_s)^2\right] - \frac{\lambda}{2\pi^2}\int \mathrm{d}x\, \sin\left(\sqrt{8\pi}\phi_s\right). \end{aligned} \tag{5.27}$$

At weak coupling, the spin and charge velocities are given by $v_{c,s} \approx 2J(1 \pm 4V/\pi J)$. The Luttinger parameters K_c and K_s encode the interactions in the charge and spin sectors, respectively. To first order in the interleg interaction, we find $K_{c,s} \approx 1 \mp 4V/\pi$. The sine potential in the spin sector, with coupling constant $\lambda \approx 4W$, has scaling dimension $2K_s$. Note that this operator is odd under time reversal, as expected for the three-spin operator in H_W. Importantly, the low-energy Hamiltonian in Eq. (5.27) remains valid beyond the regime of small W and V because the sine potential is the leading perturbation compatible with $\mathcal{L}$, $\mathcal{P}$ and $\mathrm{U}(1)_c \times \mathrm{U}(1)_s$ symmetry.

The 2TLL phase corresponds to the regime in which both charge and spin sectors in Eq. (5.27) remain gapless. This can happen with the help of a repulsive interaction, $V > 0$, which disfavors the formation of pairs by making $K_s > 1$ and rendering the sine potential irrelevant. We can write the uniform part of the σ_i^+ operator in terms of charge and spin fields as

$$\sigma_{1,2}^+(l) \propto \mathrm{e}^{\mathrm{i}\sqrt{\pi/2}[\theta_c(x) \pm \theta_s(x)]}. \tag{5.28}$$

In the 2TLL phase, single-particle correlators display a power-law decay, given by

$$\langle 0|\sigma_i^+\sigma_{i+2r}^-|0\rangle \propto r^{-(K_c+K_s)/4K_cK_s}, \tag{5.29}$$

where $|0\rangle$ stands for the ground state. Note that in Eq. (5.29) we must take two points

that belong to the same chain, otherwise the correlator vanishes identically. This is a consequence of the $\mathrm{U}(1)_c \times \mathrm{U}(1)_s$ global symmetry of the ladder and remains true even if we move away from the weak-coupling limit.

The transition to the dipole TLL phase is driven by the flow of the λ perturbation to strong coupling. For $V = 0$, the coupling is marginally relevant, and, as a result, the spin sector undergoes a BKT-type transition. In the strong-coupling limit, we minimize the potential energy by pinning the scalar field ϕ_s to one of its minima:

$$\sqrt{8\pi}\phi_s \to \frac{\pi}{2} + 2\pi\mathbb{Z}. \tag{5.30}$$

The dipole TLL phase then corresponds to a gapless charge sector and a gapped spin sector. Note that attractive V favors pairing, facilitating the transition to the dipole TLL state. Once the spin sector is gapped out, the single-particle propagator develops an exponential decay as follows:

$$\langle 0|\sigma_i^+\sigma_{i+2r}^-|0\rangle \propto \mathrm{e}^{-r/\xi}/r^{1/4K_c}. \tag{5.31}$$

The correlation length ξ is inversely proportional to the mass gap in the spin sector. In the case of a BKT transition at $V = 0$, the gap is exponentially small at weak coupling, with $\xi_{\mathrm{BKT}}^{-1} \sim \exp(-\mathrm{const}/\lambda)$ [180]. Power-law correlations in the dipole TLL phase are only found by pairing bosons in different sublattices, e.g.,

$$\langle 0|\sigma_i^+\sigma_{i+1}^+\sigma_{i+r}^-\sigma_{i+r+1}^-|0\rangle \propto r^{-1/K_c}. \tag{5.32}$$

Note that the distance r is not restricted to even multiples of the lattice spacing, cf. Eq. (5.29), since the two-particle operator $\sigma_i^+\sigma_{i+1}^+$ creates one excitation in each leg, and the correlator always respects the $\mathrm{U}(1)_c \times \mathrm{U}(1)_s$ symmetry.

Instability towards phase separation is deduced from the vanishing of either charge or spin velocities in the large V limit. Assuming a monotonic behavior and estimating the interaction dependence from the weak-coupling expressions for v_c and v_s, we predict $V^\star/J \simeq \pm 0.78$, with positive and negative values corresponding to the transitions towards PS_s and PS_c, respectively. Given that W does not enter into the renormalization of Luttinger parameters at weak-coupling, we expect the critical value $V^\star$ to be roughly independent of W. We are thus led to the phase diagram shown in Fig. 5.3.

5.3.2 Emergent dipole symmetry

Let us now use our field theory formulation to examine the dipole operator in Eq. (5.3). Our goal here is to find its long-distance representation in order to verify it commutes with the low-energy Hamiltonian of the dipole TLL state, and thus represents an emergent symmetry of this phase.

We start from the dual representation in Eq. (5.7), where the dipole operator is given by the sum of Jordan-Wigner strings. We then expand each τ^x as the product of σ^z strings in each leg. For an odd-site operator $\tau_1^x(l) = \tau_{2l-1}^x$, we get $\tau_1^x(l) = -\mathcal{S}_1(l)\mathcal{S}_2(l)$, where $\mathcal{S}_\alpha(l)$ is defined as

$$\mathcal{S}_1(l) = \prod_{m<l}\sigma_{2m}^z, \qquad \mathcal{S}_2(l) = \prod_{m<l}\sigma_{2m+1}^z. \tag{5.33}$$

Likewise, the even-site operator $\tau_2^x(l) = \tau_{2l}^x$ is given by $\tau_2^x(l) = \mathcal{S}_1(l)\mathcal{S}_2(l+1)$. We can then rewrite Eq. (5.7) as

$$D = -\frac{1}{2}\sum_l [\mathcal{S}_1(l) - \mathcal{S}_1(l+1)]\mathcal{S}_2(l), \tag{5.34}$$

where we sum over half the total number of sites.

We can now bosonize the dipole operator using the standard expression for the string operators in terms of the bosonic fields in each sublattice. Naive bosonization yields the complex form $\mathcal{S}_\alpha(l) \approx e^{i\frac{\pi}{2}x + i\sqrt{\pi}\phi_\alpha(x)}$. To obtain a manifestly Hermitian operator, we symmetrize the string, leading to

$$S_\alpha(l) \to S_{\alpha,\mathrm{reg}}(l) \approx \cos[\tfrac{\pi}{2}x + \sqrt{\pi}\phi_\alpha(x)]. \tag{5.35}$$

The product of strings at the same site gives $\mathcal{S}_1(l)\mathcal{S}_2(l) \approx \frac{1}{2}\cos[\sqrt{2\pi}\phi_s(x)]$, where we drop oscillatory terms and higher-order corrections. The second term in Eq. (5.34) is quite similar, but involves a derivative because the fields are at different points:

$$\mathcal{S}_1(l+1)\mathcal{S}_2(l) \approx -\frac{1}{2}\sin[\sqrt{2\pi}\phi_s(x)] - \frac{\sqrt{2\pi}}{4}\cos[\sqrt{2\pi}\phi_s(x)]\partial_x\phi_c(x) + \cdots \tag{5.36}$$

Taking both contributions into account, we arrive at the long-distance representation of the dipole operator:

$$D \propto \int \mathrm{d}x \left[\sin\left(\sqrt{2\pi}\phi_s + \tfrac{\pi}{4}\right) + \frac{\sqrt{\pi}}{2}\cos\left(\sqrt{2\pi}\phi_s\right)\partial_x\phi_c\right] + \cdots, \tag{5.37}$$

where we omit the prefactor and the ellipsis contains higher-order corrections.

From the continuum version of D, we readily learn that the dipole operator can only be a symmetry if ϕ_s condenses. This is clearly not the case in the 2TLL phase, where both ϕ_c and ϕ_s fluctuate and D does not commute with the low-energy Hamiltonian in Eq. (5.27). In the dipole TLL phase, however, this condition is met as the spin field is pinned to $\sqrt{8\pi}\phi_s \to \pi/2$ according to the strong-coupling flow of λ. Plugging this condition into Eq. (5.37) gives

$$D \approx \frac{1}{\sqrt{2\pi}}\int \mathrm{d}x\, \partial_x\phi_c + \cdots, \tag{5.38}$$

where we drop an unimportant additive constant, and fix the proportionality constant. In this form, the dipole operator is proportional to the total number of particles (half of it if we assume all particles are bound in pairs), and certainly commutes with the low-energy Hamiltonian.

This analysis tell us that the dipole operator describes an emergent symmetry of the dipole TLL phase. This symmetry is valid at low energies, below the spin gap, where all particles are confined into pairs but gapless excitations are still possible in the form of collective modes in the charge sector. This finding supports the dimer picture of the dipole TLL phase. While our bosonization approach started in the weak-coupling limit where the spin gap is small, we expect this picture to become more accurate as we increase W towards the special point $W = J$, where the dipole symmetry becomes exact and the pairs are strictly confined.

Single-particle excitations violate the pinning condition on ϕ_s because they carry both charge and spin quantum numbers. In the low-energy theory, the operator σ_i^+

in Eq. (5.28) creates a kink in the spin field at the position x, shifting ϕ_s as

$$\sqrt{8\pi}\phi_s(y) \to \sqrt{8\pi}\phi_s(y) + 2\pi\Theta_{\mathrm{H}}(y-x), \tag{5.39}$$

where $\Theta_{\mathrm{H}}(x)$ is the Heaviside step function. This means that the kink interpolates between two ground states of the sine potential in Eq. (5.27). On the other hand, the kink changes the sign of the dipole operator in Eq. (5.37) across the position where the single particle is created. This effect is consistent with the original definition of the dipole operator in Eq. (5.3), since inserting a single particle changes the sign of the string in $\tilde{n}_i$. Thus, we can view a local single-particle excitation as a defect in the spin field configuration. Far from this defect, we could still pin ϕ_s to a local minimum, but the dipole symmetry is spoiled if the defect is allowed to move through the lattice. In the following we will construct an effective mobile impurity model to describe the dynamics of this defect in the dipole TLL phase.

5.3.3 Mobile impurity model

According to Eq. (5.27), at low energies the spin sector of the dipole TLL is described by a sine-Gordon-type model. At weak coupling, i.e., for small spin gap $\Delta_s \ll J$, the elementary excitations are kinks or anti-kinks with relativistic dispersion $E_s(k) = \sqrt{v_s^2 k^2 + \Delta_s^2}$ [181]. As we increase the Bariev interaction strength W, the spin gap increases and the dispersion relation deviates from the relativistic dispersion. We are now interested in exploring the vicinity of the special point $W = J$, where the dipole symmetry imposes that single-particle excitations, which are charged under the $\mathrm{U}(1)_s$ symmetry, cannot move by themselves. To describe this regime, we restrict the excitation spectrum to allow at most one spin excitation. This type of problem can be tackled using effective mobile impurity models, in which the finite-energy excitation is treated as a distinguishable particle that interacts with the gapless modes of the TLL [182].

We start by approximating the spin dispersion near its minimum by

$$E_s(k) \approx \Delta_s + \frac{k^2}{2m}, \tag{5.40}$$

where m is the effective mass. For $W = J$, we expect $m \to \infty$, corresponding to localized spin excitations due to the exact dipole symmetry. We then treat the single spin excitation as an impurity mode, writing

$$\sigma_i^+ \propto \mathrm{e}^{\mathrm{i}\sqrt{\pi/2}\theta_c(x)} d_s^\dagger(x), \tag{5.41}$$

where $d_s^\dagger(x)$ is charge neutral but carries spin quantum number $\Delta M = +1/2\,(-1/2)$ if i is an odd (even) site. In this representation, the ground state $|0\rangle = |0\rangle_c \otimes |0\rangle_s$ is a vacuum of the bosonic charge modes and of the d_s particle. The effective mobile impurity model that includes the spin excitation has the form

$$H = H_c + \int \mathrm{d}x \left[d_s^\dagger \left(\Delta_s - \frac{1}{2m}\partial_x^2 \right) d_s - g\sqrt{\frac{2}{\pi}}\partial_x\phi_c d_s^\dagger d_s \right] + \ldots, \tag{5.42}$$

where H_c is the bosonic Hamiltonian in Eq. (5.27) and we omit irrelevant interaction terms. Phenomenologically, the coupling g between the impurity and the charge density can be interpreted as follows. Suppose we perturb the hardcore boson ladder in the dipole TLL phase by adding a uniform field $\delta H_Z = -\frac{h}{2}\sum_i \sigma_i^z$. In the

low-energy theory, this perturbation becomes $\delta H_Z \approx h\sqrt{\frac{2}{\pi}}\int \mathrm{d}x\, \partial_x \phi_c$. In a grand canonical ensemble formulation, the change in the particle density can be absorbed by shifting the charge boson by $\phi_c(x) \to \phi_c(x) - \frac{hK_c}{v_c}\sqrt{\frac{2}{\pi}}x$. Implementing this shift generates a renormalization of the spin gap in the mobile impurity model in Eq. (5.42). As a result, we obtain the relation

$$g = \frac{\partial \Delta_s}{\partial \bar{\rho}_c}, \tag{5.43}$$

where $\bar{\rho}_c = \frac{1}{2}\langle \sigma_i^z + \sigma_{i+i}^z \rangle$ is the average charge density in the ground state and we use $\kappa = \partial\bar{\rho}_c/\partial h = 2K_c/\pi v_c$ for the charge compressibility of the TLL. Thus, the coupling constant g depends on how the spin gap changes when we vary the total number of particles. This coupling is allowed when we have a finite-energy excitation in either spin or charge sectors [182–184].

We can eliminate the interaction between the impurity and the gapless modes using a unitary transformation. We define

$$U = \exp\left[-i\sqrt{\frac{2}{\pi}}\frac{gK_c}{v_c}\int \mathrm{d}x\, \theta_c d_s^\dagger d_s\right] \tag{5.44}$$

and the transformed fields

$$\tilde{d}_s = U^\dagger d_s U = d_s \mathrm{e}^{-\mathrm{i}\sqrt{\frac{2}{\pi}}\frac{gK_c}{v_c}\theta_c}, \tag{5.45}$$

$$\partial_x \tilde{\phi}_c = U^\dagger \partial_x \phi_c U = \partial_x \phi_c - \sqrt{\frac{2}{\pi}}\frac{gK_c}{v_c} d_s^\dagger d_s. \tag{5.46}$$

In terms of the new fields, the Hamiltonian becomes

$$H = \int \mathrm{d}x \left[\frac{v_c K_c}{2}(\partial_x \tilde{\theta}_c)^2 + \frac{v_c}{2K_c}(\partial_x \tilde{\phi}_c)^2 + \tilde{d}_s^\dagger\left(\Delta_s - \frac{1}{2m}\partial_x^2\right)\tilde{d}_s\right] + \ldots, \tag{5.47}$$

where again we drop irrelevant interactions. Importantly, the dressed impurity mode $\tilde{d}_s$ carries a charge proportional to the coupling g because the charge density operator is given by

$$\rho_c = -\sqrt{\frac{2}{\pi}}\partial_x \phi_c = -\sqrt{\frac{2}{\pi}}\partial_x \tilde{\phi}_c - \sqrt{\frac{2}{\pi}}\frac{gK_c}{v_c}\tilde{d}_s^\dagger \tilde{d}_s. \tag{5.48}$$

Since this impurity mode is non-interacting, we obtain the free propagator

$$\begin{aligned} G_d(x,\tau) &= \langle 0|\tilde{d}_s(x,\tau)\tilde{d}_s^\dagger(0,0)|0\rangle = \int_{-\infty}^{\infty}\frac{\mathrm{d}k}{2\pi}\mathrm{e}^{\mathrm{i}kx - \mathrm{i}\Delta_s\tau - \mathrm{i}k^2\tau/2m - a^2k^2/2} \\ &= \frac{1}{\sqrt{2\pi}}\left(a^2 + \frac{\mathrm{i}\tau}{m}\right)^{-1/2}\exp\left(-\frac{x^2}{2a^2 + 2\mathrm{i}\tau/m}\right), \end{aligned} \tag{5.49}$$

where a^{-1} is a momentum cutoff, with a of the order of the lattice spacing. Note that the propagator is a scaling function of τ/m.

To probe the time evolution of the defect, let us consider the time-dependent variation in the local density:

$$C(j,\tau) = \langle\Omega|\, \sigma_0^- n_j(\tau)\sigma_0^+ \,|\Omega\rangle - \langle\Omega|\, n_j \,|\Omega\rangle\,, \tag{5.50}$$

where $|\Omega\rangle$ denotes the ground state of the hardcore boson ladder. In the mobile impurity model, this quantity becomes

$$C(x,\tau) \approx C_c(x,\tau) + C_s(x,\tau). \tag{5.51}$$

The first term involves the charge density. Defining the vertex operator $V_c = \mathrm{e}^{-\mathrm{i}\sqrt{\pi/2}(1-g\kappa)\tilde{\theta}_c}$, we obtain $C_c(x,\tau) \propto \langle 0|V_c(0)\partial_x\phi_c(x,\tau)V_c^\dagger(0)|0\rangle_c$. This contribution spreads ballistically with the charge velocity v_c and decays algebraically at long times. The second contribution involves the impurity propagator:

$$C_s(x,\tau) \propto \langle 0|\tilde{d}_s(0)\tilde{d}_s^\dagger(x,\tau)\tilde{d}_s(x,\tau)\tilde{d}_s^\dagger(0)|0\rangle_s = G_d(x,\tau)G_d(-x,-\tau). \tag{5.52}$$

Using Eq. (5.49) and setting $x = 0$, we find that the density measured at the same position where the defect is created decays with time as $C(0,\tau) \propto m/\tau$ for any finite mass. In the limit of an immobile defect, $m \to \infty$, $C(0,\tau)$ converges to a finite non-universal value for $\tau \to \infty$, implying that some charge remains at $x = 0$ while the other fraction propagates away with velocity v_c.

We can also use the mobile impurity model to study the dynamics of the dipole moment within the low-energy theory. To reproduce the properties of the dipole operator in Eqs. (5.3) and (5.38), we propose the following expression in the continuum:

$$D \approx \int_{-\infty}^{\infty} \mathrm{d}x\, x d_s^\dagger(x)d_s(x) + \frac{1}{\sqrt{2\pi}}\int_{-\infty}^{\infty} \mathrm{d}x\, \hat{\mathrm{S}}(x)\partial_x\phi_c(x), \tag{5.53}$$

where we define $\hat{\mathrm{S}}(x) = 1 - 2\int_{-\infty}^{x} \mathrm{d}x'\, d_s^\dagger(x')d_s(x')$. The first term simply accounts for the dipole moment of the single defect. The second term represents the contribution from bound pairs, where $\hat{\mathrm{S}}(x)$ implements the sign change of the string when we cross the position of the defect. In the defect-free sector, the impurity density vanishes identically, and the dipole operator reduces to the total number of pairs, a conserved quantity within the low-energy theory. By contrast, if we consider the initial state $|\Psi(\tau=0)\rangle = \sigma_j^+|\Omega\rangle$, we expect the variance of the dipole operator to increase with time as the defect moves through the system. We can capture this effect by calculating the variance due to the first term in Eq. (5.53). We obtain

$$\langle \Delta D^2(\tau)\rangle = \langle\Psi(\tau)|\, D^2\, |\Psi(\tau)\rangle - \langle\Psi(\tau)|\, D\, |\Psi(\tau)\rangle^2 \approx \int \mathrm{d}x\, x^2 |G_d(x,\tau)|^2, \tag{5.54}$$

which can be interpreted as the mean squared displacement of the defect. We find

$$\langle \Delta D^2(\tau)\rangle \approx a^2 + \left(\frac{\tau}{ma}\right)^2. \tag{5.55}$$

The variance is finite at $\tau = 0$ because the initial state is not an eigenstate of the dipole operator. For any finite mass, the variance is a function of τ/m and increases quadratically with time. For $m \to \infty$, the variance remains approximately constant, in agreement with the picture of a localized defect enforced by the exact dipole moment conservation law.

5.4 Numerical simulations

In this section we present our numerical findings, obtained from a combination of ED and matrix product states (MPS) based methods, such as TDVP and TEBD. We

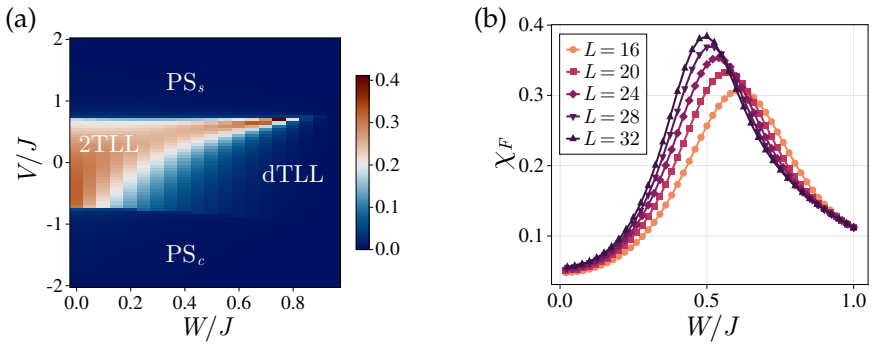

FIGURE 5.6: Ground state characterization with ED. (a) Phase diagram showing the variance of the dipole operator $\langle \delta D^2 \rangle / L$ as a function of W and V for an open chain with $L = 28$ sites. (b) Fidelity susceptibility at $V = 0$ for various system sizes with periodic boundary conditions.

begin with an examination of the phase diagram from the viewpoint of the emergent dipole conservation. We use ED results to provide insight into the conservation of the dipole moment in both ground state and low-energy excited states. We then move to the benchmark of the quasi-adiabatic state preparation. We focus on the more challenging preparation with cold atoms, simulating the dynamical preparation with TDVP. We close our numerical survey by studying the isolated defect dynamics close to the dipole TLL ground state.

5.4.1 Phase diagram and emergent dipole symmetry

We start with a phase diagram characterization of the dipole symmetry. Our goal here is not to precisely determine transition points, but rather to uncover the emergent status of the dipole symmetry in the dipole TLL state.

We first check how the ground state variance of the dipole operator, $\langle \Delta D^2 \rangle = \langle D^2 \rangle - \langle D \rangle^2$, behaves as we navigate across different portions of the phase diagram. In Fig. 5.6(a) we plot the results obtained for a chain with $L = 28$ sites and open boundary conditions. We observe a great similarity with the phase diagram sketched in Fig. 5.3. Near the origin, where we find the 2TLL state, we see the ground state is far from being dipole symmetric as flagged by the higher variance. Moving either up or down we eventually cross to vanishing dipole variance regions, which we associate to the classically ordered states. Coincidentally, we find the transitions take place around the values $V/J \approx \pm 0.75$, quite close to the ones predicted from the weak-coupling bosonization. Finally, when we leave the 2TLL state moving in the direction of increasing W, we appear to cross a smoother region after which the dipole variance also approaches zero. This would correspond to the BKT-type transition into the dipole TLL state, supporting the picture of an emergent dipole-conserving liquid groundstate.

The BKT nature of the transition to the dipole TLL phase makes it difficult to use finite-size scaling techniques effectively. This limitation leads to an overestimation of the 2TLL phase in finite-size numerics, as can be seen in Fig. 5.6(a). This becomes clear when we compute the fidelity susceptibility χ_F, conventionally used to detect critical points via finite-size scaling techniques [81] and defined as

$$\chi_F(\eta) = \lim_{\delta\eta \to 0} \frac{2}{L} \frac{1 - F(\eta, \delta\eta)}{(\delta\eta)^2}, \tag{5.56}$$

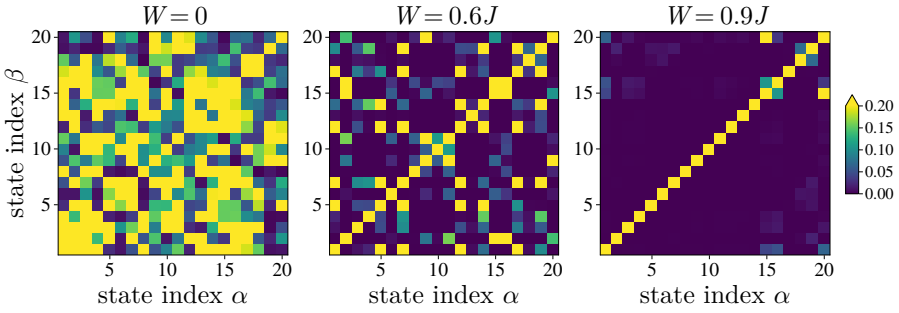

FIGURE 5.7: Matrix elements of the dipole operator for three values of W. We plot the absolute values $|D_{\alpha\beta}| = |\langle\alpha|D|\beta\rangle|$, obtained from the 20 lowest-energy excited states. Data obtained from the ED of an open chain with $L = 28$ sites and $V = 0$.

where $F(\eta, \delta\eta) = |\langle\psi(\eta)||\psi(\eta+\delta\eta)\rangle|$ is the fidelity and η is a parameter of the Hamiltonian. We show in Fig. 5.6(b) the ground state fidelity susceptibility as a function of W/J for a few different sizes L. We find that the transition slowly moves towards weak coupling as we increase the size L, indicating that the 2TLL may actually be much smaller in the thermodynamic limit.

Next, we address the behavior of the dipole operator for excited states. Figure 5.7 shows the matrix elements $|D_{\alpha\beta}| = |\langle\alpha|D|\beta\rangle|$ of the dipole operator, computed in the basis of eigenstates for $W/J = 0$, 0.60 and 0.90. Note that we plot absolute values, so we can focus on the strength of nonzero terms. We observe off-diagonal terms are gradually supressed as we move from $W/J = 0$ to $W/J = 0.90$, in support to the emergent status of the symmetry. In particular, for $W/J = 0.90$, we can see a low-energy block, whose nonzero elements are concentrated on the diagonal.

5.4.2 State preparation

Let us now consider the state preparation protocol. We start from the simple initial state $|\text{Néel} \times \text{Néel}\rangle = |01100110\ldots\rangle$, and evolve it according to the following time-dependent Hamiltonian:

$$H_{\text{exp}}(\tau) = H_{\text{BH}}(\tau) + h(\tau)\sum_l (-1)^l (n^a_{2l} + n^a_{2l+1}), \tag{5.57}$$

where $H_{\text{BH}}(\tau)$ is a time-dependent variant of the Bose-Hubbard model shown in Eq. (5.13). At the initial time, $\tau = 0$, coupling parameters are chosen so the initial state is the actual ground state of the full Hamiltonian $H_{\text{exp}}(0)$ in the symmetry sector where both sublattices are half-filled. This means, initially, the Bose-Hubbard model only includes the potential terms $U = U_0$ and $\mu = \mu_0$, while the hopping elements are set to zero, $t_0 = t'_0 = 0$. Note that we also add an extra time-dependent staggering field $h(\tau)$, whose initial value $h = h_0$ favors the $|\text{Néel} \times \text{Néel}\rangle$ configuration.

The preparation then proceeds by slowly tuning the coupling parameters in $H_{\text{exp}}(\tau)$. We vary three parameters t, t', and h, while keeping the potentials U and μ static along the evolution. The hopping parameters t and t' are increased up to the terminal values $t_f = 1$ and $t'_f = 0.1$, while h is decreased all the way down to $h_f = 0$. The parameter sweep is shown in Fig. 5.8(a) as a function of τ/T, where T denotes the duration of the sweep. We use ED to verify how the many-body spectrum evolves along our parameter flow. In Fig. 5.8(b) we plot the spectrum evolution

of the Hamiltonian (5.57) for a modest chain with $L = 16$ sites. We observe the low-energy manifold remains separated, below the rest of the spectrum, during the whole evolution. Note that we choose the parameters to be as close as possible to the strictly confined point of the Bariev-like model, so we perform the ED in the limit of hard-core bosons ($U \to \infty$) with potential bias set to $\mu = 10$. In this parameter regime, we should ideally end up in the effective model of Eq. (5.15), with parameters $J_\alpha = t'$, $W_\alpha = t^2/\mu$, and $V = 0$, as estimated from Eq. (5.16).

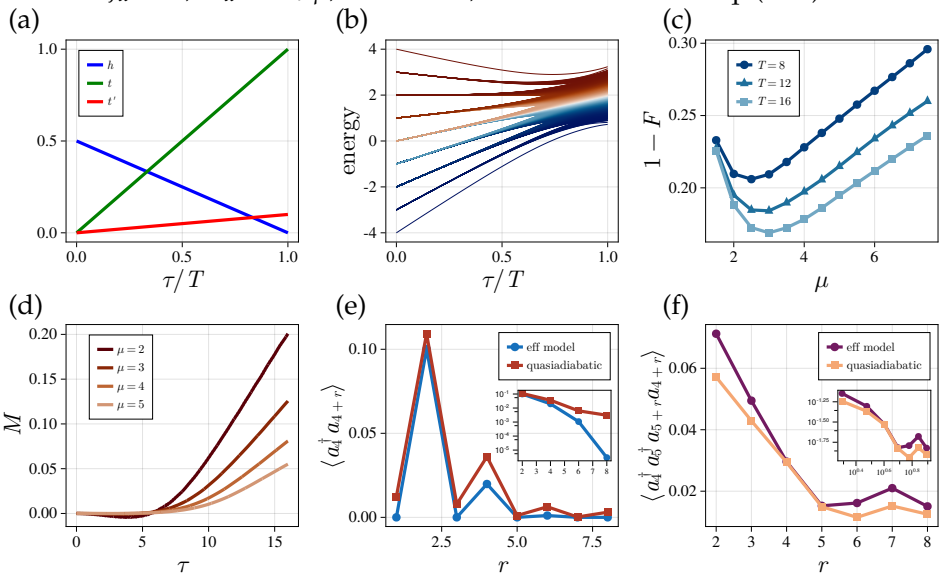

FIGURE 5.8: Quasiadiabatic preparation protocol. (a) Parameter sweep profile employed. (b) Energy spectrum evolution along the parameter sweep. Obtained from the ED of $H_{\text{exp}}(\tau)$ in the limit of hardcore bosons, with $\mu = 10$ and a chain with $L = 16$ sites. (c) Overlap between the dynamically prepared state in the TDVP evolution and the ground state of the target model as a function of μ. (d) Time evolution of the inter-leg magnetization for the initial $|\text{Néel} \times \text{Néel}\rangle$ state. (e) Single-particle and (f) two-particle correlators of the dynamically prepared state, compared with the correlators obtained from the ED of the target model. Insets in (e) and (f) are respectively the log-linear and log-log behavior of the corresponding correlators. For the inset in (e) we only plot even values of r.

We now consider a quasi-adiabatic protocol with a finite preparation time T [68]. To perform the dynamical evolution of the initial state we then resort to TDVP, using a MPS representation of the boson states with maximum occupation number equal to four. We study this preparation as a function of the duration time T and the potential bias μ, fixing the on-site potential to $U = 50$.

Figure 5.8(c) shows the behavior of the overlap between the dynamically prepared and the (DMRG obtained) target state of the Bariev model, $F = |\langle \Psi_{\text{prep}}(T) | \Psi_{\text{target}} \rangle|$. As expected, we see that the fidelity improves with increasing T (or, equivalently, with decreasing sweep rate). We also observe that the maximal overlap is reached at intermediate μ, while small and large values of μ lead to significantly smaller overlaps with the target state. For small μ, higher-order terms in the perturbation theory become sizeable and cannot be neglected. On the other hand, for large μ, the energy gaps, which scale as t^2/μ, become small, such that a higher density of excitations are created in the quasi-adiabatic protocol. We then verify that, while the experimentally prepared state does not conserve the magnetization number M exactly, its

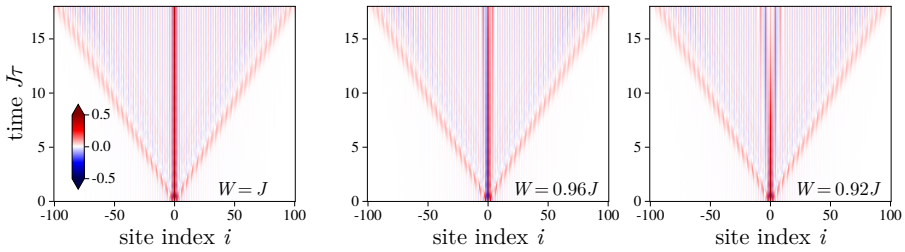

FIGURE 5.9: Defect dynamics on top the dipole TLL state. Time evolution of the local density variation $\langle \delta n_i(\tau) \rangle$ for three different values of W. From left to right, $W/J = 1$, 0.96, and 0.92. The Ising-like interaction is set to $V/J = 0.1$ in all cases. Results obtained with TEBD on a chain with $L = 201$ sites.

expectation value approaches zero with increasing μ as shown in Fig. 5.8(d).

To conclude, we compare the behavior of the single- and two-particle correlators obtained at the end of the protocol with the ones computed from the ED of the target, hardcore boson model Eq. (5.1), with $W = J$ and $V = 0$. As shown in panels (e) and (f) of Fig. 5.8, these are in good agreement with the ideal results obtained from the target model. We point out, however, that the single-particle correlator exhibits greater deviations at larger distances, aligning with predictions from the Kibble-Zurek mechanism [185, 186]. We have also tried the state preparation protocol in the limit $U \ll \mu$. However, we observe that the state does not appear to enter the dipole TLL phase, using experimentally realizable parameter regimes.

5.4.3 Dynamics of defects

Finally, we investigate the out-of-equilibrium dynamics of single-particle excitations. The philosophy here is that, after approaching a target ground state in the quasi-adiabatic preparation, one acts locally with an operator that creates an excitation in the center of the chain letting it evolve coherently for some time. With this in mind, we however leave microscopic models behind and concentrate on the ground state and dynamics produced by the effective hardcore boson ladder.

Numerically our quench protocol goes as follows. First, we use DMRG to prepare the ground state $|\Omega\rangle$ of the Bariev-like Hamiltonian, Eq. (5.1). We then act with σ_0^+, where $j = 0$ represents the center site of a chain with an odd number of sites. Finally, we use a three-site gate TEBD to approximate the time evolution $|\Psi(\tau)\rangle = e^{-iH\tau} |\Psi_0\rangle$, with $|\Psi_0\rangle = \sigma_0^+ |\Omega\rangle$ the prepared initial state.

We apply this recipe to examine how the defect behaves above the dipole TLL ground state. In order to get cleaner results, we choose lattice parameters so we are deep in the dipole TLL phase, close to the strictly confined point $W = J$. We consider values of W in the range from $W/J = 1$ to $W/J = 0.92$, always with a small $V/J = 0.1$ interaction for generality. We run the DMRG for a chain with $L = 201$ sites and quantum numbers fixed to $N = (L-1)/2 = 100$ and $M = 0$. For the TEBD part, we use moderately small time steps $J\delta\tau = 0.01$, and stop the evolution at $J\tau = 18.0$, roughly when the light cone reaches the edges of the chain. The maximum truncation error is set to 10^{-8} during the whole numerical experiment. Attained with a maximum bond dimension of $\chi = 1000$, the results appear well-converged for the times considered.

In Fig. 5.9 we plot the time evolution of the variation in the local density for three different values of W. In agreement with the field theory prediction, we observe the

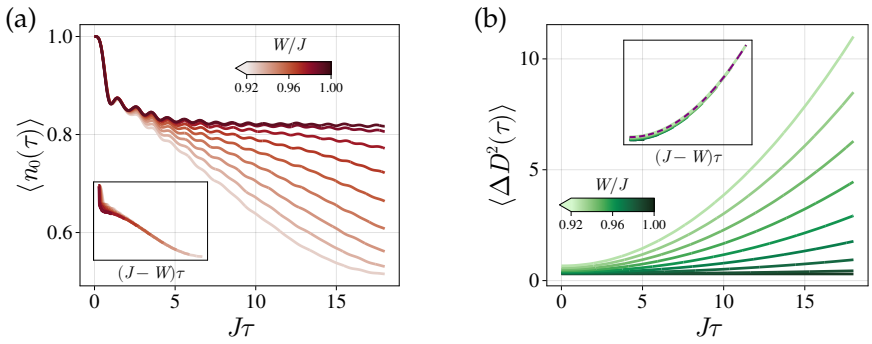

FIGURE 5.10: Time correlators for the defect in the dipole TLL state. (a) Time evolution of the charge density in the central site of the chain for different values of W ranging from $W/J = 1$ (darker) to $W/J = 0.92$ (lighter). The inset shows the rescaling of the time axis by the factor $J - W$. (b) Time evolution of variance of the lattice dipole operator. Inset shows the rescaling of the time axis by the factor $J - W$. The purple dashed line represents a quadratic behavior of the form $a + b\tau^2$, with a and b constants. Results obtained via TEBD on a chain with $L = 201$ sites.

defect exhibits two different spreading patterns as it carries both quantum numbers of charge and spin. After emitting the gapless part, which spreads ballistically, leaving a clear light cone signal, the remaining part of the defect features a substantial slowdown in the relaxation towards equilibrium. For $W/J = 1$ the effect is most dramatic, since the spin part of the defect lies still at the central site where it was created. However, as we move away from the strictly confined point, we are able to observe a slow spreading of the contribution associated with defect.

The time evolution of the density at the central site for various values of W is shown in Fig. 5.10(a). There we can spot two time regimes. At short times we observe a rapid decay due to the formation of the wave front that spreads ballistically. After this initial decay, the density leak slows down. In particular, for $W = J$ the density does not seem to decay significantly for the time scales observed, staying close to $\langle n_0\rangle \approx 0.8$. This is compatible with the limit $m \to \infty$ of the mobile impurity model, where a finite amount of the density excess remains localized at infinitely long times. For $W < J$ we start to observe a slow decay in the density. The inset of Fig. 5.10(a) we show that these curves collapse onto a single curve upon scaling time has been rescaled by $(J - W)\tau$. The data collapse gives the estimate $m \sim |W - J|^{-1}$ for the behavior of the effective mass parameter in the mobile impurity model. Note however in the available time windows we could not directly verify the long-time behavior of $1/\tau$ predicted by the impurity model, controlled by the limit $\tau \gg ma^2$, with a a short-distance cutoff.

We show the time evolution of the variance of the dipole operator in Fig. 5.10(b). As expected, we observe that the dipole variance vanishes for $W = J$ and increases with the difference $|W - J|$. We use this correlator to cross compare time scales as extracted from the time evolution of the central site density. As showed in the inset of Fig. 5.10(b), the time scales here are also compatible with an effective mass for the mobile impurity model given by $m \sim 1/|W - J|$, displaying a quadratic form as predicted in Eq. (5.55).

To complete the picture, we consider the same quench protocol but with a defect added on top of the 2TLL state. However, due to the large entanglement pattern of the $c = 2$ state, we observe a greater difficulty to prepare well-converged ground

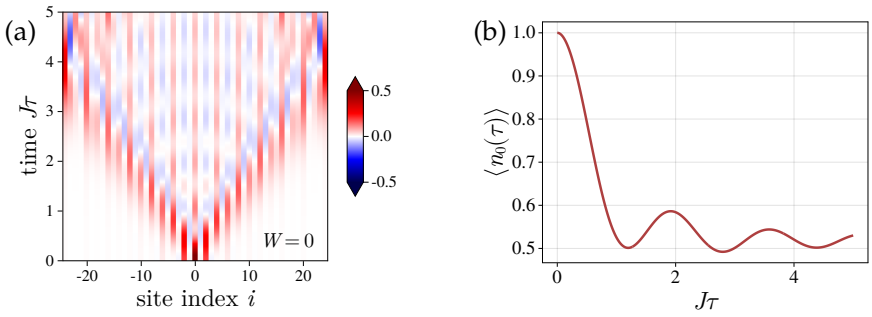

FIGURE 5.11: Ballistic dynamics for defect in the 2TLL phase. (a) Spacetime dependence of the charge excess. (b) Time evolution of the charge density at the central site. Here the parameters of the lattice model are $W = 0$, and $V/J = 0.1$. Results obtained by TEBD on a chain with $L = 49$ sites.

states with DMRG. In view of that we reduce the system size and consider a modest chain of $L = 49$ sites. We set the lattice parameters to $W = 0$ and $V/J = 0.1$, setting the truncation error to 10^{-12}, with maximum bond dimension to $\chi = 600$ during the ground state search. The rest of the numerical protocol goes the same as before and we arrive at the results shown in Fig. 5.11.

Given that the 2TLL phase is adiabatically connected to the fixed point of decoupled chains, the numerical results confirm the natural expectation, and demonstrate the defect thermalizes quickly, spreading ballistically throughout the system. In Fig. 5.11(a) we plot the spacetime dependence of the charge variation $\langle \delta n_j(\tau) \rangle$ during the quench with respect to the unperturbed ground state. Note that for the system size considered, and small difference in velocities, it is difficult to tell apart the lightcones associated with the fractionalization of the single-particle excitation into gapless modes of charge and spin. Another contrast is provided in Fig. 5.11(b), where we plot the time evolution for the number occupation at the central site. When compared to the behavior in the dipole TLL phase, we can see the charge leak does not exhibit any sort of slowdown, relaxing at time scales of the order $J\tau \sim 1$.

Next, we discuss the quench dynamics of a pair of defects on top the dipole TLL state. The two excitations are created upon the action of $\sigma_i^+ \sigma_j^+$ onto the half-filled ground state.

We remain close to the strictly confined point, i.e., $|W - J|$ small, and consider two different scenarios. On the first case we create a pair in consecutive sites $\sigma_i^+ \sigma_{i+1}^+$, while on the second we take them far apart $\sigma_{i-r}^+ \sigma_{i+1+r}^+$, with $r = 20$. Figure 5.12 shows the results obtained for a chain with $L = 200$ sites. In Fig. 5.12(a) we observe a clear lightcone signal formed upon the time evolution of a creation of the local pair. Note that the ballistic spreading of the local pair is in agreement with the continuum limit field theory. Note the motion of the local pair is compatible with the emergent dipole symmetry. This is further showcased in 5.12(c), where we observe the variance of the dipole does not evolve significantly in time. Finally, in Fig. 5.12(b) a separated pair exhibits the approximate behavior of independent single-particle defects. This is further reinforced in5.12(c) where we see the dipole variance changes with time whenever $|W - J| \neq 0$.

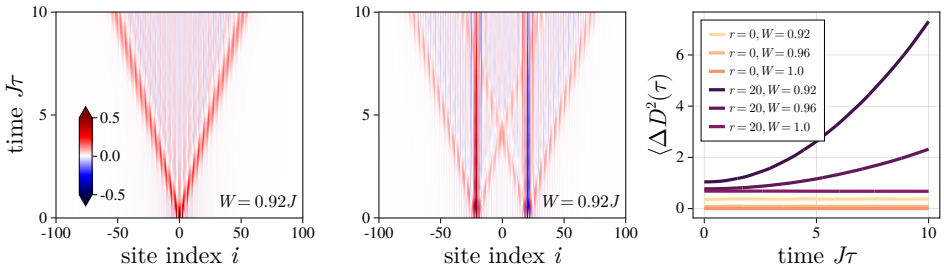

FIGURE 5.12: Two-particle dynamics in the dipole TLL state. (a) Time evolution of the density variation when two defects are created in consecutive sites. (b) Time evolution of the density variation when defects are created far apart. (c) Variance of dipole as a function of time for a local pair ($r = 0$) and a separated pair ($r = 20$).

5.5 Outlook

We investigated a Bariev-type model for hardcore bosons and its non-equilibrium implementation in biased atomic ladders. We considered how deviations from a strictly confined point, still leaves significant imprints in the low-energy physics. In particular we uncovered the emergence of a global non-local symmetry in the dipole TLL state, which constrains the dynamics in the ground state, binding excitations into pairs. Through the use of extensive numerical methods, we simulated and verified the effectiveness of the quasi-adiabatic preparation in the context of a Bose-Hubbard model. We further considered the out-of-equilibrium dynamics of single-particle defects created above the dipole TLL state. We showed that they exhibit a substantial slowdown in the spreading dynamics and compared their slow motion to that of a heavy particle whose mass diverges as we approach the special point where the dipole symmetry is exact.

We leave some open directions for future works. The continuum-limit description of single-particle defects may be improved by treating the sine-Gordon model in its entirety, which may open the possibility of better understanding the role of the emergent constraint as well as extending the theory to finite densities of such defects. Another promising direction is the exploration of a potential link to the theory of $\mathbb{Z}_2$ lattice gauge theories coupled to spinless fermions [162, 164], which exhibits a Bariev-type dynamics in the strong string-tension limit. Driving inspiration from works on the folded XXZ model [160, 161], it may also be of interest to explore the role of the emergent dipole symmetry (if there is any) in the realm of finite temperature transport [148].

Our predictions are of particular relevance to atomic physics experiments, where the protocol we describe could be implemented in a controllable way. We note the use of staggering fields has also been proposed to implement gauge symmetries [187] in quantum analog simulators, as an alternative to tilting potentials [143–145] which need to scale with system size. The core idea of splitting a bipartite lattice with a bias potential is quite generic, and one may envision extensions to 2D systems, where the number of excitations is separately conserved in each sublattice. These ideas might also be of relevance to trapped ion chains, where the implementation of three-body terms similar to those discussed here has recently been proposed [188], or via effective dynamics similar to the Rydberg case, but at the price of introducing longer-range interactions [189, 190].

Bibliography

1. Chen, X., Gu, Z.-C. & Wen, X.-G. Classification of gapped symmetric phases in one-dimensional spin systems. *Physical Review B* **83.** ISSN: 1550-235X. http://dx.doi.org/10.1103/PhysRevB.83.035107 (Jan. 2011).
2. Chen, X., Gu, Z.-C. & Wen, X.-G. Complete classification of one-dimensional gapped quantum phases in interacting spin systems. *Physical Review B* **84.** ISSN: 1550-235X. http://dx.doi.org/10.1103/PhysRevB.84.235128 (Dec. 2011).
3. Schuch, N., Pérez-García, D. & Cirac, I. Classifying quantum phases using matrix product states and projected entangled pair states. *Physical Review B* **84.** ISSN: 1550-235X. http://dx.doi.org/10.1103/PhysRevB.84.165139 (Oct. 2011).
4. Pollmann, F. & Turner, A. M. Detection of symmetry-protected topological phases in one dimension. *Physical Review B* **86.** ISSN: 1550-235X. http://dx.doi.org/10.1103/PhysRevB.86.125441 (Sept. 2012).
5. Sauerwein, D., Molnar, A., Cirac, J. I. & Kraus, B. Matrix Product States: Entanglement, Symmetries, and State Transformations. *Physical Review Letters* **123.** ISSN: 1079-7114. http://dx.doi.org/10.1103/PhysRevLett.123.170504 (Oct. 2019).
6. Schollwöck, U. The density-matrix renormalization group in the age of matrix product states. *Annals of Physics* **326,** 96–192. ISSN: 0003-4916. http://dx.doi.org/10.1016/j.aop.2010.09.012 (Jan. 2011).
7. Silvi, P. *et al.* The Tensor Networks Anthology: Simulation techniques for many-body quantum lattice systems. *SciPost Physics Lecture Notes.* https://doi.org/10.21468/scipostphyslectnotes.8 (Mar. 2019).
8. Ran, S.-J. *et al. Tensor network contractions: methods and applications to quantum many-body systems* (Springer Nature, 2020).
9. Orús, R. A practical introduction to tensor networks: Matrix product states and projected entangled pair states. *Annals Phys.* **349,** 117–158. ISSN: 0003-4916. https://www.sciencedirect.com/science/article/pii/S0003491614001596 (2014).
10. Bañuls, M. C. Tensor Network Algorithms: A Route Map. *Annu. Rev. Condens. Matter Phys* **14,** null. https://doi.org/10.1146/annurev-conmatphys-040721-022705 (2023).
11. Hastings, M. B. An area law for one-dimensional quantum systems. *Journal of Statistical Mechanics: Theory and Experiment* **2007,** P08024–P08024. ISSN: 1742-5468. http://dx.doi.org/10.1088/1742-5468/2007/08/P08024 (Aug. 2007).
12. Calabrese, P. & Cardy, J. Entanglement entropy and quantum field theory. *Journal of Statistical Mechanics: Theory and Experiment* **2004,** P06002. ISSN: 1742-5468. http://dx.doi.org/10.1088/1742-5468/2004/06/P06002 (June 2004).

13. Plenio, M. B., Eisert, J., Dreißig, J. & Cramer, M. Entropy, Entanglement, and Area: Analytical Results for Harmonic Lattice Systems. *Physical Review Letters* **94.** ISSN: 1079-7114. http://dx.doi.org/10.1103/PhysRevLett.94.060503 (Feb. 2005).

14. Gioev, D. & Klich, I. Entanglement Entropy of Fermions in Any Dimension and the Widom Conjecture. *Physical Review Letters* **96.** ISSN: 1079-7114. http://dx.doi.org/10.1103/PhysRevLett.96.100503 (Mar. 2006).

15. Wolf, M. M. Violation of the Entropic Area Law for Fermions. *Physical Review Letters* **96.** ISSN: 1079-7114. http://dx.doi.org/10.1103/PhysRevLett.96.010404 (Jan. 2006).

16. Barthel, T., Chung, M.-C. & Schollwöck, U. Entanglement scaling in critical two-dimensional fermionic and bosonic systems. *Physical Review A* **74.** ISSN: 1094-1622. http://dx.doi.org/10.1103/PhysRevA.74.022329 (Aug. 2006).

17. Verstraete, F. & Cirac, J. I. Matrix product states represent ground states faithfully. *Physical Review B* **73.** ISSN: 1550-235X. http://dx.doi.org/10.1103/PhysRevB.73.094423 (Mar. 2006).

18. White, S. R. & Feiguin, A. E. Real-Time Evolution Using the Density Matrix Renormalization Group. *Physical Review Letters* **93.** ISSN: 1079-7114. http://dx.doi.org/10.1103/PhysRevLett.93.076401 (Aug. 2004).

19. Stoudenmire, E. & White, S. R. Studying Two-Dimensional Systems with the Density Matrix Renormalization Group. *Annual Review of Condensed Matter Physics* **3,** 111–128. ISSN: 1947-5462. http://dx.doi.org/10.1146/annurev-conmatphys-020911-125018 (Mar. 2012).

20. Gerster, M. *et al.* Unconstrained tree tensor network: An adaptive gauge picture for enhanced performance. *Phys. Rev. B* **90,** 125154. https://link.aps.org/doi/10.1103/PhysRevB.90.125154 (12 Sept. 2014).

21. Vidal, G., Latorre, J. I., Rico, E. & Kitaev, A. Entanglement in Quantum Critical Phenomena. *Physical Review Letters* **90.** ISSN: 1079-7114. http://dx.doi.org/10.1103/PhysRevLett.90.227902 (June 2003).

22. Haegeman, J. *et al.* Time-Dependent Variational Principle for Quantum Lattices. *Physical Review Letters* **107.** ISSN: 1079-7114. http://dx.doi.org/10.1103/PhysRevLett.107.070601 (Aug. 2011).

23. Haegeman, J., Lubich, C., Oseledets, I., Vandereycken, B. & Verstraete, F. Unifying time evolution and optimization with matrix product states. *Physical Review B* **94.** ISSN: 2469-9969. http://dx.doi.org/10.1103/PhysRevB.94.165116 (Oct. 2016).

24. Fishman, M., White, S. R. & Stoudenmire, E. M. The ITensor Software Library for Tensor Network Calculations. *SciPost Phys. Codebases,* 4. https://scipost.org/10.21468/SciPostPhysCodeb.4 (2022).

25. Verresen, R., Lukin, M. D. & Vishwanath, A. Prediction of Toric Code Topological Order from Rydberg Blockade. *Phys. Rev. X* **11,** 031005. https://link.aps.org/doi/10.1103/PhysRevX.11.031005 (3 July 2021).

26. Tarabunga, P. S., Surace, F. M., Andreoni, R., Angelone, A. & Dalmonte, M. Gauge-Theoretic Origin of Rydberg Quantum Spin Liquids. *Phys. Rev. Lett.* **129,** 195301. https://link.aps.org/doi/10.1103/PhysRevLett.129.195301 (19 Nov. 2022).

27. Tarabunga, P. S., Giudici, G., Chanda, T. & Dalmonte, M. Classification and emergence of quantum spin liquids in chiral Rydberg models. *Physical Review B* **108.** ISSN: 2469-9969. http://dx.doi.org/10.1103/PhysRevB.108.075118 (Aug. 2023).
28. Weber, S. *et al.* Experimentally Accessible Scheme for a Fractional Chern Insulator in Rydberg Atoms. *PRX Quantum* **3,** 030302. https://link.aps.org/doi/10.1103/PRXQuantum.3.030302 (3 July 2022).
29. Semeghini, G. *et al.* Probing topological spin liquids on a programmable quantum simulator. *Science* **374,** 1242–1247. https://www.science.org/doi/abs/10.1126/science.abi8794 (2021).
30. Feynman, R. P. Simulating physics with computers. *International Journal of Theoretical Physics* **21,** 467–488. ISSN: 1572-9575. http://dx.doi.org/10.1007/BF02650179 (June 1982).
31. Browaeys, A. & Lahaye, T. Many-body physics with individually controlled Rydberg atoms. *Nature Physics* **16,** 132–142. ISSN: 1745-2481. http://dx.doi.org/10.1038/s41567-019-0733-z (Jan. 2020).
32. Robicheaux, F. & Hernández, J. V. Many-body wave function in a dipole blockade configuration. *Physical Review A* **72.** ISSN: 1094-1622. http://dx.doi.org/10.1103/PhysRevA.72.063403 (Dec. 2005).
33. Lukin, M. D. *et al.* Dipole Blockade and Quantum Information Processing in Mesoscopic Atomic Ensembles. *Physical Review Letters* **87.** ISSN: 1079-7114. http://dx.doi.org/10.1103/PhysRevLett.87.037901 (June 2001).
34. Fendley, P., Sengupta, K. & Sachdev, S. Competing density-wave orders in a one-dimensional hard-boson model. *Physical Review B* **69.** ISSN: 1550-235X. http://dx.doi.org/10.1103/PhysRevB.69.075106 (Feb. 2004).
35. Turner, C. J., Michailidis, A. A., Abanin, D. A., Serbyn, M. & Papić, Z. Quantum scarred eigenstates in a Rydberg atom chain: Entanglement, breakdown of thermalization, and stability to perturbations. *Physical Review B* **98.** ISSN: 2469-9969. http://dx.doi.org/10.1103/PhysRevB.98.155134 (Oct. 2018).
36. Lin, C.-J. & Motrunich, O. I. Exact Quantum Many-Body Scar States in the Rydberg-Blockaded Atom Chain. *Physical Review Letters* **122.** ISSN: 1079-7114. http://dx.doi.org/10.1103/PhysRevLett.122.173401 (Apr. 2019).
37. Bernien, H. *et al.* Probing many-body dynamics on a 51-atom quantum simulator. *Nature* **551,** 579–584. ISSN: 1476-4687. http://dx.doi.org/10.1038/nature24622 (Nov. 2017).
38. Barredo, D., Lienhard, V., de Léséleuc, S., Lahaye, T. & Browaeys, A. Synthetic three-dimensional atomic structures assembled atom by atom. *Nature* **561,** 79–82. ISSN: 1476-4687. http://dx.doi.org/10.1038/s41586-018-0450-2 (Sept. 2018).
39. Zeiher, J. *et al.* Coherent Many-Body Spin Dynamics in a Long-Range Interacting Ising Chain. *Physical Review X* **7.** https://doi.org/10.1103%2Fphysrevx.7.041063 (Dec. 2017).
40. De Léséleuc, S. *et al.* Observation of a symmetry-protected topological phase of interacting bosons with Rydberg atoms. *Science* **365,** 775–780. ISSN: 1095-9203. http://dx.doi.org/10.1126/science.aav9105 (Aug. 2019).

41. Ebadi, S. *et al.* Quantum phases of matter on a 256-atom programmable quantum simulator. *Nature* **595,** 227–232. ISSN: 1476-4687. http://dx.doi.org/10.1038/s41586-021-03582-4 (July 2021).
42. Scholl, P. *et al.* Quantum simulation of 2D antiferromagnets with hundreds of Rydberg atoms. *Nature* **595,** 233–238. ISSN: 1476-4687. http://dx.doi.org/10.1038/s41586-021-03585-1 (July 2021).
43. Chen, C. *et al.* Continuous symmetry breaking in a two-dimensional Rydberg array. *Nature* **616,** 691–695. ISSN: 1476-4687. http://dx.doi.org/10.1038/s41586-023-05859-2 (Feb. 2023).
44. Kitaev, A. Fault-tolerant quantum computation by anyons. *Annals of Physics* **303,** 2–30. ISSN: 0003-4916. http://dx.doi.org/10.1016/S0003-4916(02)00018-0 (Jan. 2003).
45. Savary, L. & Balents, L. Quantum spin liquids: a review. *Reports on Progress in Physics* **80,** 016502. ISSN: 1361-6633. http://dx.doi.org/10.1088/0034-4885/80/1/016502 (Nov. 2016).
46. Einarsson, T. Fractional statistics on a torus. *Physical Review Letters* **64,** 1995–1998. ISSN: 0031-9007. http://dx.doi.org/10.1103/PhysRevLett.64.1995 (Apr. 1990).
47. Wegner, F. J. Duality in generalized Ising models. *arXiv preprint arXiv:1411.5815.* https://arxiv.org/abs/1411.5815 (2014).
48. Wu, F., Deng, Y. & Prokof'ev, N. Phase diagram of the toric code model in a parallel magnetic field. *Physical Review B* **85.** ISSN: 1550-235X. http://dx.doi.org/10.1103/PhysRevB.85.195104 (May 2012).
49. Tupitsyn, I. S., Kitaev, A., Prokof'ev, N. V. & Stamp, P. C. E. Topological multicritical point in the phase diagram of the toric code model and three-dimensional lattice gauge Higgs model. *Physical Review B* **82.** ISSN: 1550-235X. http://dx.doi.org/10.1103/PhysRevB.82.085114 (Aug. 2010).
50. Baskaran, G. & Anderson, P. W. Gauge theory of high-temperature superconductors and strongly correlated Fermi systems. *Phys. Rev. B* **37,** 580–583. https://link.aps.org/doi/10.1103/PhysRevB.37.580 (1 Jan. 1988).
51. Baskaran, G., Zou, Z. & Anderson, P. The resonating valence bond state and high-Tc superconductivity — A mean field theory. *Solid State Communications* **63,** 973–976. https://doi.org/10.1016/0038-1098(87)90642-9 (Sept. 1987).
52. Becca, F. & Sorella, S. *Quantum Monte Carlo Approaches for Correlated Systems* ISBN: 9781316417041. http://dx.doi.org/10.1017/9781316417041 (Cambridge University Press, Nov. 2017).
53. Wen, X.-G. Colloquium: Zoo of quantum-topological phases of matter. *Rev. Mod. Phys.* **89,** 041004. https://link.aps.org/doi/10.1103/RevModPhys.89.041004 (4 Dec. 2017).
54. Moessner, R. & Sondhi, S. L. Ising models of quantum frustration. *Physical Review B* **63.** ISSN: 1095-3795. http://dx.doi.org/10.1103/PhysRevB.63.224401 (May 2001).
55. Lacroix, C., Mendels, P. & Mila, F. *Introduction to frustrated magnetism: materials, experiments, theory* (Springer Science & Business Media, 2011).
56. Fradkin, E. *Field theories of condensed matter physics* (Cambridge University Press, 2013).

57. Moessner, R. & Moore, J. E. *Topological Phases of Matter* (Cambridge University Press, 2021).
58. Wilson, K. G. Confinement of quarks. *Phys. Rev. D* **10,** 2445. https://journals.aps.org/prd/abstract/10.1103/PhysRevD.10.2445 (1974).
59. Creutz, M. *Quarks, gluons and lattices* (Cambridge University Press, 1983).
60. Kaufman, A. M. & Ni, K.-K. Quantum science with optical tweezer arrays of ultracold atoms and molecules. *Nature Physics* **17,** 1324–1333. ISSN: 1745-2481. http://dx.doi.org/10.1038/s41567-021-01357-2 (Nov. 2021).
61. Samajdar, R., Ho, W. W., Pichler, H., Lukin, M. D. & Sachdev, S. Quantum phases of Rydberg atoms on a kagome lattice. *Proceedings of the National Academy of Sciences* **118.** https://doi.org/10.1073%2Fpnas.2015785118 (Jan. 2021).
62. Lesanovsky, I. & Katsura, H. Interacting Fibonacci anyons in a Rydberg gas. *Physical Review A* **86.** ISSN: 1094-1622. http://dx.doi.org/10.1103/PhysRevA.86.041601 (Oct. 2012).
63. Glaetzle, A. W. *et al.* Quantum Spin-Ice and Dimer Models with Rydberg Atoms. *Phys. Rev. X* **4,** 041037. https://link.aps.org/doi/10.1103/PhysRevX.4.041037 (4 Nov. 2014).
64. Celi, A. *et al.* Emerging Two-Dimensional Gauge Theories in Rydberg Configurable Arrays. *Phys. Rev. X* **10,** 021057. https://link.aps.org/doi/10.1103/PhysRevX.10.021057 (2 June 2020).
65. Glaetzle, A. W. *et al.* Designing Frustrated Quantum Magnets with Laser-Dressed Rydberg Atoms. *Phys. Rev. Lett.* **114,** 173002. https://link.aps.org/doi/10.1103/PhysRevLett.114.173002 (17 Apr. 2015).
66. Surace, F. M. *et al.* Lattice Gauge Theories and String Dynamics in Rydberg Atom Quantum Simulators. *Physical Review X* **10.** ISSN: 2160-3308. http://dx.doi.org/10.1103/PhysRevX.10.021041 (May 2020).
67. Giudice, G., Surace, F. M., Pichler, H. & Giudici, G. Trimer states with $\mathbb{Z}_3$ topological order in Rydberg atom arrays. *Phys. Rev. B* **106,** 195155. https://link.aps.org/doi/10.1103/PhysRevB.106.195155 (19 Nov. 2022).
68. Giudici, G., Lukin, M. D. & Pichler, H. Dynamical Preparation of Quantum Spin Liquids in Rydberg Atom Arrays. *Phys. Rev. Lett.* **129,** 090401. https://link.aps.org/doi/10.1103/PhysRevLett.129.090401 (9 Aug. 2022).
69. Misguich, G., Serban, D. & Pasquier, V. Quantum Dimer Model on the Kagome Lattice: Solvable Dimer-Liquid and Ising Gauge Theory. *Physical Review Letters* **89.** https://doi.org/10.1103%2Fphysrevlett.89.137202 (Sept. 2002).
70. Hao, Z., Inglis, S. & Melko, R. Destroying a topological quantum bit by condensing Ising vortices. *Nature Communications* **5.** https://doi.org/10.1038%2Fncomms6781 (Dec. 2014).
71. Fradkin, E. & Shenker, S. H. Phase diagrams of lattice gauge theories with Higgs fields. *Physical Review D* **19,** 3682–3697. ISSN: 0556-2821. http://dx.doi.org/10.1103/PhysRevD.19.3682 (June 1979).
72. Kogut, J. B. An introduction to lattice gauge theory and spin systems. *Rev. Mod. Phys.* **51,** 659–713. https://link.aps.org/doi/10.1103/RevModPhys.51.659 (4 Oct. 1979).
73. Slagle, K. *et al.* Quantum spin liquids bootstrapped from Ising criticality in Rydberg arrays. *Physical Review B* **106.** ISSN: 2469-9969. http://dx.doi.org/10.1103/PhysRevB.106.115122 (Sept. 2022).

74. Ohler, S., Kiefer-Emmanouilidis, M. & Fleischhauer, M. Quantum spin liquids of Rydberg excitations in a honeycomb lattice induced by density-dependent Peierls phases. *Phys. Rev. Res.* **5,** 013157. https://link.aps.org/doi/10.1103/PhysRevResearch.5.013157 (1 Feb. 2023).

75. Beekman, A. J. *et al.* Dual gauge field theory of quantum liquid crystals in two dimensions. *Physics Reports* **683,** 1–110. https://doi.org/10.1016%2Fj.physrep.2017.03.004 (Apr. 2017).

76. Fredenhagen, K. & Marcu, M. Confinement criterion for QCD with dynamical quarks. *Physical Review Letters* **56,** 223–224. ISSN: 0031-9007. http://dx.doi.org/10.1103/PhysRevLett.56.223 (Jan. 1986).

77. Tschirsich, F., Montangero, S. & Dalmonte, M. Phase diagram and conformal string excitations of square ice using gauge invariant matrix product states. *SciPost Physics* **6.** ISSN: 2542-4653. http://dx.doi.org/10.21468/SciPostPhys.6.3.028 (Mar. 2019).

78. Schuch, N., Poilblanc, D., Cirac, J. I. & Pérez-García, D. Resonating valence bond states in the PEPS formalism. *Physical Review B* **86.** ISSN: 1550-235X. http://dx.doi.org/10.1103/PhysRevB.86.115108 (Sept. 2012).

79. Blöte, H. W. J. & Deng, Y. Cluster Monte Carlo simulation of the transverse Ising model. *Phys. Rev. E* **66,** 066110. https://link.aps.org/doi/10.1103/PhysRevE.66.066110 (6 Dec. 2002).

80. Powalski, M., Coester, K., Moessner, R. & Schmidt, K. P. Disorder by disorder and flat bands in the kagome transverse field Ising model. *Phys. Rev. B* **87,** 054404. https://link.aps.org/doi/10.1103/PhysRevB.87.054404 (5 Feb. 2013).

81. Gu, S.-J. & Lin, H.-Q. Scaling dimension of fidelity susceptibility in quantum phase transitions. *EPL (Europhysics Letters)* **87,** 10003. ISSN: 1286-4854. http://dx.doi.org/10.1209/0295-5075/87/10003 (July 2009).

82. Sandvik, A. W. & Kurkijärvi, J. Quantum Monte Carlo simulation method for spin systems. *Phys. Rev. B* **43,** 5950–5961. https://link.aps.org/doi/10.1103/PhysRevB.43.5950 (1991).

83. Sandvik, A. W. Stochastic series expansion method for quantum Ising models with arbitrary interactions. *Phys. Rev. E* **68,** 056701. https://link.aps.org/doi/10.1103/PhysRevE.68.056701 (2020) (Nov. 2003).

84. Henkel, N., Nath, R. & Pohl, T. Three-Dimensional Roton Excitations and Supersolid Formation in Rydberg-Excited Bose-Einstein Condensates. *Phys. Rev. Lett.* **104,** 195302. https://link.aps.org/doi/10.1103/PhysRevLett.104.195302 (19 May 2010).

85. Pupillo, G., Micheli, A., Boninsegni, M., Lesanovsky, I. & Zoller, P. Strongly Correlated Gases of Rydberg-Dressed Atoms: Quantum and Classical Dynamics. *Phys. Rev. Lett.* **104,** 223002. https://link.aps.org/doi/10.1103/PhysRevLett.104.223002 (22 June 2010).

86. Macrì, T. & Pohl, T. Rydberg dressing of atoms in optical lattices. *Physical Review A* **89.** ISSN: 1094-1622. http://dx.doi.org/10.1103/PhysRevA.89.011402 (Jan. 2014).

87. Löw, R. *et al.* An experimental and theoretical guide to strongly interacting Rydberg gases. *Journal of Physics B: Atomic, Molecular and Optical Physics* **45,** 113001. https://doi.org/10.1088/0953-4075/45/11/113001 (May 2012).

88. Jau, Y.-Y., Hankin, A. M., Keating, T., Deutsch, I. H. & Biedermann, G. W. Entangling atomic spins with a Rydberg-dressed spin-flip blockade. *Nature Physics* **12,** 71–74. ISSN: 1745-2481. https://www.nature.com/articles/nphys3487 (2021) (Jan. 2016).

89. Zeiher, J. *et al.* Many-body interferometry of a Rydberg-dressed spin lattice. *Nature Physics* **12,** 1095–1099. https://doi.org/10.1038/nphys3835 (Aug. 2016).

90. Guardado-Sanchez, E. *et al.* Quench Dynamics of a Fermi Gas with Strong Nonlocal Interactions. *Physical Review X* **11,** 021036. https://link.aps.org/doi/10.1103/PhysRevX.11.021036 (2021) (May 2021).

91. Mattioli, M., Dalmonte, M., Lechner, W. & Pupillo, G. Cluster Luttinger Liquids of Rydberg-Dressed Atoms in Optical Lattices. *Phys. Rev. Lett.* **111,** 165302. https://link.aps.org/doi/10.1103/PhysRevLett.111.165302 (2013).

92. Cinti, F., Macrì, T., Lechner, W., Pupillo, G. & Pohl, T. Defect-induced supersolidity with soft-core bosons. *Nat Commun* **5,** 1–6. ISSN: 2041-1723. https://www.nature.com/articles/ncomms4235 (2020) (Feb. 2014).

93. Dalmonte, M. *et al.* Cluster Luttinger liquids and emergent supersymmetric conformal critical points in the one-dimensional soft-shoulder Hubbard model. *Phys. Rev. B* **92,** 045106. https://link.aps.org/doi/10.1103/PhysRevB.92.045106 (2015).

94. Angelone, A., Mezzacapo, F. & Pupillo, G. Superglass Phase of Interaction-Blockaded Gases on a Triangular Lattice. *Phys. Rev. Lett.* **116,** 135303. https://link.aps.org/doi/10.1103/PhysRevLett.116.135303 (2016).

95. Masella, G., Angelone, A., Mezzacapo, F., Pupillo, G. & Prokof'ev, N. V. Supersolid Stripe Crystal from Finite-Range Interactions on a Lattice. *Phys. Rev. Lett.* **123,** 045301. https://link.aps.org/doi/10.1103/PhysRevLett.123.045301 (2019) (July 2019).

96. Angelone, A. *et al.* Nonequilibrium scenarios in cluster-forming quantum lattice models. *Phys. Rev. A* **101,** 063603. https://link.aps.org/doi/10.1103/PhysRevA.101.063603 (2020) (June 2020).

97. Johnson, J. E. & Rolston, S. L. Interactions between Rydberg-dressed atoms. *Phys. Rev. A* **82,** 033412. https://link.aps.org/doi/10.1103/PhysRevA.82.033412 (3 Sept. 2010).

98. Borish, V., Markovi ć, O., Hines, J. A., Rajagopal, S. V. & Schleier-Smith, M. Transverse-Field Ising Dynamics in a Rydberg-Dressed Atomic Gas. *Phys. Rev. Lett.* **124,** 063601. https://link.aps.org/doi/10.1103/PhysRevLett.124.063601 (6 Feb. 2020).

99. Cappellini, G. *et al.* Coherent Manipulation of Orbital Feshbach Molecules of Two-Electron Atoms. *Physical Review X* **9.** ISSN: 2160-3308. http://dx.doi.org/10.1103/PhysRevX.9.011028 (Feb. 2019).

100. Norcia, M. A. *et al.* Seconds-scale coherence on an optical clock transition in a tweezer array. *Science* **366,** 93–97. eprint: https://www.science.org/doi/pdf/10.1126/science.aay0644. https://www.science.org/doi/abs/10.1126/science.aay0644 (2019).

101. Madjarov, I. S. *et al.* High-fidelity entanglement and detection of alkaline-earth Rydberg atoms. *Nature Physics* **16,** 857–861. ISSN: 1745-2481. http://dx.doi.org/10.1038/s41567-020-0903-z (May 2020).

102. Wilson, J. T. *et al.* Trapping Alkaline Earth Rydberg Atoms Optical Tweezer Arrays. *Physical Review Letters* **128.** ISSN: 1079-7114. http://dx.doi.org/10.1103/PhysRevLett.128.033201 (Jan. 2022).

103. Schine, N., Young, A. W., Eckner, W. J., Martin, M. J. & Kaufman, A. M. Long-lived Bell states in an array of optical clock qubits. *Nature Physics* **18,** 1067–1073. ISSN: 1745-2481. http://dx.doi.org/10.1038/s41567-022-01678-w (Aug. 2022).

104. Gil, L. I. R., Mukherjee, R., Bridge, E. M., Jones, M. P. A. & Pohl, T. Spin Squeezing in a Rydberg Lattice Clock. *Physical Review Letters* **112.** ISSN: 1079-7114. http://dx.doi.org/10.1103/PhysRevLett.112.103601 (Mar. 2014).

105. Okuno, D. *et al.* High-resolution Spectroscopy and Single-photon Rydberg Excitation of Reconfigurable Ytterbium Atom Tweezer Arrays Utilizing a Metastable State. *Journal of the Physical Society of Japan* **91.** ISSN: 1347-4073. http://dx.doi.org/10.7566/JPSJ.91.084301 (Aug. 2022).

106. Trebst, S., Schollwöck, U., Troyer, M. & Zoller, P. d-Wave Resonating Valence Bond States of Fermionic Atoms in Optical Lattices. *Physical Review Letters* **96.** ISSN: 1079-7114. http://dx.doi.org/10.1103/PhysRevLett.96.250402 (June 2006).

107. Scholl, P. *et al.* Microwave Engineering of Programmable X X Z Hamiltonians in Arrays of Rydberg Atoms. *PRX Quantum* **3.** ISSN: 2691-3399. http://dx.doi.org/10.1103/PRXQuantum.3.020303 (Apr. 2022).

108. Geier, S. *et al.* Floquet Hamiltonian engineering of an isolated many-body spin system. *Science* **374,** 1149–1152. ISSN: 1095-9203. http://dx.doi.org/10.1126/science.abd9547 (Nov. 2021).

109. Gross, C. & Bloch, I. Quantum simulations with ultracold atoms in optical lattices. *Science* **357,** 995–1001. https://doi.org/10.1126/science.aal3837 (Sept. 2017).

110. Schauss, P. Quantum simulation of transverse Ising models with Rydberg atoms. *Quantum Science and Technology* **3,** 023001. https://doi.org/10.1088/2058-9565/aa9c59 (Jan. 2018).

111. Tarabunga, P. S., Surace, F. M., Andreoni, R., Angelone, A. & Dalmonte, M. Gauge-Theoretic Origin of Rydberg Quantum Spin Liquids. *Phys. Rev. Lett.* **129,** 195301. https://link.aps.org/doi/10.1103/PhysRevLett.129.195301 (19 Nov. 2022).

112. Samajdar, R., Joshi, D. G., Teng, Y. & Sachdev, S. Emergent $\mathbb{Z}_2$ Gauge Theories and Topological Excitations in Rydberg Atom Arrays. *Phys. Rev. Lett.* **130,** 043601. https://link.aps.org/doi/10.1103/PhysRevLett.130.043601 (4 Jan. 2023).

113. Cheng, Y., Li, C. & Zhai, H. Variational approach to quantum spin liquid in a Rydberg atom simulator. *New Journal of Physics* **25,** 033010. https://doi.org/10.1088/1367-2630/acc125 (Mar. 2023).

114. Peter, D. *et al.* Topological bands with a Chern number $C = 2$ by dipolar exchange interactions. *Phys. Rev. A* **91,** 053617. https://link.aps.org/doi/10.1103/PhysRevA.91.053617 (5 May 2015).

115. Weber, S. *et al.* Topologically protected edge states in small Rydberg systems. *Quantum Science and Technology* **3,** 044001. https://doi.org/10.1088/2058-9565/aaca47 (July 2018).

116. Lienhard, V. *et al.* Realization of a Density-Dependent Peierls Phase in a Synthetic, Spin-Orbit Coupled Rydberg System. *Phys. Rev. X* **10,** 021031. https://link.aps.org/doi/10.1103/PhysRevX.10.021031 (2 May 2020).

117. Wen, X.-G. Quantum orders and symmetric spin liquids. *Phys. Rev. B* **65,** 165113. https://link.aps.org/doi/10.1103/PhysRevB.65.165113 (16 Apr. 2002).

118. Wen, X.-G. Quantum order: a quantum entanglement of many particles. *Physics Letters A* **300,** 175–181. https://doi.org/10.1016/s0375-9601(02)00808-3 (July 2002).

119. Bieri, S., Lhuillier, C. & Messio, L. Projective symmetry group classification of chiral spin liquids. *Phys. Rev. B* **93,** 094437. https://link.aps.org/doi/10.1103/PhysRevB.93.094437 (9 Mar. 2016).

120. Zhu, W., Gong, S. S. & Sheng, D. N. Interaction-driven fractional quantum Hall state of hard-core bosons on kagome lattice at one-third filling. *Phys. Rev. B* **94,** 035129. https://link.aps.org/doi/10.1103/PhysRevB.94.035129 (3 July 2016).

121. Kitaev, A. & Preskill, J. Topological Entanglement Entropy. *Phys. Rev. Lett.* **96,** 110404. https://link.aps.org/doi/10.1103/PhysRevLett.96.110404 (11 Mar. 2006).

122. Levin, M. & Wen, X.-G. Detecting Topological Order in a Ground State Wave Function. *Phys. Rev. Lett.* **96,** 110405. https://link.aps.org/doi/10.1103/PhysRevLett.96.110405 (11 Mar. 2006).

123. White, S. R. Density matrix formulation for quantum renormalization groups. *Phys. Rev. Lett.* **69,** 2863–2866. https://link.aps.org/doi/10.1103/PhysRevLett.69.2863 (19 Nov. 1992).

124. White, S. R. Density-matrix algorithms for quantum renormalization groups. *Phys. Rev. B* **48,** 10345–10356. https://link.aps.org/doi/10.1103/PhysRevB.48.10345 (14 Oct. 1993).

125. Dodds, T., Bhattacharjee, S. & Kim, Y. B. Quantum spin liquids in the absence of spin-rotation symmetry: Application to herbertsmithite. *Phys. Rev. B* **88,** 224413. https://link.aps.org/doi/10.1103/PhysRevB.88.224413 (22 Dec. 2013).

126. Reuther, J., Lee, S.-P. & Alicea, J. Classification of spin liquids on the square lattice with strong spin-orbit coupling. *Phys. Rev. B* **90,** 174417. https://link.aps.org/doi/10.1103/PhysRevB.90.174417 (17 Nov. 2014).

127. Wen, X. G., Wilczek, F. & Zee, A. Chiral spin states and superconductivity. *Phys. Rev. B* **39,** 11413–11423. https://link.aps.org/doi/10.1103/PhysRevB.39.11413 (16 June 1989).

128. Lu, Y.-M. & Ran, Y. $\mathbb{Z}_2$ spin liquid and chiral antiferromagnetic phase in the Hubbard model on a honeycomb lattice. *Phys. Rev. B* **84,** 024420. https://link.aps.org/doi/10.1103/PhysRevB.84.024420 (2 July 2011).

129. Hermele, M. SU(2) gauge theory of the Hubbard model and application to the honeycomb lattice. *Phys. Rev. B* **76,** 035125. https://link.aps.org/doi/10.1103/PhysRevB.76.035125 (3 July 2007).

130. Zhang, Y., Grover, T. & Vishwanath, A. Topological entanglement entropy of $\mathbb{Z}_2$ spin liquids and lattice Laughlin states. *Phys. Rev. B* **84,** 075128. https://link.aps.org/doi/10.1103/PhysRevB.84.075128 (7 Aug. 2011).

131. Zhang, Y. & Vishwanath, A. Establishing non-Abelian topological order in Gutzwiller-projected Chern insulators via entanglement entropy and modular $\mathcal{S}$-matrix. *Phys. Rev. B* **87,** 161113. https://link.aps.org/doi/10.1103/PhysRevB.87.161113 (16 Apr. 2013).

132. Laughlin, R. B. Anomalous Quantum Hall Effect: An Incompressible Quantum Fluid with Fractionally Charged Excitations. *Phys. Rev. Lett.* **50,** 1395–1398. https://link.aps.org/doi/10.1103/PhysRevLett.50.1395 (18 May 1983).

133. Mei, J.-W. & Wen, X.-G. Modular matrices from universal wave-function overlaps in Gutzwiller-projected parton wave functions. *Phys. Rev. B* **91,** 125123. https://link.aps.org/doi/10.1103/PhysRevB.91.125123 (12 Mar. 2015).

134. Thouless, D. *Topological quantum numbers in nonrelativistic physics* (World Scientific, 1998).

135. Wietek, A., Sterdyniak, A. & Läuchli, A. M. Nature of chiral spin liquids on the kagome lattice. *Phys. Rev. B* **92,** 125122. https://link.aps.org/doi/10.1103/PhysRevB.92.125122 (12 Sept. 2015).

136. Wietek, A. & Läuchli, A. M. Chiral spin liquid and quantum criticality in extended $S = \frac{1}{2}$ Heisenberg models on the triangular lattice. *Phys. Rev. B* **95,** 035141. https://link.aps.org/doi/10.1103/PhysRevB.95.035141 (3 Jan. 2017).

137. Wang, Y.-F., Gu, Z.-C., Gong, C.-D. & Sheng, D. N. Fractional Quantum Hall Effect of Hard-Core Bosons in Topological Flat Bands. *Phys. Rev. Lett.* **107,** 146803. https://link.aps.org/doi/10.1103/PhysRevLett.107.146803 (14 Sept. 2011).

138. He, Y.-C., Zaletel, M. P., Oshikawa, M. & Pollmann, F. Signatures of Dirac Cones in a DMRG Study of the Kagome Heisenberg Model. *Phys. Rev. X* **7,** 031020. https://link.aps.org/doi/10.1103/PhysRevX.7.031020 (3 July 2017).

139. Hu, S., Zhu, W., Eggert, S. & He, Y.-C. Dirac Spin Liquid on the Spin-1/2 Triangular Heisenberg Antiferromagnet. *Phys. Rev. Lett.* **123,** 207203. https://link.aps.org/doi/10.1103/PhysRevLett.123.207203 (20 Nov. 2019).

140. Ferrari, F., Parola, A. & Becca, F. Gapless spin liquids in disguise. *Phys. Rev. B* **103,** 195140. https://link.aps.org/doi/10.1103/PhysRevB.103.195140 (19 May 2021).

141. He, Y.-C., Bhattacharjee, S., Moessner, R. & Pollmann, F. Bosonic Integer Quantum Hall Effect in an Interacting Lattice Model. *Phys. Rev. Lett.* **115,** 116803. https://link.aps.org/doi/10.1103/PhysRevLett.115.116803 (11 Sept. 2015).

142. Wen, X.-G. Topological Order: From Long-Range Entangled Quantum Matter to a Unified Origin of Light and Electrons. *ISRN Condensed Matter Physics* **2013,** 1–20. https://doi.org/10.1155/2013/198710 (Mar. 2013).

143. Guardado-Sanchez, E. *et al.* Subdiffusion and Heat Transport in a Tilted Two-Dimensional Fermi-Hubbard System. *Phys. Rev. X* **10,** 011042. https://link.aps.org/doi/10.1103/PhysRevX.10.011042 (1 Feb. 2020).

144. Scherg, S. *et al.* Observing non-ergodicity due to kinetic constrainernts in tilted Fermi-Hubbard chains. *Nature Communications* **12.** ISSN: 2041-1723. http://dx.doi.org/10.1038/s41467-021-24726-0 (July 2021).

145. Kohlert, T. *et al.* Exploring the Regime of Fragmentation in Strongly Tilted Fermi-Hubbard Chains. *Phys. Rev. Lett.* **130,** 010201. https://link.aps.org/doi/10.1103/PhysRevLett.130.010201 (1 Jan. 2023).

146. Nandkishore, R. M. & Hermele, M. Fractons. *Annual Review of Condensed Matter Physics* **10,** 295–313. ISSN: 1947-5462. http://dx.doi.org/10.1146/annurev-conmatphys-031218-013604 (Mar. 2019).

147. Morningstar, A., Khemani, V. & Huse, D. A. Kinetically constrained freezing transition in a dipole-conserving system. *Phys. Rev. B* **101,** 214205. https://link.aps.org/doi/10.1103/PhysRevB.101.214205 (21 June 2020).

148. Feldmeier, J., Witczak-Krempa, W. & Knap, M. Emergent tracer dynamics in constrained quantum systems. *Phys. Rev. B* **106,** 094303. https://link.aps.org/doi/10.1103/PhysRevB.106.094303 (9 Sept. 2022).

149. Burchards, A. G., Feldmeier, J., Schuckert, A. & Knap, M. Coupled hydrodynamics in dipole-conserving quantum systems. *Phys. Rev. B* **105,** 205127. https://link.aps.org/doi/10.1103/PhysRevB.105.205127 (20 May 2022).

150. Delfino, G., Fontana, W. B., Gomes, P. R. S. & Chamon, C. Effective fractonic behavior in a two-dimensional exactly solvable spin liquid. *SciPost Phys.* **14,** 002. https://scipost.org/10.21468/SciPostPhys.14.1.002 (2023).

151. Yang, F., Yarloo, H., Zhang, H.-C., Mølmer, K. & Nielsen, A. E. B. *Probing Hilbert Space Fragmentation with Strongly Interacting Rydberg Atoms* 2024. arXiv: 2403.13790 [quant-ph]. https://arxiv.org/abs/2403.13790.

152. Zechmann, P., Altman, E., Knap, M. & Feldmeier, J. Fractonic Luttinger liquids and supersolids in a constrained Bose-Hubbard model. *Phys. Rev. B* **107,** 195131. https://link.aps.org/doi/10.1103/PhysRevB.107.195131 (19 May 2023).

153. Boesl, J., Zechmann, P., Feldmeier, J. & Knap, M. Deconfinement Dynamics of Fractons in Tilted Bose-Hubbard Chains. *Phys. Rev. Lett.* **132,** 143401. https://link.aps.org/doi/10.1103/PhysRevLett.132.143401 (14 Apr. 2024).

154. Morera, I., Bohrdt, A., Ho, W. W. & Demler, E. Attraction from kinetic frustration in ladder systems. *Phys. Rev. Res.* **6,** 023196. https://link.aps.org/doi/10.1103/PhysRevResearch.6.023196 (2 May 2024).

155. Khemani, V., Hermele, M. & Nandkishore, R. Localization from Hilbert space shattering: From theory to physical realizations. *Phys. Rev. B* **101,** 174204. https://link.aps.org/doi/10.1103/PhysRevB.101.174204 (17 May 2020).

156. Sala, P., Rakovszky, T., Verresen, R., Knap, M. & Pollmann, F. Ergodicity Breaking Arising from Hilbert Space Fragmentation in Dipole-Conserving Hamiltonians. *Phys. Rev. X* **10,** 011047. https://link.aps.org/doi/10.1103/PhysRevX.10.011047 (1 Feb. 2020).

157. Yang, Z.-C., Liu, F., Gorshkov, A. V. & Iadecola, T. Hilbert-Space Fragmentation from Strict Confinement. *Phys. Rev. Lett.* **124,** 207602. https://link.aps.org/doi/10.1103/PhysRevLett.124.207602 (20 May 2020).

158. Khudorozhkov, A., Tiwari, A., Chamon, C. & Neupert, T. Hilbert space fragmentation in a 2D quantum spin system with subsystem symmetries. *SciPost Phys.* **13,** 098. https://scipost.org/10.21468/SciPostPhys.13.4.098 (2022).

159. Feldmeier, J., Sala, P., De Tomasi, G., Pollmann, F. & Knap, M. Anomalous Diffusion in Dipole- and Higher-Moment-Conserving Systems. *Phys. Rev. Lett.* **125,** 245303. https://link.aps.org/doi/10.1103/PhysRevLett.125.245303 (24 Dec. 2020).

160. Zadnik, L. & Fagotti, M. The Folded Spin-1/2 XXZ Model: I. Diagonalisation, Jamming, and Ground State Properties. *SciPost Phys. Core* **4,** 010. https://scipost.org/10.21468/SciPostPhysCore.4.2.010 (2021).

161. Zadnik, L. & Garrahan, J. P. Slow heterogeneous relaxation due to constraints in dual XXZ models. *Phys. Rev. B* **108,** L100304. https://link.aps.org/doi/10.1103/PhysRevB.108.L100304 (10 Sept. 2023).

162. Borla, U., Verresen, R., Grusdt, F. & Moroz, S. Confined phases of one-dimensional spinless fermions coupled to Z_2 gauge theory. *Physical Review Letters* **124.** ISSN: 1079-7114. http://dx.doi.org/10.1103/PhysRevLett.124.120503 (Mar. 2020).

163. Gorantla, P., Lam, H. T., Seiberg, N. & Shao, S.-H. Global dipole symmetry, compact Lifshitz theory, tensor gauge theory, and fractons. *Phys. Rev. B* **106,** 045112. https://link.aps.org/doi/10.1103/PhysRevB.106.045112 (4 July 2022).

164. Das, A., Borla, U. & Moroz, S. Fractionalized holes in one-dimensional $\mathbb{Z}_2$ gauge theory coupled to fermion matter: Deconfined dynamics and emergent integrability. *Phys. Rev. B* **107,** 064302. https://link.aps.org/doi/10.1103/PhysRevB.107.064302 (6 Feb. 2023).

165. Chamon, C. Quantum Glassiness in Strongly Correlated Clean Systems: An Example of Topological Overprotection. *Phys. Rev. Lett.* **94,** 040402. https://link.aps.org/doi/10.1103/PhysRevLett.94.040402 (4 Jan. 2005).

166. Sous, J. & Pretko, M. Fractons from polarons. *Physical Review B* **102.** ISSN: 2469-9969. http://dx.doi.org/10.1103/PhysRevB.102.214437 (Dec. 2020).

167. Sous, J. & Pretko, M. Fractons from frustration in hole-doped antiferromagnets. *npj Quantum Materials* **5.** ISSN: 2397-4648. http://dx.doi.org/10.1038/s41535-020-00278-2 (Nov. 2020).

168. Bariev, R. Z. Integrable spin chain with two- and three-particle interactions. *Journal of Physics A: Mathematical and General* **24,** L549. https://dx.doi.org/10.1088/0305-4470/24/10/010 (May 1991).

169. Bariev, R. Z., Klumper, A., Schadschneider, A. & Zittartz, J. Excitation spectrum and critical exponents of a one-dimensional integrable model of fermions with correlated hopping. *Journal of Physics A: Mathematical and General* **26,** 4863. https://dx.doi.org/10.1088/0305-4470/26/19/019 (Oct. 1993).

170. Mishra, T., Greschner, S. & Santos, L. Polar molecules in frustrated triangular ladders. *Phys. Rev. A* **91,** 043614. https://link.aps.org/doi/10.1103/PhysRevA.91.043614 (4 Apr. 2015).

171. Bilitewski, T. & Cooper, N. R. Synthetic dimensions in the strong-coupling limit: Supersolids and pair superfluids. *Phys. Rev. A* **94,** 023630. https://link.aps.org/doi/10.1103/PhysRevA.94.023630 (2 Aug. 2016).

172. Chhajlany, R. W., Grzybowski, P. R., Stasi ńska, J., Lewenstein, M. & Dutta, O. Hidden String Order in a Hole Superconductor with Extended Correlated Hopping. *Phys. Rev. Lett.* **116,** 225303. https://link.aps.org/doi/10.1103/PhysRevLett.116.225303 (22 June 2016).

173. Sørensen, E. S., Gordon, J., Riddell, J., Wang, T. & Kee, H.-Y. Field-induced chiral soliton phase in the Kitaev spin chain. *Phys. Rev. Res.* **5,** L012027. https://link.aps.org/doi/10.1103/PhysRevResearch.5.L012027 (1 Feb. 2023).

174. Xavier, H. B. & Pereira, R. G. Fractons from a liquid of singlet pairs. *Phys. Rev. B* **103,** 085101. https://link.aps.org/doi/10.1103/PhysRevB.103.085101 (8 Feb. 2021).

175. Jaksch, D. & Zoller, P. The cold atom Hubbard toolbox. *Annals of Physics* **315.** Special Issue, 52–79. ISSN: 0003-4916. https://www.sciencedirect.com/science/article/pii/S0003491604001782 (2005).

176. Jaksch, D. & Zoller, P. Creation of effective magnetic fields in optical lattices: the Hofstadter butterfly for cold neutral atoms. *New Journal of Physics* **5,** 56. https://dx.doi.org/10.1088/1367-2630/5/1/356 (May 2003).

177. Aidelsburger, M. *et al.* Realization of the Hofstadter Hamiltonian with Ultracold Atoms in Optical Lattices. *Physical Review Letters* **111.** ISSN: 1079-7114. http://dx.doi.org/10.1103/PhysRevLett.111.185301 (Oct. 2013).

178. Miyake, H., Siviloglou, G. A., Kennedy, C. J., Burton, W. C. & Ketterle, W. Realizing the Harper Hamiltonian with Laser-Assisted Tunneling in Optical Lattices. *Physical Review Letters* **111.** ISSN: 1079-7114. http://dx.doi.org/10.1103/PhysRevLett.111.185302 (Oct. 2013).

179. Su, W. P., Schrieffer, J. R. & Heeger, A. J. Solitons in Polyacetylene. *Phys. Rev. Lett.* **42,** 1698–1701. https://link.aps.org/doi/10.1103/PhysRevLett.42.1698 (25 June 1979).

180. Gogolin, A. O., Nersesyan, A. A. & Tsvelik, A. M. *Bosonization and Strongly Correlated Systems* (Cambridge University Press, 2004).

181. Essler, F. H. L. & Konik, R. M. in (eds Shifman, M., Vainshtein, A. & Wheater, J.) 684–830 (World Scientific, 2005). eprint: arXiv:cond-mat/0412421. https://www.worldscientific.com/doi/abs/10.1142/9789812775344_0020.

182. Imambekov, A., Schmidt, T. L. & Glazman, L. I. One-dimensional quantum liquids: Beyond the Luttinger liquid paradigm. *Rev. Mod. Phys.* **84,** 1253–1306. https://link.aps.org/doi/10.1103/RevModPhys.84.1253 (3 Sept. 2012).

183. Essler, F. H. L., Pereira, R. G. & Schneider, I. Spin-charge-separated quasiparticles in one-dimensional quantum fluids. *Phys. Rev. B* **91,** 245150. https://link.aps.org/doi/10.1103/PhysRevB.91.245150 (24 June 2015).

184. Pereira, R. G. & Sela, E. Spin-charge coupling in quantum wires at zero magnetic field. *Phys. Rev. B* **82,** 115324. https://link.aps.org/doi/10.1103/PhysRevB.82.115324 (11 Sept. 2010).

185. Kibble, T. W. B. Topology of cosmic domains and strings. *Journal of Physics A: Mathematical and General* **9,** 1387–1398. ISSN: 1361-6447. http://dx.doi.org/10.1088/0305-4470/9/8/029 (Aug. 1976).

186. Zurek, W. H. Cosmological experiments in superfluid helium? *Nature* **317,** 505–508. ISSN: 1476-4687. http://dx.doi.org/10.1038/317505a0 (Oct. 1985).

187. Hauke, P., Marcos, D., Dalmonte, M. & Zoller, P. Quantum Simulation of a Lattice Schwinger Model in a Chain of Trapped Ions. *Phys. Rev. X* **3,** 041018. https://link.aps.org/doi/10.1103/PhysRevX.3.041018 (4 Nov. 2013).

188. Andrade, B. *et al.* Engineering an effective three-spin Hamiltonian in trapped-ion systems for applications in quantum simulation. *Quantum Science and Technology* **7,** 034001. ISSN: 2058-9565. http://dx.doi.org/10.1088/2058-9565/ac5f5b (Apr. 2022).

189. Blatt, R. & Roos, C. F. Quantum simulations with trapped ions. *Nature Physics* **8,** 277–284. ISSN: 1745-2481. http://dx.doi.org/10.1038/nphys2252 (Apr. 2012).

190. Monroe, C. *et al.* Programmable quantum simulations of spin systems with trapped ions. *Reviews of Modern Physics* **93.** ISSN: 1539-0756. http://dx.doi.org/10.1103/RevModPhys.93.025001 (Apr. 2021).

Part II

Nonstabilizerness in many-body systems

Chapter 6

Stabilizer formalism and resource theory of magic

Quantum computers hold promise for simulating quantum systems [1], a task that classical computers struggle with [2]. In order to definitively establish the advantage of quantum computers, we need to identify specific resources that are required for this goal. The classes of quantum circuits that do not possess these resources (or in limited amount) must then be easy to simulate classically. For example, it has been recognized that quantum circuits with limited entanglement are classically simulable; thus entanglement is necessary to achieve quantum advantage [3].

Nevertheless, entanglement alone is not sufficient to achieve this goal. Indeed, there is a class of quantum circuits that is known to be simulable in polynomial time, despite exhibiting high amount of entanglement. This is the class of Clifford circuits, acting on specific input states called stabilizer states [4]. Clifford circuits and stabilizer states play an important role in the field of quantum error correction as they enable a large and powerful class of error correcting codes [5, 6].

This brings us to another crucial resource: nonstabilizerness, or also known as magic. In this thesis, we will use the two terms interchangeably. Since stabilizer states can be efficiently simulated, states with properties beyond those captured by stabilizer states (nonstabilizer states) are also necessary for achieving quantum advantage. Unlike entanglement, which has been extensively studied, its quantification and characterization in many-body quantum systems have began only very recently. This suggests a potentially rich area of exploration for unlocking the true power of quantum computation, with potential impact on current and near-term quantum devices. The role of nonstabilizerness in achieving quantum advantage has also been demonstrated in recent experiments [7, 8].

In this chapter, we briefly review the stabilizer formalism and resource theory of nonstabilizerness. In Section 6.1, we provide a brief introduction to the formalism of stabilizer states and the Clifford group. In Section 6.2, we explain how nonstabilizer states can be utilized to achieve universal quantum computation. This leads to the notion of nonstabilizer states as resource, which we discuss in Section 6.3. In Section 6.4, we introduce several computable measures of nonstabilizerness, including stabilizer Rényi entropies, stabilizer nullity, and Bell magic. Finally, in Section 6.5 we discuss possible future research directions.

6.1 Pauli group, Clifford group, and stabilizer states

The single-qubit Pauli matrices are defined as

$$I = \begin{pmatrix} 1 & 0 \\ 0 & 1 \end{pmatrix}, \quad X = \begin{pmatrix} 0 & 1 \\ 1 & 0 \end{pmatrix}, \quad Y = \begin{pmatrix} 0 & -i \\ i & 0 \end{pmatrix}, \quad Z = \begin{pmatrix} 1 & 0 \\ 0 & -1 \end{pmatrix}. \tag{6.1}$$

It is convenient to label them using a pair of indices $(a, a') \in \mathbb{Z}_2 \times \mathbb{Z}_2$, such that

$$P_{a,a'} = i^{aa'} X^a Z^{a'}, \tag{6.2}$$

whereby $P_{(0,0)} = I$, $P_{(1,0)} = X$, $P_{(0,1)} = Z$, and $P_{(1,1)} = Y$.

Pauli strings of N qubits are defined as all tensor products of N Pauli matrices:

$$P_{\mathbf{w}} = P_{(u_1,v_1)} \otimes \cdots \otimes P_{(u_N,v_N)}, \tag{6.3}$$

where we define a binary vector $\mathbf{w} = (\mathbf{u}, \mathbf{v}) \in \mathbb{Z}_2^{2N}$, and $\mathbf{u}, \mathbf{v} \in \mathbb{Z}_2^N$. Finally, the Pauli group $\mathcal{P}_N$ on N qubits is defined as the group of all Pauli strings with overall phase $\pm i$ or ± 1. The size of $\mathcal{P}_N$ is thus 4^{N+1}.

The Clifford group $\mathcal{C}_N$ on N qubits is defined as the normalizer of the N-qubit Pauli group under conjugation. In other words, C is a Clifford operator if $CP_{\mathbf{w}}C^\dagger = e^{i\theta}P_{\mathbf{w}'}$, where $\mathbf{w}, \mathbf{w}' \in \mathbb{Z}_2^{2N}$, for some phase factor $e^{i\theta}$. It is known that the Clifford group can be generated by the Hadamard gate, the $\pi/4$-phase gate, and the controlled-NOT gate, defined in the following

$$H = \frac{1}{\sqrt{2}} \begin{pmatrix} 1 & 1 \\ 1 & -1 \end{pmatrix} \tag{6.4}$$

$$S = \begin{pmatrix} 1 & 0 \\ 0 & i \end{pmatrix} \tag{6.5}$$

$$CNOT = \begin{pmatrix} 1 & 0 & 0 & 0 \\ 0 & 1 & 0 & 0 \\ 0 & 0 & 0 & 1 \\ 0 & 0 & 1 & 0 \end{pmatrix} \tag{6.6}$$

, respectively. The size of Clifford group is $|\mathcal{C}_N| = 2^{N^2+2N} \prod_{i=1}^{N} (4^i - 1)$, which scales super-exponentially with the number of qubits.

Given a pure quantum state $|\psi\rangle$, we say a unitary operator U stabilizes $|\psi\rangle$ if $U|\psi\rangle = |\psi\rangle$, i.e., $|\psi\rangle$ is an eigenvector of U with eigenvalue 1. An important class of states called stabilizer states are stabilized solely by Pauli operators. These stabilizers form a group called the stabilizer group $\mathrm{Stab}(|\psi\rangle)$, which is an abelian subgroup of the Pauli group, $\mathrm{Stab}(|\psi\rangle) \subset \mathcal{P}_N$ such that $-I \notin \mathrm{Stab}(|\psi\rangle)$. Formally,

$$\mathrm{Stab}(|\psi\rangle) = \{P \in \mathcal{P}_N : P|\psi\rangle = |\psi\rangle\} . \tag{6.7}$$

The group is generated by N generators $g_1, g_2, \ldots, g_N$, which are mutually commuting Pauli operators. The basic idea of the stabilizer formalism is that stabilizer states can be more compactly and efficiently described by working with their stabilizers than the state vector description. Indeed, these generators are sufficient to represent

a given stabilizer state since we have

$$|\psi\rangle\langle\psi| = \frac{1}{2^N}\prod_{i=1}^{N}(I + g_i). \tag{6.8}$$

These generators are commonly stored in a matrix called stabilizer tableau.

Notably, the pure stabilizer states defined above are precisely the set of states that can be obtained by applying Clifford gates to the computational basis state $|0\rangle^{\otimes N}$. In other words, for a stabilizer state $|\psi\rangle$, there is $C \in \mathcal{C}_N$ such that

$$|\psi\rangle = C\,|0\rangle^{\otimes N}. \tag{6.9}$$

Moreover, updating the stabilizer tableau after a Clifford operation can be done efficiently. This operation includes the unitary gates in the Clifford group, and Pauli measurements. This implies that Clifford circuits with stabilizer states input can be efficiently simulated classically; this is indeed the celebrated Gottesman-Knill theorem [9–11].

Going beyond pure states, a special class of mixed stabilizer states has the form

$$\rho = \frac{1}{2^N}\prod_{i=1}^{K}(I + g_i). \tag{6.10}$$

where $g_1, g_2, \ldots, g_K$ are mutually commuting Pauli operators and $K < N$. That is, the main difference with pure stabilizer states in Eq. (6.8) is that the number of generators is less than N. For a mixed stabilizer state ρ with K generators, there is $C \in \mathcal{C}_N$ such that

$$\rho = \frac{1}{2^{N-K}}C(|0\rangle\langle 0|)^{\otimes K} \otimes I^{\otimes(N-K)}C^\dagger. \tag{6.11}$$

The techniques to simulate pure stabilizer states can be straightforwardly adapted to this class of states. Note however that this class of states does not encompass all stabilizer states, which will be defined below.

We denote the set of N-qubit pure stabilizer states as $\mathcal{S}_N$, which size scales superexponentially with N, $|\mathcal{S}_N| = 2^N\prod_{i=1}^{N}(2^i + 1) \propto 2^{O(N^2)}$. The full set of stabilizer states is defined as the convex hull of $\mathcal{S}_N$:

$$\mathrm{STAB}_N = \left\{\rho : \rho = \sum_j p_j\,|\sigma_j\rangle\langle\sigma_j|\,, \forall j p_j \geq 0, \sum_j p_j = 1\right\}, \tag{6.12}$$

where $|\sigma_j\rangle$ are pure stabilizer states.

6.2 Nonstabilizerness as quantum resource

As discussed above, Clifford circuits can only prepare stabilizer states when applied on a computational basis state. Since the set of stabilizer states obviously does not encompass all possible states, it follows that Clifford circuits do not lead to universal quantum computation. The key to achieving computational speedup using quantum computers lies in introducing an additional operation [4, 12, 13]. Interestingly, it turns out that it is sufficient to introduce a simple one-qubit gate. Specifically,

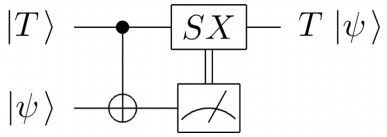

FIGURE 6.1: Quantum circuit which implements a T gate.

one can add a gate called the T gate, defined as

$$T = \begin{pmatrix} 1 & 0 \\ 0 & e^{i\pi/4} \end{pmatrix}, \tag{6.13}$$

to the set of Clifford gates, which allows to perform universal quantum computation. Another commonly used non-Clifford gate is the CCZ (controlled-controlled-Z) gate, or also known as Toffoli gate:

$$CCZ = \mathrm{diag}(1,1,1,1,1,1,1,-1), \tag{6.14}$$

which also promotes the Clifford set to a universal gate set.

The elements of Clifford group can be implemented fault-tolerantly, i.e., in a way that is resilient against noise. The T gate can be implemented by a Clifford circuit plus an ancilla state [12]

$$|T\rangle = \frac{|0\rangle + e^{i\pi/4}|1\rangle}{\sqrt{2}}, \tag{6.15}$$

which can also be written as $|T\rangle = TH|0\rangle$. The circuit is shown in Fig. 6.1. The Toffoli gate can be implemented with a similar scheme using the ancilla state [14]

$$|\psi_3\rangle = \frac{1}{2}(|000\rangle + |100\rangle + |010\rangle + |001\rangle). \tag{6.16}$$

In fact, this scheme is general in that any nonstabilizer operation can be implemented in such a way using a suitable ancilla state. Therefore, having a supply of magic states, combined with Clifford operations, would enable fault-tolerant universal quantum computation. Such magic states can be prepared by a scheme known as magic state distillation [12].

6.3 Resource theory of nonstabilizerness

In the above scheme of universal quantum computation, one can view the magic states as a "resource" that allows to achieve true quantum advantage. Such resource can be studied in a rigorous manner in the framework of quantum resource theory [15]. The basic idea is to define the set of "free states", while the states that are not free states are considered resource states. We also define "free operations" which include operations that leave the set of free states invariant, i.e., it cannot generate resource states from free states. One can further quantify how much resource that a state has by a resource measure. The most well-known example of a quantum resource theory is the theory of quantum entanglement [16], where the free states are separable states and the free operations are local operations and classical communication (LOCC). There are numerous existing entanglement measures, such as the von Neumann entanglement entropy for pure states.

In the case of magic, the free states are stabilizer states and the free operations are stabilizer operations. The latter are generated from the following elementary operations:

1. Clifford unitaries, $\rho \to C\rho C^\dagger, C \in \mathcal{C}_N$.
2. Composition with stabilizer states, $\rho \to \rho \otimes S$, where S is a stabilizer state.
3. Measurements in the computational basis, $\rho \to \sum_k P_k \rho P_k$, where P_k are the projectors on the computational basis ($\sum_k P_k = 1$).
4. Discarding of qubits, $\rho \to \mathrm{Tr}_A \rho$, for a set of qubits A.
5. The above operations conditioned on the outcomes of measurements or classical randomness.

A valid measure of magic $\mathcal{M}(\rho)$ must be faithful, i.e., $\mathcal{M}(\rho) = 0$ if and only if ρ is a stabilizer state. Moreover, it must be non-increasing under any stabilizer operations $\mathcal{E}$, i.e.,

$$\mathcal{M}(\rho) \geq \mathcal{M}(\mathcal{E}(\rho)). \tag{6.17}$$

Actually, the monotonicity becomes an invariance for operations (1) and (2) since they are reversible (by the inverse gate and discarding of qubits, respectively).

An additional property known as strong monotonicity requires that a measure is non-increasing on average under measurements. Consider the measurement of a Pauli operator P with the set of outcomes $\lambda \in \{+1, -1\}$. We denote the post-measurement state by $\rho_\lambda = V_\lambda \rho V_\lambda / p_\lambda$, where $p_\lambda = \mathrm{Tr}\, \rho V_\lambda$ is the corresponding probability and $V_\lambda = (I + \lambda Q)/2$. A measure is a strong monotone if it satisfies

$$\mathcal{M}(\rho) \geq \sum_\lambda p_\lambda \mathcal{M}(\rho_\lambda). \tag{6.18}$$

This property is not required but is particularly desirable as measurements represent an important component in stabilizer formalism. In addition, there are some features that are desirable but not necessary, such as continuity, convexity, and sub-additivity.

One approach to construct a measure of magic is based on distance: the distance between the given state and the closest stabilizer state serves as a magic measure in the given state. For example, if the distance is measured by the quantum relative entropy, $S(\rho\|\sigma) = -\mathrm{Tr}\,[\rho(\log\sigma - \log\rho)]$, we can define the relative entropy of magic as [17]

$$r_{\mathcal{M}}(\rho) = \min_{\sigma \in \mathrm{STAB}_N} S(\rho\|\sigma). \tag{6.19}$$

This is a genuine measure which satisfies strong monotonicity. Another example is the robustness of magic [18], given by

$$\mathcal{R}(\rho) = \min \left\{ \sum_{i=0}^{|\mathcal{S}_N|} |x_i| \;\middle|\; \rho = \sum_{\sigma \in \mathcal{S}_N} x_i \sigma_i, x \in \mathbb{R} \right\}, \tag{6.20}$$

which is also a strong monotone.

We note that both of these measures can be defined for a generic resource theory, and their nice properties can be established in general [15]. However, these measures are also notoriously difficult to compute as it requires an optimization over the set of stabilizer states, which grows super-exponentially with the number of qubits. As a result, their evaluation quickly becomes impractical beyond a few qubits. In the next

section, we will introduce a few measures of magic which do not involve minimization, thus making them simpler to compute. This computability is a crucial property that enables the investigation of these measures in quantum many-body systems.

6.4 Measures of nonstabilizerness

In this section, we will review the definitions and properties of several computable measures of nonstabilizerness. We note that most of the discussions below apply only to pure states, unless stated otherwise.

6.4.1 Pauli spectrum

Since the Pauli operators provide an orthonormal basis in the space of Hermitian operators, one can expand the density matrix $\rho = |\psi\rangle\langle\psi|$ as

$$|\psi\rangle\langle\psi| = \frac{1}{2^N}\sum_{\boldsymbol{u}}\langle\psi|P_{\boldsymbol{u}}|\psi\rangle P_{\boldsymbol{u}}. \tag{6.21}$$

One can see that the coefficients of $|\psi\rangle\langle\psi|$ in the basis of Pauli operators, i.e., the Pauli basis, directly correspond to the expectation values of the corresponding Pauli strings for the state $|\psi\rangle$. The set of these expectation values is called the Pauli spectrum

$$\mathrm{spec}(|\psi\rangle) = \left\{\langle\psi|\, P_{\mathbf{u}}\, |\psi\rangle\,, \mathbf{u} \in \mathbb{Z}_2^{2N}\right\}. \tag{6.22}$$

It captures the nonstabilizerness of a state, in a similar way that the entanglement spectrum captures the entanglement of a state. For a stabilizer state, the Pauli spectrum contains only 2^N non-zero values, all of them are ± 1.

6.4.2 Stabilizer Rényi entropy

Stabilizer Rényi Entropies (SREs) are a measure of nonstabilizerness recently introduced in Ref. [19]. For a pure quantum state $|\psi\rangle$ of a system of N qubits, SREs are expressed in terms of the expectation values of all Pauli strings:

$$M_n\left(|\psi\rangle\right) = \frac{1}{1-n}\log\left\{\sum_{\mathbf{u}}\frac{\langle\psi|P_{\mathbf{u}}|\psi\rangle^{2n}}{2^N}\right\}. \tag{6.23}$$

Eq. (6.23) can be seen as the Rényi-n entropy of the classical probability distribution

$$\Xi_{|\psi\rangle}(\boldsymbol{u}) = \frac{\langle\psi|P_{\boldsymbol{u}}|\psi\rangle^2}{2^N}, \tag{6.24}$$

also known as the characteristic function [20]. The SREs can also be seen as the moments of the Pauli spectrum, or equivalently, the participation entropy in the Pauli basis [21].

The SREs are a pure-state magic monotone, which is a monotone when the operations are restricted to the stabilizer protocols that map pure states to pure states. Specifically, the SREs have the following properties [19, 22]:

- faithfulness, i.e., $M_n(|\psi\rangle) = 0$ iff $|\psi\rangle \in \mathrm{STAB}$;
- invariance under Clifford unitaries $C \in \mathcal{C}_N$, i.e., $M_n(C|\psi\rangle) = M_n(|\psi\rangle)$;

- additivity, i.e., $M_n(|\psi\rangle_A \otimes |\psi\rangle_B) = M_n(|\psi\rangle_A) + M_n(|\psi\rangle_B)$;
- monotonicity under pure-state stabilizer protocols for integer $n \geq 2$.

The SREs of integer $n \geq 2$ are thus a good measure of magic from the point of view of resource theory. However, it was observed that the SREs are not a strong monotone for any n [23]. While it is possible to propose modifications like linear stabilizer entropies to address this and create a strong monotone [22, 24], it comes with its own disadvantages. We will therefore focus on the SREs in this thesis.

The definition of SREs can be extended to mixed states by properly normalizing $\Xi_{|\psi\rangle}(\mathbf{u})$. For example, for $n = 2$, the mixed state SRE is given by [19]

$$\tilde{M}_2 = -\log\left(\frac{\sum_{\mathbf{u}} \mathrm{Tr}\left(\rho P_{\mathbf{u}}\right)^4}{\sum_{\mathbf{u}} \mathrm{Tr}\left(\rho P_{\mathbf{u}}\right)^2}\right), \tag{6.25}$$

which can be seen as the Rényi-2 entropy of

$$\Xi_\rho(\boldsymbol{u}) = \frac{\mathrm{Tr}\left(\rho P_{\mathbf{u}}\right)^2}{\sum_{\mathbf{v}} \mathrm{Tr}\left(\rho P_{\mathbf{v}}\right)^2}, \tag{6.26}$$

apart from some offset. Here, the free states are defined as the mixed stabilizer states that have the form in Eq. (6.10). Since this is a restricted class of mixed stabilizer states, $\tilde{M}_2$ is not a true measure of magic for mixed states. Nevertheless, it has the advantage that it is simple to compute, similarly with the pure-state SRE.

An alternative approach to define the mixed state extension of SRE involves convex-roof construction [22]. In this way, the measure would capture the whole set of stabilizer states, not just the restricted class of mixed stabilizer states that is captured by $\tilde{M}_2$. However, convex roof construction is significantly more difficult to work with.

Since the definition of SREs do not involve minimization, they are much simpler to compute than previously known measures of nonstabilizerness. Note however that the cost for naive computation is still exponential, as there are exponentially many Pauli strings, whose expectation values need to be computed. There are by now a number of cases where the computation (analytical or numerical) can be done for large system sizes, including tensor network states [25–28], Rokhsar-Kivelson states [29], sign-problem-free models [30], hypergraph states [31], permutationally invariant systems [32], and dual-unitary circuits [33].

6.4.3 Stabilizer nullity

The stabilizer group $\mathrm{Stab}(|\psi\rangle)$ in Eq. (6.7) can in fact be defined for any quantum state. Its size $|\mathrm{Stab}(|\psi\rangle)|$ is given by the number of ± 1 in the Pauli spectrum. For a nonstabilizer state, the number of generators $k = \log_2 |\mathrm{Stab}(|\psi\rangle)|$ is less than N. This naturally leads to a simple measure of nonstabilizerness by substracting the number of generators k from the number of qubits N, i.e.

$$\nu\left(|\psi\rangle\right) = N - \log_2 |\mathrm{Stab}(|\psi\rangle)|. \tag{6.27}$$

This measure is called the stabilizer nullity [34], which is a strong monotone. It can only take integer values between 0 and N. Furthermore, it is additive under the tensor product. We will show in Chapter 10 that stabilizer nullity is related to the SRE in the limit of Rényi index $n \to \infty$.

Surprisingly, stabilizer nullity can be estimated efficiently using a protocol called Bell difference sampling [20]. Specifically, the protocol efficiently learns the stabilizer

group of a state in $O(N^3)$ time, from which we can directly obtain the stabilizer nullity. We refer to Refs. [35, 36] for details on the protocol.

6.4.4 Bell magic

Bell magic is a measure of magic that can be estimated using a protocol known as Bell sampling. The protocol involves preparing two identical copies of a state and measuring them in the Bell basis. The measurement outcome $\mathbf{r}$ appears with a probability

$$P(\mathbf{r}) = \frac{|\langle\psi| P_{\mathbf{r}} |\psi^*\rangle|^2}{2^N}. \tag{6.28}$$

Bell magic is then defined as [37]

$$\mathcal{B} = \sum P(\mathbf{r})P(\mathbf{r}')P(\mathbf{q})P(\mathbf{q}')||[\sigma_{\mathbf{r}\oplus\mathbf{r}'}, \sigma_{\mathbf{q}\oplus\mathbf{q}'}]||_\infty, \tag{6.29}$$

where the infinity norm is zero when the Pauli strings commute and 2 otherwise. In words, Bell magic quantifies the probability that sampled Pauli strings commute with each other. Bell magic is a faithful measure of nonstabilizerness, namely, it is zero for stabilizer states and greater than zero otherwise. Moreover, it is invariant under Clifford unitary. To construct a measure which is additive under tensor product, the additive Bell magic is given by

$$\mathcal{B}_a = -\log(1 - \mathcal{B}). \tag{6.30}$$

Bell magic is particularly relevant in experimental setting as it can be estimated through Bell sampling followed by $O(N)$ classical post-processing time. Its experimental measurement has already been demonstrated in Ref. [7] in a quantum circuit of up to 6 qubits.

6.5 Outlook

The characterization of nonstabilizerness in quantum many-body systems is a topic that has recently witnessed growing interest and offers numerous prospects for future investigations.

On one side, investigating nonstabilizerness in such systems poses a significant challenge, particularly due to the inherent difficulty of evaluating measures of nonstabilizerness for large system sizes. It is thus essential to address this issue by developing scalable methods to compute nonstabilizerness at large scales. In Chapter 7, we introduce a new method to measure many-body magic in quantum systems based on a statistical exploration of Pauli strings via Markov chains. We describe an efficient sampling procedure using Tree Tensor Networks (TTNs), that exploits their hierarchical structure leading to a modest $O(\log N)$ computational scaling with system size. A subsequent application of this method reveals that mutual information of nonstabilizerness grows logarithmically in critical spin chains, similarly to entanglement, as discussed in Chapter 8. Then, in Chapter 9, we show how to compute nonstabilizerness in a relevant class of many-body systems called the generalized Rokhsar-Kivelson systems. In Chapter 10, we present a novel approach for the evaluation of nonstabilizerness within the framework of matrix product states (MPS), based on expressing the MPS directly in the Pauli basis. Finally, in Chapter 11, we introduce a measurement-only circuit whose magic dynamics is efficiently simulable, allowing for large-scale simulations. These new methods have enabled initial

explorations of the connection of nonstabilizerness to many-body physical phenomena. Further applications of these approaches to other models and in various many-body phenomena will be an exciting avenue for future research. It could potentially advance our understanding of quantum systems, provide new tools for the analysis of quantum many-body models, and has significant implications for numerical simulations in many-body quantum systems.

On another side, an increasing effort is being put to understand connections between different quantum resources. This line of research is important to unravel the fundamental source of quantum computational power. Among these resources, entanglement and nonstabilizerness stand out due to their tight connection to classical simulability of quantum circuits. Delving into the relationship between these two key resources could shed light on the origins of quantum computational advantage. In Chapter 12, we show how the SRE is connected to the flatness of the entanglement spectrum, thus establishing a direct link between nonstabilizerness and entanglement. Importantly, this connection can be leveraged to develop a protocol to efficiently probe nonstabilizerness in experimental platforms. Finally, in Chapter 13, we investigate the relationship between entanglement and nonstabilizerness in MPS.

Chapter 7

Many-body magic via Pauli-Markov chains – from criticality to gauge theories

In this chapter, we present a theoretical framework to measure many-body magic that leverages on a stochastic sampling of the system wave function. Our work builds upon recent developments in the field, in particular, on the recognition of stabilizer Renyi entropies (SREs) as measures of magic (including an experimental demonstration with 4 qubits) [19, 38–40]. While a direct measure of the former is extremely challenging as it requires a number of measurements that grows exponentially with the size of the partition, we introduce a Markov chain on Pauli strings as a tool to distill the most relevant contribution to magic. We show that our protocol returns an unbiased estimator of SREs of all orders, and that it is efficient under several important scenarios: those include both full state magic (that is relevant, e.g., to quantify the overall difference from a stabilizer state), and long-range magic - a quantity that is akin to mutual information and that, crucially, is not plagued by any UV-divergences when applied to field theory.

The estimation of magic via Pauli-Markov chain is a general construction, that is broadly applicable to computations as well as experiments. We explore in detail its capabilities in the context of tree tensor networks (TTN) [41, 42]. At first, we perform extensive methodological checks, in particular, on the efficiency of Markov sampling and autocorrelations. We then showcase the flexibility of our approach with several applications, to understand advantages and overall comparison with recently introduced direct sampling methods that constitute the state of the art in terms of measuring many-body magic in numerical computations [23, 25, 27].

Firstly, we consider one-dimensional systems. There, by considering both Ising, Potts and Heisenberg models, we show that full-state magic is not always indicative of quantum critical behavior. In particular, while it works for the conceptually simple cases of Ising (as already observed in Ref. [23, 25, 27, 43]) and Potts models, it spectacularly fails detecting any criticality in the case of spin-1 XXZ models. Oppositely, long-range magic (whose computation was not accessible before our algorithm, to the best of our knowledge) displays sharp signatures of critical behavior in all models considered. Our work thus clarifies how, in the context of critical behavior, it is fundamental to construct - and to compute - UV-divergence free estimators to understand the role of magic.

Secondly, we consider two-dimensional interacting systems, where the connection between magic and many-body phenomena is uncharted territory. We focus on the $\mathbb{Z}_2$ lattice gauge theory, for two reasons: its importance as a paradigmatic model for more complicated lattice field theories, as it displays a confinement-deconfinement

transition, as well as topological order; and its direct connection to the toric code, an epitome example of quantum memory based on the stabilizer language [1, 9–11, 16, 44–48]. Thanks to the very modest $O(\ln N)$ size-scaling of our algorithm versus system size N, we are able to consider systems up to 100 spins. Our results show how both confined and deconfined phase have volume-law magic: most remarkably, magic features striking signatures of critical behavior. Close to the transition point, its behavior is akin to that of a Binder cumulant, as magic density displays a crossing as a function of volume, whose functional form is dictated by finite-size scaling theory. Even more remarkably, universal collapses are not only evident at modest volumes, but even at relatively small bond dimensions, signalling that magic might be considerably less affected than other observables by tensor network truncations. At the physical level, our results point out that magic may serve as an order parameter for confinement-deconfinement transitions, even at volumes where other quantities (e.g., order parameters) are of very limited use.

Finally, we give a glimpse of the applicability of our approach to experiments. In that context, we discuss in detail experimental errors as a function of finite sampling, size, and autocorrelations. Our results indicate that the sampling needed to scale to large systems requires very fast repetition rates, which are available in solid state settings, but constitute a challenge for atomic experiments.

The rest of the chapter is structured as follows. In Sec. 7.1, we review the SREs and extend it to qudits. In Sec. 7.2, we describe how to sample Pauli strings via Markov chains, discuss the efficiency of various estimators, and detail our implementation with tree tensor networks. In Sec. 7.3, we present our results on both one- and two-dimensional spin systems. In Sec. 7.4, we detail our experimental protocol, and then conclude in Sec. 7.5.

7.1 Stabilizer Renyi entropy

Stabilizer Rényi Entropies (SREs) are a measure of nonstabilizerness recently introduced in Ref. [19]. For a pure quantum state ρ, SREs are expressed in terms of the expectation values of all Pauli strings in $\mathcal{P}_N$:

$$M_n(\rho) = \frac{1}{1-n} \log \left\{ \sum_{P \in \mathcal{P}_N} \frac{|\operatorname{Tr}(\rho P)|^{2n}}{d^N} \right\}, \tag{7.1}$$

with d is the local dimension of the Hilbert space of N qudits and $\mathcal{P}_N$ is the generalized Pauli group of N qudits [49]. The SREs have the following properties: [19] (i) faithfulness: $M_n(\rho) = 0$ iff $\rho \in$ STAB, (ii) stability under Clifford unitaries $C \in \mathcal{C}_N$: $M_n(C\rho C^\dagger) = M_n(\rho)$, and (iii) additivity: $M_n(\rho_A \otimes \rho_B) = M_n(\rho_A) + M_n(\rho_B)$. The SREs are thus a good magic measure in the point of view of resource theory, where the free states are defined as the stabilizer states while the free operations are the Clifford unitaries. This definition is a straightforward generalization to general local dimension d from the one given in Ref. [19]. For $d > 2$, the Pauli operators are no longer Hermitian, and thus the expectation values can be complex. In Eq. (7.1), we take the absolute values of the expectation values $|\operatorname{Tr}(\rho P)|$. Eq. (7.1) can be seen as the Rényi-n entropy of the classical probability distribution:

$$\Xi_P = |\operatorname{Tr}(\rho P)|^2 / d^N. \tag{7.2}$$

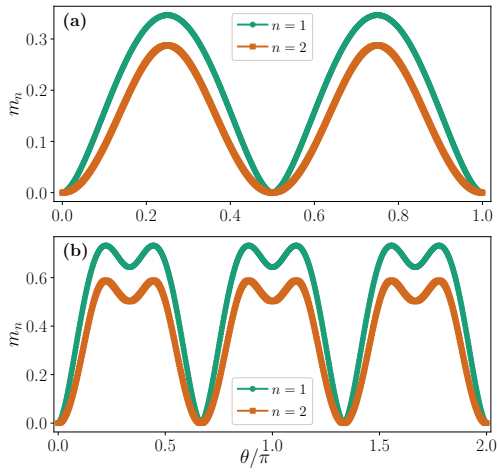

FIGURE 7.1: **Stabilizer entropies for qubit and qutrit states.** The SRE density m_1 and m_2 for single qubit state (a) defined in the Eq. (7.6), and for single qutrit state defined in Eq. (7.7) (b).

Moreover, the definition of SREs can be extended to mixed states by properly normalizing Ξ_P. For example, for $n = 2$, the mixed state SRE is given by [19]

$$\tilde{M}_2 = -\log\left(\frac{\sum_{P\in\mathcal{P}_N} |\operatorname{Tr}(\rho P)|^4}{\sum_{P\in\mathcal{P}_N} |\operatorname{Tr}(\rho P)|^2}\right), \tag{7.3}$$

which can be seen as the Rényi-2 entropy of

$$\tilde{\Xi}_P = |\operatorname{Tr}(\rho P)|^2 / \sum_{P\in\mathcal{P}_N} |\operatorname{Tr}(\rho P)|^2, \tag{7.4}$$

apart from some offset. Here, the free states are defined as the mixed states that can be obtained from pure stabilizer states by partial tracing [19].

Furthermore, the long-range magic can be quantified by

$$L(\rho_{AB}) = \tilde{M}_2(\rho_{AB}) - \tilde{M}_2(\rho_A) - \tilde{M}_2(\rho_B) \tag{7.5}$$

where A and B are two separated subsystems (see Fig. 7.2 (a)- (b)). A similar quantity has been considered previously in the context of mana [50, 51] and robustness of magic [52, 53]. $L(\rho_{AB})$ measures how magic is contained in the correlation between the subsystems, and thus it quantifies the degree to which magic cannot be removed by finite-depth quantum circuits [50]. Indeed, due to the additivity of SRE, $L(\rho_{AB})$ vanishes for a product state $\rho_A \otimes \rho_B$. On the other hand, a non-vanishing value of $L(\rho_{AB})$ effectively quantifies the extent of deviation from the additivity in the case of entangled subsystems.

The long-range magic is directly reminiscent of mutual information, that has played a major role in characterizing the distribution of both classical information and quantum correlations in many-body systems [4, 54–65]. On the lattice, the main motivation for looking at functionals such as in Eq. (7.5) is that they are much more meaningful than simple bipartition properties from a field theory standpoint. Indeed, these quantities are expected to be free of UV divergences, and thus solely dominated by infrared, universal properties of the lattice theory. This parallels the f-functions used in field theory [66].

7.1.1 Examples

To familiarize with the behavior of SREs in many-body systems, here we provide some examples of SREs in simple wave functions. First of all, we stress that the SREs are basis-dependent, i.e., it is not invariant under local basis change. In particular, the SREs of a single-qubit state may be non-trivial. For example, consider the following one-parameter family of single-qubit states

$$|\psi(\theta)\rangle = \frac{1}{\sqrt{2}}\left[|0\rangle + e^{i\theta}|1\rangle\right]. \tag{7.6}$$

Note that $|\psi(\pi/4)\rangle$ corresponds to the canonical T-state. The SREs can be computed easily by evaluating the expectation values of $P \in \{I, X, Y, Z\}$, and then plugging it in Eq. (7.1). The result is shown in Fig. 7.1 (a). As can be seen, the SREs are non-zero apart from some special points $\theta = m\pi/2$ with integer m.

Now, the SREs of a product state of N copies of $|\psi(\theta)\rangle$ can also be computed straightforwardly, utilizing the additivity property of SRE, $M_n(\rho_A \otimes \rho_B) = M_n(\rho_A) + M_n(\rho_B)$. The SREs are then just given by $M_n(|\psi(\theta)\rangle^{\otimes N}) = NM_n(|\psi(\theta)\rangle)$.

For an example of qudit states, we consider the following family of single-qutrit states

$$|\phi(\theta)\rangle = \frac{1}{\sqrt{3}}\left[|0\rangle + e^{i\theta}|1\rangle + e^{-i\theta}|2\rangle\right]. \tag{7.7}$$

Here, $|\phi(2\pi/9)\rangle$ corresponds to the canonical qutrit T-state. We now need to compute the expectation values of 3^2 single-qutrit Pauli operators. To define the Pauli operators, we first define the shift and clock operators for d-level system as

$$X = \sum_{k=0}^{d-1} |k+1\rangle\langle k| \quad \text{and} \quad Z = \sum_{k=0}^{d-1} \omega_d^k |k\rangle\langle k|, \tag{7.8}$$

where $\omega_d = e^{2\pi i/d}$, and the addition is defined modulo d. For qutrits, we have $d = 3$. The qudit Pauli operators are defined as

$$T_{aa'} = \omega^{-2^{-1}aa'} Z^a X^{a'} \tag{7.9}$$

for $a, a' \in \mathbb{Z}_d$. Here, 2^{-1} is the inverse element of 2 in $\mathbb{Z}_d$.

Computing the expectation values of the Pauli operators in Eq. (7.9), we can compute the SREs of $|\phi(\theta)\rangle$ using Eq. (7.1). The result is shown in Fig. 7.1 (b). In this case, the SREs are non-trivial apart from some special points $\theta = m2\pi/3$ with integer m.

7.2 Markov chain Monte Carlo sampling of Pauli strings

In this work, we investigate the SREs using Monte Carlo sampling of Pauli strings according to some probability distribution Π_P, which only depends explicitly on the expectation values of Pauli strings. For example, for the calculation of M_n, we get $\Pi_P = \Xi_P$ (Eq. (7.2)), while for $\tilde{M}_2$ we have $\Pi_P = \tilde{\Xi}_P$ (Eq. (7.4)). Here we focus on Metropolis algorithm, although other sampling methods, such as heat bath, may also be employed. Since Π_P only depends on the expectation value of P, this method is applicable to any numerical methods in which expectation values of (non-local) operators can be accessed, such as exact diagonalization and tensor network methods.

Furthermore, this method can also be utilized to experimentally measure SREs (see Sec. 7.4).

Algorithm 1 Monte Carlo sampling of Pauli strings

Input: a quantum state ρ and number of sampling N_S

1: Initialize the Pauli string P.
2: Compute $\mathrm{Tr}(\rho P)$ and Π_P.
3: **for** $(i = 1; i \leq N_S; i++)$ **do**
4: Propose a candidate Pauli string P'.
5: Compute $\mathrm{Tr}(\rho P')$ and $\Pi_{P'}$.
6: Accept the move with probability: min $\left(1, \frac{\Pi_{P'}}{\Pi_P}\right)$.
7: Measure the estimators.
8: **end for**

Output: a Markov chain of P with probability Π_P.

7.2.1 Algorithm theory

The scheme is summarized in the Algorithm 1. If we sample according to Ξ_P, M_n can be estimated using the unbiased estimators

$$M_n = \frac{1}{1-n} \log \left\langle |\mathrm{Tr}(\rho P)|^{2(n-1)} \right\rangle_{\Xi_P} \tag{7.10}$$

for $n > 1$ and

$$M_1 = \left\langle -\log \left(|\mathrm{Tr}(\rho P)|^2 \right) \right\rangle_{\Xi_P} \tag{7.11}$$

for $n = 1$, where $\langle ... \rangle_{\Xi_P}$ is the average over Ξ_P obtained with sampling. For $n < 1$, a better estimation can be done by reversing Eq. (7.10), i.e.,

$$M_n = -\frac{1}{1-n} \log \left\langle |\mathrm{Tr}(\rho P)|^{2(1-n)} \right\rangle_{\Pi_{P,n}} \tag{7.12}$$

where $\Pi_{P,n} \propto |\mathrm{Tr}(\rho_{AB} P)|^{2n}$. Let us analyze the efficiency of these estimators.

SRE with $n = 1$.– For $n = 1$, the variance of M_1 is shown to be at most quadratic in N in Ref. [27]. Thus, the estimator for M_1 is efficient. Actually, we can even make a stronger statement, if we make the assumption that the SREs are linear in N, i.e., $M_\alpha = N f(\alpha) + O(1)$, where $f(\alpha)$ is a function that does not depend on N. Using the relation [67]:

$$\mathrm{Var}(M_1) = \left. \frac{d^2[(1-\alpha) M_\alpha]}{d\alpha^2} \right|_{\alpha=1}, \tag{7.13}$$

we see that $\mathrm{Var}(M_1)$ is linear in N. It follows that the variance (standard deviation) of the SRE density, $m_1 = M_1/N$, scales as $1/N$ ($1/\sqrt{N}$).

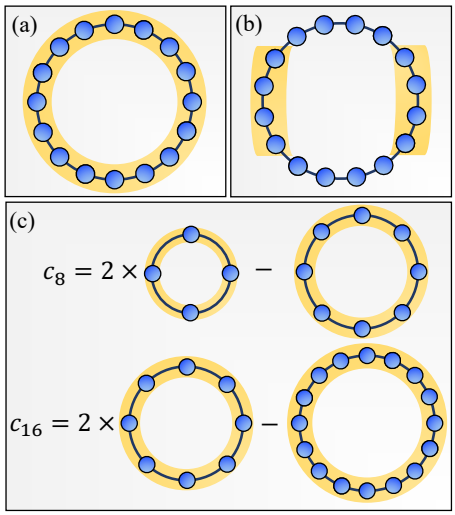

FIGURE 7.2: **Schematics of partitions.** (a) Full partition. (b) Two widely-separated partitions for the calculation of long-range magic in Eq. (7.5). (c) Subleading term as in Eq. (7.22), as well as a cartoon depicting the increment trick discussed in the main text.

SRE with $n \neq 1$.– For $n > 1$, the variance of Eq. (7.10) is given by

$$\begin{aligned} &\mathrm{Var}\left(|\operatorname{Tr}(\rho P)|^{2(n-1)}\right) \\ &\quad = \left\langle |\operatorname{Tr}(\rho P)|^{4(n-1)} \right\rangle_{\Xi_P} - \left\langle |\operatorname{Tr}(\rho P)\rangle|^{2(n-1)} \right\rangle_{\Xi_P}^2 \\ &\quad = \exp\left[-2(n-1)M_{2n-1}\right] - \exp\left[-2(n-1)M_n\right]. \end{aligned} \tag{7.14}$$

Now, by second-order approximation $\mathrm{Var}\left(\log x\right) \approx \mathrm{Var}\left(x\right)/x^2$, we have

$$\begin{aligned} \mathrm{Var}\left(M_n\right) &\approx \frac{\exp\left[-2(n-1)M_{2n-1}\right] - \exp\left[-2(n-1)M_n\right]}{|n-1|\exp\left[-2(n-1)M_n\right]} \\ &= \frac{\exp\left[2(n-1)(M_n - M_{2n-1})\right] - 1}{|n-1|}. \end{aligned} \tag{7.15}$$

For $n < 1$,

$$\begin{aligned} &\mathrm{Var}\left(|\operatorname{Tr}(\rho P)|^{2(1-n)}\right) \\ &\quad = \left\langle |\operatorname{Tr}(\rho P)|^{4(1-n)} \right\rangle_{\Pi_{P,n}} - \left\langle |\operatorname{Tr}(\rho P)|^{2(1-n)} \right\rangle_{\Pi_{P,n}}^2 \\ &\quad = \exp\left[(n-1)(M_{2-n} + M_n)\right] - \exp\left[2(n-1)M_n\right]. \end{aligned} \tag{7.16}$$

Then,

$$\begin{aligned} \mathrm{Var}\left(M_n\right) &\approx \frac{\exp\left[(n-1)(M_{2-n} + M_n)\right] - \exp\left[2(n-1)M_n\right]}{|n-1|\exp\left[2(n-1)M_n\right]} \\ &= \frac{\exp\left[(1-n)(M_n - M_{2-n})\right] - 1}{|n-1|}. \end{aligned} \tag{7.17}$$

In both cases, if the SREs grow at most logarithmically in N, the variance grows at most polynomially. Thus, by Chebyshev's inequality, the number of samples needed

for a fixed error ϵ is polynomial in N, i.e, the estimator is efficient. On the other hand, if the SREs are linear in N, as is typically the case in many-body systems [25, 43, 50], the variance grows exponentially with N when $n \neq 1$. Thus, the estimator for $M_n, n \neq 1$ is efficient only if the SREs are at most $O(\log N)$. One can also see this intuitively by noting that the quantity being estimated is exponentially small in N when M_n is linear, and thus we need exponentially small precision. We note in passing that states with logarithmically growing SREs can arise in many-body systems in the frustrated regime [40].

Note, however, that the SREs are typically linear in N. Therefore, using the estimators in Eq. (7.10), the estimation of $M_n, n \neq 1$ will almost always be exponentially costly. Nevertheless, the cost typically grows much more slowly than d^{2N} which is the cost for exact computation. Thus, in practice, using this estimator is still beneficial to extend the system sizes we can study, as we shall illustrate in Sec. 7.3. Importantly, using Monte Carlo sampling, we are not restricted to sample the Pauli strings according to Ξ_P. An alternative approach is to sample Pauli strings according to the probability distribution $\Pi_{P,n} \propto \mathrm{Tr}(\rho P)^{2n}$. We then need to estimate the normalization constant of $\Pi_{P,n}$ to estimate M_n. This is a non-trivial task, equivalent to estimating the partition function, for which a wealth of sophisticated methods have been put forward [68–78].

Long-range magic.– In addition, we are interested to estimate the long-range magic as quantified by $L(\rho_{AB})$ in Eq. (7.5). While we can in principle compute the individual $\tilde{M}_2$ for $\rho_C, C \in \{A, B, AB\}$, this is not optimal, as we have seen that the estimation for $\tilde{M}_2$ is not efficient when $\tilde{M}_2$ grows linearly with N. Moreover, we expect that the leading term of $\tilde{M}_2$ will be canceled out in $L(\rho_{AB})$. In this case, it is more desirable to estimate $L(\rho_{AB})$ directly, without having to resort to inefficient estimation of $\tilde{M}_2$. To do this, we first rewrite Eq. (7.5) as follows:

$$L(\rho_{AB}) = I_2(\rho_{AB}) - W(\rho_{AB}), \tag{7.18}$$

where

$$W(\rho_{AB}) = -\log\left(\frac{\sum_{P_A\in\mathcal{P}_A} |\mathrm{Tr}(\rho_A P_A)|^4 \sum_{P\in\mathcal{P}_B} |\mathrm{Tr}(\rho_B P_B)|^4}{\sum_{P_{AB}\in\mathcal{P}_{AB}} |\mathrm{Tr}(\rho_{AB} P_{AB})|^4}\right), \tag{7.19}$$

and $I_2(\rho_{AB}) = S_2(\rho_A) + S_2(\rho_B) - S_2(\rho_{AB})$ is the Rényi-2 mutual information. If one is to sample according to $\Pi_{P_{AB}} \propto \mathrm{Tr}(\rho_{AB} P_{AB})^4$, we can estimate $W(\rho_{AB})$ by

$$W(\rho_{AB}) = -\log\left\langle \frac{|\mathrm{Tr}(\rho_A P_A)|^4 |\mathrm{Tr}(\rho_B P_B)|^4}{|\mathrm{Tr}(\rho_{AB} P_{AB})|^4}\right\rangle_{\Pi_{P_{AB}}}, \tag{7.20}$$

where P_{AB} is decomposed as $P_{AB} = P_A \otimes P_B$. Similarly, we have

$$I_2(\rho_{AB}) = -\log\left\langle \frac{|\mathrm{Tr}(\rho_A P_A)|^2 |\mathrm{Tr}(\rho_B P_B)|^2}{|\mathrm{Tr}(\rho_{AB} P_{AB})|^2}\right\rangle_{\Xi_{P_{AB}}}. \tag{7.21}$$

Therefore, as a byproduct, our scheme can be applied to compute the Rényi mutual information for disjoint subsystems.

Subleading term.– The previous scheme can be straightforwardly modified to extract the subleading term in the expansion $M_n(N) = D_N N + c_N$ [25]. Here we consider 1D systems for simplicity. Specifically, the subleading term is approximated by

the quantity $c_N = 2M_n(N/2) - M_n(N)$ (see Fig. 7.2 (c)), which expands as

$$c_N = \log \left\langle \frac{|\operatorname{Tr}\left(\rho_{N/2}P^{(1)}\right)|^{2n}|\operatorname{Tr}\left(\rho_{N/2}P^{(2)}\right)|^{2n}}{|\operatorname{Tr}(\rho_N P)|^{2n}} \right\rangle_{\Pi_{P,n}} \tag{7.22}$$

for $n \neq 1$, where $\rho_{N,N/2}$ is the density matrix for a 1D system of size N and $N/2$, respectively. For simplicity, we have assumed translational invariance in Eq. (7.22), but the procedure can be straightforwardly generalized to any system. Here, denoting $P = P_1P_2...P_N$, where P_i is a Pauli operator acting on site i in the $N-$site system, we choose $P^{(1)} = P_1P_2...P_{N/2}$ and $P^{(2)} = P_{N/2+1}P_{N/2+2}...P_N$. Note that, differently from Eq. (7.20), here we consider two pure states of different sizes N and $N/2$. For the subleading term in 1D systems, the term inside the log in Eq. (7.22) does not decay exponentially, and thus the estimation can be done more efficiently than the estimation of the leading term in Eq. (7.10).

Increment trick for SRE.– The extraction of the subleading term in Eq. (7.22) presents an alternative strategy to estimate M_n, which circumvents the problem of exponential variance for the estimator in Eq. (7.10). The key idea is that, if the estimation in Eq. (7.22) is efficient, then we can estimate $c_N, c_{N/2}, ...$, until the size is small enough that M_n can be evaluated exactly. The number of c_M's that needs to be computed scales as $O(\log N)$ (assuming translational invariance). Then, we can determine $M_n(N)$ by considering a proper linear combination of c_M's. This strategy is reminiscent of the increment trick employed in estimation of Rényi entanglement entropies in Quantum Monte Carlo simulations [79–81], which considers the difference of Rényi entropies of smaller and smaller regions, to compute the Rényi entropy of a large entangling region with high precision. However, in this case, the form of c_N is specifically designed to cancel out the volume-law term of M_n, differently from entanglement entropy which exhibits area law.

The above strategy is effective in 1D systems because the subleading term c_N is expected to either remain independent of system size or exhibit at most logarithmic growth. However, in higher-dimensional systems, c_N may exhibit area-law scaling, leading to growth with size. In this case, more complicated linear combination of M_n's shall be considered to eliminate the area-law term (while, at the same time, also keeping the volume law one vanishing). For example, in 2D systems, the form of linear combination used in extracting the topological entanglement entropy with Kitaev-Preskill [82] or Levin-Wen scheme [83] will cancel both the volume-law and area-law term. It is convenient to partition the system into four subsystems as proposed in [84], which is also suitable with 2D TTN geometry. With this scheme, the estimation of $M_n(L \times L)$ is reduced to $M_n(L/2 \times L), M_n(L/2 \times L/2), ...$, such that only $O(\log N)$ computations are required, as in 1D case[1].

7.2.2 Efficient sampling with tensor networks: the example of tree tensor networks

The probability Π_P of a given Pauli string P only depends on the expectation value of P, and thus it is efficiently computable in TTN (or any loopless tensor network [42]). Following the convention introduced in Ref. [41], each tensor in the TTN

[1] In each computation, one estimates the linear combination $\gamma_{M_n} = M_n(L \times L) - 4M_n(L/2 \times L) + 4M_n(L/2 \times L/2)$, and similar form for $L/2 \times L$ geometry. This quantity can be recast into a form suitable for Monte Carlo estimation in a similar way as the subleading term in Eq. (7.22).

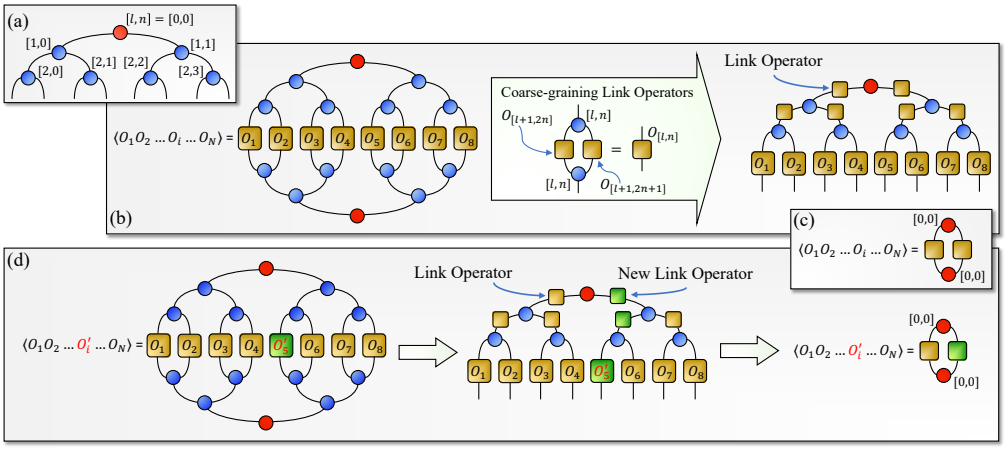

FIGURE 7.3: **Efficient Monte Carlo sampling using Tree Tensor Network.** (a) Tree Tensor Network (TTN) representation of a many-body wavefunction $|\psi\rangle$, where tensors are depicted as circles arranged in a binary-tree structure. Each tensor is identified by a pair of zero-indexed integers $[l, n]$, representing its layer index l and tensor index n at that layer. The red circle at the top-most layer represents the root tensor having index $[0, 0]$, where the isometry center of the TTN is taken. (b) To evaluate the expectation value of a tensor-product of single-site operators $\langle O_1 O_2 \dots O_N \rangle$, we first place each operator O_i at the physical site it acts on in the TTN representation. Then, we compute the effective link operators which live at the virtual links by the coarse-graining procedure as shown in the figure. The coarse-graining is performed iteratively from the physical sites to the top-most virtual links, which are directly connected to the root tensor. At each step, the link operators $O_{[l+1,2n]}$ and $O_{[l+1,2n+1]}$ are combined into $O_{[l,n]}$ by the $[l, n]$-tensor. The resulting link operator $O_{[l,n]}$ acts on the $[l-1, \lfloor n/2 \rfloor]$-tensor one layer above in the TTN structure. (c) The expectation value $\langle O_1 O_2 \dots O_N \rangle$ is calculated from the contraction of the root $[0, 0]$-tensor and the top-lost link operators as shown in the figure. (d) Considering a modified operator which differs only at a single site from the previous one, $O_1 O_2 ... O_i' ... O_N$, we only need to recompute the link operators in the path from the modified physical site i to the topmost link.

structure is denoted by the pair of zero-indexed integers $[l, n]$, where l corresponds to the layer index (starting from the top root tensor) and n denotes the tensor at a particular layer l counted from the left (see Fig. 7.3(a)). Obviously, in this notation, the top root tensor is represented by $[l, n] = [0, 0]$.

The algorithm to sample Pauli strings for the ground state of a quantum many-body system is described below.

- ⇨ After performing the adaptive variational ground-state search [41] for a many-body Hamiltonian, we arrive at the TTN representation of the many-body ground state wavefunction $|\psi\rangle$. We start by bringing the TTN into the central canonical form, where the $[0, 0]$-tensor is the orthogonality center (see Fig. 7.3(a)).

- ⇨ Given the initial Pauli string $P = P_1 P_2 \dots P_N$, where P_i is a Pauli operator at site i, we construct the coarse-grained effective "link" operators $O_{[l,n]}$ at each link iteratively from the physical sites to the top-most links, where at the bottom-most (i.e., the physical) layer these link operators are identified with

the Pauli operators (see Fig. 7.3(b)). At each step, the link operators $O_{[l+1,2n]}$ and $O_{[l+1,2n+1]}$ are coarse-grained into $O_{[l,n]}$ by $[l,n]$-tensor. The new link operator $O_{[l,n]}$ acts on the $[l-1,\lfloor n/2 \rfloor]$-tensor a layer above in the TTN structure. We keep all the link operators in memory for future uses.

- ⇨ The expectation value $\langle\psi|P|\psi\rangle$ now only involves the root $[0,0]$-tensor and top-most link operators $O_{[1,0]}$ and $O_{[1,1]}$ as seen in Fig. 7.3(c).
- ⇨ At each sampling step, we either propose a single-site update $P' = P_1 \dots P'_i \dots P_N$, or a two-site update $P' = P_1 \dots P'_i \dots P'_j \dots P_N$, following Algorithm 1. The updated sites i and j are chosen randomly.
- ⇨ We observe (Fig. 7.3(d)) that the effective link operators for P' only differ with those of P on the links that lie on the path from the site i (or j) to the root $[0,0]$-tensor. The number of such links scales only logarithmically in system size. This implies that computing $\langle\psi|P'|\psi\rangle$ can be done very efficiently with a computational cost of $O(\log(N)\chi^4)$, as opposed to $O(N\chi^4)$ for a generic many-body operator for the TTN.

The heart of our efficient sampling procedure lies within the above observation for TTN. We exploit this scaling property to perform efficient Monte Carlo sampling of Pauli strings by standard Metropolis algorithm, where the candidate Pauli string for the next configuration only differs at a few sites with the previous Pauli string configuration. Crucially, the sites can be chosen arbitrarily, and this does not change the $\log N$ scaling of the TTN sampling, provided that the number of modified sites does not scale with system size. This allows for flexible sampling strategy, which can be designed by taking into account our knowledge about the state that we want to sample – very much like Monte Carlo methods are designed to probe partition functions.

The final step for calculating the expectation value of a proposed candidate Pauli string at each Metropolis iteration is the following:

- ⇨ The link operators, that reside in the path from the updated site i (or j) to the root $[0,0]$-tensor, are updated by the coarse-graining step. The expectation value $\langle\psi|P'|\psi\rangle$ is now calculated by tensor contractions of the root tensor and top-most (updated) link operators (see Fig. 7.3(d)).

At this stage, it is important to discuss the efficiency of the more widely used MPS tensor network structure in relation to our sampling strategy. The computational cost for direct sampling of Pauli strings using MPS with OBCs scales as $O(N\chi^3)$ [23, 27, 85], that also holds for Monte Carlo sampling using MPS[2], as opposed to the $O(\log(N)\chi^4)$ that we get utilizing TTN. Consequently, our method with TTN for obtaining SREs becomes increasingly efficient as the number of qudits N grows large, particularly when $N/\log N \gtrsim \chi$. Specifically, since the MPS or the TTN bond dimension χ saturates to a constant value with N in 1D quantum systems with gapped spectrum due to the area-law of entanglement entropy, our approach involving TTN vastly outperforms MPS based methods in terms of efficiency for large N. Most importantly, the enhanced connectedness inherent in the

[2]Using the MPS structure, the cost of each iteration in Monte Carlo sampling using single-site update can be reduced from $O(N)$ to $O(1)$ in N using sequential left $\leftrightarrow$ right sweeps of updates, but this strategy trivially induces exploding autocorrelation time, making it unusable for practical purposes. Moreover, this sequential strategy becomes a real problem for two-site updates that are required for systems that preserves some symmetries (see Sec. 7.3).

TTN structure allows for efficient exploration of higher-dimensional (2D and even 3D) many-body systems (see e.g., [86–90]). This paves the way to investigate SREs in higher-dimensional systems, as we present in Sec. 7.3.

7.3 Application to Quantum Many-Body Systems

We apply the TTN based sampling method in Sec. 7.2.2 using the estimators in Eq. (7.10) and Eq. (7.11) to investigate the SREs in various many-body systems, especially near quantum critical points, both in 1D and 2D geometries. Unlike MPS, the structure of TTN allows for efficient exploration of systems under periodic boundary conditions (PBC) with similar computational cost as the open boundary conditions [41]. Therefore, we consider the periodic many-body systems, i.e., ring and torus geometry in 1D and 2D, respectively, to avoid boundary effects. In our simulations, we have ensured that the SREs have converged with bond dimensions of the TTN in each models.

To obtain the TTN representation of the ground state of many-body systems we perform variational minimization with TTN sweeping algorithm [41, 42], and then employ the sampling scheme in Sec. 7.2.2 to estimate the SREs of the ground state. In particular, since the SREs are generally linear in the number of qudits N, we focus on the SRE densities $m_n = M_n/N$.

All of the models we consider possess $\mathbb{Z}_n$ symmetry, with $n = 2$ or 3, and thus, a two-site update scheme is required to sample only the Pauli strings that preserve the symmetry. The Pauli strings that preserve the $\mathbb{Z}_n$ symmetry, generated by $\prod_i Z_i$, are generated by Z_i and $X_i^\dagger X_j$ (up to a phase constant). Here, X and Z are the shift and clock operators defined in Eq. (7.8) To ensure that only the Pauli strings that obey the $\mathbb{Z}_n$ symmetry are considered, we generate the candidate Pauli string P' by randomly multiplying the current Pauli string P with either Z_i or $X_i^\dagger X_j$. It is easy to see that the update scheme is ergodic. For $d = 3$, we set the probability to multiply with Z_i or $Z_i^\dagger$ to be equal, so as to satisfy detailed balance. For $d = 2$, when there is time-reversal-symmetry, the Pauli strings are additionally constrained to those with even numbers of $Y = iZX$. As such, the Pauli strings with odd numbers of Y can be directly rejected.

7.3.1 Non-stabilizerness in 1D many-body systems

The behavior of SREs in quantum Ising chain in 1D, i.e,

$$H_{\text{1D-Ising}} = -\sum_{\langle i,j\rangle} \sigma_i^x \sigma_j^x - h \sum_i \sigma_i^z, \tag{7.23}$$

with $\sigma^{x,z}$ being the spin-1/2 Pauli matrices, has been studied in Refs. [25, 43], where it has been shown that the SRE densities peak at the critical point $h_c = 1$, and follow universal critical finite-size scaling hypothesis. In Fig. 7.4, we show the results for Rényi-2 SRE M_2, estimated efficiently using the subleading term $c_L = 2M_2(L/2) - M_2(L)$ as described in Sec. 7.2. Surprisingly, the sampling errors of the SRE density m_2 scales slower than $\log L$, with L being the system-size, even at the critical point $h_c = 1$. Therefore, unlike the MPS-based $2n$-replica method employed in Ref. [25] that suffers from a computational cost of $O(\chi^{12})$, our Monte Carlo method for estimating m_2 provides accurate results without being severely limited by χ. Moreover, the computation of m_2 using the perfect sampling of MPS [23, 27]

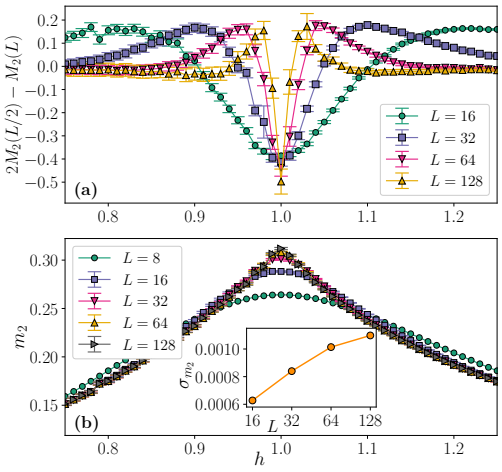

FIGURE 7.4: **Efficient estimation of Rényi-2 SRE density in 1D quantum Ising chain.** (a) The subleading term for the Rényi-2 SRE, $c_L = 2M_2(L/2) - M_2(L)$, directly estimated using the efficient scheme specified in Sec. 7.2, for various system-sizes in 1D quantum Ising chain. (b) The SRE density m_2 for the 1D quantum Ising chain near the critical point $h_c = 1$ computed using the increment method using different subleading terms. (Inset) The sampling errors for m_2 at $h_c = 1$ for various system-sizes L (in log-scale). Clearly, the errors show even slower than than logarithmic growth for the efficient sampling scheme. Here we consider TTN bond dimension $\chi = 30$ and the number of sample is $N_S = 10^6$. Error bars represent 95% confidence interval.

will necessarily incur statistical errors that are exponential in system-size as the direct estimation of the subleading term $c_L = 2M_2(L/2) - M_2(L)$ is not feasible by perfect sampling.

In the following, we extend the studies of SREs in 1D quantum many-body systems to qutrit systems by considering the three-state Clock model and the spin-1 XXZ model in 1D.

Three-state Clock model

The quantum Clock model is a generalization of the quantum Ising model with d states per site. Here we focus on the case $d = 3$, where the Hamiltonian is given by

$$H_{\text{1D-Clock}} = -\sum_{\langle i,j\rangle}(X_i X_j^\dagger + X_i^\dagger X_j) - h\sum_i (Z_i + Z_i^\dagger), \tag{7.24}$$

where X, Z are the shift and clock operators in Eq. (7.24) with $d = 3$. The model is equivalent to the three-state Potts model [91]. There is a transition from the ferromagnetic phase to the paramagnetic phase at $h_c = 1$, as in the quantum Ising model. The critical point is described by Z_3 parafermion CFT, with central charge $c = 4/5$. The exact correlation length exponent is $\nu_{\text{Potts}} = 5/6$ [91]. It is to be noted that, since the system obeys $\mathbb{Z}_3$ symmetry, a two-site update scheme (see Sec. 7.2.2) is required to sample the Pauli strings that preserve the symmetry. Indeed, the Pauli strings that preserve the $\mathbb{Z}_3$ symmetry, generated by $\prod_i Z_i$, are generated by Z_i and $X_i^\dagger X_j$ (up to a phase constant).

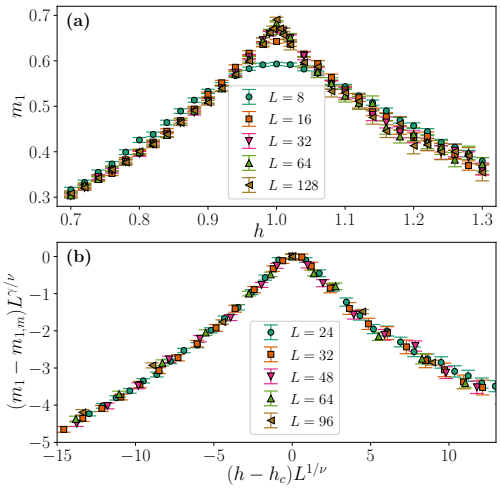

FIGURE 7.5: **Magic density in 1D quantum three-state Clock model.** (a) The SRE density m_1 in the ground-state of the three-state Clock model as a function of h. (b) Finite-size scaling for m_1. Here. $m_{1,m}$ is the maximum m_1 at $h_c = 1$. We extract the critical exponent $\nu \approx 0.844$ and $\gamma \approx 0.66$. The correlation-length exponent ν is close to the known $\nu_{Potts} = 5/6$. We used bond dimension up to $\chi = 36$ and the number of sample is $N_S = 10^6$. Error bars represent 95% confidence interval.

In the three-state Clock model, the magic density displays similar behavior as in the quantum Ising model [25, 43], as shown in Fig. 7.5(a). Namely, m_1 displays maximum at the critical point $h_c = 1$. We further investigate the finite-size scaling of m_1, that has been done for the quantum Ising chain [25], using the finite-size scaling hypothesis:

$$m_1 - m_{1,m} = L^{-\gamma/\nu} f\left(L^{1/\nu}(h - h_c)\right), \tag{7.25}$$

where $m_{1,m}$ is the maximum SRE density at $h_c = 1$. In Fig. 7.5(b), we show the data collapse corresponding to the finite-size scaling relation of Eq. (7.25), where we obtain the critical exponent $\nu \approx 0.844$, close to the expected theoretical value $\nu_{\text{Potts}} = 5/6$.

Spin-1 XXZ chain

Next, we consider a spin-1 XXZ chain with single-ion anisotropy, whose Hamiltonian reads

$$H_{\text{XXZ}} = -\sum_{\langle i,j\rangle}\left[S_i^x S_j^x + S_i^y S_j^y + \Delta S_i^z S_j^z\right] + D\sum_i (S_i^z)^2, \tag{7.26}$$

where S^α's, $\alpha = x, y, z$, are the spin-1 operators, Δ is the easy-axis anisotropy, and D is the single-ion anisotropy. The model has a global $U(1)$ symmetry corresponding to the conservation of total magnetization $\sum_i S_i^z$, and here we consider the scenario of zero total magnetization.

The phase diagram of the model has been studied in previous works [92–95]. For $\Delta > 0$, the model hosts three phases (with increasing D): the antiferromagnetic Néel order, the symmetry-protected topological (SPT) Haldane phase, and the large-D trivial phase. The Néel to Haldane transition is an Ising transition, while the Haldane to large-D transition is a Gaussian transition.

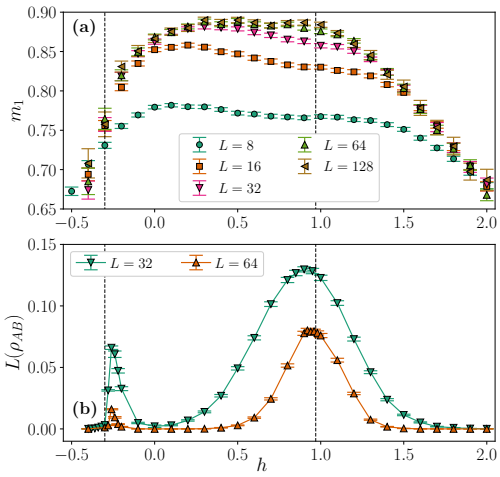

FIGURE 7.6: **Magic density and long-range magic in spin-1 XXZ chain.** (a) the magic density m_1 and (b) long-range magic $L(\rho_{AB})$ of the ground-state of the spin-1 XXZ model with $\Delta = 1$ as a function of D. We consider bond dimension up to $\chi = 60$ and the number of sample is $N_S = 10^6$. Error bars represent 95% confidence interval. The dashed vertical lines represent the best estiamtes available for the transition points.

Here, we focus on the isotropic case, i.e., $\Delta = 1$. In this case, the transition is known to be at $D \sim -0.3$ and $D \sim 0.97$ for Néel-Haldane and Haldane-large D transitions, respectively [93–95]. Fig. 7.6(a) shows the SRE density m_1. We observe that m_1 is large and rather constant in the topological Haldane phase, while it becomes smaller in the neighboring phases. Note that the maximum value of m_1 for a product state is $\frac{2}{3}\log(4) \approx 0.92$, achieved by the tensor product of single-qutrit states, each of which has $\langle P\rangle^2 = 1/4$ for all $P \neq I$. Thus, it is seen that the magic in the SPT Haldane phase almost saturates the maximum value.

Long-range SRE

In the spin-1 XXZ chain, while the onset of the topological Haldane phase is rather apparent from the magic density, there is no clear peak at the transitions, rendering the determination of the critical point difficult. Here we show that, unlike the magic density, the long-range magic L_{AB} (see Eq. (7.5)), using the estimators in Eq. (7.20) and Eq. (7.21), can be used as a faithful indicator of quantum phase transitions. For the analysis of L_{AB}, we consider the spatially separated, extended subsystems $A = \{1, 2, ..., L/4\}$ and $B = \{L/2 + 1, ..., 3L/4\}$ in a perioidic chain of L sites, as depicted in Fig. 7.2b.

The long-range magic, for the the spin-1 XXZ chain, as plotted in Fig. 7.6(b) shows clear extremums at the two transitions. Although $L(\rho_{AB})$ is still non-zero for small L away from criticality, it quickly decays to zero as the system size is increased. The peak at the Gaussian transition is very close to $D \sim 0.97$, as obtained with DMRG up to $L = 20000$ spins [94]. Notably, our results are obtained with only moderate sizes, and without any prior knowledge of the order parameter. At the Ising transition, the extremum occurs at a negative value as a minimum. Unlike entanglement, the SRE is not known to satisfy subadditivity, meaning that it is not always the case that

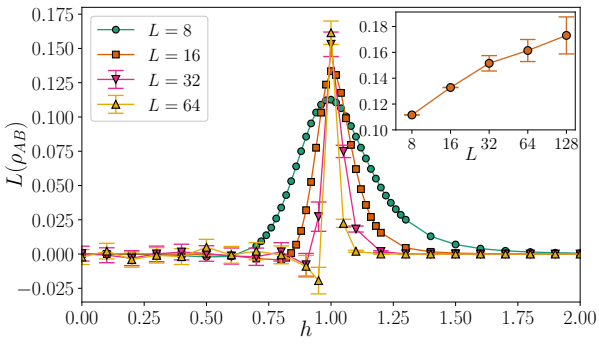

FIGURE 7.7: **Long-range magic in 1D quantum Ising chain.** The long-range magic $L(\rho_{AB})$ as in Eq. (7.5) in the ground state of 1D quantum Ising chain as a function of the transverse field h. It peaks at the critical point $h_c = 1$. (Inset) $L(\rho_{AB})$ at $h_c = 1$ for various system sizes L (in log-scale). We consider TTN bond dimension up to $\chi = 30$ and the number of sample is $N_S = 10^6$. Error bars represent 95% confidence interval.

$L(\rho_{AB}) \geq 0$. Nevertheless, the non-trivial value at criticality is a useful indicator for detecting criticality.

The decay of long-range SRE away from criticality can be understood through a simple physical argument. Within a gapped phase characterized by a finite correlation length, when considering two subsystems A and B separated by a distance exceeding the correlation length, A and B are approximately uncorrelated. More formally, $\rho_{AB} \approx \rho_A \otimes \rho_B$, which implies $L(\rho_{AB}) \approx 0$. In contrast, at criticality, the correlation length becomes infinite, such that A and B are always correlated regardless of their distance. This results in a non-trivial value of $L(\rho_{AB})$.

We also come back to the quantum Ising chain (Eq. (7.23)), and investigate the long-range magic across the Ising transition. We observe that $L(\rho_{AB})$ peaks at the critical point, as shown in Fig. 7.7. Furthermore, we plot $L(\rho_{AB})$ at $h_c = 1$ in the inset of Fig. 7.7, where we see that the long-range magic grows logarithmically in L. In contrast, $L(\rho_{AB})$ quickly decays away from criticality (not shown). We note that, at the critical point, we observe long autocorrelation times between samples, which is the reason for the growing errors for larger sizes. This is reminiscent of the problem of critical slowing-down in the Monte Carlo simulations at criticality [96]. It is thus interesting to develop a cluster update, akin to Wolff cluster update [97], that may overcome this issue, which we leave for future studies.

7.3.2 SRE density in 2D many-body systems: $\mathbb{Z}_2$ lattice gauge theory

Based on the favourable scaling of our scheme with system size, we investigate the non-stabilizerness in 2D systems, which so far have not been properly explored in the literature. In particular, we consider a $\mathbb{Z}_2$ lattice gauge theory, with Hamiltonian:

$$H_{\mathbb{Z}_2\text{-Gauge}} = -h \sum_{\square} \prod_{i \in \square} \tau_i^x - \sum_i \tau_i^z, \tag{7.27}$$

where the spin-1/2 Pauli operators, τ^α, $\alpha = x, z$, live on the links of the square lattice. The first term is the plaquette term that flips the four spins on an elementary square plaquette of the lattice. We are interested in the charge-free sector, that satisfies the

Gauss' law

$$\prod_{i\in+}\tau_i^z = 1, \tag{7.28}$$

on each vertices of the lattice. It is well known that the Hamiltonian in Eq. (7.27) is dual to the 2D transverse-field Ising model on the square lattice

$$H_{\text{2D-Ising}} = -\sum_{\langle i,j\rangle}\sigma_i^x\sigma_j^x - h\sum_i\sigma_i^z. \tag{7.29}$$

by Wegner duality [98]. Here, the spin-1/2 Pauli operators, σ^α, $\alpha = x, z$, live on the lattice sites of the dual square lattice. We will first show that the duality transformation preserves SREs.

Equivalence of the SRE in 2D $\mathbf{Z}_2$ gauge theory and the 2D transverse-field Ising model

The duality transformation between Eq. (7.27) and Eq. (7.29) is defined with the following transformation,

$$\begin{aligned}\sigma_i^x\sigma_j^x &= \tau_{\langle ij\rangle}^z\\ \sigma_i^z &= \prod_{i\in\square}\tau_i^x.\end{aligned} \tag{7.30}$$

More precisely, the transformation maps the charge-free sector of Eq. (7.27) to the even sector of Eq. (3.9). This mapping also sheds light on the transition point of the 2D $\mathbf{Z}_2$ gauge theory, which is precisely mapped to the transition point of the Ising model: there, the transition from ferromagnetic phase to the paramagnetic phase is known to be at $h_c \simeq 3.04$, as obtained with Quantum Monte Carlo [99]. In the lattice gauge theory framework, such transition corresponds to confined to deconfined transition, where the behavior of Wilson loops turns from area to perimeter law.

It is easy to see that the mapping in Eq. (7.30) maps Pauli strings in the Ising model to Pauli strings in $\mathbf{Z}_2$ gauge theory, because the Pauli operators on both sides of the equation generate the Pauli group in the corresponding models. Since the SREs depend only on the expectation values of Pauli strings, it follows that the SREs are preserved by the duality transformation. Therefore, the SREs in the Ising model are identical to the SREs in $\mathbf{Z}_2$ gauge theory, up to a constant shift. It should be, however, noted that equivalence relation in case of the subsystem mixed-state SRE (e.g., $\tilde{M}_2$ defined in Eq. (7.3)), and the long-range magic thereof, is non-trivial because of the non-local nature of the transformation (7.30). Consequently, the distribution of magic within the subsystems may differ in these two theories.

It is worth nothing that the same conclusion evidently holds for other dualities that map Pauli strings to Pauli strings, such as the Kramers-Wannier duality which maps $h \to h^{-1}$ in Eq. (7.23) and Eq. (7.24). As previously discussed, the long-range magic is not preserved under the duality. This is reflected in the distinct behavior of $L(\rho_{AB})$ for $h > 1$ and $h < 1$ in Fig. 7.7.

Numerical results

The duality above enables us to compute the SREs of the the $\mathbb{Z}_2$ gauge theory (7.27) by considering the ground state of the transverse-field Ising model, which is

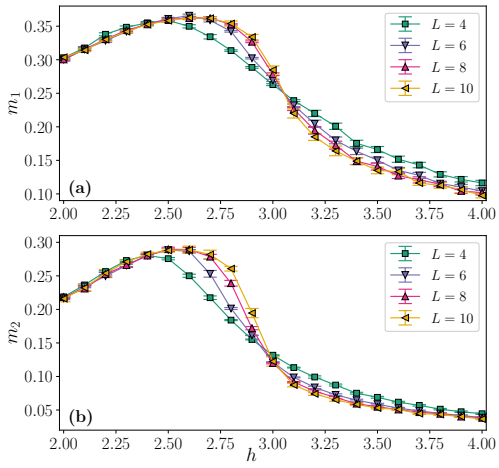

FIGURE 7.8: **Magic densities in 2D $\mathbb{Z}_2$ gauge theory.** The SRE desnities (a) m_1 and (b) m_2 of the ground-state of $\mathbb{Z}_2$ gauge theory on $L \times L$ square lattice as a function of h. We use TTN bond dimension up to $\chi = 60$ and the number of sample is $N_S = 10^6$. Error bars represent 95% confidence interval.

computationally more convenient for TTNs. In the following, we discuss the numerical results on the behavior of the SREs around the critical point of the 2D transverse-field Ising model.

The results for magic density for $n = 1, 2$ are presented in Fig. 7.8. It is seen that both quantities detect the transition. However, the observed behavior is very different from the 1D quantum Ising chain, which exhibits a peak at the transition. Instead, here we observe that the curves exhibit crossings at the transition.

In Fig. 7.9(a), we depict m_1 close to the critical point, using a fixed bond dimension $\chi = 30$. Remarkably, we observe that m_1 detects the transition point very well: all the curves cross near the critical point at $h_c = 3.04(1)$. We should highlight at this point that the TTN ansatz with such a low bond dimension of $\chi = 30$ can not approximate the ground state wave function accurately near the critical point, particularly in 2D critical systems. Consequently, the standard phase transition detectors, such as the Binder cumulant, calculated from the TTN state with $\chi = 30$, do not exhibit the expected critical crossing behavior. Therefore, the remarkable observation of the perfectly crossing behavior in m_1 near the critical point underscores the significant value of magic in detecting and characterizing quantum phase transitions. This is particularly relevant in situations where other quantities are prone to significant errors, e.g., due to limited bond dimensions in tensor network states. While we believe that a further characterization of what the scaling resources (e.g., size and bond dimension) to detect a transition point are is outside the scope of our paper, this would be very much worth pursuing based on the Ising model results we presented.

Furthermore, we show excellent data collapse for m_1 in Fig. 7.9(b), using the finite-size scaling relation of Eq. (7.25), from which we extract the correlation length exponent $\nu = 0.64 \pm 0.05$, that is close to the known $\nu_{3D} = 0.63$ for 3D (classical) Ising universality [99].

Comparison with Binder cumulant

We have demonstrated the ability of the magic density to accurately detect and characterize the quantum critical point in the 2D quantum Ising model, and thereby

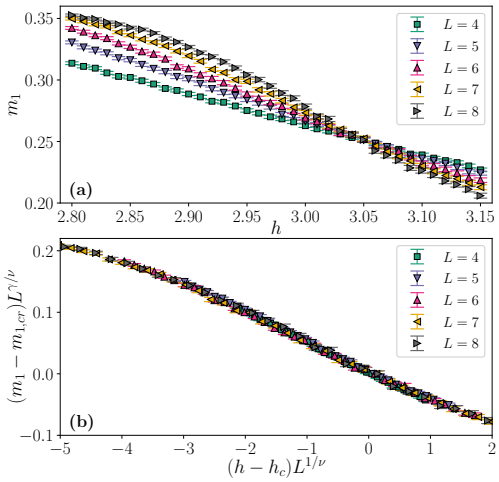

FIGURE 7.9: **Finite-size critical scaling of SRE density in 2D $\mathbb{Z}_2$ gauge theory.** (a) The SRE density m_1 near the critical point at the $\mathbb{Z}_2$ gauge theory. Even with small TTN bond dimension $\chi = 30$, m_1 captures the transition very well: all the curves cross near the known critical point $h_c = 3.04$. (b) Finite-size scaling of m_1. Here, $m_{1,cr}$ is m_1 at $h = 3.04$. We find the correlation length critical exponent $\nu = 0.64 \pm 0.05$. The extracted ν is remarkably close to the known $\nu_{3D} \simeq 0.63$ for 3D Ising universality class. Here, the number of samples is $N_S = 10^7$.

in 2D $\mathbb{Z}_2$ gauge theory. Notably, the curves of m_1 for different linear system-sizes exhibit a clear critical crossing behavior near the critical point $h_c = 3.04$, even with a modest TTN bond dimension of $\chi = 30$. However, the same level of accuracy is not achieved when utilizing the Binder cumulant, defined as

$$U = 1 - \frac{\langle s_x^4 \rangle}{3\langle s_x^2 \rangle^2}, \quad \text{with } s_x = \frac{1}{L^2}\sum_i \sigma_i^x, \tag{7.31}$$

for the 2D Ising model (3.9). Due to the inability of the TTN state with a small bond dimension of $\chi = 30$ to faithfully represent the ground state in the vicinity of the critical point, the calculation of the Binder cumulant U yields erroneous results. Consequently, the curves of U for different linear system-sizes L do not exhibit a clear crossing behavior near the critical point (Fig. 7.10). For instance, while the curves for $L = 4$ and 5 intersect at $h = 2.98$, the intersection for $L = 7$ and 8 occurs around $h = 3.14$. As such, if one attempts to perform finite size scaling on the Binder cumulant data, the resulting critical point and the correlation-length critical exponent ν will be erroneous.

7.3.3 Autocorrelations and statistical errors

Here, we analyzed the statistical errors and the autocorrelation times in the Markov chain samples. We consider the integrated autocorrelation time of m_1 and m_2 close to the critical point of the 2D transverse-field Ising model at $h = 3$. The integrated autocorrelation time is defined as $\tau_I = 1 + 2\sum_{t=1}^{\infty} \rho(t)$, where $\rho(t)$ is the autocorrelation function. The integrated autocorrelation time affects the statistical errors of the averages obtained from Monte Carlo sampling [100]. We observe that τ_I is linear for

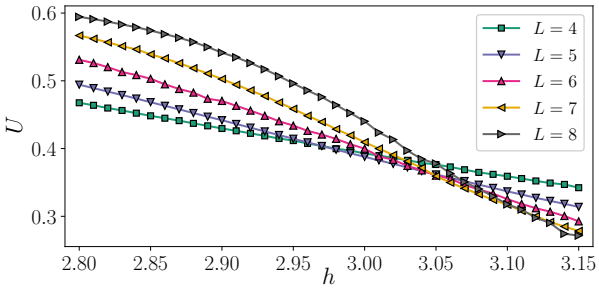

FIGURE 7.10: **The Binder cumulant across the critical point in the 2D quantum Ising model.** Here we approximate the ground state of 2D quantum Ising model with TTN having bond dimension $\chi = 30$, in parity with Fig. 7.9.

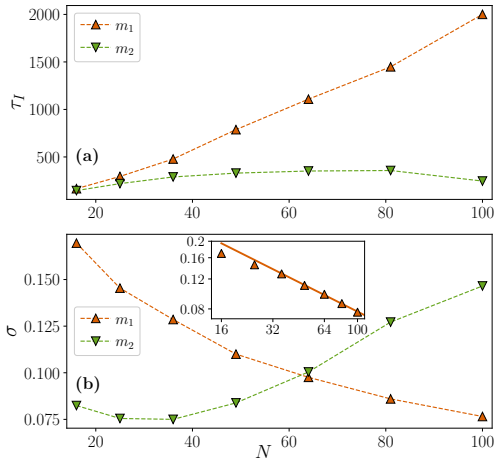

FIGURE 7.11: **Autocorrelation time and statistical errors in Monte Carlo sampling of SREs.** (a) Integrated autocorrelation time τ_I at the ground state of 2D transverse-field Ising model with $h = 3$ for various system sizes $N = L \times L$. It is linear for m_1 and saturates for m_2. (b) Standard deviation σ for various system sizes. Inset shows σ for m_1 in log-log scale. The solid line denotes a fit $\sigma = aN^{-b}$ for $L \geq 6$, with $b = 0.503$. The standard deviation is obtained by error propagation.

M_1, while it saturates for M_2, as shown in Fig. 7.11(a). We have also checked that τ_I does not show much variation with respect to bond dimension.

Moreover, the standard deviation σ for various system sizes is shown in Fig. 7.11(b). For $n = 2$, it is seen that σ grows exponentially, confirming the analysis in Sec. 7.2. On the other hand, for $n = 1$, σ is decreasing with power-law behavior (see inset). The power-law exponent is found to be compatible with $1/2$, again as anticipated in Sec. 7.2. We note here that the behavior of the integrated autocorrelation time and the standard deviations remains qualitatively similar near the critical points for other many-body systems considered here.

7.4 Experimental protocol

The numerical method described above can be easily adapted for experimental measurements of SREs. In particular, we can sample Pauli strings according to Ξ_P

using Monte Carlo sampling. We note that, although the probability distribution Ξ_P can be sampled directly through measurements in the Bell basis [37, 101], the method requires preparation of two copies of a state and joint operations on them. In practice, this may not be feasible in some experimental platforms, or difficult to scale up to larger sizes and higher-dimensional systems. Moreover, the method only works for real wavefunctions [20]. Instead, our proposal relies solely on measurements in the computational basis on a single instance of a state, and it is applicable to generic quantum states.

In experiments, the Pauli strings are measured from N_M copies of ρ where the measurement outcomes are $A_i \in \{+1, -1\}$. The expectation value is then given by the average taken over the random measurement outcomes. The sampling of Pauli strings can be performed with Metropolis algorithm, similar to our numerical calculations. However, it is important to note that in experimental setups, the candidate Pauli string is not restricted to few-site updates, as is the case of TTN. This flexibility allows for multi-site updates and can potentially reduce the autocorrelation time associated with the sampling process enormously.

For a finite number of measurements N_M, we have that

$$\bar{P} = \frac{1}{N_M} \sum_{i=1}^{N_M} A_i \tag{7.32}$$

is an estimate for $\langle P \rangle$. The total number of resources is thus $N_M \times N_S$, where N_S is the number of sampled Pauli strings. In view of Eq. (7.14), when the SREs are at most $O(\log N)$, the required N_S is polynomial in N. Note that N_M may still be exponential, but it is expected to be no larger than $O(d^N)$, with d being the local dimension. As a result, the number of resource required in our protocol is significantly lower than the protocol in Ref. [38] when the SREs are at most $O(\log N)$. Moreover, our protocol offers a possibility to measure M_1, in which case N_S is always polynomial[3].

The variance of the estimator in Eq. (7.32) is given by $\mathrm{Var}(P) = 1 - \langle P \rangle^2$. Thus, the standard error reads

$$\Delta P = \sqrt{\frac{1 - \langle P \rangle^2}{N_M}}. \tag{7.33}$$

For large N_M, the random variable $\bar{P}$ approximately has a Gaussian distribution with average $\langle P \rangle$ and standard deviation ΔP. Note that this will introduce bias to the estimators in Eq. (7.10) and Eq. (7.11). This bias can be made smaller by increasing N_M, where the estimators become unbiased in the limit $N_M \to \infty$.

Here, we simulate this situation numerically by perturbing the computed $\langle P \rangle$ with ϵ, where ϵ is a random number chosen from a Gaussian distribution centered at zero and with standard deviation ΔP. We would like to investigate the effects of taking finite N_M and N_S. Here, we consider the ground state of 1D transverse-field Ising chain at $h = 1$ for concreteness. An example of the results of such a protocol is shown in Fig. 7.12 for $L = 8$ with $N_M = 500$ and $N_S = 10000$.

[3]It is to be noted that the measurement of M_n with $n \neq 1$ in experiments by employing the increment scheme with subleading terms, as discussed in Sec. 7.2, can be challenging. This procedure necessitates the simultaneous sampling from two distinct physical systems, something that is easily achievable on some platforms (optical lattices, circuit QED, tweezer arrays) but not immediately on others (e.g., ion chains). Furthermore, in experimental measurements, the obtained expectation values are only approximations of the true values. Consequently, computing ratios of these approximate values, as in Eq. (7.22), introduces errors into the calculations.

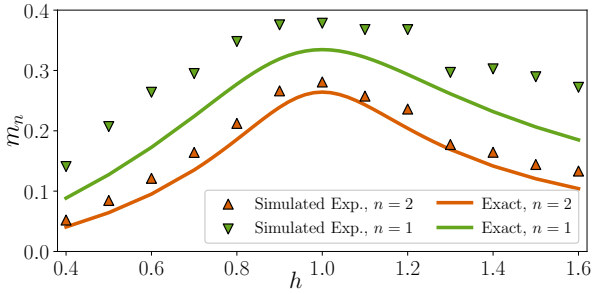

FIGURE 7.12: **Simulated experiment to measure SREs.** Simulation of experimental measurement of SREs in the ground state of 1D quantum Ising chain for $L = 8$. Here, $N_M = 500$ and $N_S = 10^4$.

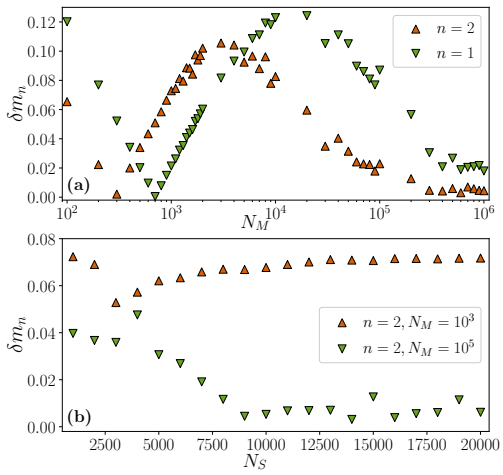

FIGURE 7.13: **The errors in SRE density for simulated experiments.** The deviation $\delta m_n = |m_{n,\text{Sim.Exp.}} - m_{n,\text{exact}}|$ for $n = 1, 2$ in the ground state of 1D quantum Ising chain at the critical point $h = 1$ for $L = 16$. In (a), we fix $N_S = 10000$ and vary N_M, while in (b), we fix $N_M = \{10^3, 10^5\}$ and vary N_S.

Next, we compute the deviation $\delta m_n = |m_{n,\text{Sim.Exp.}} - m_{n,\text{exact}}|$ for $n = 1, 2$, where $m_{n,\text{Sim.Exp.}}$ denotes the SRE density in simulated experiments. The results are shown in Fig. 7.13. We see that, for fixed N_S, the error first increases for small N_M, before it eventually decreases. We expect this is due to the bias with finite number of Pauli measurements, as mentioned above. Indeed, as shown in Fig. 7.13(b), we see that increasing N_S while fixing N_M does not result in vanishing δm_n.

7.5 Conclusions and outlook

We have proposed a Markov chain Monte Carlo approach to compute magic in many-body systems. We have discussed how the full state magic M_n can be estimated for different values of n, and demonstrated the corresponding efficiency in several scenarios. Moreover, long-range magic can be estimated efficiently in general. The implementation of our algorithm is flexible and compatible with various wave-function based methods. Specifically, we have provided detailed insights into the efficiency and flexibility of our method when applied to tree tensor networks.

Through our algorithm's flexibility, we have gained valuable insights into the role of magic in many-body systems. In one-dimensional systems, we observed that full state magic is not universally associated with critical behavior. While it displays criticality signatures in certain cases like Ising and Potts models, it does not in others. However, long-range magic overcomes this limitation and consistently exhibits indications of critical behavior across all scenarios we investigated. We speculate that the functional form of long-range magic, similar to mutual information, is free of potential UV-divergences in a field theory framework.

The very mild volume scaling cost of our sampling has also enabled us the exploration of two-dimensional $\mathbb{Z}_2$ lattice gauge theories. There, we have found that magic displays finite-volume crossings in correspondence of the confined-deconfined phase transition, and it also follows universal scaling behavior up to the volumes (100 spins) we were able to treat. Remarkably, magic was well converged even at modest bond dimensions.

Our numerical results suggest a deep connection between (long-range) magic and many-body properties, highlighting the direct links between stabilizer Renyi entropies and physical phenomena such as quantum critical behavior and confinement-deconfinement transitions. To complement our theoretical findings, we have proposed an experimental protocol for measuring stabilizer Renyi entropies solely using measurements in the computational basis.

In terms of future investigations, our technique can be extended to explore non-stabilizerness in finite-temperature scenarios by generalizing it to tree-tensor operators that efficiently represent low-temperature many-body states. In particular, it would be interesting to study the behavior of stabilizer Renyi entropies at finite-temperature phase-transition and compare it with other information-theoretic quantities, such as entanglement [102–105], quantum discord [106], and quantum coherence [107]. Along the same lines, another possible scenario would be applying our tools to faulty quantum circuits, recently discussed in the context of magic in Ref. [108]. It would also be instructive to perform a systematic investigation of magic within topological phases, extending our analysis of the Haldane phase. Another interesting perspective is to understand the role of magic in many-body quantum dynamics of closed quantum systems, whose investigation in the context of Ising models has been the subject of recent works [109]. In particular, our method allows for the investigation of genuine long-distance magic, that might be instrumental in establishing the presence or absence of propagation bounds for magic.

At the methodological level, our work opens a series of questions. The Markov chain Monte carlo approach could be extended to investigate other magic measures that depend only on expectation values, such as mana. Moreover, so far, we have only employed very basic sampling strategies. It would be worth exploring how different ones, such as heatbath or non-local updates, can be used to design better magic estimators since, in terms of experimental applicability, having shorter autocorrelations could considerably improve realistic implementations. In terms of efficiency of the increment trick in 2D models, it would be interesting to study whether a one-dimensional projection of 2D systems such as the one introduced in [110] would be beneficial. Finally, it would be interesting to understand the finer structure of sampling Pauli strings in many-body systems, that could reveal both useful insights into novel algorithms, and potentially deeper connections between many-body properties and magic.

Chapter 8

Critical behaviors of nonstabilizerness in quantum spin chains

Recent studies have established that nonstabilizerness is directly linked with entanglement and Shannon (or participation) entropy [111, 112]. Specifically, it was found that the entanglement spectrum flatness (in any bipartition) [111] and participation entropy flatness [112] is directly related to the stabilizer linear entropy [19]. Both mutual information (of entanglement) and Shannon mutual information have been shown to display the scaling relation [63, 113–118]

$$I = \frac{c}{4} \log \left[\frac{L}{\pi} \sin\left(\ell \frac{\pi}{L}\right) \right] + \gamma \tag{8.1}$$

in critical spin chain governed by conformal field theory (CFT) on a periodic chain. Here ℓ is the subsytem size, c is the central charge of the CFT, and γ is a non-universal constant. Given the connections mentioned above, it becomes natural to question whether the corresponding mutual information of nonstabilizerness exhibits similar scaling behavior as in Eq. (8.1).

Addressing this question poses significant challenges. Firstly, directly evaluating nonstabilizerness becomes increasingly difficult for larger systems (especially since in principle Eq. (8.1) holds only for $\ell, L \gg 1$). Secondly, quantifying nonstabilizerness in mixed states, necessary for studying subsystems, is significantly more difficult compared to pure states. Previous studies on nonstabilizerness have been restricted to very small sizes [50, 52], or relied on a nonstabilizerness monotone restricted to pure states [23, 25, 28, 29, 33, 119]. To overcome these hurdles, this work focuses on quantum critical spin chains with odd on-site Hilbert space dimension. In such systems, there exists a strong measure of nonstabilizerness known as mana [17, 120]. Mana quantifies the nonstabilizerness for both pure states and mixed states, and its definition does not employ minimization procedures, making it the perfect choice to address the above question on scaling behavior of nonstabilizerness in critical systems. We leverage this advantage to investigate the behavior of mana in quantum critical spin chains governed by CFT.

Prior investigations of mana have been limited to very small systems up to $L = 6$ sites [50, 121]. This work significantly expands the capability of evaluating mana in substantially larger systems. To achieve this, we first introduce a Rényi generalization of mana, which we call mana entropies. These quantities are also measures of nonstabilizerness for pure states, although unlike mana they are not good measures for mixed states. We then construct a classical statistical mechanics systems derived from the discrete Wigner function, such that the computation of mana can be recast

as a free energy calculation. We then show how this can be done by thermodynamics integration. Finally, we introduce the mutual mana and study its scaling in CFT.

Our results demonstrate that the mana is significant at the critical point, and it exhibits a finite-size scaling. Moreover, we find that the mutual mana scales linearly with $\log\left[\frac{L}{\pi}\sin\left(\ell\frac{\pi}{L}\right)\right]$, analogous to entanglement and Shannon entropy. Additionally, we show that the mutual mana instead saturates in gapped phases, thus showing the capability of the mutual mana to distinguish between critical and non-critical behavior. Our results highlight the difficulty of removing the nonstabilizerness in CFT with finite-depth quantum circuits, and in turn in classically simulating CFT.

The rest of the chapter is structured as follows. In Sec. 8.1, we briefly cover some key preliminaries to provide the necessary background for introducing the nonstabilizerness monotone mana. In Sec. 8.2, we introduce the Rényi generalizations of mana called the mana entropy, which themselves are new measures of nonstabilizerness for pure states, and in Sec. 8.3 we present a thermodynamics view on the mana entropy, such that the computation of mana can be recast in the language of classical statistical mechanics. In Sec. 8.4, we introduce the notion of mutual mana, and present a scalable method to compute them. In Sec. 7 we review the numerical method that we employ. In Sec. 8.5 we introduce the model under study and in Sec. 8.6 we present our numerical results, both on the mana and mutual mana. Finally, we conclude in Sec. 8.7.

8.1 Preliminaries

Mana is a measure of non-stabilizerness that is only defined in terms of expectation values of operators, and is thus one of measures of non-stabilizerness that is relatively easy to compute. However, mana is only well-defined for systems of odd prime power dimensions. To define mana, we first define the shift and clock operators as

$$X = \sum_{k=0}^{d-1} |k+1\rangle\langle k| \quad \text{and} \quad Z = \sum_{k=0}^{d-1} \omega_d^k |k\rangle\langle k|, \tag{8.2}$$

where $\omega_d = e^{2\pi i/d}$. Here, the addition is defined modulo d. They satisfy the commutation relation $XZ = \omega ZX$.

The generalized Pauli operators (also known as the Heisenberg-Weyl operators) are defined as

$$T_{aa'} = \omega^{-2^{-1}aa'} Z^a X^{a'} \tag{8.3}$$

for $a, a' \in \mathbb{Z}_d$. Here, 2^{-1} is the inverse element of 2 in $\mathbb{Z}_d$. For a system of N qudits, the Pauli strings are

$$T_{\mathbf{a}} = T_{a_1,a_1'} T_{a_2,a_2'} ... T_{a_N,a_N'}. \tag{8.4}$$

We denote the group of all N-qudit Pauli strings as $\mathcal{P}_N$.

Next, the phase-space point operators are defined in terms of the Pauli strings as

$$A_{\mathbf{0}} = \sum_{\mathbf{u}} T_{\mathbf{u}}, A_{\mathbf{u}} = T_{\mathbf{u}} A_{\mathbf{0}} T_{\mathbf{u}}^\dagger. \tag{8.5}$$

These operators are Hermitian with eigenvalues 1 and -1, with multiplicity $\frac{d+1}{2}$ and $\frac{d-1}{2}$, respectively. Moreover, they are orthogonal, i.e, $\mathrm{Tr}(A_{\mathbf{a}} A_{\mathbf{b}}) = d^N \delta(\mathbf{a}, \mathbf{b})$, and thus they provide an orthogonal basis for an operator in $\mathbb{C}^{d^N \otimes d^N}$. Thus, one can

expand the density matrix ρ of a state (pure or mixed) as

$$\rho = \sum_{\mathbf{u}} W_\rho(\mathbf{u}) A_{\mathbf{u}}. \tag{8.6}$$

where $W_\rho(\mathbf{u})$ is known as the discrete Wigner function [122, 123], a discrete analogue of the infinite-dimensional Wigner function [124]. Equivalently, we can write

$$W_\rho(\mathbf{u}) = \frac{1}{d^N} \mathrm{Tr}(A_{\mathbf{u}}\rho). \tag{8.7}$$

The Wigner functions satisfy the following relations

$$\sum_{\mathbf{u}} W_\rho(\mathbf{u}) = 1 \tag{8.8a}$$

$$\sum_{\mathbf{u}} W_\rho(\mathbf{u})^2 = e^{-S_2}/d^N, \tag{8.8b}$$

where S_2 is the 2-Rényi entropy.

Finally, mana is defined in terms of the Wigner functions as

$$\mathcal{M}(\rho) = \log\left(\sum_{\mathbf{u}} |W_\rho(\mathbf{u})|\right). \tag{8.9}$$

Due to the normalization condition in Eq. (8.8a), mana measures the negativity of the Wigner representation of ρ. For pure states, the set of states with positive Wigner representation is exactly the set of pure stabilizer states [122], in which case the mana vanishes. For mixed states, the set of states with positive Wigner representation is strictly larger than the convex hull of stabilizer states. Nevertheless, it is shown that states with positive Wigner representation (including those outside of the convex hull of stabilizer states) cannot be distilled [120], and moreover they are efficiently simulatable [125]. In fact, mana directly quantifies the cost of classical simulation based on Monte Carlo in Ref. [125]. Thus, mana is a useful measure to quantify the resources required for classically simulating a quantum circuit, both for pure and mixed states [17].

Crucially, mana stands out as the only known strong nonstabilizerness monotone whose definition bypasses the need for minimization procedures (Eq. (8.9)), both for pure and mixed states. This offers a significant computational advantage compared to other monotones. However, calculating mana still incurs an exponential cost as it necessitates computing the discrete Wigner function, $W_\rho(\mathbf{u})$, for all possible $\mathbf{u} \in \mathbb{Z}_d^N$. This exponential scaling renders direct calculation impractical for large systems, a key challenge that we would like to address in this work.

8.2 Rényi generalizations of mana: mana entropy (ME)

In order to compute mana, we find it useful to introduce Rényi generalizations of mana, following closely the definition of stabilizer Rényi entropies (SREs). We restrict to the case of pure states, where $\Pi_{|\psi\rangle}(\mathbf{u}) = d^N W_\rho(\mathbf{u})^2$ can be interpreted as a probability distribution (see Eq. (8.8b)), thus bearing similarity to $\Xi_{|\psi\rangle}(\mathbf{u})$. We now consider the n-Rényi entropies associated to this probability distribution in the same

spirit as the SREs, as

$$\begin{aligned}\mathcal{M}_n &= \frac{1}{1-n}\log\sum_{\mathbf{u}}\left(d^N W_\rho(\mathbf{u})^2\right)^n - N\log d \\ &= \frac{1}{1-n}\log\sum_{\mathbf{u}}\frac{\left|\tilde{W}_\rho(\mathbf{u})\right|^{2n}}{d^N}\end{aligned} \tag{8.10}$$

where we define $\tilde{W}_\rho(\mathbf{u}) := d^N W_\rho(\mathbf{u}) = \langle A_\mathbf{u}\rangle$. Comparing this with Eq. (6.23), we see that MEs are just SREs with the Pauli operators replaced by the phase-space point operators in Eq. (8.5). It follows that the MEs possess similar properties as SREs, namely (i) faithfulness, (ii) stability under Clifford unitaries, and (iii) additivity. Moreover, they are upper bounded by $\mathcal{M}_n \leq N\log d$.

Notice that the index $n = 1/2$ corresponds to mana of pure states (up to a prefactor of 2). Mana has been rigorously proven to obey both monotonicity and strong monotonicity under stabilizer operations, making it a genuine measure of nonstabilizerness, also for mixed states [17]. In contrast, SREs of all index have been shown to violate strong monotonicity, while SREs of index $0 < n < 2$ violate monotonicity [23]. It is presently unclear if such monotonicity property holds for MEs of index $n \neq 1/2$, a question that we leave for future investigations. Nonetheless, they could be useful to provide non-trivial bounds for other known measures of nonstabilizerness. Moreover, while the computational cost to compute the mana grows exponentially in N, MEs of integer indices $n > 1$ can be efficiently computed in matrix product states (MPS) with replica trick in the same way as SREs [25, 26]. The same technique can also be used to obtain analytical results [33], which may be analytically continued to $n = 1/2$ to obtain the mana.

8.2.1 Mana entropy and stabilizer Rényi entropy

Interestingly, we find that the mana entropy and SRE is equivalent under some symmetry conditions, through the following proposition:

Proposition: *Let $|\psi\rangle$ be an N-qudit pure state. If $A_\mathbf{b}$ is a phase-space operator such that $A_\mathbf{b}|\psi\rangle = \lambda|\psi\rangle$, where $\lambda \in \{+1, -1\}$, then*

$$\lambda\langle\psi|A_{\mathbf{a}+\mathbf{b}}|\psi\rangle = \langle\psi|T_{2\mathbf{a}}|\psi\rangle\omega^{2(\mathbf{b}\mathbf{a}'-\mathbf{b}'\mathbf{a})} \tag{8.11}$$

for all $\mathbf{a} \in \mathbb{Z}_d^{2N}$.

Proof. We will first prove that the following equation holds:

$$A_{\mathbf{a}+\mathbf{b}}A_\mathbf{b} = T_{2\mathbf{a}}\omega^{2(\mathbf{b}\mathbf{a}'-\mathbf{b}'\mathbf{a})} \tag{8.12}$$

Firstly, we note that $A_\mathbf{a}$ can be written as

$$A_\mathbf{a} = \frac{1}{d^N}\bigotimes_{i=1}^{N}\sum_{b,b'}\omega^{a_i b' - a_i' b}T_{b,b'} \tag{8.13}$$

The action of $A_{\mathbf{a}}$ on a basis state $|\sigma\rangle$ is

$$\begin{aligned} A_{\mathbf{a}}|\boldsymbol{\sigma}\rangle &= \frac{1}{d^N}\prod_{i=1}^{N}\sum_{b_i,b_i'}\omega^{a_i b_i' - a_i' b_i}T_{b_i,b_i'}|\sigma_i\rangle \\ &= \frac{1}{d^N}\prod_{i=1}^{N}\sum_{b_i,b_i'}\omega^{a_i b_i' - a_i' b_i}\omega^{-2^{-1}b_i b_i'}Z^{b_i}X^{b_i'}|\sigma_i\rangle \\ &= \frac{1}{d^N}\prod_{i=1}^{N}\sum_{b_i,b_i'}\omega^{a_i b_i' - a_i' b_i + b_i(\sigma_i + 2^{-1}b_i')}|\sigma_i + b_i'\rangle \\ &= \prod_{i=1}^{N}\sum_{b_i'}\omega^{a_i b_i'}\delta_{\sigma_i + 2^{-1}b_i' - a_i',0}|\sigma_i + b_i'\rangle \\ &= \omega^{2\mathbf{a}(\mathbf{a}'-\boldsymbol{\sigma})}|2\mathbf{a}' - \boldsymbol{\sigma}\rangle. \end{aligned} \tag{8.14}$$

On the other hand, the action of $T_{\mathbf{a}}$ is

$$\begin{aligned} T_{\mathbf{a}}|\boldsymbol{\sigma}\rangle &= \prod_{i=1}^{N}T_{a_i,a_i'}|\sigma_i\rangle \\ &= \prod_{i=1}^{N}\omega^{-2^{-1}a_i a_i'}Z^{a_i}X^{a_i'}|\sigma_i\rangle \\ &= \omega^{\mathbf{a}.(2^{-1}\mathbf{a}'+\boldsymbol{\sigma})}|\mathbf{a}' + \boldsymbol{\sigma}\rangle. \end{aligned} \tag{8.15}$$

From Eq. (8.14), we have that $A_{\mathbf{0}}|\boldsymbol{\sigma}\rangle = |-\boldsymbol{\sigma}\rangle$. Then,

$$A_{\mathbf{a}}A_{\mathbf{0}}|\boldsymbol{\sigma}\rangle = A_{\mathbf{a}}|-\boldsymbol{\sigma}\rangle = \omega^{2\mathbf{a}(\mathbf{a}'+\boldsymbol{\sigma})}|2\mathbf{a}' + \boldsymbol{\sigma}\rangle = T_{2\mathbf{a}}|\boldsymbol{\sigma}\rangle. \tag{8.16}$$

Since Eq. (8.16) holds for all basis states $|\boldsymbol{\sigma}\rangle$, then $A_{\mathbf{a}}A_{\mathbf{0}} = T_{2\mathbf{a}}$. This proves Eq. (8.12) in the case $\mathbf{b} = \mathbf{0}$.

Now, using $A_{\mathbf{a}} = T_{\mathbf{a}}A_{\mathbf{0}}T_{\mathbf{a}}^{\dagger}$ and the commutation relation $T_{\mathbf{a}}T_{\mathbf{b}} = \omega^{\mathbf{a}\mathbf{b}'-\mathbf{a}'\mathbf{b}}T_{\mathbf{b}}T_{\mathbf{a}}$, we have

$$\begin{aligned} A_{\mathbf{a}+\mathbf{b}}A_{\mathbf{b}} &= A_{\mathbf{a}+\mathbf{b}}T_{\mathbf{b}}A_{\mathbf{0}}T_{\mathbf{b}}^{\dagger} \\ &= T_{\mathbf{b}}T_{\mathbf{b}}^{\dagger}A_{\mathbf{a}+\mathbf{b}}T_{\mathbf{b}}A_{\mathbf{0}}T_{\mathbf{b}}^{\dagger} \\ &= T_{\mathbf{b}}A_{\mathbf{a}}A_{\mathbf{0}}T_{\mathbf{b}}^{\dagger} \\ &= T_{\mathbf{b}}T_{2\mathbf{a}}T_{\mathbf{b}}^{\dagger} \\ &= T_{2\mathbf{a}}\omega^{2(\mathbf{b}\mathbf{a}'-\mathbf{b}'\mathbf{a})}. \end{aligned} \tag{8.17}$$

This concludes the proof of Eq. (8.12).

The proposition now immediately follows as a corollary of Eq. (8.12). Indeed, if $A_{\mathbf{b}}|\psi\rangle = \lambda|\psi\rangle$, then

$$\lambda\langle\psi|A_{\mathbf{a}+\mathbf{b}}|\psi\rangle = \langle\psi|A_{\mathbf{a}+\mathbf{b}}A_{\mathbf{b}}|\psi\rangle = \langle\psi|T_{2\mathbf{a}}|\psi\rangle\omega^{2(\mathbf{b}\mathbf{a}'-\mathbf{b}'\mathbf{a})}. \quad \square \tag{8.18}$$

As a corollary, the MEs and SREs are identical for all order whenever the state is stabilized by a phase-space operator (up to a sign). Importantly, we emphasize that mana entropies remain valid measures of nonstabilizerness even in cases where the equality does not hold.

8.3 Thermodynamics approach to nonstabilizerness

We define a classical statistical system with energies $E_{\mathbf{u}} = -\log|\tilde{W}_\rho(\mathbf{u})|$, such that the free energy is given by $F_\rho(\beta) = -\frac{1}{\beta}\log\sum_{\mathbf{u}}|\tilde{W}_\rho(\mathbf{u})|^\beta$ [1]. One can see that the free energy is the same as the quantity $\frac{n-1}{2n}\mathcal{M}_n - \frac{N}{2n}\log d$ (for $n \neq 1$) with $\beta = 2n$ [2]. The calculation of $\mathcal{M}_n$ thus amounts to the computation of free energy of a classical system. Conventionally, this is commonly done by direct thermodynamics integration from infinite temperature ($\beta = 0$). This is applicable when the free energy at infinite temperature is known, which is not generally true in this case. Luckily, the free energy at $\beta = 2$ is known due to the relation in Eq. (8.8b). Indeed, for a pure state ($S_2 = 0$), Eq. (8.8b) implies $F_\rho(\beta = 2) = -\frac{N}{2}\log d$. Thus, one can perform a direct thermodynamics integration starting from $\beta = 2$,

$$\log\sum_{\mathbf{u}}\frac{|\tilde{W}_\rho(\mathbf{u})|^\beta}{d^N} = \int_2^\beta \langle\log|\tilde{W}_\rho(\mathbf{u})|\rangle_\beta \, d\beta, \tag{8.19}$$

where $\langle ...\rangle_\beta$ denotes the thermal average at inverse temperature β.

Numerically, the thermal average can be calculated via Monte Carlo sampling of the discrete Wigner function [125]. Here we perform the Monte Carlo sampling using tensor network methods, slightly modifying the method originally developed to compute SREs in Ref. [28]. In particular, we focus on mana, corresponding to $\beta = 1$.

To emphasize the computational advantage of our newly proposed thermodynamics integration approach, it is worth recalling that the number of samples required to estimate the SREs of integer indices $n > 1$ within a given error grows exponentially with N [28]. This exponential scaling becomes a significant bottleneck for studying large systems. In contrast, the thermodynamics integration approach offers a more efficient strategy. This method only requires computing the expectation value $\langle\log|\tilde{W}_\rho(\mathbf{u})|\rangle_\beta$ for different values of β from $\beta = 1$ to $\beta = 2$ (see Eq. (8.19)). Importantly, the variance of $\log|\tilde{W}_\rho(\mathbf{u})|$ only scales polynomially with N [67], making its estimation efficient for any value of β. This technique thus circumvents the exponentially difficult task of calculating the mana, enabling to study mana in large systems.

8.4 Mutual mana

We will also consider the "mutual mana" defined as

$$I_{\mathcal{M}}(A,B) = \mathcal{M}(\rho_{AB}) - \mathcal{M}(\rho_A) - \mathcal{M}(\rho_B). \tag{8.20}$$

We will use the notation $I_{\mathcal{M}}(\ell, L)$ to denote the case $A = \{1,...,\ell\}$ and $B = \{\ell+1,...,L\}$. Notice that the definition of mutual mana involves the mana of subsystems, which are mixed states. Crucially, mana is a genuine measure of nonstabilizerness both for pure and mixed states, so that the mutual mana is a meaningful quantity that quantifies the amount of resource that resides in the correlations between parts

[1] We note that similar thermodynamic description has been proposed for entanglement [67, 126, 127] and Shannon entropy [128].

[2] The case $n = 1$ is instead related to the energy at $\beta = 2$: $\mathcal{M}_1 = 2\langle E_{\mathbf{u}}\rangle_{\beta=2}$. As such, $\mathcal{M}_1$ can be directly estimated through perfect sampling techniques [23, 27]

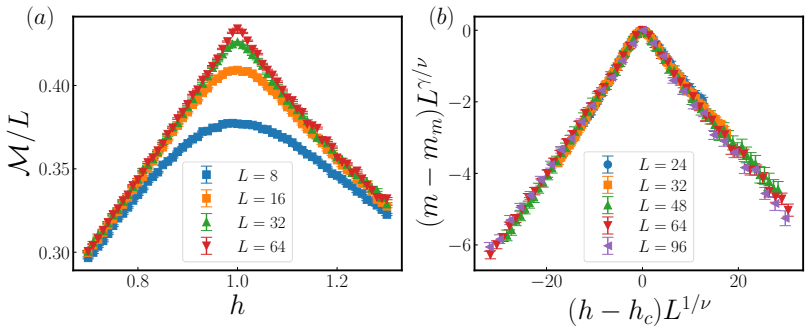

FIGURE 8.1: (a) Mana density $\mathcal{M}/L$ in the vicinity of the critical point $h = 1$ in the three-state quantum Potts model. (b) Data collapse of the mana density $m = \mathcal{M}/L$ with $\gamma \approx 0.83$ and $\nu \approx 0.85$. The correlation-length exponent ν is close to the known $\nu_{Potts} = 5/6$.

of the system. It has also been suggested that it quantifies the difficulty of removing nonstabilizerness with a finite-depth circuit [50].

We note here that mana is typically an extensive quantity. The subtraction in Eq. (8.20) thus serves to eliminate the leading extensive term, resulting in $I_{\mathcal{M}}(A, B)$ being significantly smaller than the mana itself. Extracting such a quantity through Monte Carlo samplings is known to be a challenging task, akin to the challenge of extracting topological entanglement entropy from entanglement entropy [81, 129, 130]. Indeed, if one tries to compute $I_{\mathcal{M}}(A, B)$ by directly computing each of the three terms on the right hand side of Eq. (8.20) separately (e.g., using Eq. (8.19)), the resulting error bar will be prohibitively large. We overcome this difficulty by writing $I_{\mathcal{M}}(A, B)$ as

$$I_{\mathcal{M}}(A, B) = \log\left(\frac{\sum_{\mathbf{u},\mathbf{v}} |W_{\rho_{AB}}(\mathbf{u} \oplus \mathbf{v})|}{\sum_{\mathbf{u}} |W_{\rho_A}(\mathbf{u})| \sum_{\mathbf{v}} |W_{\rho_B}(\mathbf{v})|}\right). \tag{8.21}$$

In view of the thermodynamics description in the previous section, the expression inside the logarithm can be interpreted as a ratio of partition functions of the classical systems corresponding to ρ_{AB} and $\rho_A \otimes \rho_B$. One way to estimate it in Monte Carlo simulations is by sampling from one classical system and averaging the ratio of the Boltzmann weights [3]. Concretely, we consider the probability distribution $\Pi_{\rho_{A(B)}}(\mathbf{u}) \propto |W_{\rho_{A(B)}}(\mathbf{u}))|$. We can estimate $I_{\mathcal{M}}(A, B)$ using

$$I_{\mathcal{M}}(A, B) = \log\left\langle \frac{|W_{\rho_{AB}}(\mathbf{u} \oplus \mathbf{v})|}{|W_{\rho_A}(\mathbf{u})||W_{\rho_B}(\mathbf{v})|} \right\rangle_{\Pi_{\rho_A}(\mathbf{u})\Pi_{\rho_B}(\mathbf{v})}. \tag{8.22}$$

8.5 Quantum Potts model

In this work, we consider the quantum Potts model, which can be seen as the generalization of the quantum Ising model with d states per site [91]. The Hamiltonian

[3] We note that thermodynamics integration can also be employed in this case. However, this requires to compute the discrete Wigner function of both ρ_{AB} and $\rho_A \otimes \rho_B$ at each Monte Carlo step. As the discrete Wigner function evaluation is computationally heavy, we choose the simpler technique described in the text, where we only need to sample the discrete Wigner function of $\rho_A \otimes \rho_B$.

is given by

$$H_{\text{Potts}} = -J \sum_{\langle i,j \rangle} \sum_{k=1}^{d-1} X_i^k X_j^{d-k} - h \sum_i \sum_{k=1}^{d-1} Z_i^k, \tag{8.23}$$

where X, Z are the shift and clock operators in Eq. (8.2). Here we focus on the case $d = 3$. The point $h_c = 1$ is a critical self-dual point, which is governed by a CFT for $d \leq 4$. For $d = 3$, the central charge is $c = 4/5$ in the ferromagnetic case ($J = 1$) and $c = 1$ in the antiferromagnetic case ($J = -1$) [131–133].

We will also consider an extension of the Potts model introduced in Ref. [118]. The Hamiltonian is given by

$$\begin{aligned} H_{\text{Potts}}(p) = &- \sum_{\langle i,j \rangle} \sum_{k=1}^{d-1} X_i^k X_j^{d-k} - \sum_i \sum_{k=1}^{d-1} Z_i^k \\ &- p \sum_{\langle\langle i,j \rangle\rangle} \sum_{k=1}^{d-1} X_i^k X_j^{d-k} - p \sum_{\langle i,j \rangle} \sum_{k=1}^{d-1} Z_i^k Z_j^{d-k}. \end{aligned} \tag{8.24}$$

The model is self-dual at any p, and the case $p = 0$ corresponds to the self-dual point $h = 1$ in Eq. (8.23), which is an integrable point. For $p \neq 0$, the model is not integrable, but it is expected that they are described by the same CFT at $p = 0$ for sufficiently small p [118].

8.6 Numerical results

We now present our numerical results on the mana in the quantum Potts model on a periodic chain. We obtain the ground state using TTN ground state variational search algorithm [41, 42], and then we sample the discrete Wigner function of the ground state using Monte Carlo sampling on TTN discussed in Ref. [28]. We use bond dimension up to $\chi = 36$. Here, we compute the full-state mana using Eq. (8.19), while the mutual mana is evaluated using Eq. (8.22).

The mana density is shown in Fig. 8.1a. We observe that $\mathcal{M}/L$ reaches a maximum at the critical point $h_c = 1$, which confirm the results of Ref. [50]. More importantly, with the large systems we are able to simulate, we obtain good data collapse, shown in Fig. 8.1b. Overall, these results are also similar to the behavior of SREs, which are studied for $n \in \{1, 2\}$ in Ref. [28]. Indeed, in this case the mana is identical to the SRE with $n = 1/2$ through the proposition in Sec. 8.2.1 [4].

Next, we investigated the scaling of mutual mana (Eq. (8.20)) at the critical point $h_c = 1$. The results are shown in Fig. 8.2a(b) for $J = 1$ ($J = -1$) for sizes up to $L = 64$ ($L = 32$) . We observe that the mutual mana is approximately proportional to $\log\left[\frac{L}{\pi}\sin\left(\ell\frac{\pi}{L}\right)\right]$, similarly to the entanglement and Shannon entropy in CFT. However, we cannot make a direct connection between the slope and the central charge of the associated CFT [5]. This is expected since mana is a basis-dependent quantity, and hence the proportionality factor would likely depend on the choice of basis.

We now turn to the extension of the Potts model in Eq. (8.24). Fig. 8.3 shows the mutual mana for various values of p in a chain of $L = 32$ sites. These results clearly reveal a linear scaling of the mutual mana with respect to $\log\left[\frac{L}{\pi}\sin\left(\ell\frac{\pi}{L}\right)\right]$, which

[4] In the case of three-state Potts model, the ground state satisfies $A_{\mathbf{0}}|\psi\rangle = |\psi\rangle$, due to the global S_3 symmetry of permuting the three X eigenstates. A similar statement holds for all d-state Potts model for odd prime d.

[5] Actually, there are also disputes regarding the slope of Shannon mutual information, and whether it is truly equal to $c/4$. See [115].

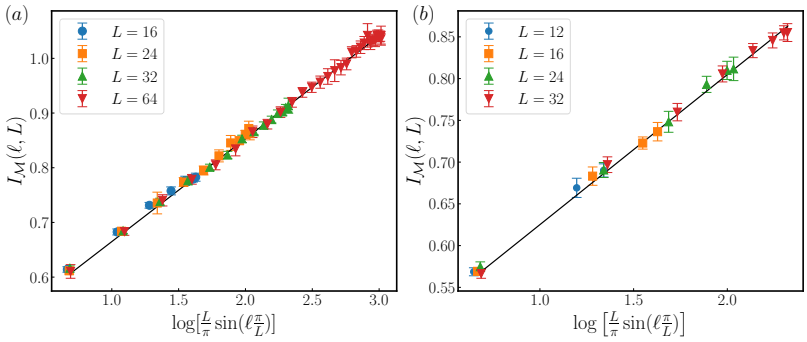

FIGURE 8.2: Mutual mana $I_{\mathcal{M}}(\ell, L)$ in the ground state of the quantum Potts model at the critical point $h/J = 1$ with (a) $J = 1$ and (b) $J = -1$. The solid line denotes the linear fit obtained for the largest size. Clearly the data of different system sizes collapse in the straight line. We observe odd-even effects for $J = -1$, and thus we plot only the results for even ℓ for clarity.

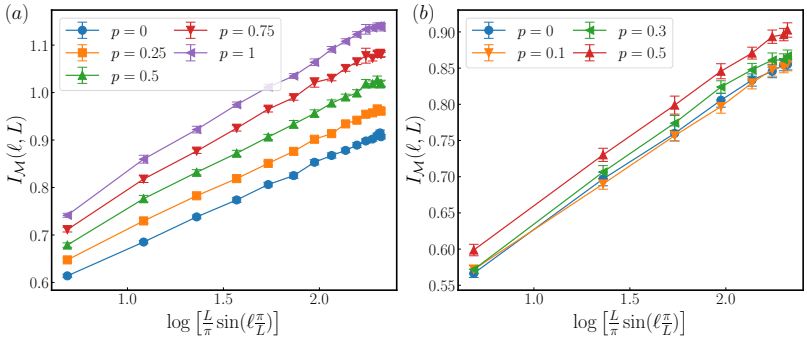

FIGURE 8.3: Mutual mana $I_{\mathcal{M}}(\ell, L)$ for various values of p in the extension of the quantum Potts model (Eq. (8.24)) with (a) $J = 1$ and (b) $J = -1$. The logarithmic scaling is also observed at the non-integrable points $p \neq 0$. The system size is $L = 32$.

holds true even at the non-integrable points. Notably, the slope of the linear growth shows little variation upon increasing p. Based on these findings, we conjecture that the slope is universal and determined by the underlying CFT, although possibly not by a simple relation with central charge as entanglement and Shannon entropy.

Since mana depends on the chosen basis, an important question is whether or not the logarithmic scaling persists under local basis change. To address this question, we show the mutual mana after applying unitary transformation $T_\theta^{\otimes N}$, where $T_\theta = \mathrm{diag}(1, e^{i\theta}, e^{-i\theta})$, to the ground state at $h = 1$ in Fig. 8.4a. Note that $\theta = 2/9$ corresponds to the canonical T-gate for qutrit. We see that the logarithmic scaling remains evident up to $\theta = 2/9$, while it becomes less apparent for $\theta = 3/9$, possibly due to finite-size effects.

Finally, in order to contrast with the behavior away from criticality, we plot the scaling of mutual mana both at and away from the critical point in Fig. 8.4b. We see that the logarithmic scaling is observed only at the critical point, while away from the critical point the mutual mana saturates at large ℓ.

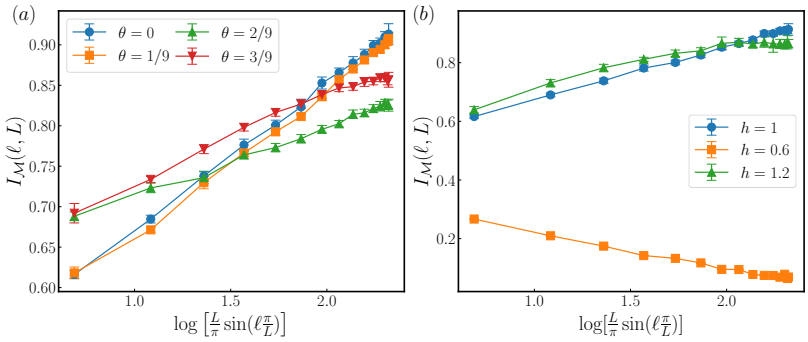

FIGURE 8.4: (a) Mutual mana $I_{\mathcal{M}}(\ell, L)$ after performing the unitary transformation $T_\theta^{\otimes N}$, where $T_\theta = \mathrm{diag}(1, e^{i\theta}, e^{-i\theta})$, to the ground state at $h = 1$ and $J = 1$. (b) Mutual mana $I_{\mathcal{M}}(\ell, L)$ in the ground state of the three-state Potts model and at three different transverse field strength. The logarithmic scaling is only observed at the critical point at $h = 1$. In contrast, the mutual mana saturates both at $h > 1$ and $h < 1$. The system size is $L = 32$.

8.7 Conclusions and outlook

In this work, we investigate the behavior of mana around criticality in quantum Potts models and its extension. We introduce Rényi version of mana, which enables us to calculate mana for large system sizes. Our results on mutual mana provide clear evidence of logarithmic scaling with distance in CFT, while it reaches saturation in gapped phases. This illustrates that, much like entanglement, the scaling of mutual mana provides a means to distinguish between critical and non-critical behaviors. Moreover, our results on the non-integrable extension indicate the universal character of the logarithmic scaling at criticality. Combined with the findings of recent studies indicating that nonstabilizerness is considerably less susceptible to errors arising from finite bond dimensions [25, 28, 119], our work highlights the potential of nonstabilizerness as a useful tool to detect and characterize conformally invariant quantum chains, particularly in the context of tensor network simulations.

Our work opens up many interesting directions for future investigations. Although mana is only defined for odd prime local dimension, several possible extensions have been proposed for qubits [134–138]. It would be interesting to employ them to investigate the qubit case, in particular regarding its scaling in CFT. A more comprehensive examination of mutual mana in CFT also warrants futher investigation, for instance by looking at different partitioning schemes. Additionally, it would be interesting to study the behavior of mana minimized over all possible bases.

Furthermore, our methods enable the exploration of mana in various scenarios, such as quench dynamics [121, 139], open systems and finite-temperature scenarios. In addition, it would be interesting to adapt our approach in different classes of tensor network states such as PEPS [140] to investigate the mana in higher dimensions. Another interesting direction is to systematically study and compare the behavior of mana entropy and SRE, which may provide insights into how to construct a genuine measure of nonstabilizerness for qubits that is efficiently computable. Finally, while here the mana entropy is introduced to facilitate the numerical computations of mana, it may also be helpful in the analytical investigation of mana in important classes of states, such as the quantum hypergraph states [141].

Chapter 9

Magic in generalized Rokhsar-Kivelson wavefunctions

In this chapter, we introduce an approach to compute the stabilizer Rényi entropy (SRE) [19] with integer Renyi index $n > 1$ in many-body wavefunction, by expressing it in terms of wavefunction coefficients that make it amenable to computation using Monte Carlo sampling (provided the wavefunction can be gauged to have non-negative coefficients).

We apply this approach to a class of models known as generalized Rokhsar-Kivelson systems [142, 143], or Hamiltonians that allow a stochastic matrix form (SMF) decomposition [144]. The ground state wavefunctions of these systems can be written explicitly throughout their phase diagram, and their properties can be related to associated classical statistical mechanics problems in thermodynamic equilibrium at temperature T, which plays the role of a parameter in the phase diagram of the original quantum systems. This correspondence allows powerful analytical and numerical approaches to be deployed, that are not usually available in conventional quantum many body settings [1].

Since the early work of Rokhsar and Kivelson [146], SMF Hamiltonian and wavefunctions have appeared in many different physics contexts. Of late, a resurgence of attention has derived from the fact that they can be naturally realised using tensor networks and PEPS [147], and they can be implemented in measurement-prepared quantum states and (monitored) quantum circuits [148–153]. In this context, the magic of SMF wavefunctions thus directly quantifies the amount of non-Clifford resources required to prepare these systems in the circuits.

We are able to express the SRE of SMF wavefunctions in terms of a free energy difference of related classical problems, which can then be efficiently computed by thermodynamic integration. We apply this insight to a range of quantum many body SMF Hamiltonians, which affords us to study numerically the SRE of large high-dimensional systems, unattainable using existing tensor network-based techniques, and in some cases we obtain explicit analytical results.

We observe that the behaviour of the SRE is relatively featureless across quantum phase transitions in these systems [154], although it is indeed singular in its first or higher order derivative, depending on the first or higher order nature of the transition. On the contrary, we find that the maximum of the SRE generically occurs at a cusp away from the quantum critical point, where the derivative suddenly changes sign. Furthermore, we compare the SRE to the logarithm of overlaps with specific stabilizer states, that are asymptotically realised in the ground state phase diagrams of these systems. We find that they display strikingly similar behaviors, which in turn establish rigorous bounds on the min-relative entropy of magic.

[1] We note that a study of the SRE in related Rokhsar-Kivelson-sign wavefunctions was presented in Ref. [145].

The rest of the chapter is structured as follows. In Sec. 9.1 and Sec. 9.2 we give a brief review of SMF Hamiltonians and SRE, respectively. We then state our general results in Sec. 9.3 about the SRE and its upper bounds in SMF systems. In Sec. 9.4 we then present a study of a range of models, encompassing the Ising ferromagnet in 1D, 2D, 3D, and infinite dimensions; the $J_1 - J_2$ model on the square lattice; the triangular Ising antiferromagnet; and the Edwards-Anderson model on the cubic lattice. Finally, we conclude in Sec. 9.5.

9.1 Brief review of Stochastic Matrix Form (SMF) Hamiltonians

The stochastic matrix form wavefunctions, dependent on the parameter β, are given by [142–144]

$$|\psi_{\text{SMF}}\rangle = \frac{1}{\sqrt{Z(\beta)}} \sum_{\sigma} e^{-\beta E_\sigma/2} |\sigma\rangle \,, \tag{9.1}$$

where

$$Z(\beta) = \sum_{\sigma} e^{-\beta E_\sigma} \,. \tag{9.2}$$

$Z(\beta)$ can be seen as a classical partition function at temperature $T = 1/\beta$. One can design a quantum Hamiltonian for arbitrary choice of E_σ, such that $|\psi_{\text{SMF}}\rangle$ is the ground state of the Hamiltonian. In particular, for a locally interacting E_σ, the Hamiltonian also contains only local interactions. The quantum Hamiltonian is said to be SMF decomposable [144]. The equal-time correlation function of diagonal operators of SMF wavefunctions are given by the equal-time correlations functions in the associated classical systems in thermal equilibrium. It follows that the ground state phase diagram of the quantum Hamiltonian contains the thermal phase diagram of the classical system in thermal equilibrium. Since the wave function coefficients are known exactly by design, the wave function can be sampled with classical Monte Carlo simulations of the corresponding classical system.

9.2 Stabilizer Rényi entropy and upper bounds

The SRE is related to another magic monotone called the min-relative entropy of magic, defined as

$$D_{min}(|\psi\rangle) = -\log F_{\text{STAB}}(|\psi\rangle) \tag{9.3}$$

where F_{STAB} is the stabilizer fidelity defined as

$$F_{\text{STAB}}(|\psi\rangle) = \max_{|\phi\rangle \in \text{STAB}} |\langle\phi|\psi\rangle|^2 \,. \tag{9.4}$$

The following inequality holds [23]

$$M_n(|\psi\rangle) \leq \frac{2n}{n-1} D_{\min}(|\psi\rangle) \,, \quad n \geq 1 \,. \tag{9.5}$$

In particular, setting $n = 2$, and defining $D(|\psi\rangle, |\phi\rangle) = -\log |\langle\phi|\psi\rangle|^2$, one finds that

$$M_2(|\psi\rangle) \leq 4 D_{\min}(|\psi\rangle) \leq 4 D(|\psi\rangle, |\phi\rangle) \,, \tag{9.6}$$

for any $|\phi\rangle \in$ STAB.

Because the SRE is defined in terms of the characteristic function $\Xi_P(|\psi\rangle)$, it is natural to estimate it through statistical sampling of $\Xi_P(|\psi\rangle)$. Indeed, this was the core of previous numerical methods that have been introduced to compute the SRE [23, 27, 28], which are so far limited to tensor network techniques. To obtain reliable statistics, a large number of samples is required, often resulting in computations being restricted to small bond dimension. This limitation poses a challenge when studying highly entangled systems, such as higher dimensional ones. Unfortunately, the existing methods are not directly suitable for Quantum Monte Carlo approaches due to the inherent difficulty in evaluating the expectation values of high-weight Pauli strings within.

9.3 Magic in SMF ground states

In this section we show how the special form of the ground state wave functions of SMF systems allows for analytical and numerical routes into the calculation of their magic, that are not afforded to general quantum many body systems. In doing so, we develop the machinery that will later be used to study a broad range of model systems, to gain insight in the behaviour of this intriguing quantity.

9.3.1 Stabilizer Rényi entropy

Consider a $N-$qubit wave-function $|\psi\rangle = \sum_\sigma c_\sigma |\sigma\rangle$, where $c_\sigma = \langle\sigma|\psi\rangle$ and σ labels all tensor product basis states (e.g., the σ_i^z basis for a spin-1/2 system, $i = 1, ..., N$). We firstly show that the SRE M_2 can be expressed as follows

$$\begin{aligned}\exp(-M_2) = \sum_{\sigma^{(1)},\sigma^{(2)},\sigma^{(3)},\sigma^{(4)}} \big[& c_{\sigma^{(1)}} c_{\sigma^{(2)}} c_{\sigma^{(3)}} c_{\sigma^{(1)}\sigma^{(2)}\sigma^{(3)}} \\ & c^*_{\sigma^{(1)}\sigma^{(2)}\sigma^{(4)}} c^*_{\sigma^{(1)}\sigma^{(3)}\sigma^{(4)}} c^*_{\sigma^{(2)}\sigma^{(3)}\sigma^{(4)}} c^*_{\sigma^{(4)}} \big] \,,\end{aligned} \tag{9.7}$$

where $c_{\sigma^{(1)}\sigma^{(2)}\sigma^{(3)}}$ denotes the coefficient $c_{\tilde{\sigma}}$ corresponding to the tensor product label $\tilde{\sigma}$ given by the point product of $\sigma^{(1)}$, $\sigma^{(2)}$, and $\sigma^{(3)}$: $\tilde{\sigma}_i = \sigma_i^{(1)}\sigma_i^{(2)}\sigma_i^{(3)}$, $\forall\, i = 1, \ldots, N$. Similarly for the other equivalent terms in Eq. (9.7). We can imagine $\sigma^{(a)}$, $a = 1, 2, 3, 4$ as four copies of the N qubits. Similar expressions can be obtained for SREs of integer index $n > 2$.

Proof: Consider the single-qubit Pauli operators (including the identity) $P \in \{I, X, Y, Z\}$. It is convenient to label them using a pair of indices $a, a' \in \{0, 1\}$, such that $P_{a,a'} = i^{aa'} X^a Z^{a'}$ whereby $P_{0,0} = I$, $P_{1,0} = X$, $P_{0,1} = Z$, and $P_{1,1} = Y$. For a system of N qubits, the Pauli strings can then be written as

$$P_{\mathbf{a},\mathbf{a}'} = P_{a_1,a_1'} P_{a_2,a_2'} ... P_{a_N,a_N'} \,, \tag{9.8}$$

where $\mathbf{a}, \mathbf{a}'$ are n-bit strings. We also denote $s = (-1)^a$, for later convenience.

Substituting $|\psi\rangle = \sum_\sigma c_\sigma |\sigma\rangle$ to the SRE in Eq. (6.23), and using the representation of $P_{a,a'}$ above, we obtain

$$
\begin{aligned}
\exp(-M_2) &= \frac{1}{d}\sum_{\mathbf{a},\mathbf{a}'}\left[\sum_{\sigma,\sigma'} c_\sigma c^*_{\sigma'}\langle\sigma'|P_{\mathbf{a},\mathbf{a}'}|\sigma\rangle\right]^4 \\
&= \frac{1}{d}\sum_{\mathbf{a},\mathbf{a}'}\left[\sum_{\sigma,\sigma'} c_\sigma c^*_{\sigma'}\prod_{j=1}^{N} i^{a_j a'_j}\langle\sigma'_j|X^{a_j}Z^{a'_j}|\sigma_j\rangle\right]^4 \\
&= \frac{1}{d}\sum_{\mathbf{a},\mathbf{a}'}\left[\sum_{\sigma,\sigma'} c_\sigma c^*_{\sigma'}\prod_{j=1}^{N} \sigma_j^{a'_j}\langle\sigma'_j|X^{a_j}|\sigma_j\rangle\right]^4 \\
&= \frac{1}{d}\sum_{\mathbf{a},\mathbf{a}'}\left[\sum_{\sigma,\sigma'} c_\sigma c^*_{\sigma'}\prod_{j=1}^{N} \sigma_j^{a'_j}\langle\sigma'_j|s_j\sigma_j\rangle\right]^4 \\
&= \frac{1}{d}\sum_{\mathbf{a},\mathbf{a}'}\left[\sum_{\sigma} c_\sigma c^*_{s\sigma}\prod_{j=1}^{N} \sigma_j^{a'_j}\right]^4,
\end{aligned}
\tag{9.9}
$$

where $s\sigma$ represents the tensor product state label where $\sigma'_j = s_j\sigma_j$, $\forall\, j$. Note that the factor $\prod_j i^{a_j a'_j}$ in the second line is independent of σ, σ', and therefore factors out of the summation and disappears due to the fourth power ($i^4 = 1$). Expanding the fourth power explicitly, we can further simplify the expression

$$
\begin{aligned}
\exp(-M_2) &= \frac{1}{d}\sum_{\mathbf{a},\mathbf{a}'}\sum_{\sigma^{(1)},\sigma^{(2)},\sigma^{(3)},\sigma^{(4)}}\left[\prod_{i=1}^{4} c_{\sigma^{(i)}} c^*_{s\sigma^{(i)}}\prod_{j=1}^{N}\left(\sigma_j^{(i)}\right)^{a'_j}\right] \\
&= \frac{1}{d}\sum_{\mathbf{a}}\sum_{\sigma^{(1)},\sigma^{(2)},\sigma^{(3)},\sigma^{(4)}}\left[\prod_{i=1}^{4} c_{\sigma^{(i)}} c^*_{s\sigma^{(i)}}\right]\left[\prod_{j=1}^{N}\sum_{a'_j=0,1}\left(\prod_{i=1}^{4}\sigma_j^{(i)}\right)^{a'_j}\right] \\
&= \frac{1}{d}\sum_{\mathbf{a}}\sum_{\sigma^{(1)},\sigma^{(2)},\sigma^{(3)},\sigma^{(4)}}\left[c_{\sigma^{(1)}}c_{\sigma^{(2)}}c_{\sigma^{(3)}}c_{\sigma^{(4)}}c^*_{s\sigma^{(1)}}c^*_{s\sigma^{(2)}}c^*_{s\sigma^{(3)}}c^*_{s\sigma^{(4)}}\prod_{j=1}^{N}\left(1+\sigma_j^{(1)}\sigma_j^{(2)}\sigma_j^{(3)}\sigma_j^{(4)}\right)\right].
\end{aligned}
\tag{9.10}
$$

Since the product $\sigma_j^{(1)}\sigma_j^{(2)}\sigma_j^{(3)}\sigma_j^{(4)} \in \{-1, 1\}$, the term in square brackets in the last line above is nonzero only if $\sigma_j^{(1)}\sigma_j^{(2)}\sigma_j^{(3)}\sigma_j^{(4)} = 1$ for all sites j. This effectively constraints the fourth layer $\sigma^{(4)} = \sigma^{(1)}\sigma^{(2)}\sigma^{(3)}$:

$$
\begin{aligned}
\exp(-M_2) \;=\; \sum_{\mathbf{a},\sigma^{(1)},\sigma^{(2)},\sigma^{(3)}} &\big[c_{\sigma^{(1)}}c_{\sigma^{(2)}}c_{\sigma^{(3)}}c_{\sigma^{(1)}\sigma^{(2)}\sigma^{(3)}} \\
&\quad c^*_{s\sigma^{(1)}}c^*_{s\sigma^{(2)}}c^*_{s\sigma^{(3)}}c^*_{s\sigma^{(1)}\sigma^{(2)}\sigma^{(3)}}\big].
\end{aligned}
\tag{9.11}
$$

Finally, we can replace the summation over $\mathbf{a}$ for a summation over $\sigma^{(4)} = s\sigma^{(1)}\sigma^{(2)}\sigma^{(3)}$, to bring the expression into a more symmetric form,

$$
\begin{aligned}
\exp(-M_2) \;=\; \sum_{\sigma^{(1)},\sigma^{(2)},\sigma^{(3)},\sigma^{(4)}} &\big[c_{\sigma^{(1)}}c_{\sigma^{(2)}}c_{\sigma^{(3)}}c_{\sigma^{(1)}\sigma^{(2)}\sigma^{(3)}} \\
&\quad c^*_{\sigma^{(1)}\sigma^{(2)}\sigma^{(4)}}c^*_{\sigma^{(1)}\sigma^{(3)}\sigma^{(4)}}c^*_{\sigma^{(2)}\sigma^{(3)}\sigma^{(4)}}c^*_{\sigma^{(4)}}\big]. \quad \square
\end{aligned}
\tag{9.12}
$$

For the SMF systems introduced in Sec. 9.1, and in particular their ground state wavefunctions, these known expressions for the magic can be further manipulated upon substituting $c_\sigma = e^{-\beta E_\sigma/2}/\sqrt{Z}$ in Eq. (9.7) to obtain:

$$M_2 = -\log \frac{Z_M}{Z^4} \tag{9.13}$$

where

$$\begin{aligned} Z_M &= \sum e^{-\beta E_M} \\ &= \sum_{\substack{\sigma^{(1)},\sigma^{(2)},\\ \sigma^{(3)},\sigma^{(4)}}} \exp\left[-\beta \sum_a E_{\sigma^{(a)}} - \beta \sum_a E_{\prod_{b\neq a}\sigma^{(b)}}\right]. \end{aligned} \tag{9.14}$$

One can interpret Z_M as a classical partition function constructed from four copies of the original classical degrees of freedom. The second term in the square bracket describes the energy of a configuration obtained from the spin product of three out of four copies. The expression in Eq. (9.13) can thus be seen as (proportional to) the difference between the free energy of the classical system described by Z_M and four non-interacting copies of the original classical system described by Z.

This manipulation is not only interesting from a conceptual point of view, but also from a pragmatic one: it provides a new angle to compute the magic of a quantum (SMF) state using classical statistical mechanics tools in the same number of dimensions. As we demonstrate later, it affords us the ability to access significantly larger system sizes and higher dimensional lattices than previously possible [23, 27, 28].

In practice, rather than computing ratios of partition functions or differences in free energies, it is convenient to notice that the derivative of M_2 with respect to temperature reduces to:

$$\frac{dM_2}{dT} = \frac{4\langle E\rangle - \langle E_M\rangle_M}{T^2}. \tag{9.15}$$

Thus, M_2 can be more efficiently obtained by computing the energies $\langle E\rangle$ and $\langle E_M\rangle_M$ and then proceding to integrate the r.h.s. of Eq. (9.15).

9.3.2 Upper bound of M_2

As discussed in Sec. 9.2, M_2 is bounded from above by $D(|\psi\rangle, |\phi\rangle) = -\log|\langle\phi|\psi\rangle|^2$ for any $|\phi\rangle \in$ STAB. In the following sections, we compute $D(|\psi\rangle, |\phi\rangle)$ for several ad hoc choices of states $|\phi\rangle$, specific to the system being considered. Once again, in the case of SMF wavefunctions, these overlaps can be reduced to classical statistical mechanical objects, amenable to corresponding analytical or numerical estimates.

Here, we illustrate the procedure to compute $D(|\psi\rangle, |\phi\rangle)$ in a couple of cases that will often be used in the following. Consider for example $|\phi\rangle = |+++...\rangle$, where $|+\rangle = \frac{|\uparrow\rangle+|\downarrow\rangle}{2}$ (i.e., a spin-1/2 state polarized in the x direction). In the context of SMF wavefunctions, this is the ground state at $\beta = 0$. We denote $D_x(|\psi\rangle) = D(|\psi\rangle, |\phi\rangle =$

$|+++...\rangle$). From the overlap

$$\langle\psi(\beta)|\psi(\beta=0)\rangle = \frac{1}{\sqrt{Z(\beta)2^N}}\sum_{\sigma,\sigma'} e^{-\beta E_\sigma/2}\langle\sigma'|\sigma\rangle \tag{9.16}$$

$$= \frac{1}{\sqrt{Z(\beta)2^N}}\sum_{\sigma} e^{-\beta E_\sigma/2} \tag{9.17}$$

$$= \frac{Z(\beta/2)}{\sqrt{Z(\beta)2^N}}\,, \tag{9.18}$$

we then obtain

$$D_x(|\psi(\beta)\rangle) = -\log\frac{Z(\beta/2)^2}{Z(\beta)2^N}\,. \tag{9.19}$$

Another useful example is $|\phi\rangle = (|\uparrow\uparrow\uparrow...\rangle + |\downarrow\downarrow\downarrow...\rangle)/\sqrt{2}$. In the ferromagnetic Ising model, this is the ground state at $T = 0$ (namely, the exact ground state, ignoring spontaneous symmetry breaking effects). We denote $D_{zz}(|\psi\rangle) = D(|\psi\rangle, |\phi\rangle = (|\uparrow\uparrow\uparrow...\rangle + |\downarrow\downarrow\downarrow...\rangle)/\sqrt{2})$. From the overlap

$$\langle\psi(\beta)|\phi\rangle = \sqrt{\frac{2}{Z(\beta)}}e^{-\beta E_{zz}/2}\,, \tag{9.20}$$

where E_{zz} is the energy of the configuration $\sigma_i = 1(-1)$, for all i, we obtain

$$D_{zz}(|\psi(\beta)\rangle) = \beta E_{zz} - \log\frac{2}{Z(\beta)}\,. \tag{9.21}$$

In all cases, the overlaps $D(|\psi\rangle, |\phi\rangle)$ are related to the partition function of the classical model. Therefore, similarly to M_2, we compute them using direct thermodynamics integration.

9.4 SMF models

Armed with the tools developed above, we proceed to investigate a broad range of models, in the attempt to deepen our understanding of stabilizerness and magic in many body systems – albeit of the fine tuned SMF kind – and its relation to quantum phase transitions. For this purpose, we consider in the first instance quantum Ising ferromagnets in 1D, 2D, 3D, and infinite dimensions (mean field); we also consider the J_1-J_2 model tuned to exhibit a first order phase transition, for comparison. We then move on to more exotic examples, such as the quantum triangular Ising antiferromagnet (which is fully frustrated in the SMF realisation) and the Edwards-Anderson model (exemplifying a spin glass transition in the droplet picture).

Since the SREs are generally an extensive quantity, we focus on the SRE densities M_n/N, where $N = L^d$ is the total number of sites in the system with linear size L and dimensionality d. For the numerical simulations at finite volume, we impose periodic boundary conditions.

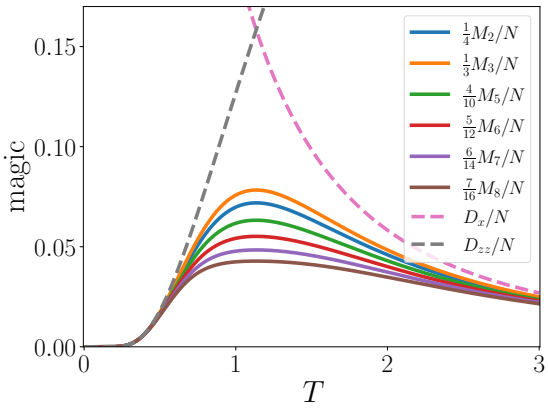

FIGURE 9.1: Behaviour of various measures of magic, including two stabilizer bounds, for the SMF 1D Ising ferromagnet. For each n, we plot $\frac{n-1}{2n} M_n / N$, which are upper bounded by D_x and D_{zz} by Eq. (9.5).

9.4.1 1D SMF Ising ferromagnet

The quantum SMF Hamiltonian for the 1D Ising ferromagnet is related to the classical 1D Ising model with energy

$$E_\sigma = -\sum_i \sigma_i \sigma_{i+1} \,, \tag{9.22}$$

where the spins σ_i live on a chain, and it reflects its thermodynamic behaviour. In particular, there is no phase transition and the system orders only in the limit $\beta \to \infty$ (we stress that β plays the role of inverse temperature for the classical system whereas it is merely a tunable parameter in the SMF quantum Hamiltonian, which is considered to be at zero temperature in its ground state, for the purpose of this work).

Despite its simplicity, this model serves as a useful warmup example and the magic can be computed analytically using Eq. (9.13). Indeed, we recall that the partition function of the 1D (nearest-neighbour) Ising model can be computed with transfer matrix techniques:

$$\begin{aligned} Z &= \sum_\sigma e^{\beta \sum_i \sigma_i \sigma_{i+1}} \\ &= \sum_\sigma e^{\beta \sigma_1 \sigma_2} e^{\beta \sigma_2 \sigma_3} \ldots e^{\beta \sigma_L \sigma_1} \\ &= \sum_\sigma V_{\sigma_1, \sigma_2} V_{\sigma_2, \sigma_3} \ldots V_{\sigma_L, \sigma_1} \\ &= \mathrm{Tr}(V^L) \,, \end{aligned} \tag{9.23}$$

where $V_{\eta,\eta'} = e^{\beta \eta \eta'}$ is a 2×2 matrix. The eigenvalues of V are $\lambda_1 = 2 \cosh \beta$ and $\lambda_2 = 2 \sinh \beta$. Thus,

$$Z = \mathrm{Tr}(V^L) = \lambda_1^L + \lambda_2^L = [2 \cosh \beta]^L + [2 \sinh \beta]^L \,. \tag{9.24}$$

We can similarly compute Z_M by interpreting the four layers of the 1D chain as a 1D chain with 16 states per site: $Z_M = \mathrm{Tr}\big(V_M^L\big)$, where V_M is a 16×16 matrix.

More generally, for an integer index $n > 1$, the transfer matrix $V_{M,n}$ is a $2^{2n} \times 2^{2n}$ matrix with elements

$$V_M\left(\{\eta^{(1)},...,\eta^{(2n)}\},\{\eta'^{(1)},...,\eta'^{(2n)}\}\right) = \exp\left[\frac{\beta}{2}\sum_a \eta^{(a)}\eta'^{(a)} + \frac{\beta}{2}\sum_a\prod_{b\neq a}\eta^{(b)}\eta'^{(b)}\right]. \tag{9.25}$$

To compute $Z_{M,n} = \mathrm{Tr}\left(V_{M,n}^L\right)$ we work in the thermodynamic limit $L \to \infty$, where we only need to find the largest eigenvalue of $V_{M,n}$. One can verify that the column vector with all elements equal to 1 is an eigenvector of $V_{M,n}$. By the Perron-Frobenius theorem, the corresponding eigenvalue is the unique largest eigenvalue:

$$\lambda_n = \frac{2^{2n} + [2\cosh(\beta)]^{2n} + [2\sinh(\beta)]^{2n}}{2}. \tag{9.26}$$

Finally, using Eq. (9.26) and (9.24), we find

$$M_n/N = \frac{1}{1-n}\log\frac{1+\cosh(\beta)^{2n}+\sinh(\beta)^{2n}}{2\cosh(\beta)^{2n}}, \tag{9.27}$$

for integer $n > 1$.

Furthermore, D_x and D_{zz} can be computed directly by plugging in the partition function Eq. (9.24) into Eq. (9.19) and (9.21), respectively. In Fig. 9.1, we show the SREs, D_x, and D_{zz} of the SMF 1D Ising model, observing the expected asymptotic agreement in the limits $T \to 0$ and $T \to \infty$.

To avoid confusion, we remark here that the SMF Hamiltonian and corresponding GS wavefunction related to the classical 1D Ising ferromagnet are strikingly different from the conventional 1D Ising ferromagnet in a transverse field. Most notably, in the SMF case there is no phase transition and ordering occurs only asymptotically in the limit $T \to 0$.

9.4.2 2D SMF Ising ferromagnet

The quantum SMF Hamiltonian of the 2D Ising ferromagnet is related to the 2D classical Ising model with energy

$$E_\sigma = -\sum_{\langle ij\rangle}\sigma_i\sigma_j, \tag{9.28}$$

where the spins σ_i are taken without loss of generality to live on the 2D square lattice. There is a phase transition between the ferromagnetic and the paramagnetic phase at $T_c = 2/\log\left(1+\sqrt{2}\right) \approx 2.269815$.

To study the thermodynamics properties of Z_M, we perform Monte Carlo simulations augmented with Wolff cluster algorithm [97] and parallel tempering [155, 156]. We study the energy $\langle E_M\rangle_M$ as a function of temperature for a range of system sizes as shown in Fig. 9.2 (top panel). We observe a behaviour compatible with a first-order transition from a high-temperature paramagnetic phase to a low-temperature ordered phase, at some value $T^* \neq T_c$ (whereas we know $\langle E\rangle$ from the classical 2D Ising model to be smooth, with a singularity in its first derivative at T_c). The presence of a first order transition in the classical system described by Z_M will be a common

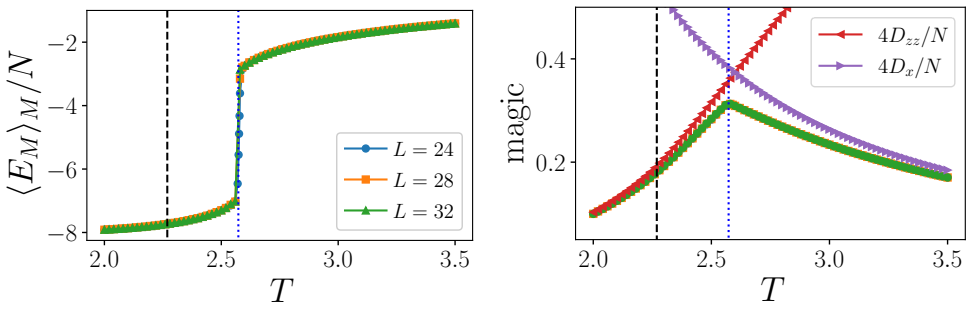

FIGURE 9.2: Magic and stabilizer bounds for the SMF 2D Ising ferromagnet. The top panel shows the behaviour of $\langle E_M \rangle_M$ introduced in Sec. 9.3.1 as a stepping stone to compute M_2/N (bottom panel). The vertical dashed lines indicate the location of the quantum phase transition, whereas the vertical dotted lines indicate the location of the transition in the coupled layered system Z_M (resulting in a cusp in the magic M_2).

feature in all examples considered in our work; however, while $T^* > T_c$ for the 2D Ising case, we will find for example that $T^* < T_c$ in higher-dimensional systems.

Integrating the energy as in Eq. (9.15) from high temperature, we obtain the SRE M_2. In contrast to the results of previous studies [25, 28], we see that M_2 is continuous and does not exhibit a maximum nor minimum at the transition point. In fact, we know that at T_c, M_2 inherits a singularity in its second derivative from the singularity in the first derivative of the energy $\langle E \rangle$ of the associated classical system described by the partition function Z (which undergoes a second order phase transition). The maximum of M_2 occurs instead away from the quantum critical point (into the paramagnetic phase), at a cusp that can be related to the first order transition point of the classical system described by Z_M. Furthermore, we observe that the bounds $4D_x$ and $4D_{zz}$ lie very close above M_2. By Eq. (9.6), this also establishes strict upper and lower bounds for $D_{\min}$. This is again a common feature that we consistently observe in all examples considered in this work.

Although the SRE M_2 appears relatively featureless across T_c, we know from Eq. (9.15) that it must inherit any singularity present in $\langle E \rangle$ and in $\langle E_M \rangle_M$. The well-known critical behaviour of the 2D Ising model gives a singularity in the second derivative of M_2, which is related to the specific heat of the classical 2D Ising model: $d^2 M_2/dT^2$ exhibits a peak at T_c which diverges logarithmically, as shown in Fig. 9.3. A (negative) peak is observed at T^*, due to the the specific heat of Z_M; here the transition is first order and the peak diverges as N, much faster than the known logarithmic divergence at T_c.

We note that, by Wegner duality [98], the SMF groundstates corresponding to the 2D Ising model are dual to a wavefunction deformation of the toric code studied in Ref. [157]. Therefore, the SREs of the two wavefunctions are identical (up to a constant shift), since the SREs are preserved by Wegner duality [28].

9.4.3 3D SMF Ising ferromagnet

The discussion of the 3D Ising ferromagnet goes along the same line as in 2D, with the spins σ_i living without loss of generality on the 3D cubic lattice. The model is known to exhibit a second-order phase transition between the ferromagnetic and

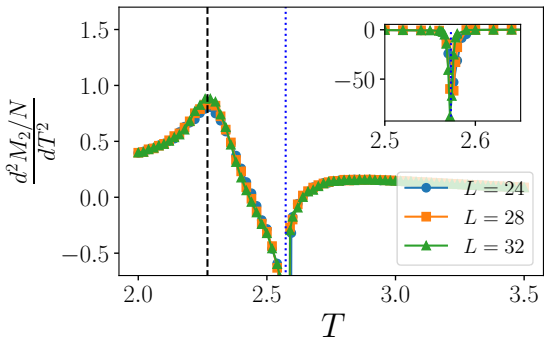

FIGURE 9.3: Second derivative of M_2 for the 2D SMF Ising ferromagnet. The vertical dashed line indicates the location of the quantum phase transition, whereas the vertical dotted line indicates the location of the transition T^* in the coupled layered system Z_M. The inset shows the full extent of $d^2(M_2/N)/dT^2$ near T^*, which is truncated in the main plot for visualisation purposes.

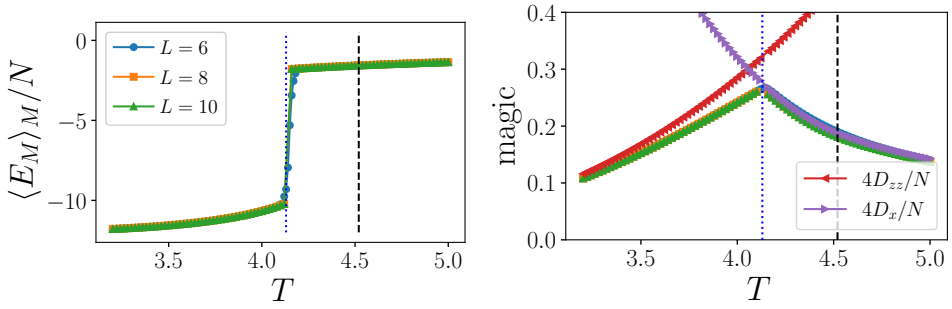

FIGURE 9.4: Magic and stabilizer bounds for the SMF 3D Ising ferromagnet. The top panel shows the behaviour of $\langle E_M \rangle_M$, and the bottom panel shows the SRE density M_2/N (same system sizes). The vertical dashed lines indicate the location of the quantum phase transition, whereas the vertical dotted lines indicate the location of the transition in the coupled layered system Z_M (resulting in a cusp in the magic M_2).

the paramagnetic phase. Through large-scale Monte Carlo simulations, the critical point was found to be at $T_c \approx 4.5115$ [158].

The results are shown in Fig. 9.4. The energy $\langle E_M \rangle_M$ once again exhibits a first-order transition that induces a cusp in the behaviour of M_2 at T^*, where it reaches its maximum value. At the quantum phase transition, M_2 is once again continuous, with a singularity in its second derivative. Differently from the 2D case, the cusp (and maximum) of M_2 occurs in the ferromagnetic phase instead of the paramagnetic one. Once again, the upper bounds $4D_x$ and $4D_{zz}$ lie very close to M_2.

9.4.4 Infinite-range Ising model

For completeness, we consider the case of an infinite-range Ising ferromagnet, with classical energy

$$E_\sigma = -\frac{1}{2N}\sum_{i\neq j}\sigma_i\sigma_j \tag{9.29}$$

$$= -\frac{1}{2N}\left(\sum_i \sigma_i\right)^2 + 1/2\,, \tag{9.30}$$

which becomes again analytically tractable. Hereafter, we shall neglect the trivial constant energy shift in the last line.

The partition function of the infinite-range model can be evaluated by first recasting it to a Gaussian integral and then performing a saddle-point approximation, which is exact in the thermodynamic limit $L \to \infty$ (see e.g., Ref. [159]). Explicitly, the free energy is given by

$$\beta F/N = \frac{\beta}{2}m^2 - \log\left[2\cosh(\beta m)\right]\,, \tag{9.31}$$

where the saddle point magnetisation is found by solving the self-consistency equation

$$m = \tanh(\beta m)\,. \tag{9.32}$$

The system exhibits a second-order phase transition at $T_c = 1$ between the ferromagnetic and the paramagnetic phase.

The evaluation of $\beta F_M = -\log Z_M$ follows along the same lines. First, we write the partition function as

$$\begin{aligned} Z_M \;=\; & \sum_\sigma \exp\left[\frac{\beta}{4N}\sum_{a=1}^4\left(\sum_i \sigma_i^{(a)}\right)^2\right. \\ & \left. +\frac{\beta}{4N}\sum_{a=1}^4\left(\sum_i\prod_{b\neq a}\sigma_i^{(b)}\right)^2\right]\,. \end{aligned} \tag{9.33}$$

Then, we make use of the identity

$$e^{\alpha x^2/2} = \sqrt{\frac{\alpha N}{2\pi}}\int_{-\infty}^{\infty} dm\, e^{-N\alpha m^2/2+\sqrt{N}\alpha m x} \tag{9.34}$$

to obtain

$$Z_M = \left(\frac{\beta N}{4\pi}\right)^4 \int_{-\infty}^{\infty}\prod_{a=1}^4 dm_a \prod_{b=1}^4 dq_b \tag{9.35}$$

$$\times \exp\left[-\frac{N\beta m_a^2}{4} - \frac{N\beta q_b^2}{4} + N\beta\tilde{F}\right]\,, \tag{9.36}$$

where

$$e^{\beta\tilde{F}} = \sum_{\eta^{(1,\ldots,4)}=\pm 1} \exp\left[\sum_a \frac{\beta m_a}{2}\eta^{(a)} + \sum_b \frac{\beta q_b}{2}\prod_{c\neq b}\eta^{(c)}\right]\,.$$

In the limit $L \to \infty$, we can evaluate the above integral using the saddle-point approximation, such that the free energy is given by

$$\beta F_M = \frac{N\beta}{4} \sum_a m_a^2 + \frac{N\beta}{4} \sum_b q_b^2 - N\beta \tilde{F}. \tag{9.37}$$

Taking partial derivative with respect to all m_a and q_b, we obtain the self-consistent equations

$$m_a = \frac{\sum \eta^{(a)} \exp\left[\sum_c \frac{\beta m_c}{2} \eta^{(c)} + \sum_d \frac{\beta q_d}{2} \prod_{c\neq d} \eta^{(c)}\right]}{\sum \exp\left[\sum_c \frac{\beta m_c}{2} \eta^{(c)} + \sum_d \frac{\beta q_d}{2} \prod_{c\neq d} \eta^{(c)}\right]}, \tag{9.38}$$

and

$$q_b = \frac{\sum \prod_{c\neq b} \eta^{(c)} \exp\left[\sum_c \frac{\beta m_c}{2} \eta^{(c)} + \sum_d \frac{\beta q_d}{2} \prod_{c\neq d} \eta^{(c)}\right]}{\sum \exp\left[\sum_c \frac{\beta m_c}{2} \eta^{(c)} + \sum_d \frac{\beta q_d}{2} \prod_{c\neq d} \eta^{(c)}\right]}, \tag{9.39}$$

respectively, for $a, b = 1, 2, 3, 4$. The outer summations above are over $\eta^{(1)}, \eta^{(2)}, \eta^{(3)}, \eta^{(4)} = \pm 1$. The quantity m_a corresponds to the magnetization of the a-th layer,

$$m_a = \frac{1}{N} \left\langle \sum_i \sigma_i^{(a)} \right\rangle . \tag{9.40}$$

while q_b corresponds to

$$q_b = \frac{1}{N} \left\langle \sum_i \prod_{c\neq b} \sigma_i^{(c)} \right\rangle . \tag{9.41}$$

The procedure outlined above can be straightforwardly generalized to higher (integer) index $n > 2$. If we assume, by symmetry, that the solution satisfies $m_1 = m_2 = ... = m_{2n} = q_1 = ... = q_{2n} = m$ [2], then the self-consistent equations simplify to

$$m = \frac{\cosh(\beta m)^{2n-1} \sinh(\beta m) + \sinh(\beta m)^{2n-1} \cosh(\beta m)}{1 + \cosh(\beta m)^{2n} + \sinh(\beta m)^{2n}} \tag{9.42}$$

One can verify that Eq. (9.42) always admits $m = 0$ as a solution, which minimizes F_M at high temperature; it also admits the solution $m = 1$, which minimizes F_M at $T = 0$, and the transition between the two is first-order.

We solve Eq. (9.42) numerically and compute M_n for $n \in \{2, 3, 4, 5, 6, 7, 8\}$ (see Fig. 9.5). In the limit $n \to \infty$, Eq. (9.42) reduces to $m = \tanh(\beta m)$, which is exactly the self-consistent equation for the infinite-range model. This implies that $M_n \to 0$ as $n \to \infty$, as expected.

Furthermore, D_x and D_{zz} can be computed directly from Eq. (9.19) and (9.21), respectively, using the free energy in Eq. (9.31). We plot them along the SREs in Fig. 9.5.

Similarly to the 3D Ising ferromagnet, and contrary to the 2D case, the cusp (and maximum) of M_2 occurs well within the ferromagnetically ordered phase. In fact, the behavior of M_2 along with D_x and D_{zz} are very similar to the 3D case. Interestingly, the stabilizer bound to the magic is exactly met by D_x for any T larger than the

[2] The symmetry between m_a and q_b may not be immediately obvious, but it can be seen as follows: for each site i in the layer a, define spin $s_i^{(a)} = \prod_{c\neq a} \sigma_i^{(c)}$. After this change of variable, we obtain $q_a = \frac{1}{N} \left\langle \sum_i s_i^{(a)} \right\rangle$ and $m_b = \frac{1}{N} \left\langle \sum_i \prod_{c\neq b} s_i^{(c)} \right\rangle$. Namely, the role of m_a and q_b is interchanged after the change of variable.

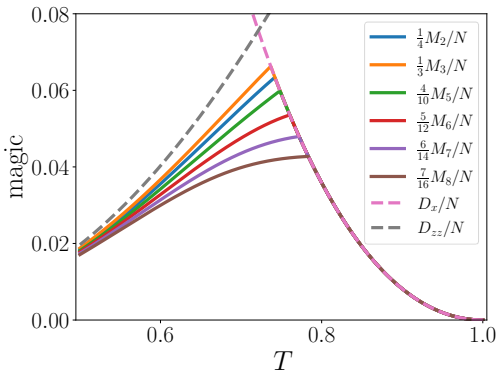

FIGURE 9.5: Magic and stabilizer bounds for the SMF infinite-range Ising ferromagnet. For each n, we plot $\frac{n-1}{2n}M_n/N$, which are upper bounded by D_x and D_{zz} by Eq. (9.5). The system undergoes a quantum phase transition at $T_c = 1$.

cusp value. This is because in this regime $\log Z_{M,n} = 2n \log 2$, while $\log Z(\beta/2) = \log 2$ in Eq. (9.19), which implies $M_n = \frac{2n}{n-1}D_x$. By Eq. (9.5), it follows that $D_{\min} = \frac{n-1}{2n}M_n$ for any T larger than the cusp value of an index n. For $T \geq 1$, all M_n and D_x vanish, i.e., the states are asymptotically close to the stabilizer state $|+++...\rangle$.

9.4.5 J1-J2 model and first order behaviour

Up to now we considered quantum SMF Hamiltonians that exhibit continuous phase transitions. Here we investigate what happens at a first order quantum phase transition by looking at the SMF J_1-J_2 Ising model on the square lattice, related to a classical model with energy

$$E_\sigma = -J_1 \sum_{\langle ij \rangle} \sigma_i \sigma_j + J_2 \sum_{\langle\langle ij \rangle\rangle} \sigma_i \sigma_j \,, \tag{9.43}$$

where $J_1, J_2 > 0$. The first term corresponds to a ferromagnetic Ising nearest-neighbour interaction, while the second term is an antiferromagnetic interaction across the diagonals of the square plaquettes. For an appropriate choice of the system parameters, e.g., when the ratio $g = J_1/J_2 = 0.55$, the system exhibits a first-order transition between a high-temperature paramagnetic phase and a low-temperature stripe phase at $T_c \approx 0.772$ (setting $J_1 = 1$ as the reference energy scale) [100]. In the stripe phase, the ground states are fourfold degenerate, and can be understood as two decoupled antiferromagnetic ground states.

We also observe a first order phase transition in the associated coupled layered system Z_M, but at a higher temperature T^*, well into the paramagnetic phase (as in the 2D Ising ferromagnet, and contrary to 3D and infinite-range). Therefore, in this system we expect two discontinuities in the first derivative of M_2 with respect to T: One at the quantum phase transition (T_c), where the slope is positive on both sides and approximately doubles across it; the other at T^*, where the slope changes sign abruptly, giving rise once again to a maximum in M_2, where a cusp occurs.

In Fig. 9.6 we also compare M_2 with the bounds provided by the paramagnetic (D_x, asymptotically accurate for $T \to \infty$) and stripe (D_{stripe}, asymptotically accurate for $T \to 0$) phases. The latter appears to be remarkably close for all $T < T^*$.

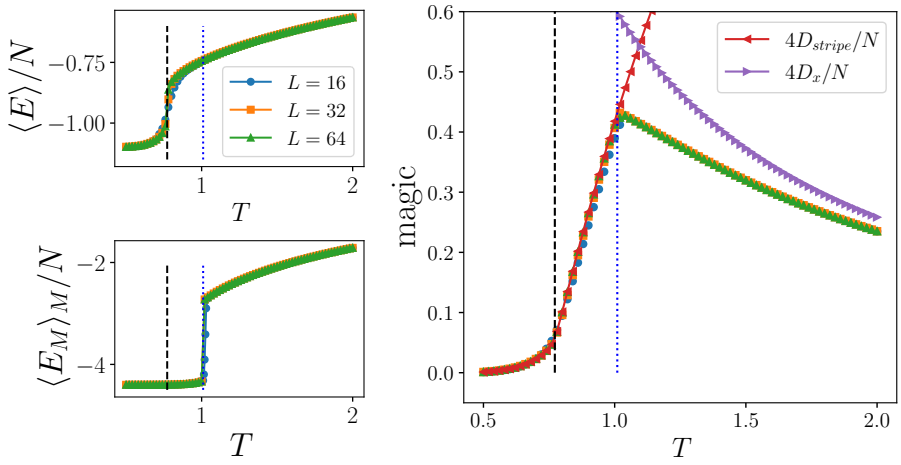

FIGURE 9.6: Magic and stabilizer bounds for the SMF 2D J_1-J_2 Ising model. The top panels show the behaviour of $\langle E\rangle$ and $\langle E_M\rangle_M$, and the bottom panel shows the SRE density M_2/N (same system sizes). The vertical dashed lines indicate the location of the quantum phase transition, whereas the vertical dotted lines indicate the location of the transition in the coupled layered system Z_M (resulting in a cusp in the magic M_2).

9.4.6 Antiferromagnetic triangular Ising model

We now proceed to a more exotic model where the quantum SMF Hamiltonian is related to the classical antiferromagnetic triangular Ising model [160, 161], with energy

$$E_\sigma = \sum_{\langle ij\rangle} \sigma_i \sigma_j, \tag{9.44}$$

where the spins σ_i live on the sites of a triangular lattice, $i = 1, \ldots, N$. The model features an extensive ground state degeneracy with algebraically decaying correlations at $T = 0$, while it is disordered at all temperatures $T \neq 0$ [160].

We first show that the classical system described by Z_M also features an extensive ground state degeneracy. To this end, we provide a lower bound on the zero-point entropy by explicitly constructing an extensive set of states with lowest energy. To do so, let us divide the triangular lattice on each layer into three sublattices. Let us then fix the spins on two of the sublattices to 1 and -1, respectively, with the same choice for all four layers. One can then straightforwardly verify that the spins on the remaining sublattice on each layer can be chosen arbitrarily without affecting the energy E_M of the system, and that the latter is indeed minimised. The number of such states is $2^{4N/3}$, which implies

$$S_M(0) \geq \frac{4N}{3} \ln 2\,. \tag{9.45}$$

As one can straightforwardly think of other configurations that minimize the energy, this bound is not tight.

We find that the corresponding Z_M features a phase transition that appears to be first-order, as displayed in Fig. 9.7, albeit of a less strong nature than in the cases discussed previously. Once again, M_2 exhibits a cusp at the transition point T^* of the classical system described by Z_M.

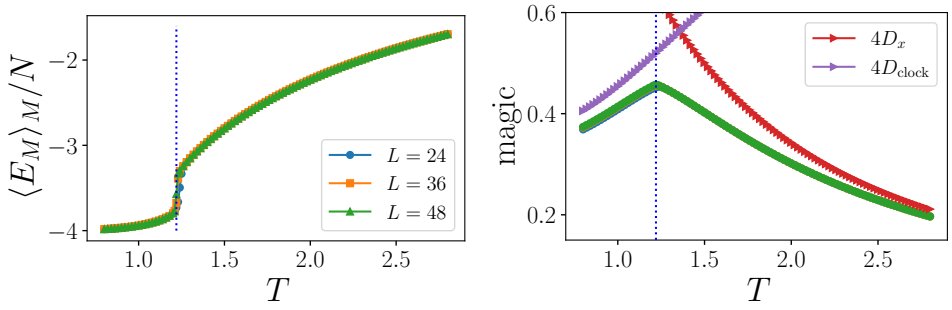

FIGURE 9.7: Magic and stabilizer bounds for the SMF triangular antiferromagnetic Ising model. The top panel shows the behaviour of $\langle E_M \rangle_M$, and the bottom panel shows the SRE density M_2/N (same system sizes). The vertical dotted lines indicate the location of the transition in the coupled layered system Z_M (resulting in a cusp in the magic M_2).

Unlike in the other models considered so far, in this case the ground state at $T = 0$ is not a stabilizer state. We note that the configurations with the three sublattice structure given above is also known as the clock state, which arises as the quantum ground state of the quantum triangular Ising antiferromagnet at small magnetic field [162–165]. While it is not the exact ground state for $T = 0$, it constitutes a significant part of the ground state. Thus, we compare M_2 with $D_{\text{clock}}(|\psi\rangle) = D(|\psi\rangle, |\phi\rangle)$ where $|\phi\rangle$ is the clock state defined above, which is a stabilizer state. D_{clock} is obtained in a similar way as D_{zz} (see Sec. 9.3.2). At $T = 0$, D_{clock} is given by

$$D_{\text{clock}}(T = 0) = S(0) - \frac{N}{3} \ln 2 \,, \tag{9.46}$$

where $S(0) \simeq 0.3383\, N$ is the zero-point entropy of the antiferromagnetic triangular Ising model [160]. On the other hand, M_2 is given by

$$M_2(T = 0) = 4S(0) - S_M(0) \,. \tag{9.47}$$

This is obtained by setting $T = 0$ in Eq. (9.13). In this case, the observation that $4D_{\text{clock}}$ is strictly larger than M_2 can be attributed to the fact that the zero-point entropy $S_M(0)$ is strictly larger than $\frac{4N}{3} \ln 2$. In turn, this is also a manifestation of the fact that the ground state of the classical system described by $Z(T)$ is not a stabilizer state for $T = 0$.

9.4.7 Edwards-Anderson model

Finally, we consider an example of a disordered system, where the quantum SMF Hamiltonian is related to the Edwards-Anderson (EA) model, with energy

$$E_\sigma = -\sum_{\langle ij \rangle} J_{ij} \sigma_i \sigma_j \,, \tag{9.48}$$

where the spins σ_i live on the 3D cubic lattice. Here, the couplings J_{ij} are independently drawn from a Gaussian distribution with zero mean and unit variance. The system is known to undergo a continuous transition from the high-temperature phase to the low-temperature spin glass phase at $T_c \approx 0.95$ [166].

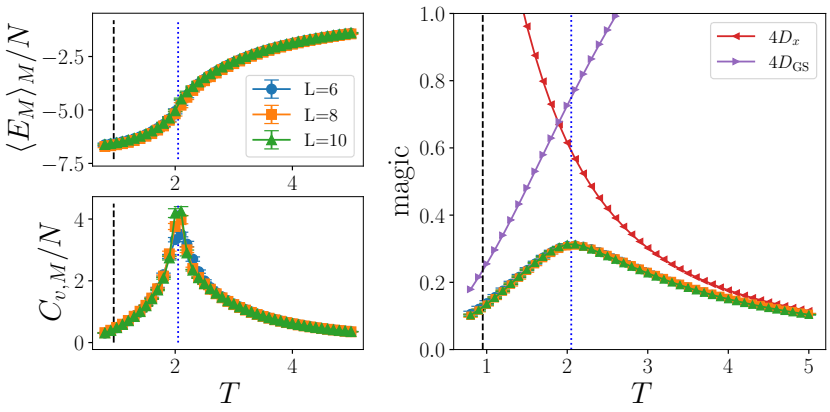

FIGURE 9.8: Magic and stabilizer bounds for the 3D SMF EA model. The top panels show the behaviour of $\langle E_M \rangle_M$ (left) and of the specific heat $C_{v,M}$ (right), and the bottom panel shows the SRE density M_2/N (all for the same set of system sizes). The vertical dashed lines indicate the location of the quantum phase transition, whereas the vertical dotted lines indicate the location of the transition at T^* in the coupled layered system Z_M (resulting in a maximum in the magic M_2). The results are averaged over 100, 50, and 30 realizations for linear sizes $L = 6, 8, 10$, respectively.

This model has a unique ground state for any realization of J_{ij} (up to global spin flip). For system sizes up to $L = 10$, the exact ground states and their energy can be readily obtained using the McGroundstate server [167].

We show the energy $\langle E_M \rangle_M$, the specific heat $C_{v,M}$ and the magic M_2 in Fig. 9.8. Again, the maximum occurs well into the paramagnetic phase, at the transition point of the coupled layered system Z_M. Unlike in the previous cases, where the first order behaviour of the Z_M transition was self-evident because of the noticeable discontinuity in $\langle E_M \rangle_M$, the situation is less clear-cut here. While the maximum of the specific heat appears to grow slower than N, suggesting a second order transition, we are unable to identify a clear scaling of the specific heat within the accessible system sizes. We further compute equilibrium energy histograms at different temperatures around T^*, shown in Fig. 9.9. The behaviour closely resembles a trade off between two different peaks, whose positions are approximately temperature-independent (although we are unable to see the minimum in between them scale to zero as a function of system size, within the systems accessed in this work). Overall, we suggest that the transition in this model is weakly first-order.

In Fig. 9.8 we also compare M_2 with bounds from D_x and D_{GS}, where D_{GS} is obtained from the overlaps with the exact ground state for each realization, computed by thermodynamic integration as discussed in Sec. 9.3.2, using the McGroundstate server [167] to obtain the exact ground state energy. In this case, the bounds are somewhat higher than encountered in previous cases. Nevertheless, the crossing between D_x and D_{GS} still occurs close to the maximum of M_2.

Finally, we investigate the nature of the low-temperature phase of Z_M. A natural candidate is a spin glass phase, accompanied by replica symmetry breaking (RSB), akin to the low-temperature phase of the 3D EA model. To detect RSB, we compute the spin overlap

$$q = \frac{1}{N} \sum_{i=1}^{N} \langle \sigma_i^{\alpha} \sigma_i^{\beta} \rangle \,, \tag{9.49}$$

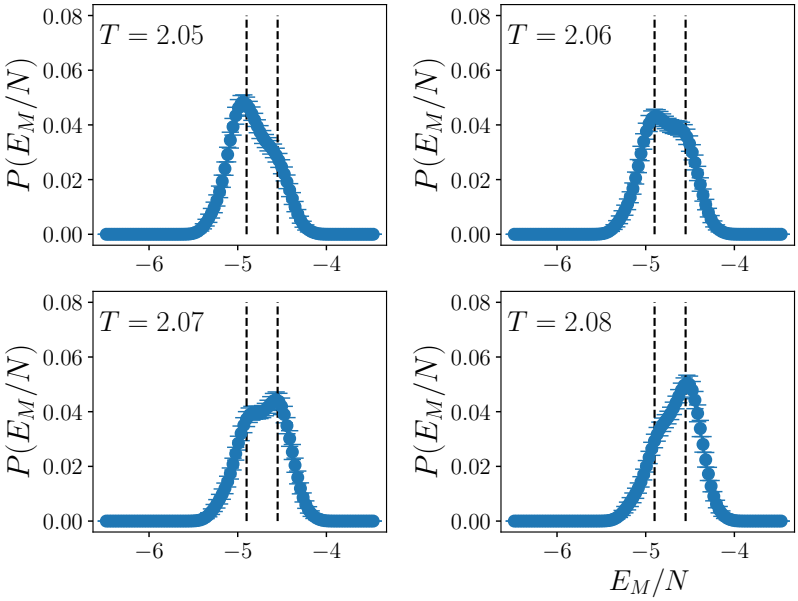

FIGURE 9.9: Energy histograms of the coupled layered system Z_M corresponding to the 3D EA model, in thermodynamic equilibrium at different temperatures for a system of size $L = 12$. The vertical dashed lines are guides to the eye tracking the (same) location location of the two peaks across the panels.

where α and β represents two copies of the system with the same disorder. We show the spin overlap in the coupled system Z_M in Fig. 9.10. It can be seen that the spin overlap is vanishing in the high-temperature paramagnetic phase, while it becomes non-zero in the low-temperature phase, signifying RSB.

9.5 Conclusions

We introduced a way to compute the SRE [19] with integer Renyi index $n > 1$ in terms of wavefunction coefficients in many body systems, that make it amenable to efficient computation using Monte Carlo sampling. We applied this approach to generalized Rokhsar-Kivelson systems whose Hamiltonians allow a stochastic

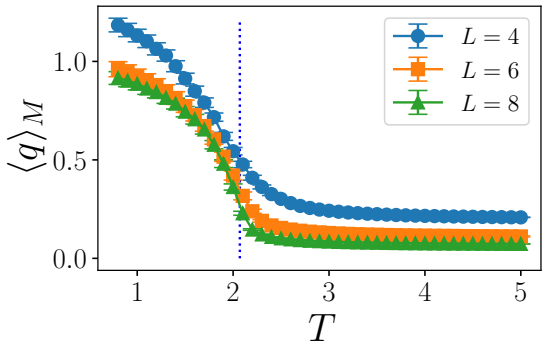

FIGURE 9.10: Spin overlap $\langle q \rangle_M$ for the coupled layered system Z_M corresponding to the 3D EA model, for system sizes $L \in \{4, 6, 8\}$.

matrix form decomposition [144]. Thanks to the known correspondence between ground states of these systems and associated classical statistical mechanics problems, we have been able to express the SRE in terms of classical free energy differences, which can be efficiently computed by thermodynamic integration. Crucially, temperature plays the role of a tunable parameter in the quantum Hamiltonians, allowing us to drive these systems across quantum phase transitions and study the behaviour of their SRE. With this approach we were able to study the SRE of large high-dimensional systems, unattainable using existing tensor network-based techniques, and in some cases obtaining explicit analytical results.

We applied this insight to a range of quantum many body SMF Hamiltonians, encompassing the Ising ferromagnet in 1D, 2D, 3D, and infinite dimensions; the $J_1 - J_2$ model on the square lattice (exhibiting a first order transition); the triangular Ising antiferromagnet (fully frustrated, devoid of ordering); and the Edwards-Anderson model on the cubic lattice (which undergoes a glass transition). Generally, we observed that the behaviour of the SRE is relatively featureless across quantum phase transitions in these systems, although it is indeed singular in its first or higher order derivative, depending on the first or higher order nature of the transition. We found that the maximum of the SRE generically occurs at a cusp away from the quantum critical point, where the derivative suddenly changes sign. Curiously, the cusp appears to occur in the disordered phase in two dimensions, and in the ordered phase in higher dimensions, suggesting that it may be altogether unrelated to the ordering behaviour of the quantum system.

We further compared the SRE to the logarithm of overlaps with specific stabilizer states, that are asymptotically realised in the ground state phase diagrams of these systems. We find that they display strikingly similar behaviors, which in turn establish rigorous bounds on the min-relative entropy of magic.

In our work we were able to make some progress in understanding the behaviour of the magic and its maximum in many body quantum (SMF) systems, throughout their phase diagrams, in terms of partition functions and thermodynamic properties of associated classical problems, and by comparing it with overlaps of asymptotic stabilizer states. One wonders whether further progress could be made using field theoretic approaches for the associated classical problems, in particular ε-expansions just above 2D or just below 3D to shed light on the location of the SRE maximum with respect to the quantum phase transitions. We shall leave these and other interesting open questions for future work.

As we discussed at the end of Sec. 9.4.2, our results for the 2D SMF Ising ferromagnet straightforwardly extend to the toric code [168] and SMF variations thereof [157], which are some of the simplest examples of $\mathbb{Z}_2$ lattice gauge theories. It will be interesting to consider other quantum SMF Hamiltonians constructed from classical systems that exhibit an emergent gauge symmetry, such as dimer [169, 170], (spin) ice [171–173] and vertex models in general. Simulating these systems in their low temperature phases typically requires the use of loop updates, which pose a nontrivial challenge for the partition function Z_M introduced in Sec. 9.3.1, and is beyond the scope of the present work.

Chapter 10

Nonstabilizerness via matrix product states in the Pauli basis

In this chapter, we demonstrate how, for states represented by matrix product states (MPS), several nonstabilizerness measures can be cast in the language of tensor networks (TN) [42, 174–178], whose contractions can be approximated using standard algorithms. More concretely, we represent the Pauli spectrum of the state as an MPS, cf. Fig. 10.1 (a,b). This allows one to compute not only the SRE, but also Bell magic, which has so far not been quantified in large systems, as it is too costly to compute by existing methods. For the SRE in particular, we express it as a two-dimensional tensor network as shown in Fig. 10.1 (c), thereby enabling approximate contraction using established MPS methods. Furthermore, we explain how our framework leads to efficient computation of stabilizer nullity, a genuine nonstabilizerness monotone, which in turn allows us to identify the stabilizer group of the state. We benchmark our method through various examples, including the quantum Ising chain, the XXZ chain, and random Clifford circuits with nonstabilizer states input. We further applied our method to compute Bell magic in a scrambling circuit (see Fig. 10.1 (d)) recently experimentally implemented in Rydberg atom arrays [7]. Reaching system sizes beyond the current experimental capabilities, our method can thus be used to verify and benchmark future experiments.

10.1 MPS in the Pauli basis

Let us consider a system of N qubits in a pure state $|\psi\rangle$ given by an MPS of bond dimension χ:

$$|\psi\rangle = \sum_{s_1,s_2,\cdots,s_N} A_1^{s_1} A_2^{s_2} \cdots A_N^{s_N} |s_1, s_2, \cdots s_N\rangle \tag{10.1}$$

with $A_i^{s_i}$ being $\chi \times \chi$ matrices, except at the left (right) boundary where $A_1^{s_1}$ ($A_N^{s_N}$) is a $1 \times \chi$ ($\chi \times 1$) row (column) vector. Here $s_i \in \{0, 1\}$ is a local computational basis. The state is assumed right-normalised, namely $\sum_{s_i} A_i^{s_i\dagger} A_i^{s_i} = 1$. Let us define the binary string $\boldsymbol{\alpha} = (\alpha_1, \cdots, \alpha_N)$ with $\alpha_j \in \{00, 01, 10, 11\}$. The Pauli strings are defined as $P_{\boldsymbol{\alpha}} = P_{\alpha_1} \otimes P_{\alpha_2} \otimes \cdots \otimes P_{\alpha_N}$ where $P_{00} = I$, $P_{01} = \sigma^x$, $P_{11} = \sigma^y$, and $P_{10} = \sigma^z$. We define the Pauli vector of $|\psi\rangle$ as $|P(\psi)\rangle$ with elements $\langle \boldsymbol{\alpha}|P(\psi)\rangle = \langle\psi|P_{\boldsymbol{\alpha}}|\psi\rangle/\sqrt{2^N}$. Also known as the Pauli spectrum [34], this was recently studied in the context of many-body systems [21]. When $|\psi\rangle$ has an MPS structure as in Eq. (10.1), the Pauli vector can also be expressed as an MPS as follows

$$|P(\psi)\rangle = \sum_{\alpha_1,\alpha_2,\cdots,\alpha_N} B_1^{\alpha_1} B_2^{\alpha_2} \cdots B_N^{\alpha_N} |\alpha_1, \cdots, \alpha_N\rangle \tag{10.2}$$

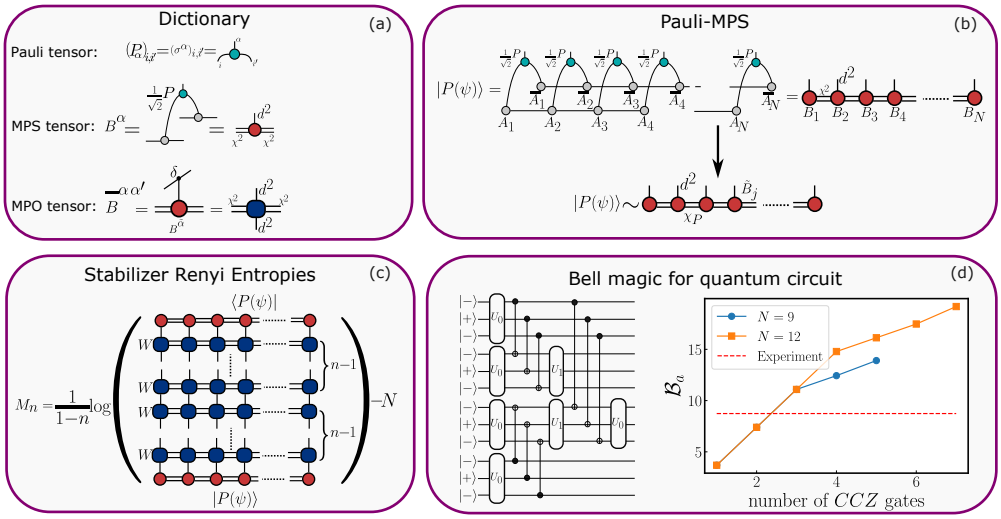

FIGURE 10.1: (a) Definitions of tensors used for the construction of Pauli-MPS. (b) Construction of Pauli-MPS. (c) The SRE represented as the contraction of a two-dimensional tensor network. (d) The additive Bell magic in a scrambling circuit recently experimentally realized in Ref. [7]. The red dashed line indicates the highest value of the additive Bell magic experimentally measured in Ref. [7].

where $B_i^{\alpha_i} = \sum_{s,s'} \langle s|P_{\alpha_i}|s'\rangle A_i^s \otimes \overline{A_i^{s'}}/\sqrt{2}$ are $\chi^2 \times \chi^2$ matrices, as shown in Fig. 10.1. Note that the MPS is normalized due to the relation $\frac{1}{2^N}\sum_{\boldsymbol{\alpha}} \langle\psi|P_{\boldsymbol{\alpha}}|\psi\rangle^2 = 1$ which holds for pure states. Moreover, it retains the right normalization, due to the identity $\frac{1}{2}\sum_{\alpha} P_\alpha(\cdot)P_\alpha = \mathbb{1}\,\mathrm{Tr}[\cdot]$. Consequently, the entanglement spectrum of $|P(\psi)\rangle$ is given by $\lambda'_{i,j} = \lambda_i\lambda_j$ for $i,j = 1,2,\cdots,\chi$, where λ_i is the entanglement spectrum of $|\psi\rangle$, and hence the von Neumann entropy is doubled. Note also that the coefficients of $|P(\psi)\rangle$ in the Pauli basis (10.2) are real, since the Pauli operators are Hermitian for spin-1/2 systems, although the local tensors B_i are not necessarily real.

Since the Pauli operators provide an orthonormal basis in the space of Hermitian operators, one can expand the density matrix as $|\psi\rangle\langle\psi| = \frac{1}{2^N}\sum_{\mathbf{ff}} \langle\psi|P_{\boldsymbol{\alpha}}|\psi\rangle P_{\boldsymbol{\alpha}}$. Therefore, the Pauli spectrum is simply the coefficients of $|\psi\rangle\langle\psi|$ in the basis of Pauli operators, i.e., the Pauli basis. As we show below, the MPS representation in the Pauli basis provides a powerful and versatile tool to compute various measures of nonstabilizerness. Specifically, we will consider the measures SRE [19], stabilizer nullity [34], and Bell magic [37]. We refer to Sec. 6.4 for their detailed definitions and properties.

10.2 Replica Pauli-MPS

The replica method in MPS was introduced to compute the SRE of MPS in Ref. [25]. While exact, for practical purposes, the original formulation performed inferiorly with respect to Pauli sampling methods due to the extremely high cost with respect to the bond dimension [23, 27, 28]. Indeed, evaluating the SRE for an integer index $n > 1$ required a computational cost of $O\left(\chi^{6n}\right)$, rendering it impractical for even the simplest case $n = 2$, where previous computations were restricted to $\chi = 12$ [23, 25]. Note that sampling methods have their own limitations, as the number of samples

has to scale exponentially [1]. Here, we show that the MPS in the Pauli basis can be exploited to significantly reduce the cost of the replica trick, opening doors for its use in practical application and making it superior also compared to sampling methods in terms of computational efficiency and scalability.

To do so, we define a diagonal operator W whose diagonal elements are the components of the Pauli vector, $\langle \boldsymbol{\alpha'}|W|\boldsymbol{\alpha}\rangle = \delta_{\boldsymbol{\alpha'},\boldsymbol{\alpha}}\langle \boldsymbol{\alpha'}|P(\psi)\rangle$. The MPO form of W reads

$$W = \sum_{\boldsymbol{\alpha},\boldsymbol{\alpha'}} \overline{B}_1^{\alpha_1,\alpha'_1}\overline{B}_2^{\alpha_2,\alpha'_2}\cdots\overline{B}_N^{\alpha_N,\alpha'_N}|\alpha_1,\cdots,\alpha_N\rangle\langle\alpha'_1,\cdots,\alpha'_N| \tag{10.3}$$

where $\overline{B}_i^{\alpha_i,\alpha'_i} = B_i^{\alpha_i}\delta_{\alpha_i,\alpha'_i}$. Applying $n-1$ times W to $|P(\psi)\rangle$, we obtain $|P^{(n)}(\psi)\rangle = W^{n-1}|P(\psi)\rangle$, which is a vector with elements $\langle\boldsymbol{\alpha}|P^{(n)}(\psi)\rangle = \langle\psi|P_{\boldsymbol{\alpha}}|\psi\rangle^n/\sqrt{2^{Nn}}$. We denote the local tensors of $|P^{(n)}(\psi)\rangle$ by $B_i^{(n)\alpha_i}$. We have

$$\frac{1}{2^{Nn}}\sum_{\boldsymbol{\alpha}}\langle\psi|P_{\boldsymbol{\alpha}}|\psi\rangle^{2n} = \langle P^{(n)}(\psi)|P^{(n)}(\psi)\rangle \tag{10.4}$$

and [2]

$$M_n = \frac{1}{1-n}\log\langle P^{(n)}(\psi)|P^{(n)}(\psi)\rangle - N. \tag{10.5}$$

The exact bond dimension of $|P^{(n)}\rangle$ is $\min\left(\chi^{2n}, 4^{N/2}\right)$, i.e., for large systems it grows exponentially with the order n, as the cost in Ref. [25]. However, by interpreting it as the repeated application of a MPO W onto an MPS, we can sequentially compress the resulting MPS after every iteration, and keep the best description of the resulting state as a MPS with some upper-bounded bond dimension χ_n. This can be done with standard tensor network routines used, e.g., in the simulation of time evolution [179, 180]. These methods allow us to monitor the error of the truncation, for example, by doing convergence analysis [3].

The Pauli-MPS itself can also be approximated with a bond dimension $\chi_P < \chi^2$. The computational cost of this compression is $O\left(\chi_P^2\chi^2 + \chi^3\chi_P\right)$. This is particularly advantageous for states with exponentially decaying entanglement spectrum (e.g. in gapped phases), in which case χ_P can be truncated to a value much smaller than χ^2. Assuming $\chi_P \approx \chi$, this results in the overall cost of $O\left(N\chi^4\right)$. By comparison, the computational cost of direct Pauli sampling is $O\left(NN_S\chi^3\right)$ [23, 27], where N_S is the number of samples. Consequently, our method becomes superior compared to the latter when $N_S \gtrsim \chi$. Since N_S typically grows exponentially with N for the estimation of M_2, our method offers significant efficiency gains for large N, for states with bounded χ. Although this is at the cost of introducing an approximation, convergence can be controlled by monitoring truncation error, a standard practice in tensor networks. On the other hand, if χ scales exponentially (e.g. in volume-law phases), our method may become too expensive compared to sampling.

[1] The required number of samples is polynomial for M_1, and hence its estimation is efficient. However, it has been shown in Ref. [23] that M_1 is not a good measure of nonstabilizerness, unlike M_n for $n \geq 2$.

[2] We note that, since $|P^{(n)}(\psi)\rangle$ is real, the computation of the norm does not require complex conjugation.

[3] Notice that we aim to compute the same object as the method in Ref. [25], namely the expectation value of $2n$ replicas of Pauli operators. The computational advantage of our approach stems from reorganizing the order of contractions and applying a controlled approximation. Notice also that the physical dimension in our approach is constantly 4, while Ref. [25] requires a physical dimension of $2^{2(n-1)}$, which grows exponentially with n.

We benchmarked the method in the XXZ chain, whose Rényi-2 SRE could not be computed accurately for $N > 30$ in the previous study [23] In addition, as a concrete application, we calculated the SRE in the quantum Ising chains, $H_{\text{Ising}} = -\sum_{\langle i,j\rangle} \sigma_i^x \sigma_j^x - h\sum_i \sigma_i^z$, previously considered in Refs. [25, 28, 43, 109]. We obtain the ground states using DMRG with $\chi = 40$ and compute the SRE using replica Pauli-MPS, imposing a truncation error threshold of $\epsilon = 10^{-9}$. Fig. 10.2 shows the derivatives of the SRE around the critical point $h = 1$. We observe that the second derivative appears to diverge at the critical point, mirroring the results of Ref. [29] for Rokhsar-Kivelson states. These results further solidify the role of nonstabilizerness as a useful diagnostic tool for identifying criticality in quantum systems [25, 28, 29, 181]. Note that calculating derivatives with sampling-based approaches become increasingly challenging with the derivative order due to the presence of statistical errors.

We further notice that the norm of $|P^{(n)}(\psi)\rangle$ can be interpreted as the contraction of a two-dimensional tensor network (see Fig. 10.1 (c)). This allows for alternative strategies to perform the contraction. For example, one can perform the contraction in the transversal (space) direction [182–184]. To do so, we first contract the $2n$ tensors in the first site to form a transfer matrix with $2n$ indices, each with bond dimension χ^2. Then, we iteratively absorb the tensors on the right to the transfer matrix, up until the rightmost tensors. Without compression, the cost of this contraction scheme is $O\left(\chi^{4n+2}\right)$, which is cheaper than the exact contraction in the direction of Rényi index, or the contraction in Ref. [25]. Of course, the contractions can also be done approximately by representing the transfer matrix as an MPS. Whether or not this would yield a better performance compared to the approximate contraction in the direction of Rényi index is an intriguing question that we leave for future research avenue.

In the case of translation-invariant (TI) MPS in the thermodynamic limit, we can compute the SRE by introducing the transfer matrix

$$\begin{aligned}\tau &= \sum_\alpha B^{(n)\alpha} \otimes B^{(n)\alpha} \\ &= \sum_\alpha (B^\alpha)^{\otimes 2n}.\end{aligned} \tag{10.6}$$

Here, we recall that $B^{(n)\alpha}$ is the local tensor of $|P^{(n)}(\psi)\rangle$, which is site independent for TI MPS. The transfer matrix τ is identical to the one introduced in Ref. [25], however the local tensors that build τ differ. In particular, with our approach, the transfer matrix can be viewed as an MPO with physical dimension χ^2 and constant bond dimension of 4, i.e., the MPO satisfies an area law. The calculation of the SRE is then reduced to the computation of the dominant eigenvalue of τ. This can be done by approximating the dominant eigenvector $|L\rangle$ as an MPS, and performing power iteration or Lanczos algorithm by repeated MPO-MPS multiplication.

10.3 Generalization to Matrix Product Operator

The technique presented above can be straightforwardly adapted to matrix product operators (MPO), which represent mixed states. We consider a density matrix O of N qubits represented in the following MPO form:

$$O = \sum_{\boldsymbol{s},\boldsymbol{s'}} U_1^{s_1,s'_1} U_2^{s_2,s'_2} \cdots U_N^{s_N,s'_N} |s_1,\cdots,s_N\rangle\langle s'_1,\cdots,s'_N| \tag{10.7}$$

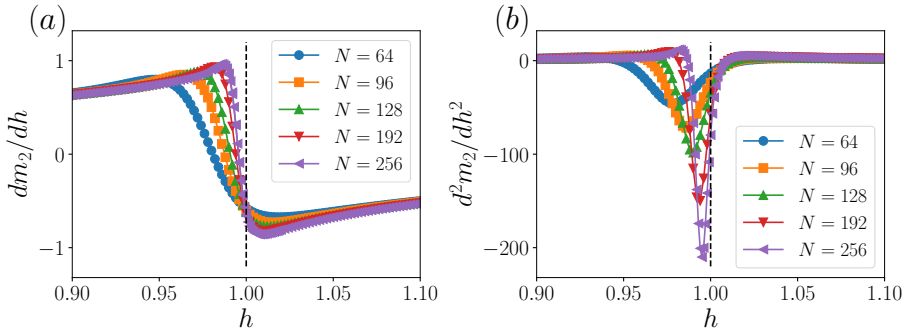

FIGURE 10.2: (a) The first and (b) second derivative of the SRE density $m_2 = M_2/N$ in the ground states of the quantum Ising chain as a function of the transverse field h.

with $U_i^{s_i,s_i'}$ being $\chi \times \chi$ matrices, except at the left (right) boundary where $U^{s_1,s_1'}$ (or $U^{s_N,s_N'}$) is a $1 \times \chi$ ($\chi \times 1$) row (column) vector.

The Pauli vector $|P(O)\rangle$ can be obtained in a similar way as in MPS, namely

$$|P(O)\rangle = \sum_{\boldsymbol{\alpha}} V_1^{\alpha_1} V_2^{\alpha_2} \cdots V_N^{\alpha_N} |\alpha_1, \cdots, \alpha_N\rangle \tag{10.8}$$

where $V_i^{\alpha_i} = \sum_{a,b} \langle a|P_{\alpha_i}|b\rangle U_i^{a,b}/\sqrt{2}$ are $\chi \times \chi$ matrices. The procedure above can be seen as MPO version of the method recently discussed in Ref. [185] to obtain Pauli vector representation from the full density matrix. Notice that, unlike in the MPS case, in this case the bond dimension remains the same. Indeed, the transformation above is simply a local basis transformation from the computational basis to the Pauli basis. Note also that the norm of $|P(O)\rangle$ is $\mathrm{Tr}\left[O^2\right]$, which is generally different from 1. Using $|P(O)\rangle$, one can compute the SRE in the same way as in the MPS case. However, we note that the SRE is only faithful for pure states. Nevertheless, we expect that this technique could be useful, e.g., to compute the mana [17, 120, 186], which is a good nonstabilizerness measure for mixed states.

10.4 Bell magic

Next, we consider Bell magic [25], that has recently been experimentally measured in Ref. [7]. To compute Bell magic, we first evaluate the self-convolution of $|P^{(2)}(\psi)\rangle$:

$$|Q(\psi)\rangle = \sum_{\alpha_1,\alpha_2,\cdots,\alpha_N} C_1^{\alpha_1} C_2^{\alpha_2} \cdots C_N^{\alpha_N} |\alpha_1, \cdots, \alpha_N\rangle \tag{10.9}$$

where $C_i^{\alpha_i} = \sum_{\beta,\gamma} \delta_{\beta\oplus\gamma,\alpha_i} B_i^{(2)\beta} \otimes B_i^{(2)\gamma}$. The MPS $|Q(\psi)\rangle$, which has physical dimension 4 and exact bond dimension χ^8, stores the probability distribution that can be obtained by Bell difference sampling [20]. As before, we can compress $|Q(\psi)\rangle$ to keep the computational cost manageable. Its tensor network representation is shown in Fig. 10.3. Then, the additive Bell magic is given by

$$\mathcal{B}_a = -\log \langle Q(\psi)|\Lambda \otimes \Lambda \otimes \cdots \otimes \Lambda|Q(\psi)\rangle \tag{10.10}$$

where $\langle \alpha'|\Lambda|\alpha\rangle = 1$ if $[P_\alpha, P_{\alpha'}] = 0$ and $\langle \alpha'|\Lambda|\alpha\rangle = -1$ otherwise.

We have benchmarked the additive Bell magic calculations in the Ising and XXZ chains, where we find similar behavior to that of the SRE in both cases. Furthermore,

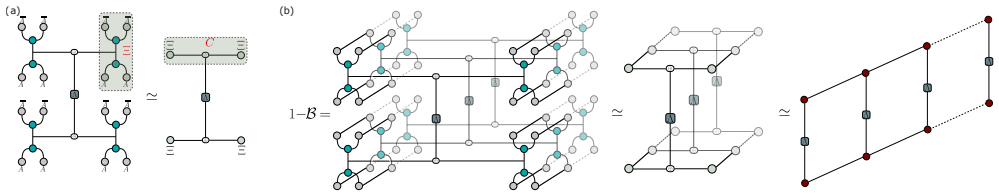

FIGURE 10.3: Tensor network representation of Bell magic.

.

we computed Bell magic in a state prepared by a quantum circuit recently realized in Ref. [7], shown in Fig. 10.1 (d). We verify that the additive Bell magic increases as a function of the number of CCZ gates applied.

10.5 Stabilizer nullity and stabilizer group

Here, we show that stabilizer nullity [34] can be calculated using MPS in the Pauli basis. The key insight is that stabilizer nullity can be expressed as a particular limit of the SRE [4]:

$$\nu = \lim_{n\to\infty} (n-1) M_n. \tag{10.11}$$

This is evident from the definition of SRE, where taking the limit $n \to \infty$ effectively eliminates all Pauli strings except those for which $\langle\psi|P_\alpha|\psi\rangle = \pm 1$, i.e., those within the stabilizer group $\mathrm{Stab}(\psi)$.

Algorithm 2 Stabilizer nullity via Pauli-MPS

Input: Pauli vector $|P(\psi)\rangle$ and threshold ϵ
Output: Stabilizer nullity ν

$|P_0\rangle \leftarrow |P(\psi)\rangle$
$T_0 \leftarrow \||P_0\rangle\|$
$k \leftarrow 1$
repeat
  $|P_{k-1}\rangle \leftarrow |P_{k-1}\rangle / T_{k-1}$
  $W_k \leftarrow \mathrm{diag}(|P_{k-1}\rangle)$
  $|P_k\rangle \leftarrow W_k |P_{k-1}\rangle$
  $T_k \leftarrow \||P_k\rangle\|$
  $k \leftarrow k+1$
until $|1 - T_k/T_{k-1}| \leq \epsilon$
$\nu \leftarrow N + 2\log_2 T_k$.

From Eq. (10.11) and Eq. (10.5), we see that the nullity can be obtained by applying W repeatedly to $|P(\psi)\rangle$. Furthermore, one can apply the trick employed in the exponential tensor renormalization group [187] to reach the large n limit exponentially faster. The idea is to iteratively construct a new diagonal MPO W_k after each iteration, based on the current MPS $|P_k\rangle$. We monitor the MPS norm $T_k = \||P_k\rangle\| = \sqrt{\langle P_k|P_k\rangle}$, which is related to the nullity by $\nu = \lim_{k\to\infty} N + 2\log_2 T_k$,

[4] We stress however that, unlike the SRE, stabilizer nullity satisfies strong monotonicity. Indeed, while Ref. [23] proves that the SRE is not a strong monotone for any finite index n, their argument does not extend to the limit $n \to \infty$.

and convergence is achieved when the change in T_k falls below a threshold ϵ. The scheme is summarized in Algorithm 2. The final MPS is the fixed point $|G(\psi)\rangle$ which satisfies $W_\infty|G(\psi)\rangle = \sqrt{2^{\nu-N}}|G(\psi)\rangle$ [5].

The rate of convergence of the algorithm is determined by the "magic gap" [188], defined as

$$MG(|\psi\rangle) = 1 - \max_{\boldsymbol{\alpha},\langle\psi|P_{\boldsymbol{\alpha}}|\psi\rangle\neq\pm1} |\langle\psi|P_{\boldsymbol{\alpha}}|\psi\rangle|, \tag{10.12}$$

through the following upper bound [189]

$$|\nu_k - \nu| \leq 3\log_2\left[1 + (1 - MG(|\psi\rangle))^{2^{k+1}-2}2^\nu)\right]. \tag{10.13}$$

Here, ν_k is the approximate nullity obtained if the algorithm is terminated at the k-th iteration. One can verify that

$$\nu_k = \log_2\left\{\sum_{\boldsymbol{\alpha}} \frac{|\langle\psi|P_{\boldsymbol{\alpha}}|\psi\rangle|^{2^{k+1}}}{2^N}\right\} - 2\log_2\left\{\sum_{\boldsymbol{\alpha}} \frac{|\langle\psi|P_{\boldsymbol{\alpha}}|\psi\rangle|^{2^k}}{2^N}\right\}. \tag{10.14}$$

Based on the upper bound in Eq. (10.13), approximating the nullity with a fixed error requires $k = O\left(\log_2 \frac{\nu}{-\log_2[1-MG(|\psi\rangle)]}\right)$ iterations. It can also be shown that ν_k monotonically increases with k:

$$\begin{aligned}
\nu_{k+1} - \nu_k &= \left(\log_2\left\{\sum_{\boldsymbol{\alpha}} \frac{|\langle\psi|P_{\boldsymbol{\alpha}}|\psi\rangle|^{2^{k+2}}}{2^N}\right\} - 2\log_2\left\{\sum_{\boldsymbol{\alpha}} \frac{|\langle\psi|P_{\boldsymbol{\alpha}}|\psi\rangle|^{2^{k+1}}}{2^N}\right\}\right) \\
&\quad - \left(\log_2\left\{\sum_{\boldsymbol{\alpha}} \frac{|\langle\psi|P_{\boldsymbol{\alpha}}|\psi\rangle|^{2^{k+1}}}{2^N}\right\} - 2\log_2\left\{\sum_{\boldsymbol{\alpha}} \frac{|\langle\psi|P_{\boldsymbol{\alpha}}|\psi\rangle|^{2^k}}{2^N}\right\}\right) \\
&= \log_2\left\{\sum_{\boldsymbol{\alpha}} \frac{|\langle\psi|P_{\boldsymbol{\alpha}}|\psi\rangle|^{2^{k+2}}}{2^N}\right\} + 2\log_2\left\{\sum_{\boldsymbol{\alpha}} \frac{|\langle\psi|P_{\boldsymbol{\alpha}}|\psi\rangle|^{2^k}}{2^N}\right\} - 3\log_2\left\{\sum_{\boldsymbol{\alpha}} \frac{|\langle\psi|P_{\boldsymbol{\alpha}}|\psi\rangle|^{2^{k+1}}}{2^N}\right\} \\
&= \log_2\left\{\frac{\left(\sum_{\boldsymbol{\alpha}} |\langle\psi|P_{\boldsymbol{\alpha}}|\psi\rangle|^{2^{k+2}}\right)\left(\sum_{\boldsymbol{\alpha}} |\langle\psi|P_{\boldsymbol{\alpha}}|\psi\rangle|^{2^k}\right)^2}{\left(\sum_{\boldsymbol{\alpha}} |\langle\psi|P_{\boldsymbol{\alpha}}|\psi\rangle|^{2^{k+1}}\right)^3}\right\} \\
&\geq 0.
\end{aligned} \tag{10.15}$$

The last line follows by applying Hölder's inequality to the term inside the logarithm in the second-to-last line. Consequently, ν_k provides a rigorous lower bound to the nullity for each k.

Thus, the time complexity of the algorithm is $O\left(N\log(\nu)\chi_{\max}^4\right)$, where $\chi_{\max}$ is the maximum bond dimension across iterations [6]. The linear scaling with N surpasses existing methods utilizing Bell difference sampling [35, 36], that can be applied directly to an MPS through perfect Pauli sampling [23, 27] with cost $O\left(N^3 + N^2\chi^3\right)$. Our algorithm thus establishes a new state-of-the-art for states efficiently represented by MPS.

[5] One can see $|G(\psi)\rangle$ as the Pauli vector of $\rho^{(\infty)}$, whose Pauli expectation values are 1 if $\langle\psi|P_{\boldsymbol{\alpha}}|\psi\rangle = \pm1$, and 0 otherwise. $\rho^{(\infty)}$ is thus a (normalized) projector onto the stabilizer group of $|\psi\rangle$.

[6] Our numerical data consistently show that the bond dimension is non-increasing after each iterations, although we were not able to provide a proof. This also implies that $\chi_{\max}$ never exceeds χ^2.

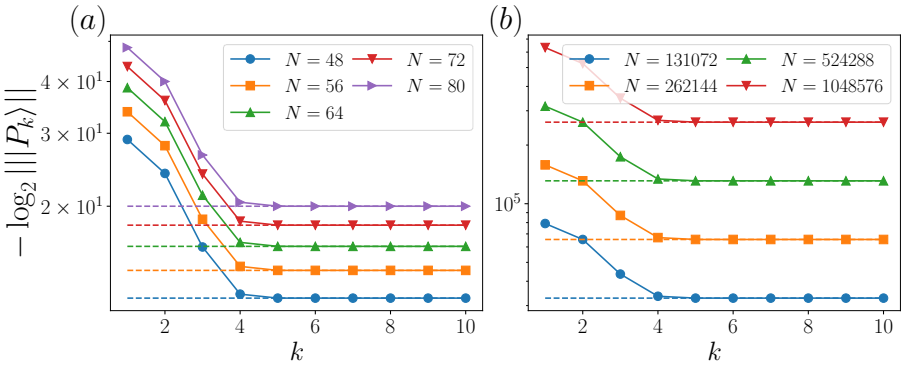

FIGURE 10.4: We show $-\log_2 |||P_k\rangle||$ at iteration k in the outputs of random Clifford circuits with $N_T = N/2$ number of T gates and circuit depth (a) $D = N/4$ and (b) $D = 10$. After sufficiently many iterations, $-\log_2 |||P_k\rangle||$ flows to $(N-\nu)/2$, denoted by the dashed lines for each system with the same color.

.

The information about the stabilizer group of $|\psi\rangle$ can be extracted from $|G(\psi)\rangle$, since we have

$$\langle \boldsymbol{\alpha}|G(\psi)\rangle = \begin{cases} \sqrt{2^{\nu-N}}, & \text{if } P_{\boldsymbol{\alpha}}|\psi\rangle = \pm|\psi\rangle \\ 0, & \text{otherwise .} \end{cases} \tag{10.16}$$

The unsigned generators of the stabilizer group can be extracted using perfect MPS sampling [190] on $|G(\psi)\rangle$. The protocol is equivalent to learning a stabilizer state by Bell sampling [101], which can be done efficiently in $O\left(N^3\right)$ time. Once all the unsigned generators are found, the signs of the generators can be extracted from $|P(\psi)\rangle$. In this way, the generators of the stabilizer group can be determined in $O\left(N^2(N-\nu) + N(N-\nu)\chi_G^2\right)$ time, where χ_G is the bond dimension of $|G(\psi)\rangle$.

To benchmark our algorithm, we consider T-doped states $|+\rangle^{\otimes N-N_T}|T\rangle^{\otimes N_T}$, for $|+\rangle = \frac{|0\rangle+|1\rangle}{\sqrt{2}}$ and $|T\rangle = T|+\rangle$. Notably, for product states, the MPS $|P_k\rangle$ for each k remains a product state, allowing for highly efficient nullity computation. We then apply a random Clifford circuit of depth D, which preserves the nullity $\nu = N_T$. The Clifford gates are drawn randomly from the set $\{S, H, CNOT, CZ\}$ in each layer. The two-qubit gates are applied only to nearest-neighbors. Fig. 10.4 (a) shows convergence of $-\log_2 |||P_k\rangle||$ for $D = N/4$ and $N_T = N/2$, which according to the algorithm above should flow to $\frac{N-\nu}{2}$ as $k \to \infty$. For this calculation, we imposed a fixed truncation error threshold $\epsilon = 10^{-6}$. For $N = 80$, the bond dimension of $|\psi\rangle$ reaches $\chi = 32$, while χ_P reaches $\chi_P = 1024$. We see that convergence occurs rapidly (within 10 iterations) in all cases. For shallow circuits with constant depth $D = 10$, we were able to perform simulations up to $N = 1048576$ (2^{20}), as shown in Fig. 10.4 (b). Here, the maximum bond dimension of $|\psi\rangle$ is $\chi = 16$. We have verified that the computational time approximately grows linearly with N. The total CPU time was 1.5 days for $N = 1048576$ with 10 iterations [7]. This demonstration represents a significant leap forward by orders of magnitude in computing genuine nonstabilizerness monotones, compared to the previous attempts [185, 191] limited to $O(10)$ qubits. These results would also be extremely challenging to reproduce using approaches based on Bell sampling [35, 36], due to its unfavorable scaling with system size.

[7] The initial iterations, where the bond dimensions are the largest, require the most computational resources. The bond dimensions grow smaller with each iteration, resulting in significantly faster computations in the subsequent iterations.

10.5.1 Learning states prepared with few non-Clifford gates

Learning the stabilizer group of a state has previously been used as a first step to learn the full description of states prepared with few non-Clifford gates [35, 36, 192], i.e., states with small ν. In this section, we detail how to perform this task within our MPS framework.

Let $|\psi\rangle$ be a pure state of N qubits whose stabilizer group is generated by m Pauli strings $s_j P_{\boldsymbol{\alpha}_j}$ for $j = 1, 2, \cdots, m$ and $s_j = \pm 1$. We will make use of the algebraic structure of T-doped stabilizer states [192]:

$$|\psi\rangle\langle\psi| = \frac{1}{2^N} \sum_{i=0}^{l} \langle\psi|P_{\boldsymbol{\beta}_i}|\psi\rangle P_{\boldsymbol{\beta}_i} \prod_{j=1}^{m} (I + s_j P_{\boldsymbol{\alpha}_j}), \tag{10.17}$$

where $P_{\boldsymbol{\beta}_i}$ for $i = 0, 1, \cdots, l$ are referred to as the bad generators, and $P_{\boldsymbol{\beta}_0} = I$. Therefore, to fully characterize the state $|\psi\rangle$, it is sufficient to learn its stabilizer group and the bad generators. In the main text, we have detailed how to learn the stabilizer group from $|G(\psi)\rangle$ obtained from Algorithm 2. The next step is to learn the l bad generators. One possible approach involves constructing a Clifford circuit C such that $C|\psi\rangle = |\phi\rangle \otimes |x\rangle$, where $|\phi\rangle$ is a state of ν qubits and $|x\rangle$ is a computational basis state of $N - \nu$ qubits [193]. The bad generators can then be learned directly from the Pauli vector of $|\phi\rangle$. However, applying a Clifford ciruit to an MPS in general leads to a significant increase in the bond dimension of the MPS. It is thus preferable to perform the task in a way that avoids explicit application of a Clifford circuit.

We achieve this by iteratively extracting the bad generators with large expectation values. First, we project out the stabilizer group from the Pauli vector: $|P'(\psi)\rangle = |P(\psi)\rangle - \sqrt{2^{N-\nu}} W_\infty |P(\psi)\rangle$. Then, we repeat Algorithm 2 to obtain a fixed point $|G^{(2)}(\psi)\rangle$ encoding a union of left disjoint cosets $P_{\boldsymbol{\beta}_1}\mathrm{Stab}(\psi) \cup \cdots \cup P_{\boldsymbol{\beta}_{l_2}}\mathrm{Stab}(\psi)$. The Pauli strings $P_{\boldsymbol{\beta}_1}, \cdots, P_{\boldsymbol{\beta}_{l_2}}$ are those with the second-largest expectation values (in magnitude) in the Pauli spectrum of $|\psi\rangle$. This process repeats, each time projecting out previously found bad generators and using Algorithm 2 to identify the next cosets of Pauli strings with large expectation values. The procedure stops when the Pauli vector is finally empty. In the end, we will have a set of fixed points $|G^{(n)}(\psi)\rangle$, each encoding the bad generators with the n-th largest expectation values (in magnitude) in the Pauli spectrum of $|\psi\rangle$. Then, similarly as the stabilizer generators, the bad generators can be learned using perfect MPS sampling on each $|G^{(n)}(\psi)\rangle$. The total time complexity to obtain the fixed points is $O\left(lN \log(\nu) \chi_{\max}^4\right)$. Importantly, this allows us to directly access the full content of the Pauli spectrum. Learning the generators themselves then takes $O\left(l\left[N^2(N-\nu) + N(N-\nu)\chi_G^2\right]\right)$. Since $l < 4^\nu$, our algorithm learns the generators of the state efficiently for $\nu = O(\log N)$.

Note that, while the MPS form itself is already an efficient classical description of a state, the description in terms of the stabilizer group could be useful, e.g., for simulating Clifford circuits. Furthermore, with the knowledge of the stabilizer group, one can construct a symmetric MPS in the Pauli basis, potentially leading to efficient MPS simulations of Clifford circuits.

10.6 Conclusions

We have proposed a new MPS framework in the Pauli basis in order to investigate nonstabilizerness in quantum many-body systems. We discuss how several measures of nonstabilizerness, including the SREs, stabilizer nullity, and Bell magic

can be efficiently approximated within our approach, and we demonstrated its usefulness in several scenarios, from ground states of spin chains to quantum circuits.

In terms of future investigations, it would be interesting if our MPS approach could facilitate analytical treatment of the SRE by exploiting its simple representation as a two-dimensional tensor network. Furthermore, we expect that our method would be useful to understand the role of nonstabilizerness in hybrid quantum circuits, a topic explored in recent works [194, 195]. Notably, our method allows for the efficient computation of stabilizer nullity, which is a strong monotone, and is thus suitable to characterize nonstabilizerness in such scenarios. Finally, it would be fascinating to explore the applicability of our framework to compute nonstabilizerness measures that require optimization, such as the stabilizer fidelity [196] and the robustness of magic [18].

Chapter 11

Magic transition in measurement-only circuits

Despite its crucial role in achieving quantum advantage, little is known about magic transitions in monitored random quantum circuits. Recent studies have provided evidence for the existence of magic transitions in different contexts [108, 194, 195, 197]. In particular, Refs [194, 195] investigated magic transitions in the context of monitored Clifford circuits doped by T gates. We recall that Clifford gates along with the T gate form a universal gate set for quantum computation. Thus, such T-doped Clifford circuits interpolate between classically simulable and universal circuits, and the above works found that the two limits are separated by a transition in magic. In Ref. [194], Bejan et al computed the magic using Pauli-based computation [198] that essentially maps the quantum dynamics to a magic state register subject to mutually commuting measurements. They found cases where magic and entanglement transitions coincide, but also others with a magic transition in a volume-law entangled phase. Instead in Ref. [195], Fux et al studied both magic and entanglement transition using matrix product states (MPS) simulations, providing evidence that a transition in magic can occur independently of one in entanglement. However, both studies have some limitations. Ref. [194] only computed a proxy of magic which can increase under Clifford operations, while the results presented in [195] may suffer systematic errors due to MPS truncation. As such, a proper characterization of magic transition using a true measure of magic remains an outstanding challenge.

Investigating magic transitions in quantum circuits presents significant challenges compared to entanglement transitions. While large-scale simulations of entanglement transitions often rely on efficiently simulable Clifford circuits, these circuits are inherently incapable of hosting magic transitions. In this paper, we introduce and study the magic in a measurement-only circuit consisting of Clifford and non-Clifford measurements, depicted in Fig. 11.1. Here, differently from previous studies, magic is injected through the non-Clifford measurements. We show that the magic dynamics in this circuit is efficiently simulable, employing any measure of magic that is additive for all tensor products of single-qubit states. This allows us to perform large-scale simulations to study the magic transition in this circuit, which can be viewed as a result of the competition between Clifford and non-Clifford measurements.

The study of entanglement transitions has benefited significantly from the construction of linear combinations of entanglement measures [199–203]. Motivated by this success, we initiate a parallel investigation in the context of magic. We analyze the mutual magic and topological magic, which will be defined according to some partitioning of the system (see Fig. 11.2(b)). Quantifying magic in mixed states, which arise when considering subsystems, is notoriously difficult compared to pure states. For qubits, there are currently no known computable measures for mixed

states. Despite the general difficulty, we can demonstrate that in our specific setup, the magic of subsystems exhibits a simplified form, allowing us to leverage existing, robust measures of magic.

With constant density of non-Clifford measurements per time step, our results demonstrate that the magic scales extensively with no distinctive features near the percolation critical point. However, mutual magic serves as a clear indicator of the transition, showcasing a distinct peak at the critical point. Specifically, it displays a logarithmic divergence with system size in one dimension and an area-law scaling in two dimension, analogous to entanglement entropy. Further analysis using topological magic enables precise finite-size scaling, allowing us to extract critical exponents which are found to match the bond percolation values. On the other hand, with vanishing non-Clifford measurement rate, we found that the magic saturates to a constant, in agreement with previous studies. Finally, we discuss a specific scenario where the dynamics of mutual magic is exactly identical to the entanglement dynamics. Overall, our work provides a genuine understanding of the nontrivial dynamics of magic and its linear combinations, which importantly utilizes true measures of magic.

The rest of the chapter is structured as follows. In Sec. 4.1, we introduce the quantum circuit with Clifford and non-Clifford measurements. In Sec. 11.2, we present a classical simulation of the circuit. In Sec. 11.3, we discuss the magic properties of the circuit and introduce mutual magic and topological magic. In Sec. 11.4, we present our numerical results in both one- and two-dimensional lattices. In Sec. 11.5, we briefly comment on the connection to the participation entropy and then conclude in Sec. 11.6.

11.1 Model

Consider a system with spin-1/2 degrees of freedom in every site i. Each spin is represented by Pauli matrices σ_i^α with $\alpha = \{x, y, z\}$. The quantum circuit is defined by projective measurements of observables O, and the action of such a measurement is given by

$$M[O]|\psi\rangle = \frac{P_\lambda|\psi\rangle}{\sqrt{\langle\psi|P_\lambda|\psi\rangle}}, \tag{11.1}$$

which is the post-measurement state after measurement of the discrete eigenvalue λ of O with probability $\Pr(\lambda) = \langle\psi|P_\lambda|\psi\rangle$. Here, P_λ denotes the projector onto the corresponding eigenspace. We are interested in measurements of the observables $\tilde{\sigma}_i^x(\theta) = e^{-i\theta/2\sigma_i^z}\sigma_i^x e^{i\theta/2\sigma_i^z}$ and $\sigma_i^z\sigma_{i+1}^z$. The angle θ, which can vary in space and time, will play an important role on the behavior of magic, as discussed further below. The eigenvectors of $\tilde{\sigma}_i^x(\theta)$ are $|\pm_\theta\rangle = |0\rangle \pm e^{i\theta}|1\rangle$. The projectors associated with the two measurements are

$$P_\lambda^{\tilde{\sigma}^x} = \frac{1}{2}\left(1 + \lambda\tilde{\sigma}^x\right) \tag{11.2}$$

$$P_\lambda^{\sigma_i^z\sigma_{i+1}^z} = \frac{1}{2}\left(1 + \lambda\sigma_i^z\sigma_{i+1}^z\right), \tag{11.3}$$

with the set of outcomes $\lambda \in \{+1, -1\}$. Each time step comprises one row of M_{zz} measurements followed by a row of M_x measurements. Each edge $e = (i, i+1)$ is measured by the observable $\sigma_i^z\sigma_{i+1}^z$ with probability $1 - p$ and each site i is measured by the observable $\tilde{\sigma}_i^x(\theta)$ with probability p (see Fig. 11.1 (a)). Given the state $|\psi(t)\rangle$

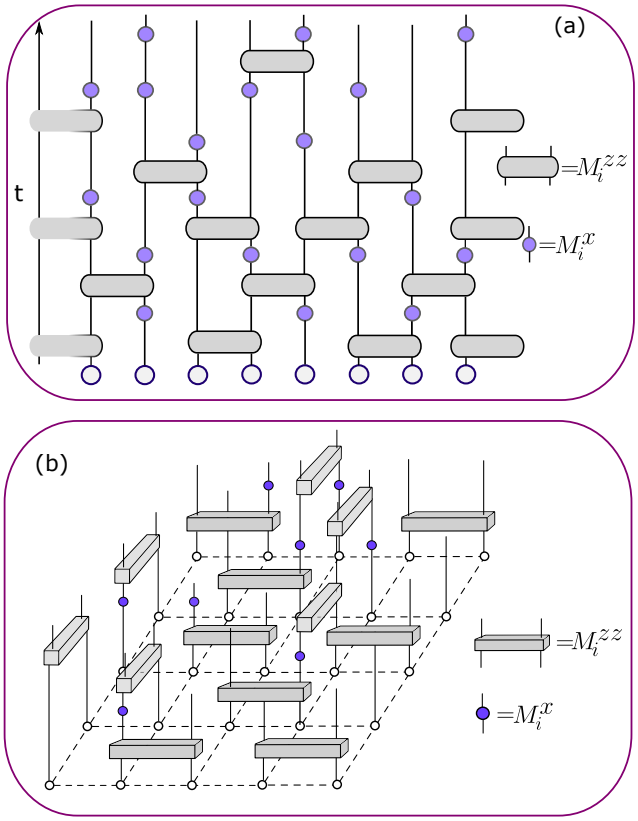

FIGURE 11.1: Measurement-only quantum circuit with two types of competing measurements in (a) one-dimensional and (b) two-dimensional lattices. Gray boxes on edges denote measurements M_{zz} on adjacent spins and violet circles denote measurements M_x on a single spin. Each time step comprises one row of M_{zz} measurements followed by a row of M_x measurements.

at time t, the new wave function at $t+1$ is given by

$$|\psi(t+1)\rangle = M_x M_{zz} |\psi(t)\rangle \tag{11.4}$$

with measurements

$$M_x = \prod_i M_i^x \quad M_{zz} = \prod_i M_i^{zz}. \tag{11.5}$$

For any realization of such a circuit there is an ensemble of quantum trajectories of pure states, where each trajectory is labeled by the sequence of measurement outcomes. We are interested in the long time limit of magic averaged over both quantum circuit realizations and quantum trajectories.

11.2 Classical simulation

For the circuit described above, it can be shown that the state of the system can always be described as a tensor product of "rotated Bell clusters" (RBCs) defined as states that can be written as

$$|\mathbf{m}\rangle + e^{i\theta} |\overline{\mathbf{m}}\rangle , \tag{11.6}$$

where $\overline{\mathbf{m}} = \prod_i \sigma_i^x \mathbf{m}$, as depicted in Fig. 11.1(b). To see this, let us consider the example of two-qubit:

- Measuring $\tilde{\sigma}_1^x(\theta)$ in the two-qubit RBC

$$\begin{aligned} &|00\rangle + e^{i\varphi} |11\rangle \\ =&(|+_\theta 0\rangle + e^{i(\varphi-\theta)} |+_\theta 1\rangle) + (|-_\theta 0\rangle - e^{i(\varphi-\theta)} |-_\theta 1\rangle) \end{aligned} \tag{11.7}$$

  yields either $|+_\theta\rangle \otimes (|0\rangle + e^{i(\varphi-\theta)} |1\rangle)$ or $|-_\theta\rangle \otimes (|0\rangle - e^{i(\varphi-\theta)} |1\rangle)$ with equal probability. Notice that all the states are RBCs. The number of clusters in the state is increased by one.

- Measuring $\sigma_1^z \sigma_2^z$ in the product state

$$\begin{aligned} &(|0\rangle + e^{i\varphi_1} |1\rangle) \otimes (|0\rangle + e^{i\varphi_2} |1\rangle) \\ =&(|00\rangle + e^{i(\varphi_1+\varphi_2)} |11\rangle) + (e^{i\varphi_2} |01\rangle + e^{i\varphi_1} |10\rangle) \end{aligned} \tag{11.8}$$

  yields either $|00\rangle + e^{i(\varphi_1+\varphi_2)} |11\rangle$ or $|01\rangle + e^{i(\varphi_1-\varphi_2)} |10\rangle$ with equal probability. Notice that all the states are again RBCs. This process can be seen as a merging of RBCs.

Generalization to higher number of qubits is straightforward.

Consequently, the circuit can be efficiently simulated by a classical stochastic process. The state of the system is characterized by vectors $\mathbf{s} \in \mathbb{N}_0^L$ and $\mathbf{b} \in \mathbb{Z}_2^L$. The nonnegative integer $s_i \in \mathbb{N}_0$ encodes that site i belongs to an RBC with label s_i. Moreover, an RBC labeled by n is associated with a phase p_n. Let $A_n = \{q_i\}$ be the set of sites that belongs to the RBC n. The state of the RBC reads

$$|\mathbf{b}_i\rangle_{i\in A_n} + e^{ip_n} \left|\overline{\mathbf{b}}_i\right\rangle_{i\in A_n} \tag{11.9}$$

Since the state is simply a product states of RBCs, the vectors $\mathbf{s} \in \mathbb{N}_0^L$, $\mathbf{b} \in \mathbb{Z}_2^L$ and the phase p_n for each RBC completely specify the state. Moreover, they can be updated very efficiently, as we shall discuss in detail below.

We will provide the update rule for the two types of measurements. Here, sites that are not mentioned remain unchanged.

- *Measurement of* $\tilde{\sigma}_i^x(\theta)$. The outcome is $\lambda = \pm 1$ with equal probability. Set $s_i' := \mathrm{next}(\mathbf{s})$. Here, $\mathrm{next}(\mathbf{s}) = \min(n \in \mathbb{N}_0 \setminus \mathbf{s})$ returns the smallest integer that is not currently used as a cluster label in $\mathbf{s}$. Set $b_i' = 0$, $p'_{s_i} = p_{s_i'} - (-1)^{b_i}\theta + \delta_{\lambda,-1}\pi$, and $p'_{s_i'} = \theta + \delta_{\lambda,-1}\pi$.

- *Measurement of* $\sigma_i^z \sigma_j^z$. The outcome is $\lambda = \pm 1$ with equal probability. Set $s_l' = s_i$ for all sites l with $s_l = s_j$. There are two cases:
  - $\lambda = 1 - 2b_i \oplus b_j$. Set $p'_{s_i} = p_{s_i} + p_{s_j}$.
  - $\lambda = 2b_i \oplus b_j - 1$. Set $b_l' = 1 - b_l$ for all sites l with $s_l = s_j$. Set $p'_{s_i} = p_{s_i} - p_{s_j}$.

Notice that the dynamics of the the vectors $\mathbf{s}$ and $\mathbf{b}$ are not affected by the angles θ. Thus, they are identical also to the stabilizer case when all $\theta = 0$, whose entanglement transition has been studied in Ref. [204] (see also [205]). Setting nonzero θ is however crucial to induce nontrivial magic dynamics. In the following, we perform the simulation of the circuit using the update rules above. We have also benchmarked our results numerically against MPS simulations [25, 26].

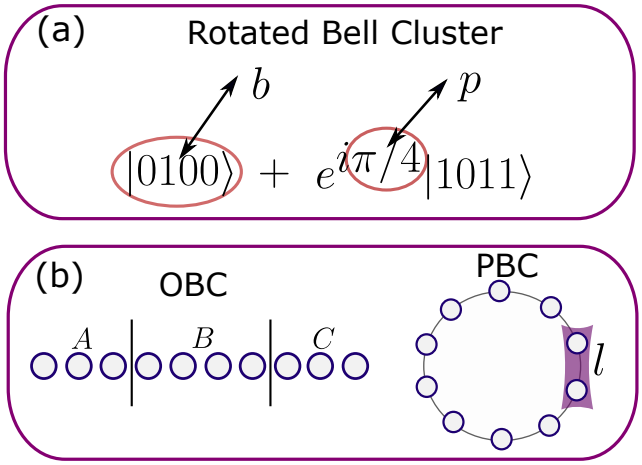

FIGURE 11.2: (a) Sketch of rotated Bell cluster. (b) Schematics of partitions: in the left part we show the partition for an open chain for the calculation of topological magic in Eq. (11.13). In the right part we show the partition for periodic boundary condition for the calculation of mutual magic in Eq. (11.11).

11.3 Magic measures

The fact that the states at each time step are composed of RBCs offers a significant advantage for quantifying magic. To see this, consider an RBC with size L_B. We can define a Clifford unitary consisting of CNOT operations

$$C = CNOT_{1,2}CNOT_{2,3}\dots CNOT_{L_B-1,L_B}. \tag{11.10}$$

Applying C to the RBC $|\psi\rangle = |\mathbf{b}\rangle + e^{i\theta}\left|\overline{\mathbf{b}}\right\rangle$ results in the state $C|\psi\rangle = (|b_0\rangle + e^{i\theta}|1-b_0\rangle) \otimes |c_2\rangle \otimes \cdots \otimes |c_{L_B}\rangle$, where $c_k = b_{k-1} \oplus b_h$. In other words, RBCs can be transformed to a product state of a single-qubit magic state and stabilizer states by applying Clifford unitaries. This observation is crucial because magic measures must be invariant under Clifford unitaries and composition with stabilizer states [17]. It follows that the magic within the original circuit can be determined solely by considering the tensor product of these single-qubit magic states. This significantly simplifies the task of calculating magic in such circuits.

Our analysis extends to investigating the magic of subsystems $\rho_A = \mathrm{Tr}_{A^c}[|\psi\rangle\langle\psi|]$, where A^c is the complement of A. The key point is that partially tracing an RBC yields a classical mixture of two computational basis states, irrespective of its phase. Therefore, the reduced density matrix has the form of a tensor product of pure RBCs and classical mixtures. Since such a classical mixture is a mixed stabilizer state, the magic of ρ_A can again be reduced to the magic of tensor-product of single-qubit pure magic states.

The above observations pave the way for efficient magic calculations in these circuits. Since the magic of the entire system boils down to the magic of single-qubit pure magic states in a tensor product structure, we can leverage magic measures that exhibit a key property: additivity for all tensor products of single-qubit states. Such measures exist [19, 34, 196, 206, 207], including those whose original definitions involve minimization procedures, and are thus generally difficult to compute beyond

a few qubits. Importantly, this includes *bona fide*, strong measures of magic for both pure states and mixed states, such as the relative entropy of magic [17]. Hereafter, we will use $\mathcal{M}$ to denote any measure of magic that is additive for all tensor products of single-qubit states. For any $\mathcal{M}$, the magic of the full state is simply given by the total sum of the magic of individual RBCs, measured by $\mathcal{M}$.

For a magic measure $\mathcal{M}$, we will consider the "mutual magic", defined in a subsystem A as

$$I_{\mathcal{M}}(A) = \mathcal{M}(|\psi\rangle) - \mathcal{M}(\rho_A) - \mathcal{M}(\rho_{A^c}). \tag{11.11}$$

We will use the notation $I_{\mathcal{M}}(\ell)$ to denote the case $A = \{1, ..., \ell\}$. This quantity can be viewed as the amount of magic that resides in the correlations between subsystems. A similar quantity has been studied previously in the context of mana [50, 181] and SRE [28, 33, 119], where it was shown that such mutual-information-like quantity is able to detect the transition when the full-state magic does not show any features at the transition.

In terms of RBCs, $I_{\mathcal{M}}(A)$ is given by the sum of the magic of RBCs with support both in A and A^c. This interpretation offers a physical picture of mutual magic as entanglement modulo stabilizer contributions. In particular, it immediately follows that it is upper bounded by the entanglement entropy [1]:

$$I_{\mathcal{M}}(A) \leq S(A). \tag{11.12}$$

Finally, in order to distinguish the magic content between different phases, we will consider the topological magic defined as

$$\mathcal{M}^t_{\text{topo}} = \mathcal{M}(\rho_{ABC}) + \mathcal{M}(\rho_B) - \mathcal{M}(\rho_{AB}) - \mathcal{M}(\rho_{BC}), \tag{11.13}$$

for systems with open boundary condition. Here, the system is divided into three non-overlapping parts A, B, and C. Such linear combination was first introduced in the context of entanglement by the name of "generalized topological entanglement entropy" [208, 209] to probe symmetry-breaking orders. The latter has also been considered in the context of measurement-induced entanglement transition [200, 202]. In our setup, $\mathcal{M}^t_{\text{topo}}$ is given by the sum of the magic of RBCs with support in A, B and C.

11.4 Numerical results

11.4.1 Magic in (1+1)D circuits

We will focus on the case of fixed $\theta = \pi/4$. In this case, the possible phases of the RBCs become restricted to multiples $\pi/4$. If the phase is a mutiple of $\pi/2$, the state is a stabilizer state. If it is not, then it is equivalent to the canonical T state, up to a Clifford unitary. We will denote the magic of a T state as $\mathcal{M}_T$. Applying the update rule in Sec. 11.2, one can see that any RBC of even size is a stabilizer state, while an RBC of odd size has the magic equal to $\mathcal{M}_T$. This simplification allows for faster simulations by solely tracking the parity of the sizes of the RBCs.

We now present our numerical results. We start with the initial product state $|\psi(0)\rangle = |+_\theta\rangle^{\otimes L}$ and run the circuit for $2L$ time steps for the system to reach the steady state. We then average the quantities of interest over $10^4 - 10^5$ trajectories. We show the magic and the mutual magic in Fig. 11.3 as a function of p for systems

[1] Here, we assume that $\mathcal{M}$ is upper bounded by one for single-qubit states, which is typically the case (or can be made so after rescaling).

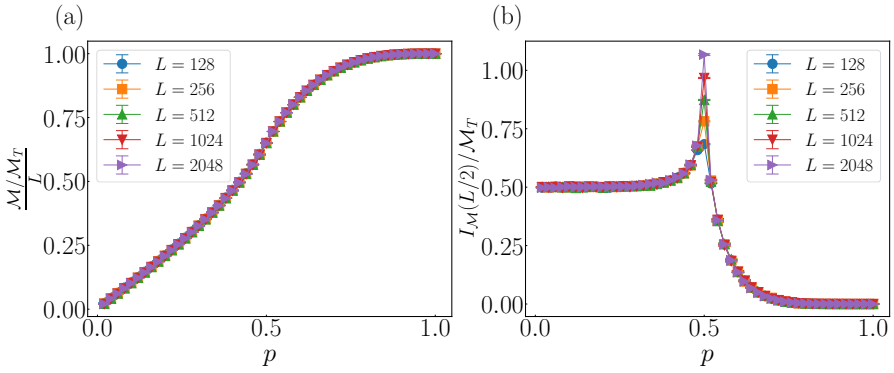

FIGURE 11.3: (a) Magic density $\frac{\mathcal{M}/\mathcal{M}_T}{L}$ and (b) mutual magic of half subsystem $I_{\mathcal{M}}(L/2)/\mathcal{M}_T$ with periodic boundary condition.

with periodic boundary condition. Here, we only consider even L, such that $\mathcal{M}$ vanishes for $p = 0$ as the state is a global (stabilizer) Bell cluster. If L is odd, the state becomes a global RBC, whose magic is $\mathcal{M} = \mathcal{M}_T$. For $p = 1$, the state is a tensor product of T states, such that the magic is given by $\mathcal{M}/L = \mathcal{M}_T$. Our numerical results show that the magic scales extensively at any nonzero p, as shown in Fig. 11.3(a). However, around the percolation transition at $p_c = 0.5$ [210], the magic appears rather featureless. Instead, the transition is clearly identified using the mutual magic, which appears to diverge with L (see Fig. 11.3(b)). This behavior is reminiscent of entanglement entropy, which grows logarithmically at $p_c = 0.5$ [63, 204, 211]:

$$S(\ell) = \frac{\tilde{c}}{3} \log_2 \left[\frac{L}{\pi} \sin\left(\ell \frac{\pi}{L}\right) \right] + \gamma, \tag{11.14}$$

where $\tilde{c} = 3\sqrt{3}\ln(2)/(2\pi) \approx 0.573$, and γ is a non-universal constant. We thus postulate that the mutual magic follows similar scaling:

$$I_{\mathcal{M}}(\ell) = \frac{\tilde{c}_{\mathcal{M}}}{3} \log_2 \left[\frac{L}{\pi} \sin\left(\ell \frac{\pi}{L}\right) \right] + \gamma'. \tag{11.15}$$

We show the scaling of $I_{\mathcal{M}}(\ell) - I_{\mathcal{M}}(L/2)$ at p_c in Fig. 11.4(a), which confirms the hypothesis in Eq. (11.15). Indeed, we observe that $I_{\mathcal{M}}(\ell) - I_{\mathcal{M}}(L/2) \approx \frac{\tilde{c}_{\mathcal{M}}}{3} \log_2 \left[\sin\left(\ell \frac{\pi}{L}\right)\right]$, where $\tilde{c}_{\mathcal{M}} \approx \mathcal{M}_T \tilde{c}/2$.

We further investigate the magic growth with time, particularly at the critical point. At criticality, and for timescales significantly shorter than the saturation time, we postulate,

$$I_{\mathcal{M}}(\ell, t) = \frac{\tilde{c}_{\mathcal{M},t}}{3} \log_2 t + \gamma'' \tag{11.16}$$

where γ'' is a non-universal constant. Fig. 11.4(b) shows the dynamics of $I_{\mathcal{M}}(L/2)$ as a function of time t, which supports the postulate in Eq. (11.16). Remarkably, we find that $\tilde{c}_{\mathcal{M},t} = \tilde{c}_{\mathcal{M}}$, mirroring the behavior observed for entanglement in conformal field theories (CFTs) with dynamical exponent $z = 1$.

We then turn to open boundary condition and investigate the topological magic $\mathcal{M}^t_{\text{topo}}$. Here, we set $L = 4L_A = 4L_C = 2L_B$. The results are shown in Fig. 11.5. It is clear that $\mathcal{M}^t_{\text{topo}}$ tends to 0.5(0) for $0 < p < p_c (p > p_c)$ with increasing system sizes. This is again reminiscent of the behavior of the generalized topological entanglement entropy; however, the topological magic does not seem to be quantized to an integer value. Note that, for $p = 0$, $\mathcal{M}^t_{\text{topo}}$ vanishes since the magic itself vanishes

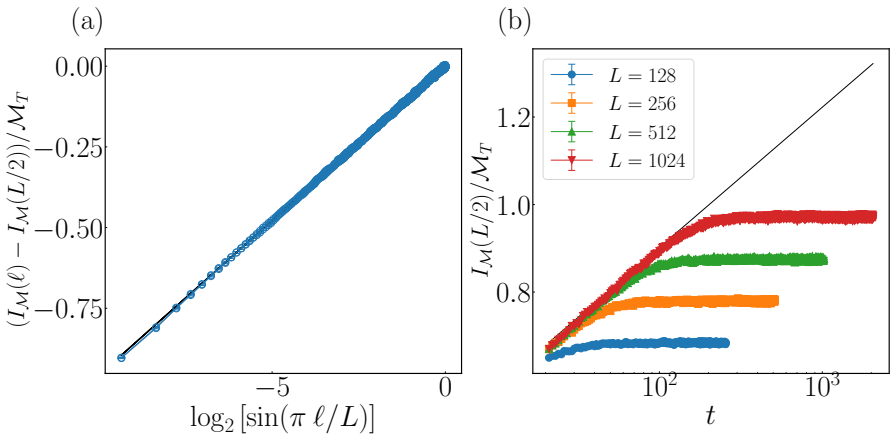

FIGURE 11.4: (a) Mutual magic $(I_{\mathcal{M}}(\ell) - I_{\mathcal{M}}(L/2))/\mathcal{M}_T$ at $p = p_c$ and $L = 2048$ and (b) the dynamics of $I_{\mathcal{M}}(L/2)/\mathcal{M}_T$ as a function of time t for different system sizes with periodic boundary condition. The black line denotes a linear fit.

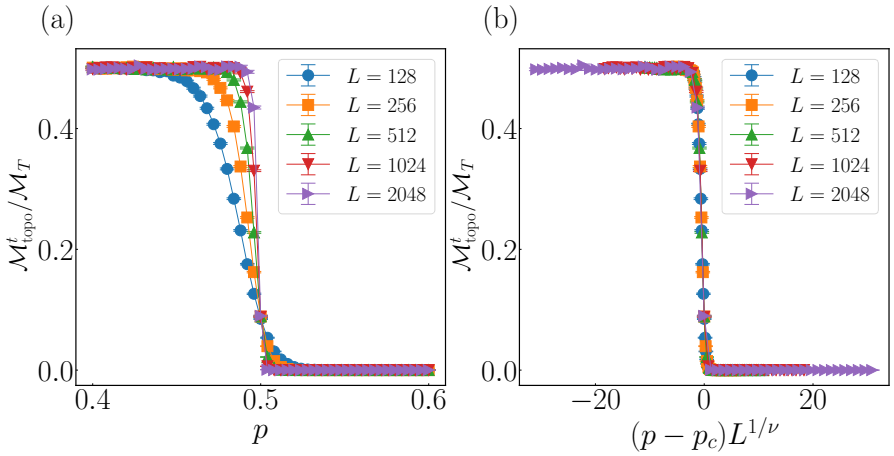

FIGURE 11.5: (a) The topological magic $\mathcal{M}^t_{\text{topo}}/\mathcal{M}_T$ with open boundary condition. (b) Data collapse for the topological magic, showing excellent agreement with the percolation value $p_c = 0.5$ and $\nu = 4/3$.

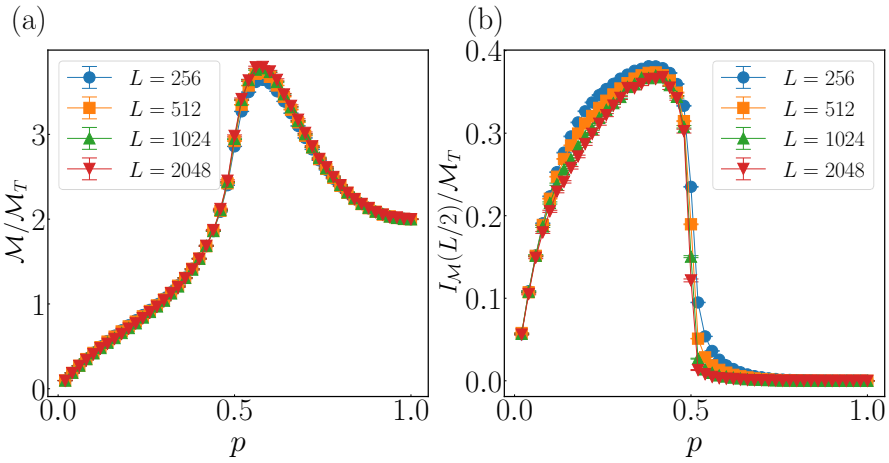

FIGURE 11.6: (a) Magic density $\frac{\mathcal{M}/\mathcal{M}_T}{L}$ and (b) mutual magic of half subsystem $I_{\mathcal{M}}(L/2)/\mathcal{M}_T$ with periodic boundary condition and $q = 2/L$.

(for even L). However, we found that $\mathcal{M}^t_{\text{topo}} \to 0.5$ for any infinitesimal value of p. This observation can be explained as follows: for $p \to 0$, a macroscopic Bell cluster emerges [204], which weight have the same probability of being odd or even, on general grounds.

We further investigate the finite-size scaling of $\mathcal{M}^t_{\text{topo}}$, using the finite-size scaling hypothesis:

$$\mathcal{M}^t_{\text{topo}} = f\left(L^{1/\nu}(p - p_c)\right), \tag{11.17}$$

where $f(x)$ is some unknown function, p_c is the critical value of tuning parameter p, and ν is the correlation length critical exponent. We found that our numerical data exhibits excellent data collapse with $p_c = 0.5$ and $\nu = 4/3$, expected from 2D bond percolation.

Let us now consider a different scenario. We introduce a parameter q, such that the measurement of $\tilde{\sigma}^x$ is performed at an angle $\theta = \pi/4$ with probability q and $\theta = 0$ (Clifford measurement) with probability $1 - q$. Note that the previous scenario corresponds to $q = 1$. To mimic previous studies [194, 195] where non-Clifford operations occur at a vanishing rate, we set $q = 2/L$. The magic behavior is shown in Fig. 11.6. In contrast to the previous case, the magic no longer exhibits extensive scaling with system size. Instead, it saturates to a constant value. This observation confirms the existence of such $O(1)$ magic phase that emerges when non-Clifford operations are introduced at a vanishing rate. In this case, the mutual magic appears to play the role of an order parameter, being zero for $p > p_c$ and nonzero for $p < p_c$.

11.4.2 Magic in (2+1)D circuits

We extend our analysis to a 2D square lattice, where the model exhibits a connection to three-dimensional bond percolation on the cubic lattice with a critical rate $p_c \approx 0.75$, as numerically determined in Ref. [212]. We will again consider the scenario of fixed $\theta = \pi/4$. Employing a simulation procedure similar to the 1D case, we simulate systems of size $N = L \times L$ with periodic boundary conditions, and we run the circuit for L time steps to reach the steady state. Fig. 11.7 displays the behavior of magic and mutual magic ($I_{\mathcal{M}}(\ell_x \times \ell_y)$ for a region of size $\ell_x \times \ell_y$) as a function of the parameter p. Similar to the 1D scenario, magic remains featureless while mutual

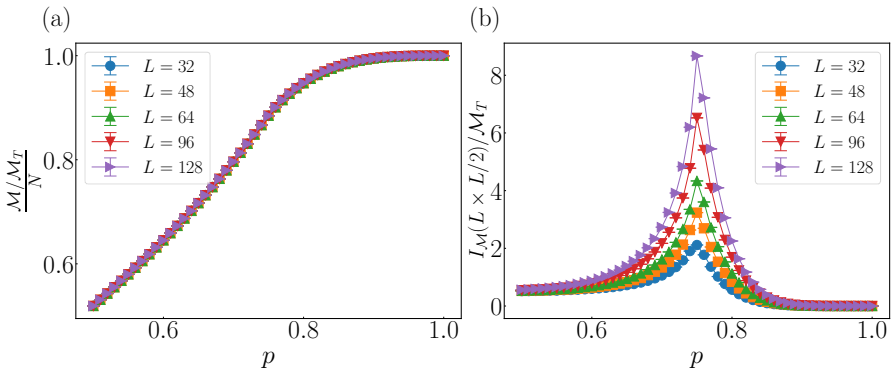

FIGURE 11.7: (a) Magic density $\frac{\mathcal{M}/\mathcal{M}_T}{L}$ and (b) mutual magic of half subsystem $I_{\mathcal{M}}(L \times L/2)/\mathcal{M}_T$ on 2D square lattice with periodic boundary conditions.

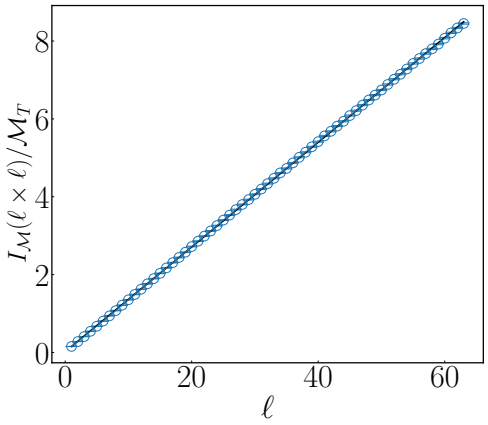

FIGURE 11.8: Mutual magic $I_{\mathcal{M}}(\ell \times \ell)/\mathcal{M}_T$ at $p = p_c$ and $L = 128$ on 2D square lattice with periodic boundary conditions. The black line denotes a linear fit.

magic captures the transition at $p = p_c$. However, in the 2D case, the mutual magic exhibits area-law scaling at the critical point, as shown in Fig. 11.8. This is again consistent with the behavior of entanglement.

Setting $q = 2/N$, we again observe a similar behavior as in the 1D case. The magic and mutual magic are shown in Fig. 11.9. While the total magic saturates to a constant value, the mutual magic emerges as a clear order parameter, signaling the phase transition.

11.4.3 Random θ

We now discuss the case when the angles θ are chosen uniformly at random in the interval $[0, 2\pi)$, both in space and time. We will show that the dynamics of mutual magic can be tuned to be identical to the entanglement.

To this end, we will focus on a specific measure of magic called the stabilizer nullity [34]. It is simply related to the size of the stabilizer group $\mathrm{Stab}(\psi)$, which is the group of Pauli strings that stabilize $|\psi\rangle$. The stabilizer nullity is defined as [34]

$$\nu(|\psi\rangle) = N - \log_2\left(|\mathrm{Stab}(\psi)|\right). \tag{11.18}$$

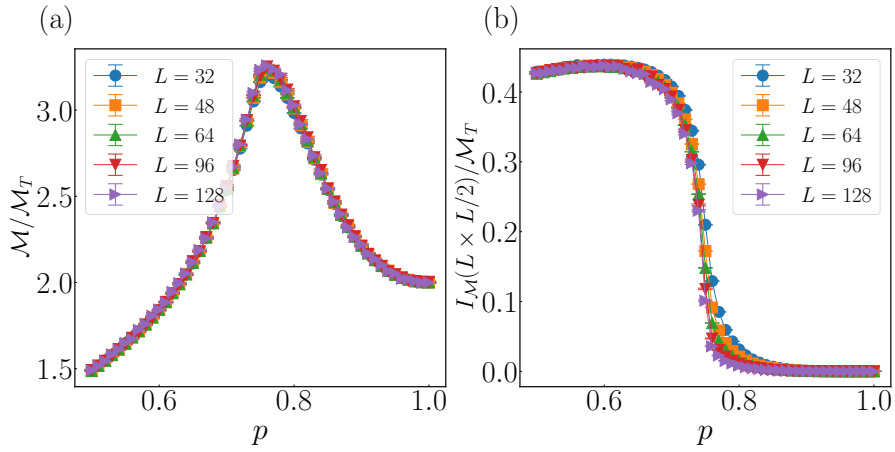

FIGURE 11.9: (a) Magic density $\frac{\mathcal{M}/\mathcal{M}_T}{L}$ and (b) mutual magic of half subsystem $I_{\mathcal{M}}(L/2)/\mathcal{M}_T$ on 2D square lattice with periodic boundary conditions and $q = 2/N$.

It is known that ν is a strong magic monotone, which is also additive under tensor product.

Stabilizer nullity has only been formally defined for pure states. To analyze the mutual magic, we would need to extend it to mixed states. One possible extension is by using the convex roof construction:

$$\nu(\rho) = \min_{\{p_i, |\psi_i\rangle\}} \sum_i p_i \nu(|\psi_i\rangle), \tag{11.19}$$

where the minimum is taken over all possible convex pure-state decompositions of ρ: $\rho = \sum_i p_i |\psi_i\rangle \langle\psi_i|$. Note that, the particular extension is not relevant, as long as it is invariant under composition with stabilizer states (see Sec. 11.3). The convex roof construction is convenient as it satisfies such condition.

A peculiar property of stabilizer nullity is that it can only take integer values. In particular, for a single-qubit state, it is zero for the single-qubit stabilizer states, and one otherwise. In terms of the RBCs, it is zero for an RBC with phase $\theta = k\pi/2$ with integer k, and one otherwise. With randomly chosen θ, the probability of encountering an RBC as a stabilizer state is essentially zero. This implies that any RBC that has support in both A and A^c will contribute one to the mutual nullity $I_\nu(A)$, that is exactly the same procedure to compute entanglement entropy [204]. We thus conclude that the mutual nullity in this setup is identical to the entanglement, as claimed.

11.5 Connection to participation entropy

While this work focuses on the magic transition, we find it insightful to explore the connection with participation (Shannon) entropy, defined as

$$S^{\text{part}}(|\psi\rangle) = \sum_\sigma -|\langle\sigma|\psi\rangle|^2 \log_2 |\langle\sigma|\psi\rangle|^2. \tag{11.20}$$

This quantity measures the spread of the wavefunction across different computational basis states. In our setup, one can see that it simply counts the total number of RBCs. This observation allows us to establish an inequality (that holds in our

circuit):

$$\mathcal{M} \leq S^{\text{part}}(|\psi\rangle). \tag{11.21}$$

Therefore, like magic, the participation entropy is extensive at any nonzero p [213]. Note that the inequality is saturated in the case of random θ (see Sec. 11.4.3).

For reduced density matrix ρ_A, the participation entropy is defined as

$$S^{\text{part}}(\rho_A) = \sum_{\sigma_A} -\langle\sigma_A|\rho_A|\sigma_A\rangle \log_2\langle\sigma_A|\rho_A|\sigma_A\rangle, \tag{11.22}$$

i.e., it is the Shannon entropy of the diagonal elements of ρ_A. We can consider the Shannon mutual information [114]:

$$I_S(A) = S^{\text{part}}(\rho_A) + S^{\text{part}}(\rho_{A^c}) - S^{\text{part}}(|\psi\rangle). \tag{11.23}$$

Previous studies have shown that it exhibits a scaling behavior similar to entanglement entropy [114–118]. In our specific case, it is straightforward to see that the Shannon mutual information is exactly equal to the entanglement. This model thus provides an interesting example where the entanglement and Shannon mutual information exhibit the same scaling behavior, which can be understood on a microscopic level.

While the dynamics of entanglement and Shannon mutual information are not affected by the angles of $\tilde{\sigma}^x$, we have seen in Sec. 11.4 that the dynamics of magic highly depends on them. By adjusting these angles (and potentially using different measures), we can manipulate the prefactor of the logarithmic scaling observed in the mutual magic, while the prefactors for entanglement and Shannon mutual information remain fixed. This highlights a significant distinction in how magic behaves compared to the other two resource quantities.

11.6 Conclusions and outlook

In this work, we have introduced a measurement-only circuit which exhibits nontrivial magic dynamics. Notably, we show that, although the circuit is tuned away from the Clifford limit, it remains efficiently simulable through a mapping to a classical stochastic model. This allows for large-scale numerical simulations, revealing a competition between Clifford and non-Clifford measurements driving a magic transition between two distinct phases in which magic scales extensively with volume. These two phases can be distinguished from the topological magic, which takes a constant nonzero value for $p < p_c$, but vanishes for $p > p_c$. Furthermore, the mutual magic exhibits divergence at $p = p_c$, with logarithmic scaling in 1D and area-law scaling in 2D, similar to entanglement entropy. In the 1D case, this behavior aligns with the previous observation in (1+1)D CFT [181]. Our results highlight the intriguing behavior of specific linear combinations of magic (that draws inspiration from entanglement), motivating further exploration in generic models.

Interestingly, magic appears to exhibit distinct behavior compared to entanglement and participation entropy, as the latter two are completely independent of the angles of $\tilde{\sigma}^x$. This raises general questions about the relationship between various quantum resources [111, 112, 214] in a broader class of circuits.

Let us note that, unlike previous studies [194, 195], we find that the magic and entanglement transitions coincide. Future investigations could explore modifications, such as correlated monitoring [194], to potentially separate these transitions. Moreover, our approach readily extends to simulating magic in symmetry-protected

topological phases [200] and toric code phases [201]. This opens exciting avenues to explore the role of topology on magic dynamics.

Chapter 12

Quantifying nonstabilizerness through entanglement spectrum flatness

In this chapter, we establish a deep connection between the SRE and the flatness of the entanglement spectrum associated to a subsystem density operator. At the conceptual level, this connection shows clearly how this resource is associated with entanglement structure: nonstabilizerness is directly tied to entanglement response, a quantum analogue of 'heat capacity' for thermodynamic systems. At the very same time, it opens the door for important practical applications. We present a simple practical protocol for experimentally probing this quantity efficiently using randomized measurement techniques.

Our main findings are summarized in Fig. 12.1. In Fig. 12.1 (a), we show the set-up that we use to make the connection between nonstabilizerness and entanglement response concrete: we prepare initial states as a product states and evolve them using random Clifford gates, followed by the measurement of the entanglement spectrum flatness. We find that a state possesses nonstabilizerness if and only if its entanglement spectrum is not flat. In the second panel (Fig. 12.1 (b)), we illustrate the Clifford orbit of a pure state: its nonstabilizerness is proportional to its average flatness over the orbit. Finally, in the third panel (Fig. 12.1 (c)), we present an algorithm for detecting nonstabilizerness and show the probability of success as a function of their degree of nonstabilizerness.

12.1 Stabilizer Rényi entropy and the flatness of entanglement spectrum

In this section, we establish a connection between the SRE with the flatness of the entanglement spectrum. In particular, we will show that we can quantify the nonstabilizerness of an arbitrary pure state by taking the average of the flatness along its Clifford orbit.

To this end, we will consider a measure of nonstabilizerness called the stabilizer linear entropy, defined as

$$M_{\text{lin}}(|\psi\rangle) = 1 - d\left\|\Xi_\psi\right\|_2^2, \tag{12.1}$$

which obeys the following properties: (i) faithfulness $M_{\text{lin}}(|\psi\rangle) = 0$ iff $|\psi\rangle \in \text{STAB}$, otherwise $M_{\text{lin}}(|\psi\rangle) > 0$, (ii) stability under Clifford operations: $\forall \Gamma \in C_n$ we have that $M_{\text{lin}}(\Gamma|\psi\rangle) = M_{\text{lin}}(|\psi\rangle)$ and (iii) upper bound $M_{\text{lin}} < 1 - 2(d+1)^{-1}$. The relationship between the second SRE M_2 and the linear non-stabilizing entropy follows

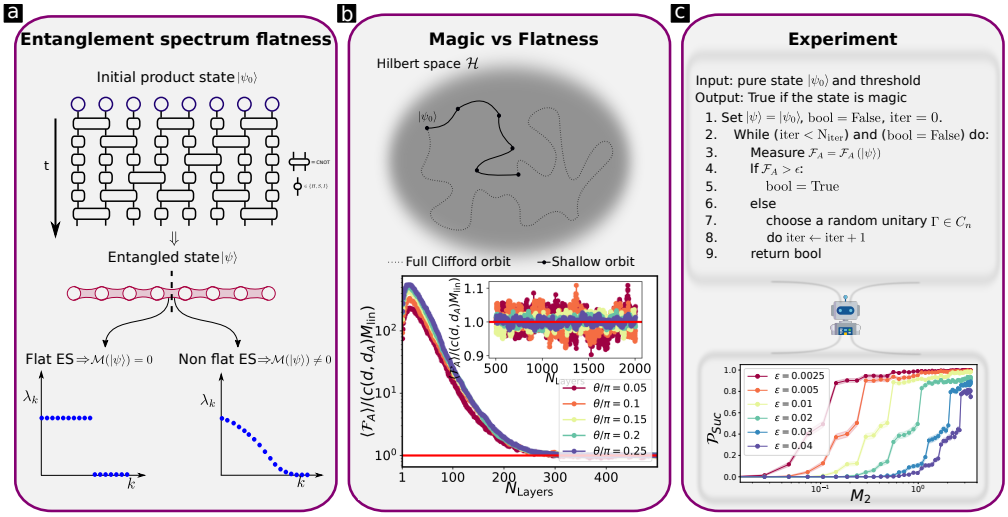

FIGURE 12.1: **Summary of the results:** (a) A schematic of the method to quantify the nonstabilizerness of a pure state. We start from a product state and then we apply random Clifford gates (both single and two-qubit gates, see text). After N_{Layers}, the state is fully entangled. Checking the entanglement spectrum in any bipartition, we can distinguish whether the initial state possesses nonstabilizerness. (b) In the upper panel, a sketch of the Clifford orbit of a pure state is shown. In the lower panel, we show the relation between flatness $\mathcal{F}_A$ and nonstabilizerness, quantified by $c(d, d_A) M_{\text{lin}}$. We initialize the system as a product state $|\psi(0)\rangle = \otimes_{i=1}^{n} |\psi_i\rangle$, where $|\psi_i\rangle = \frac{1}{\sqrt{2}} \left(|0\rangle + e^{i\theta}|1\rangle\right)$ and $n = 14$, for different values of θ. Then we apply several random Clifford layers N_{Layers}. In the limit of a very deep circuit, the ratio approaches 1 as predicted by the theorem as shown in the inset. (c) Algorithm to determine if a state is a stabilizer state or possesses some nonstabilizerness. We show the pseudocode in the upper part of the panel. In the lower part, we show the probability of catching a nonstabilizerness. We generate product states $|\psi(0)\rangle = \otimes_{i=1}^{n} |\psi_i\rangle$, where $|\psi_i\rangle = \frac{1}{\sqrt{2}} \left(|0\rangle + e^{i\theta}|1\rangle\right)$ for $n = 12$ qubits, and, we fix the number of Clifford layers $N_{\text{Layers}} = 100$. After performing $N_R = 1000$ realizations, we compute the probability of success $\mathcal{P}_{\text{suc}}$ for different values of threshold, as a function of the initial value of nonstabilizerness in the initial state calculated using the second SRE.

easily from the equation below

$$M_2(|\psi\rangle) = -\log\left[1 - M_{\text{lin}}(|\psi\rangle)\right]. \tag{12.2}$$

Let us now discuss the relationship between the SRE and the flatness of the entanglement spectrum. Consider a pure state $|\psi\rangle$ in a bipartite system $\mathcal{H} = \mathcal{H}_A \otimes \mathcal{H}_B$ and its reduced density operator $\rho_A = \text{Tr}_B |\psi\rangle \langle\psi|$. The (anti-)flatness of its entanglement spectrum is defined as

$$\mathcal{F}_A(|\psi\rangle) := \text{Tr}\left(\rho_A^3\right) - \text{Tr}^2\left(\rho_A^2\right) \tag{12.3}$$

One can easily check that $\mathcal{F}_A(|\psi\rangle) = 0$ if the entanglement spectrum is flat, i.e. if the spectrum $\lambda_\alpha = 1/\chi$ for some integer $1 \leq \chi \leq \min(\text{d}_\text{A}, \text{d}_\text{B})$, whereas $\mathcal{F}_A(|\psi\rangle) > 0$ in other cases. Notice that in order for $\mathcal{F}_A(|\psi\rangle) \neq 0$ the state must be either not

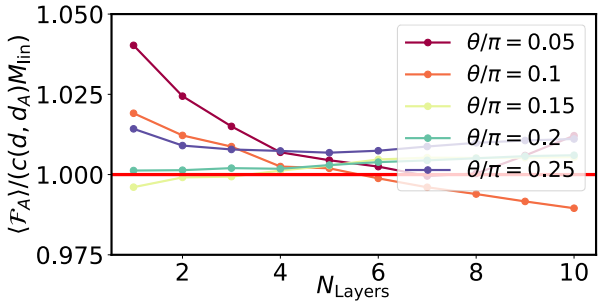

FIGURE 12.2: **Numerical simulations of shallow circuits:** We prepared the initial state in the volume law phase and we plot the ratio $\mathcal{F}_A / c(d, d_A) M_{\text{lin}}$ as a function of number of Clifford layers N_{Layers} of shallow circuit. As shown in the plot, the ratio approaches 1 very fast verifying Eq. (12.4).

entangled or without any magic. While every linear combination of different moments would be a sensible measure of (anti-)flatness, the one proposed above is the most natural one as it is the variance of the corresponding probability distribution according to itself: if a state σ is given in its spectral resolution $\sigma = \sum_i p_i \sigma_i$, then $\mathcal{F}(\sigma) = \text{Var}(\{p_i\}) := \langle (p_i - \langle p \rangle_p)^2 \rangle_p$.

Here, we use the flatness of the entanglement spectrum to quantify or witness nonstabilizerness of a pure state.

Theorem: *The Stabilizer Linear Entropy M_{lin} of a pure state $|\psi\rangle$) is proportional to the anti-flatness of the entanglement spectrum averaged over the Clifford orbit:*

$$\langle \mathcal{F}_A(\Gamma |\psi\rangle) \rangle_{C_n} = c(d, d_A) M_{\text{lin}}(|\psi\rangle)\,, \tag{12.4}$$

where $\langle \cdot \rangle_{C_n}$ denotes the average over the Clifford orbit $\Gamma |\psi\rangle$ and the proportionality constant $c(d, d_A) \sim (d^2 - d_A^2) d^{-3}$ for large d.

Proof.— We need to compute the average of the flatness over the Clifford orbit $\Gamma |\psi\rangle$ where $\Gamma \in C_n$, i.e. $\langle \mathcal{F}_A(\Gamma |\psi\rangle) \rangle_{C_n}$. Note that we can write

$$\langle \mathcal{F}_A(\Gamma |\psi\rangle) \rangle_{C_n} = \langle \text{tr}\left(\rho_{\Gamma,A}^3\right) \rangle_{C_n} - \langle \text{tr}^2(\rho_{\Gamma,A}^2) \rangle_{C_n} \tag{12.5}$$

where $\rho_{\Gamma,A} = \text{tr}_B(\Gamma |\psi\rangle\langle\psi| \Gamma^\dagger)$. We can now use the swap trick, i.e. $\text{tr}\left(O^3\right) = \text{tr}\left(T_{(123)} O^{\otimes 3}\right)$ and $\text{tr}^2(O^2) = \text{tr}\left(T_{(12)(34)} O^{\otimes 4}\right)$ to linearize the above averages over multiple copies of $|\psi\rangle$

$$\begin{aligned} \langle \mathcal{F}_A(\Gamma |\psi\rangle) \rangle_{C_n} &= \text{tr}\left(T^A_{(123)} \langle (\Gamma |\psi\rangle\langle\psi| \Gamma^\dagger)^{\otimes 3} \rangle_{C_n}\right) \\ &- \text{tr}\left(T^A_{(12)(34)} \langle (\Gamma |\psi\rangle\langle\psi| \Gamma^\dagger)^{\otimes 4} \rangle_{C_n}\right) \end{aligned} \tag{12.6}$$

where $T^A_{(123)}$ and $T^A_{(12)(34)}$ are permutations acting non-identically on the subsystem A only. For the first average in the r.h.s. of Eq. (12.6), we use the fact that the Clifford group is a 3-design [215, 216] and thus

$$\langle (\Gamma |\psi\rangle\langle\psi| \Gamma^\dagger)^{\otimes 3} \rangle_{C_n} = \frac{\Pi^{(3)}_{sym}}{\text{tr}\left(\Pi^{(3)}_{sym}\right)} \tag{12.7}$$

where $\Pi^{(3)}_{sym} = \sum_{\pi_3 \in S_3} T_{\pi_3}/3!$ is the symmetric projector, S_3 is the symmetric group acting on 3 copies of the Hilbert space of n qubits and T_{π_3} are unitary representations of permutations $\pi_3 \in S_3$. Therefore, the first term in Eq. (12.6) can be computed as

$$\frac{1}{\operatorname{tr}\Pi^{(3)}_{sym}} \operatorname{tr}\left(T^A_{(123)}\Pi^{(3)}_{sym}\right) = \frac{\sum_{\pi\in S_3} \operatorname{tr}_A(T^A_{(123)}T^A_\pi)\operatorname{tr}_B(T^B_\pi)}{\operatorname{tr}\Pi^{(3)}_{sym}} \tag{12.8}$$

where we used the fact that any permutation operator T_π for $\pi \in S_3$ obey $T_\pi = T^A_\pi \otimes T^B_\pi$. For the second average of the r.h.s. of Eq. (12.6), we use the technical results presented in [217, 218] that shows

$$\langle (\Gamma\,|\psi\rangle\langle\psi|\,\Gamma^\dagger)^{\otimes 4}\rangle_{C_n} \;=\; \alpha Q\Pi^{(4)}_{sym} + \beta\Pi^{(4)}_{sym} \tag{12.9}$$

where $Q = d^{-2}\sum_{P\in\mathcal{P}_n} P^{\otimes 4}$ and $\Pi^{(4)}_{sym}$ is the symmetric projector on S_4, defined as $\Pi^{(4)}_{sym} \equiv \sum_{\pi_4\in S_4} T_{\pi_4}/4!$. Then we defined

$$\begin{aligned} \alpha &:= \frac{\|\Xi_\psi\|_2^2}{(d+1)(d+2)/6} - \beta \\ \beta &:= \frac{1-\|\Xi_\psi\|_2^2}{(d^2-1)(d+2)(d+4)/24} \end{aligned} \tag{12.10}$$

Therefore, the second term in Eq. (12.6) can be computed as

$$\begin{aligned} \langle \operatorname{tr}^2(\rho^2_{\Gamma,A})\rangle_{C_n} &= \operatorname{tr}\left[T^A_{(12)(34)}(\alpha Q + \beta I)\Pi^{(4)}_{sym}\right] \\ &= \sum_{\pi\in S_4} [\alpha \operatorname{tr}_A(T^A_\pi T^A_{(12)(34)}Q^A)\operatorname{tr}_B(T^B_\pi Q^B) \\ &+ \beta \operatorname{tr}_A(T^A_\pi T^A_{(12)(34)})\operatorname{tr}_B(T^B_\pi)] \end{aligned} \tag{12.11}$$

where we used the fact that $Q = Q_A \otimes Q_B$ and $Q_X = d_X^{-2}\sum_{P\in\mathcal{P}_X} P_X^{\otimes 4}$ for $X = A, B$. Notice that $\operatorname{tr}(QT_\pi)$ are computed in [217] and tabulated in [219]. After a straightforward algebra, recalling that $M_{lin}(|\psi\rangle) = 1 - d\|\Xi_\psi\|_2^2$, one finds:

$$\begin{aligned} \langle \mathcal{F}_A(\operatorname{tr}_B(\Gamma\,|\psi\rangle\,\langle\psi|\,\Gamma^\dagger))\rangle_{C_n} &= \frac{(d^2-d_A^2)(d_A^2-1)}{(d^2-1)(d+2)d_A^2} M_{lin}(|\psi\rangle) \\ &\equiv c(d,d_A)M_{\text{lin}}(|\psi\rangle) \end{aligned} \tag{12.12}$$

which concludes the proof. □

Notice that the above result holds true for any bipartition of the system, which is reflected in the constant $c(d, d_A)$. We see that a pure stabilizer state possesses a flat entanglement spectrum over all its Clifford orbit and anti-flatness is stable under Clifford operations. Moreover, one can utilize a measurement of anti-flatness to measure M_{lin}. The theorem above poses also a relationship between entanglement and magic. Indeed, without entanglement, there is no anti-flatness in the reduced density operator. Along the Clifford orbit, entanglement is near-maximal and this is reflected in $c(d, d_A)$. It would be interesting to see whether (for an equal bipartition) anti-flatness assumes the form $\mathcal{F}_A(|\psi\rangle) \sim g(d_A)\text{Pur}^\beta(\rho_A)M_{\text{lin}}(|\psi\rangle)$ or if this relation only holds for highly entangled states.

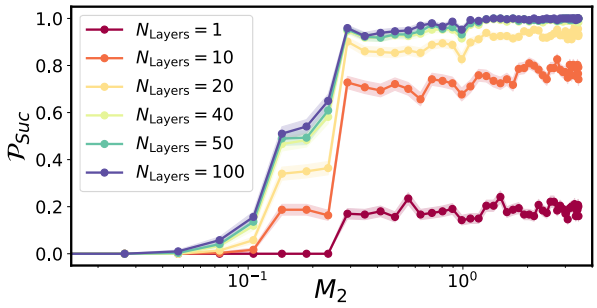

FIGURE 12.3: **Algorithm sensitivity:** Probability of success $\mathcal{P}_{\text{Suc}}$, for a fixed threshold $\epsilon = 0.005$ and for different N_{Layers}. After collecting $N_{\text{R}} = 1000$ realizations, we compute the probability of success $\mathcal{P}_{\text{Suc}}$, as a function of the initial value of nonstabilizerness calculated using the second SRE $M_2(|\psi_0\rangle)$.

12.2 Numerical experiments

As it was shown in [38], SRE can be experimentally measured via randomized unitaries [220], providing an important handle on the quality of a quantum circuit. However, SRE is a very expensive quantity to measure, requiring in general exponential resources (though better than state tomography). The result of the theorem opens the way to a very efficient way to measure SRE. However, things are not so simple. In the best case scenario, $c(d, d_A) = O(d^{-1})$, which means that one needs to resolve an exponentially small quantity, thereby requiring again exponential resources - even if with the considerable advantage that operations on a small subset are needed, thus relaxing one of the most challenging requirements of previous methods. This is because ψ_A is typically very entangled over C_n and therefore $\mathcal{F}_A$ is very close to be flat. Another issue is that, for weakly entangled states, direct exploitation of the theorem is extremely challenging in practice, as we shall demonstrate numerically in the following. One can intuitively understand that as for very weakly entangled states there are very few eigenvalues at all in the entanglement spectrum. As an extreme example, the entanglement spectrum of a product state is absolutely flat, regardless whether the state possesses any degree of nonstabilizerness. A very long circuit (inevitably, very sensitive to noise) will thus be required in those cases.

The key insight is that we can get around the requirement of a full Clifford orbit by (numerically) analyzing the intermediate regime. Approaching volume law one might be able to see a deviation from a flat spectrum without having to resolve an exponentially small quantity. If this is true, one would have found a witness for nonstabilizerness that is efficiently computable and measurable. Moreover, as one gets into the volume law for the entanglement phase, one should be able to evaluate accurately the actual value of M_{lin}, even without averaging over all the Clifford orbit. Of course, in this case, one still needs to resolve a very small quantity.

We consider an initial state that is a product state of n qubits with linear topology $|\psi_0\rangle = \otimes_{i=1}^{n} |\psi_i\rangle$, where $|\psi_i\rangle = \frac{1}{\sqrt{2}}\left(|0\rangle + e^{i\theta}|1\rangle\right)$. This state has initially computable nonstabilizerness (vanishing for $\theta = 0, \pi/2$). Note that $\theta = \pi/4$ corresponds to the canonical T-state. The state $|\psi_0\rangle$ is then evolved under a random Clifford circuit of depth N_{Layers} denoted by $U_{\text{Cl}} = \prod_k^{N_{Layers}} U_k$, where U_k contains $n-1$ Clifford gates (Hadamard, phase $e^{i\pi/2}$ gate and CNOT)[4] between nearest neighbors.

We are interested in how the entanglement spectrum, that is, the eigenvalues of the reduced density matrix $\rho_A = \mathrm{Tr}_B |\psi\rangle\langle\psi|$ (for $d_A = d_B = 2^{n/2}$ and $n = 14$ qubits) evolves under random Clifford circuit evolution. In Fig. 12.1 (b), we present the average of the anti-flatness $\langle \mathcal{F}_A \rangle$ as a function of the circuit depth N_{Layers}. The average is obtained from $N_R = 1000$ different realizations and it is calculated for various values of θ. For a small number of Clifford layers, the anti-flatness increases and exhibits a sharp dependence on θ. When the circuit is very deep, the system explores a very large portion of its Clifford orbit, and the ratio between average anti-flatness $\langle \mathcal{F}_A \rangle$ and $c(2^n, 2^{n/2}) M_{\text{lin}}$ approaches 1 (the solid red line in the inset of Figure 12.1), as predicted by the Theorem.

In Fig. 12.2, we show that one can accurately estimate M_{lin} even by shallow Clifford circuits provided one starts with volume law entanglement. We again consider a $n = 14$ qubit system in a volume law phase by subjecting the initial state $|\psi_0\rangle$ to $N_{\text{Layers}} = 1500$ Clifford layers, for various values of θ. We then plot the ratio $\langle \mathcal{F}_A \rangle / c(2^n, 2^{n/2}) M_{\text{lin}}$ as a function of the number of Clifford N_{Layers}. The theoretical line predicted by the theorem is shown as a solid red line. Notably, we observe that even for circuits as short as $N_{\text{Layers}} = 7$ Clifford layers, the average anti-flatness reaches the value predicted by the theorem [221].

12.3 Probing nonstabilizerness through flatness

As we discussed above, one could probe nonstabilizerness by probing flatness, which is amenable to be measured in experiments [222–225]. However, a naïve application of the theorem would result in a very costly procedure. We present an algorithm that can efficiently witness magic by exploring the Clifford orbit in the intermediate region between weak and volume-law entanglement [221]. Since measuring nonstabilizerness can be resource-intensive, the concept of witness provides a scalable approach to assess the accurate implementation of stabilizer operations or evaluate the fit of quantum hardware for preparing magic states.

The procedure works as follows: (1) Start with $|\psi_0\rangle$, a pure state. (2) Draw a random Clifford gate Γ and apply it to the initial state: $|\psi_\Gamma\rangle \equiv \Gamma|\psi_0\rangle$. (3) Measure the entanglement spectrum anti-flatness $\mathcal{F}_A(\psi_\Gamma)$ [1]. If the original state $|\psi_0\rangle$ is a stabilizer state, the output of the circuit is still a stabilizer state with zero anti-flatness. On the contrary, if $|\psi_0\rangle$ has a non-vanishing amount of nonstabilizerness, we expect that even a modest exploration of the Clifford orbit will result into a non-flat entanglement spectrum. Therefore, if after a number of Clifford unitaries we measure $\mathcal{F}_A > 0$ we can establish that the initial state possesses nonstabilizerness. The resulting algorithm is summarized in Fig. 12.1 (c). In this algorithm, we set both the number of iterations (which determines the number of Clifford layers) and the threshold for measuring flatness.

Notably, our proposed protocol does not demand an exhaustive exploration of the Clifford group, which is exponentially large. Instead, our findings in the previous section demonstrate that a shallow quantum circuit generated by fixing the number of Clifford layers to a reasonably small value is sufficient for detecting nonstabilizerness with a high probability. This is illustrated in Fig. 12.1 (c): we show the probability of success $\mathcal{P}_{\text{Suc}}$ (for $n = 12$ qubits) as a function of the initial value of nonstabilizerness calculated using the second SRE defined in Eq.(6.23). In order to address the role of errors in the measurement of $\mathcal{F}_A$, we introduce a threshold value

[1] For small partitions, this can be done either via state tomography, or utilizing the random unitary toolbox [220]

ϵ for our test. The success probability is defined as the number of times in which the algorithm gives True as output, thus detecting the nonstabilizerness of the initial state normalized to the total number of iterations.

Fig. 12.1 panel (c) displays a knee point effect of the probability of success $\mathcal{P}_{\text{Suc}}$ as a function of the nonstabilizerness calculated using the second SRE M_2, depending on the threshold value ϵ. While, as argued earlier, away from volume law, the general behavior of this algorithm requires a numerical analysis, the knee-point can be explained analytically in a rigorous way through the stabilizer fidelity

$$\mathcal{S}_{\max}(\psi) = \max_{\sigma \in \text{STAB}} |\langle \sigma|\psi\rangle|^2. \tag{12.13}$$

by the following proposition:

Proposition: *Define* $\mathcal{S}_{\max}(\psi) := \max_\sigma |\langle \sigma|\psi\rangle|^2$ *the stabilizer fidelity with* σ *a stabilizer state. Then, if* $\mathcal{S}_{\max}(\psi) > 1 - (\epsilon/7)^2$*, i.e. if the state is too close to a stabilizer state, the success probability is zero, that is,* $\mathcal{P}_{\text{Suc}}(\epsilon) = 0$.

Proof.—

Let us first prove the following lemma.

Lemma: *Given a pure state* $|\psi\rangle$ *and a bipartition* $A|B$*, then we have that the flatness* $\mathcal{F}_A$ *is upper bounded by*

$$\mathcal{F}_A(\psi) \leq 7\sqrt{1 - \mathcal{S}_{\max}(\psi)} \tag{12.14}$$

Proof.— Notice that for every stabilizer state σ we have $\mathcal{F}_A(\sigma) = 0$. Then, we have the following chain of inequalities

$$\begin{aligned}
& \mathcal{F}_A(\psi) = \mathcal{F}_A(\psi) - \mathcal{F}_A(\sigma) \\
= \;& \text{tr}\left[T^{(A)}_{123}(\psi^{\otimes 3} - \sigma^{\otimes 3})\right] - \text{tr}\left[T^{(A)}_{(12)(34)}(\psi^{\otimes 4} - \sigma^{\otimes 4})\right] \\
\leq \;& |\,\text{tr}\left[T^{(A)}_{123}(\psi^{\otimes 3} - \sigma^{\otimes 3})\right]| + |\,\text{tr}\left[T^{(A)}_{(12)(34)}(\psi^{\otimes 4} - \sigma^{\otimes 4})\right]| \\
\leq \;& \left\|T^A_{(123)}\right\|_\infty \|\psi^{\otimes 3} - \sigma^{\otimes 3}\|_1 + \left\|T^A_{(12)(34)}\right\|_\infty \left\|\psi^{\otimes 4} - \sigma^{\otimes 4}\right\|_1 \\
= \;& 7\|\psi - \sigma\|_1 = 7\sqrt{1 - |\langle \sigma|\psi\rangle|^2}.
\end{aligned} \tag{12.15}$$

In the third line, we used triangle inequality. In the fourth line we used the bound of Schatten p-norms, namely $|\,\text{tr}(AB)| \leq \|A\|_p \|A\|_q$ for $p^{-1} + q^{-1} = 1$ and chosen $p = \infty$ and $q = 1$. In the last line, we made use of the following inequality multiple times

$$\begin{aligned}
\left\|\psi^{\otimes 4} - \sigma^{\otimes 4}\right\| &= \left\|\psi^{\otimes 4} - \psi \otimes \sigma^{\otimes 3} + \psi \otimes \sigma^{\otimes 3} - \sigma^{\otimes 4}\right\| \\
&\leq \|\psi\|\left\|\psi^{\otimes 3} - \sigma^{\otimes 3}\right\| + \|\psi - \sigma\|\left\|\sigma^{\otimes 3}\right\| \\
&= \left\|\psi^{\otimes 3} - \sigma^{\otimes 3}\right\| + \|\psi - \sigma\| \\
&\leq 4\|\psi - \sigma\|
\end{aligned} \tag{12.16}$$

Then choosing in Eq. (12.16) $\min_{\sigma \in \text{STAB}}$, one obtain Eq. (12.14). □

The proposition is now a corollary of the above lemma. Indeed, given the threshold ϵ for the algorithm in Fig. 12.1 panel (c), then if $\mathcal{S}_{\max} > 1 - (\epsilon/7)^2$ then $\mathcal{F}_A(\psi) < \epsilon$ and thus $\mathcal{P}_{\text{Suc}}(\epsilon) = 0$. □

The above proposition provides insight into the sensitivity of the algorithm shown in Fig. 12.1 with respect to the stabilizer fidelity $\mathcal{S}_{\max}$, which is closely linked to the stabilizer entropy M_{lin}.

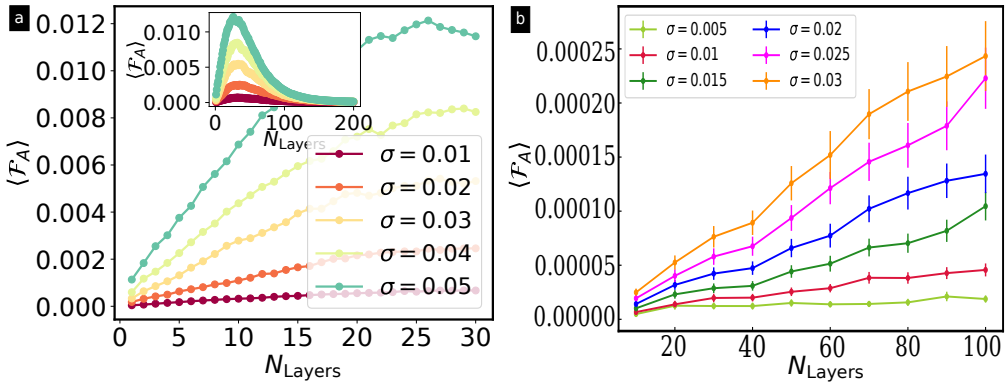

FIGURE 12.4: **Flatness in noisy circuit:** (a) We show the average of the anti-flatness, over $N_{\text{R}} = 1000$ realizations, as a function of N_{Layers}. We start from an initial STAB state $|\psi_0\rangle = \frac{1}{\sqrt{2}}(|0\rangle + |1\rangle)$. We inject magic using a modified CNOT gate and the average of the anti-flatness $\mathcal{F}_A$ increases after few layers of our circuit. (b) We show the average of flatness, over $N_{\text{R}} = 1000$ realizations, as a function N_{Layers}. We initialize the system in the ground state of Toric code, that is a STAB state, on a 4×2 unit cell (16 spins). We show that the anti-flatness increases almost linearly with the number of Clifford layers N_{Layers}. Error bars correspond to a 95% confidence interval.

In Fig. 12.3, we present the probability of success $\mathcal{P}_{\text{Suc}}$ (for $n = 12$ qubits) for a different maximum number of Clifford layers N_{Layers}. We fix the threshold $\epsilon = 0.005$ and we compute the probability as a function of nonstabilizerness calculated by $M_2(|\psi_0\rangle)$ of the initial state. The plot shows that increasing the number of algorithmic iterations N_{Layers} push the probability of success to 1 for any fixed values of nonstabilizerness.

12.4 Noisy Clifford circuit

So far we assumed that Clifford unitaries are ideal. In reality, they have a residual noise due to the fact that Clifford circuits are fine-tuned. In this situation, it is more natural to perform error mitigation at the level of channels rather than states. Consider a simple error model where each two-qubit Clifford $U(k)$ is independently affected by unitary noise. In particular, every two-qubit gate is transformed as follows:

$$\tilde{U}(k) = e^{-i\sum_\alpha \epsilon_\alpha P^\alpha} U(k) e^{i\sum_\alpha \epsilon_\alpha P^\alpha} \tag{12.17}$$

where ϵ_α is a random number chosen from a Gaussian distribution with average zero and standard deviation σ that represents here the strength of the noise. The choice of coherent noise is due to the fact that SRE is a proper measure of distillable magic only for pure states. For mixed states, it still has an important operational meaning in quantifying resources beyond Clifford [19]: for example, it is the key resource for establishing the cost of direct fidelity estimation [39], cleansing algorithms and efficient purity estimation [197]. The study of the effect of incoherent noise is to be carried out in future work.

Introducing noise to Clifford gates represents a magic-state injection that can be accurately captured by measuring the anti-flatness $\mathcal{F}_A$. In Fig. 12.4 (a) we present the evolution of the average of the anti-flatness $\mathcal{F}_A$ for a noisy Clifford circuit with

$n = 14$ qubits. We initialize our system in a stabilizer state $|\psi\rangle = \frac{1}{\sqrt{2}}(|0\rangle + |1\rangle)$ and then we measure the anti-flatness after every Clifford layer. Moreover, we also investigate the effect of noise starting from the ground state of the toric code - a stabilizer code formulated on a square lattice [226–229]. The basic construction of the toric code is a square lattice with a spin-1/2 degree of freedom on every bond, the physical qubits. The model is given in terms of a Hamiltonian $\hat{H} = -\sum_v A_v - \sum_p B_p$, where p runs over all plaquettes and v over all vertices (sites). The ground state of the toric code is a stabilizer state of the sets $\{A_v\}$ and $\{B_p\}$. After applying a Clifford circuit with a transformed CNOT gate, we measure the anti-flatness $\mathcal{F}_A$ after every layer. In Fig. 12.4 (b) we show the evolution of $\mathcal{F}_A$ for different strengths of noisy σ. It increases almost linearly with the number of Clifford layers. These results quantify how, upon close inspection of the microscopic imperfections, it is possible to define an error threshold that is able to discriminate between magic injected by errors along the Clifford orbit, and intrinsic magic of the original state.

12.5 Conclusions

We have demonstrated how nonstabilizerness of quantum states, while completely unrelated to entanglement *per se*, is deeply and exactly related to entanglement response, via the entanglement spectrum flatness of arbitrary partitions. Leveraging on this connection, we have formulated a simple protocol to efficiently witness and quantify nonstabilizerness in quantum systems, that is applicable to both atom and solid state settings where local operations and probing are available. The protocol is particularly efficient for states with volume law entanglement, and can cope with the inevitable presence of noise, as we demonstrate utilizing both random states and toric code dynamics. Our results pave the way for witnessing nonstabilizerness in large scale experiments - a pivotal step to demonstrate computational advantage -, and motivate further study of nonstabilizerness in quantum many-body systems, in particular, in connection to critical behavior, where entanglement response is expected to be particularly relevant.

Chapter 13

Nonstabilizerness versus entanglement in matrix product states

In this chapter, we study the connection between nonstabilizerness and the bond dimension of matrix product states (MPSs) [140]. We pursue a two-pronged approach. First, we investigate the broader question of how these two quantum resources, crucial for realizing states intractable to classical computers, are interrelated in many-body systems. Both nonstabilizerness and entanglement are known to be essential for such simulations. Second, we focus on the convergence properties of magic within the context of MPS simulations. Essentially, for a given variational simulation with a fixed bond dimension χ, we explore how quickly these approximations converge to the true values.

We address the magic-bond dimension relationship in two distinct, yet equally intriguing, many-body scenarios: full state magic and mutual magic of ground states (GSs). These scenarios offer diverse perspectives on the interplay between magic and entanglement. In the first case, we compare a global property (magic) with correlations between arbitrary sub-system parts (entanglement). Conversely, mutual magic examines shared resources between partitions, potentially relevant to field theory due to the cancellation of all boundary terms inherent to the chosen lattice regularization.

Our investigations encompass the scaling of full-state magic for critical points in spin-1 chains, as well as within gapped phases. We observe polynomial scaling for critical points, while gapped phases exhibit saturation at low bond dimensions, where sampling errors hinder clear scaling analysis. Notably, the observed polynomial scaling is compatible with a $1/\chi^2$ dependence across all cases, suggesting a convergence rate exceeding that of bipartite entanglement. This holds for both perfect sampling and Pauli MPS representations.

Subsequently, we leverage mutual magic to study quantities independent of the UV cutoff, employing Pauli-Markov chains. The findings reveal remarkably fast convergence for this approach. Surprisingly, Pauli-Markov chains exhibit an inverse scaling of autocorrelation time, facilitating sampling at larger system sizes. However, formulating definitive statements remains challenging due to potential transition-dependent effects.

Collectively, these findings shed light on the remarkably strong connection between magic and entanglement within the context of MPS, a connection that appears robust in different classes of criticality.

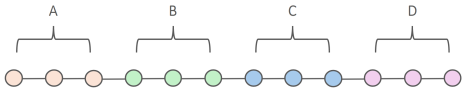

FIGURE 13.1: Schematic representation of the partitions of the chain considered for the calculation of long-range magic.

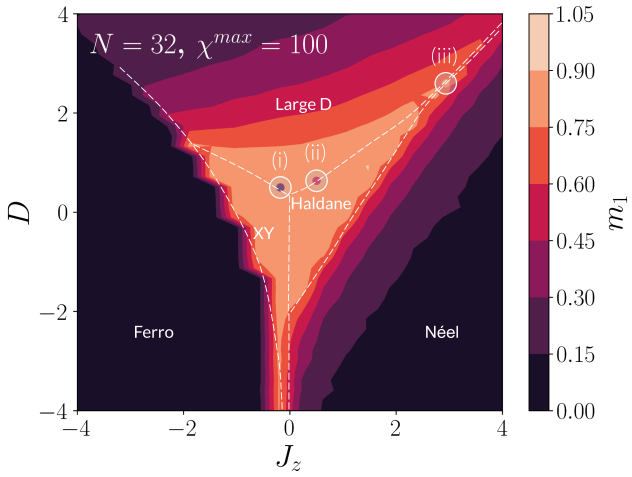

FIGURE 13.2: Phase diagram of the $S = 1$ XXZ chain with uniaxial single ion-type anisotropy. The three marked points correspond to the transitions examined in the rest of the paper: (i) Large D-XY ($J_z \sim -0.183$, $D \sim 0.5$); (ii) Haldane-Large D ($J_z \sim 0.5$, $D \sim 0.635$) and (iii) Haldane-Néel ($J_z \sim 2.93$, $D \sim 2.6$). m_1 is computed with perfect Pauli sampling with $N_S = 10^3$ samples.

13.1 SRE in spin-1 XXZ chain

We consider a $S = 1$ XXZ chain with uniaxial single ion-type anisotropy:

$$H = \sum_{i=1}^{N} [S_i^x S_{i+1}^x + S_i^y S_{i+1}^y + J_z S_i^z S_{i+1}^z] + D \sum_{i=1}^{N} S_i^{z2} \tag{13.1}$$

where S^α's, $\alpha = x, y, z$, are the spin-1 operators, J_z is the easy-axis anisotropy, and D is the single-ion anisotropy. The model has a global $U(1)$ symmetry corresponding to the conservation of total magnetization $\sum_i S_i^z$, and here we consider the ground states at the sector of zero total magnetization. The model displays a rich phase diagram, as sketched in Fig. 13.2, making it a good playground to explore magic in phase transitions [92].

For $J_z > 0$, the model hosts three phases (with increasing D): the antiferromagnetic Néel order, the symmetry-protected topological (SPT) Haldane phase, and the large-D trivial phase. The Néel to Haldane transition is an Ising transition, while the Haldane to large-D transition is a Gaussian transition.

For $Jz \leq 0$ the model hosts a ferromagnetic phase, the large-D trivial phase and two different XY phases: for large negative D (XY2) $\langle S_i^x S_j^x \rangle$ and $\langle S_i^x S_j^x \rangle$ decay exponentially, while for small negative D (XY1) they decay with a power law, therefore

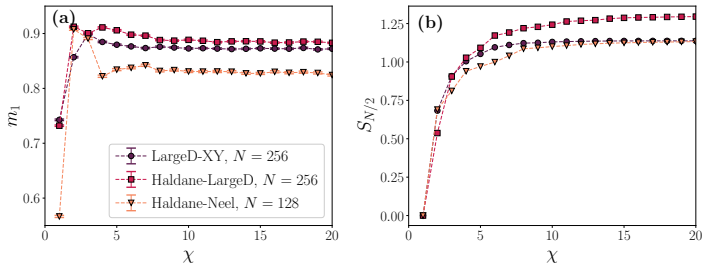

FIGURE 13.3: **(a)** The SRE density m_1 computed via perfect Pauli sampling for various bond dimensions χ. The number of samples is $N_S = 10^4$. **(b)** The entanglement entropy $S_{N/2}$ for various bond dimensions χ.

they can be regarded as two different phases. The XY to Haldane and XY to large-D transitions are BKT transitions, while XY to ferromagnetic and large-D to ferromagnetic are first order transitions.

In what follows, we consider three different transitions that are present in the model's phase diagram: Haldane-Néel (Ising transition at $J_z \sim 2.93$, $D \sim 2.6$), Haldane-LargeD (Gaussian transition at $J_z \sim 0.5$, $D \sim 0.635$) and Large D-XY (BKT transition at $J_z \sim -0.183$, $D \sim 0.5$) [92].

In terms of quantity, we will consider both the SRE and the long-range magic, defined as [28]:

$$L_n(\rho_{AB}) = \tilde{M}_n(\rho_{AB}) - \tilde{M}_n(\rho_B) - \tilde{M}_n(\rho_A) \tag{13.2}$$

where A and B are two separated subsystems and $\tilde{M}_n$ is the mixed state SRE. The long-range (or, probably better, mutual) magic is a UV cut-off independent quantity, similar to the mutual information in the context of entanglement entropies, that has played a major role in characterizing the distribution of both classical information and quantum correlations in many-body systems. It is important to say that, similar to mutual Renyi entropies, L_n will in general not being strictly positive (they will for the case $n = 1/2$, as discussed below). Still, from the many-body viewpoint, they are very appealing quantities, whose connection to physical phenomena has already been pointed out.

In the following, we will focus on $L_2(\rho_{AB})$, and drop the subscript for convenient notation. We will examine two different partitioning scenarios: two connected partitions (as B and C in Fig. 13.1); two disconnected partitions, with one positioned at the boundary and the other one in the bulk of the chain (A and C). In all two cases, we fix the lengths of the partitions by a fixed ratio of the total number of sites in the chain, specifically $N/4$. These situations will be referred to as: case BC and case AC.

The SRE in $S = 1$ XXZ chain was recently investigated in Ref. [28] using Pauli-Markov method. It was shown that, while the full-state magic appears rather featureless at the critical points, long-range magic is able to identify the transitions.

To obtain the MPS approximation of the ground state with a given bond dimension χ, we perform DMRG simulations using the iTensor package [230, 231]. We then employ three different methods: (1) Perfect Pauli sampling [27], (2) Pauli-Markov [28], and (3) replica Pauli-MPS [26] to compute the SRE in various scenarios. The full-state magic is generally linear in the system size N, and thus we will consider the SRE density $m_n = M_n/N$. Note that, since the phase-space operator $A_{\mathbf{0}}$ commutes with the Hamiltonian of the $S = 1$ XXZ chain, the ground state SREs coincide with the mana entropies (see Sec. 8).

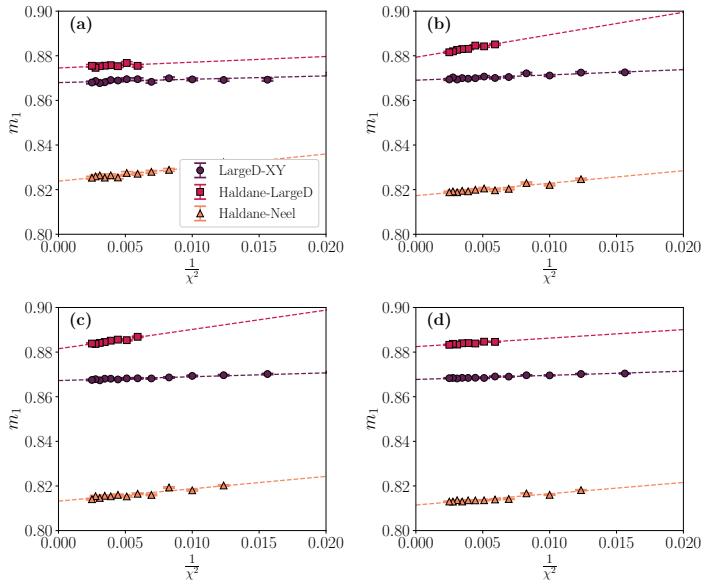

FIGURE 13.4: Scaling of the SRE density m_1 with the bond dimension χ in different critical points. The number of samples is $N_S = 10^4$. The different panels correspond to different system sizes: **(a)** $N = 128$; **(b)** $N = 256$; **(c)** $N = 512$ and **(d)** $N = 1024$.

For the Pauli-Markov method, due to the presence of $U(1)$ symmetry, a two-site update scheme is required to sample only the Pauli strings that are compatible with the symmetry. To this end, we generate the candidate Pauli string P' by randomly multiplying the current Pauli string P with either Z_i or $X_i^\dagger X_j$. Moreover, we set the probability to multiply with Z_i or $Z_i^\dagger$ to be equal, so that detailed balance is satisfied.

Fig. 13.2, obtained utilizing perfect Pauli sampling, illustrates the variation of m_1 within the model's phase diagram. Notably, magic reaches its peak within the topological phases (Haldane and XY) and rapidly declines in the trivial phases (Ferromagnetic, Large D, and Néel). However, no distinct characteristics are observed at the critical point, consistently with previous findings [28].

13.1.1 Scaling of full-state magic

We calculate the SRE and study how it scales with the bond dimension of the MPS. Initially, we utilize perfect Pauli sampling, focusing on the $n = 1$ SRE, where the number of samples only needs to scale polynomially with system size to achieve a desired level of accuracy in estimation. In Fig. 13.3, the SRE density m_1 is compared with the entanglement entropy at half chain, $S_{N/2}$. The graph displays three distinct transitions: Haldane-Néel, Haldane-Large D, and Large D-XY. We observe that convergence of non-stabilizerness occurs at smaller bond dimensions compared to those required for entanglement entropy. Indeed, as shown in Fig. 13.3a, a bond dimension of $\chi \sim 8$ is sufficient for an accurate computation of magic density, presenting a significant practical benefit.

Moreover, in Fig. 13.4 and Fig. 13.5, we demonstrate that m_1 scales as $\frac{1}{\chi^2}$ at critical points. Fig. 13.4 shows the linear dependence of m_1 from $\frac{1}{\chi^2}$ for different system sizes ($N \in \{128, 256, 512, 1024\}$), while Fig. 13.5 provides a detailed view of the largest system size. The dashed lines in these figures represent the fits performed with the functional form $m_1(1/\chi^2) = m_0 + c\,1/\chi^2$. Note that the slope c is size independent in

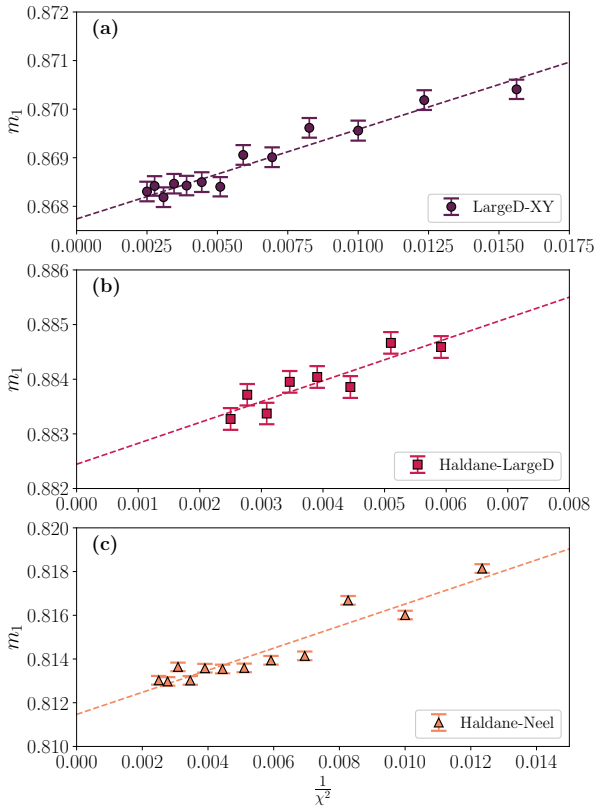

FIGURE 13.5: Scaling of the SRE density m_1 with the bond dimension χ in critical points at fixed $N = 1024$. The number of samples is $N_S = 10^4$ The different panels correspond to different transitions: **(a)** Large D-XY transition; **(b)** Haldane-Large D transition and **(c)** Haldane-Néel transiton.

the Large D-XY and Haldane-Neel transitions, while it changes non-monotonically with N in the Haldane-Large D case. Regarding the intercepts, we expect them to be size invariant since the SRE is generally linear with size N and what we're computing is its density, namely $m_1 = M_1/N$. Indeed, this expectation holds true for the Large D-XY and Haldane-Large D transitions but not for the Haldane-Néel one, which appears to exhibit a more pronounced finite-size effect.

Moreover, in Fig. 13.6, we show the behavior of m_2 as a function of bond dimension χ obtained from Pauli-MPS with bond dimension $\chi_P = 2 * \chi$. In Fig. 13.6a we show m_2 vs χ in the three distinct transitions: Haldane-Neel, Haldane-Large F and Large D-XY. We observed that the convergence of the m_2 occurs at small bond dimension. In Fig 13.6b, we show that m_2 scales as $\frac{1}{\chi^2}$ at the critical points for system size $N = 64$. In the three different panels, the dashed lines represent the fits performed with the functional form $m_2(1/\chi^2) = m_0 + c\ 1/\chi^2$.

13.1.2 Mutual information and long-range magic scaling

To evaluate long-range magic we employ the Pauli-Markov sampling technique. This choice is motivated by the limitations encountered with perfect Pauli sampling when estimating the quantities defined in Eq.s (7.20), (7.21). Perfect Pauli is efficient in these two scenarios: when ρ is a pure state; when ρ is the reduced density matrix of

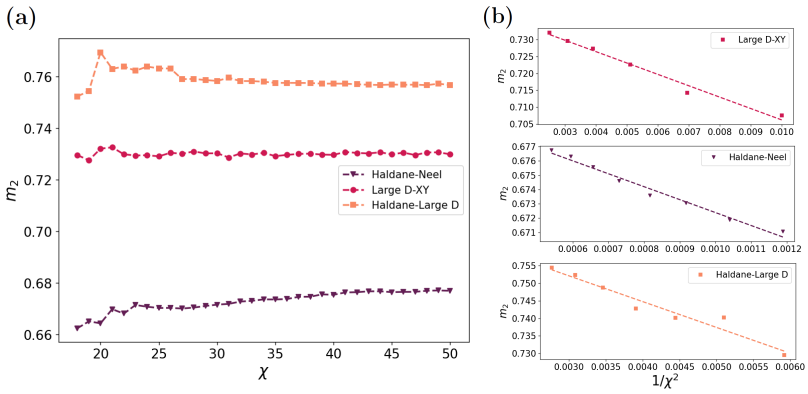

FIGURE 13.6: **(a)** The SRE density m_2 computed via Pauli-MPS for various bond dimensions χ. **(b)** Scaling of the SRE density m_2 with the bond dimension χ in the critical points at fixed $N = 64$.

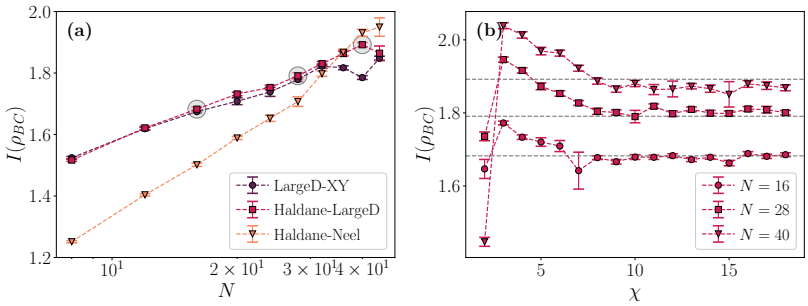

FIGURE 13.7: Mutual information scalings for connected partitions (case BC). The number of samples is $N_S = 10^6$. Panel **(a)**: scaling with the size for different transitions (in log scale). The three circles correspond to the sizes used for the scaling in the bond dimension χ. The bond dimension here is fixed at $\chi = 20$. Panel **(b)**: scaling with the bond dimension χ in the Haldane-Large D transition (Gaussian transition at $J_z \sim 0.5$, $D \sim 0.635$), for different sizes. The dashed lines here correspond the value of the mutual information at $\chi = 20$.

a partition that falls at the boundary of a larger pure state (both rightmost subsystem, in that case one should sample with the right-normalized form of the MPS, and leftmost, where instead one should use the left-normalized form). However, it is not efficient in the case of two (possibly disconnected) partitions.

We first focus on the mutual information I, obtained by means of the estimator defined in Eq. (7.21). Results are presented in Fig. 13.7 and Fig. 13.8, for case BC and AC respectevely. In particular, Fig. 13.7a shows the scaling with size in case BC. We observe that $I(\rho_{BC})$ exhibits logarithmic scaling. This corresponds with the expected scaling behavior for connected partitions, mirroring that of entanglement entropy in critical phases, which is well-established result in Conformal Field Theory [232, 233]. However, what differs from entanglement entropy is the scaling of $I(\rho_{BC})$ with the bond dimension χ, as illustrated in Fig. 13.7b. We focus on a single transition: the Haldane-Large D transition, and perform the scaling for $N \in \{16, 28, 40\}$. Notably, unlike what happens for $S_{N/2}$, the mutual information converges at a fixed value from above. What plays a role in this discrepancy are the partitions under examination. In our study, we analyze a four-partite system, unlike the bipartite case of

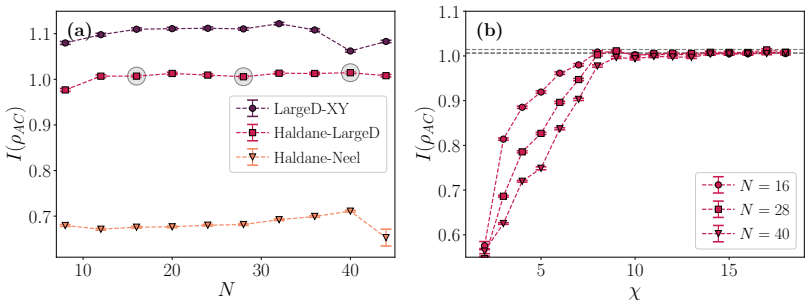

FIGURE 13.8: Mutual information scalings for disconnected partitions (case AC). The number of samples is $N_S = 10^6$. Panel **(a)**: scaling with the size for different transitions. The three circles correspond to the sizes used for the scaling in the bond dimension χ. The bond dimension here is fixed at $\chi = 20$. Panel **(b)**: scaling with the bond dimension χ in the Haldane-Large D transition (Gaussian transition at $J_z \sim 0.5$, $D \sim 0.635$), for different sizes. The dashed lines here correspond the value of the mutual information at $\chi = 20$.

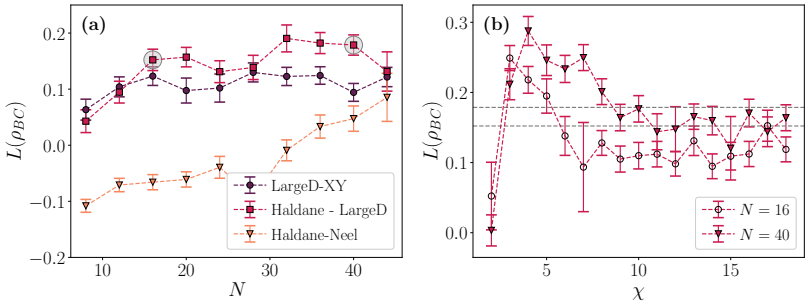

FIGURE 13.9: Long-range magic scalings for connected partitions (case BC). The number of samples is $N_S = 10^6$. Panel **(a)**: scaling with the size for different transitions. The two circles correspond to the sizes used for the scaling in the bond dimension χ. The bond dimension here is fixed at $\chi = 20$. Panel **(b)**: scaling with the bond dimension χ in the Haldane-Large D transition (Gaussian transition at $J_z \sim 0.5$, $D \sim 0.635$), for different sizes. The dashed lines correspond the value of the long-range magic at $\chi = 20$.

entanglement entropy. Hence, the information extracted is not directly comparable to that obtained from the latter. In the case of AC, as depicted in Fig. 13.8a, we observe that the mutual information $I(\rho_{BC})$ remains constant with increasing size, consistently with previously known results [234]. Fig. 13.8b shows the scaling with χ for the Haldane-LargeD transition and for the same three sizes as in the previous case. Even in this scenario, we observe a rapid saturation in the bond dimension.

As concerns long-range magic, the numeric results are challenging to interpret due to statistical error. In Fig. 13.9a and Fig. 13.10a, we display the scaling with the system size N for case BC and AC, respectively. Comparing with the behavior of mutual information, long-range magic appears to increase less rapidly for two connected partitions, while remaining constant for disconnected partitions. Turning to the scaling with the bond dimension χ, depicted in Fig. 13.9b, Fig. 13.10b, we notice parallels with the behavior of mutual information. However, unlike for the full-state magic case, we are not able to predict a functional form for the correction in the bond dimension. Specifically, to estimate the χ-dependence, in the previous

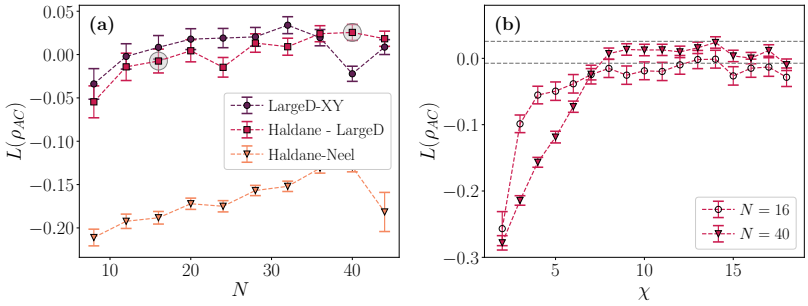

FIGURE 13.10: Long-range magic scalings for disconnected partitions (case AC). The number of samples is $N_S = 10^6$. Panel **(a)**: scaling with the size for different transitions. The two circles correspond to the sizes used for the scaling in the bond dimension χ. The bond dimension here is fixed at $\chi = 20$. Panel **(b)**: scaling with the bond dimension χ in the Haldane-Large D transition (Gaussian transition at $J_z \sim 0.5$, $D \sim 0.635$), for different sizes. The dashed lines correspond the value of the long-range magic at $\chi = 20$.

section we focused on $\chi \geq 5$. Yet, at these values of χ, it is difficult to discern the scaling, as the fluctuations we aim to fit are of the same order as the error bars with a sample size of $N_S = 10^6$. This is because our estimation of long-range magic comprises a sum of two terms, each associated with its own statistical error, and the W term defined in Eq. (7.20) is more challenging to estimate. As a consequence, we cannot predict the precise scaling of long-range magic in χ, but we consistently observe rapid saturation.

13.2 Autocorrelations

In this section we show a detailed analysis of the autocorrelation of the long-range magic. The normalized autocorrelation function of the stochastic process that generated the chain for f, denoted as $\rho_f(t)$, can be estimated for a finite set of N_S samples, as

$$\rho_f(t) = c_f(t)/c_f(0) \,, \tag{13.3}$$

where

$$c_f(t) = \frac{1}{N_S - t} \sum_{n=1}^{N_S - t} (f_n - \mu_f)(f_{n+t} - \mu_f) \tag{13.4}$$

and

$$\mu_f = \frac{1}{N_S} \sum_{n=1}^{N_S} f_n \,. \tag{13.5}$$

We estimate the integrated autocorrelation time τ as

$$\tau = 1 + 2 \sum_{t=1}^{M} \rho_f(t) \tag{13.6}$$

for some $M \ll N_S$. Extending the sum to N_S is inconvenient because, for $t \gg \tau$, $\rho_f(t)$ diminishes, leading to a situation where noise dominates over signal. Hence, introducing the cut-off M helps to reduce the variance of the estimator τ, at the cost of adding some bias. A good tradeoff between decreasing variance and introducing bias can be accomplished by choosing the smallest M that satisfies $M \geq C\tau(M)$,

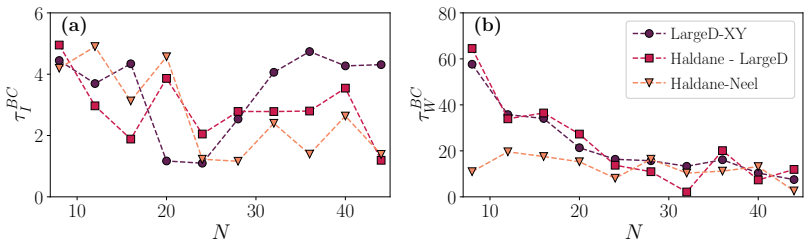

FIGURE 13.11: Integrated autocorrelation times scaling with size N for connected partitions B, C of length $L = N/4$ (see Fig. 13.1). **(a)** Integrated autocorrelation time in the estimation of $I(\rho_{BC})$ (Eq. (7.21)). **(b)** Integrated autocorrelation time in the estimation of $W(\rho_{BC})$ (Eq. (7.20)).

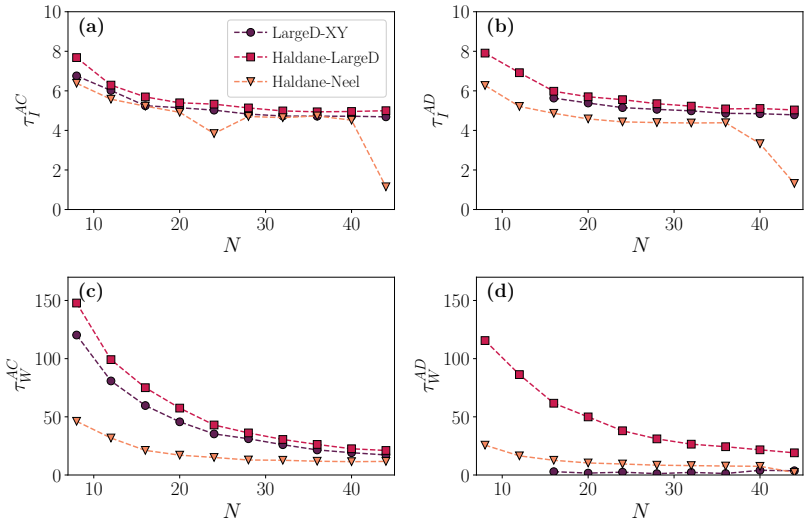

FIGURE 13.12: Integrated autocorrelation times scaling with size N for disconnected partitions of length $L = N/4$. Panels **(a)** and **(c)** refer to the choice of partitions A and C in Fig.13.1 (one in the boundary and one in the bulk, with distance $N/4$ between the two), while **(b)** and **(d)** refer to the choice A and D in Fig.13.1 (both at the boundary, with distance $N/2$ between the two). Panels **(a)** and **(b)** show the integrated autocorrelation times in the estimation of $I(\rho_{AC/AD})$ (Eq. (7.21)), while **c** and **d** show the integrated autocorrelation times in the estimation of $W(\rho_{AC/AD})$.

tipically with $C \sim 5$. We estimated the autocorrelation times using the emcee library [235] which employs the iterative procedure outlined in [236] to determine a suitable window size M.

Note that, for each computation of long-range magic, we make use of two Markov chains: one for the estimation of $I(\rho_{AB})$ defined in Eq. (7.21), the other one for the estimation of $W(\rho_{AB})$, as in Eq. (7.20). The two autocorrelation times are thus not directly related.

In Fig. 13.11, we show the results for two connected partitions (as B, C in Fig. 13.1). We observe that increasing the size of the system N, τ_I^{BC} is always ≤ 5, hence essentially constant. τ_W^{BC} is instead decreasing with size.

Fig. 13.12 shows the results for disconnected partitions. We study two possible scenarios: both partitions at the boundary of the chain (A, D of Fig. 13.1) or one

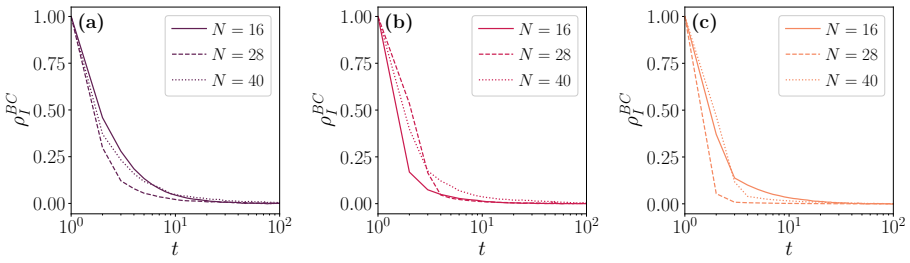

FIGURE 13.13: Normalized autocorrelation function of the mutual information I in case BC, for different sizes. Panel **(a)**: Large D-XY transition (BKT at $J_z \sim -0.183$, $D \sim 0.5$). Panel **(b)**: Haldane-Large D transition (Gaussian at $J_z \sim 0.5$, $D \sim 0.635$). Panel (**c**): Haldane-Néel (Ising at $J_z \sim 2.93$, $D \sim 2.6$).

at the boundary and one in the bulk (A, C). We observe that again τ_I is approximately constant while τ_W is decreasing with size, for both cases. This decreasing trend can be understood in terms of our proposal of the candidate string: at each Markov step we update either a single site or two sites, that are randomly chosen. The updated sites can then fall in two different partitions. When the two partitions are disconnected, as the size of the system increases, so does the distance between the two, making it easier to generate non-correlated Pauli strings. Indeed, when the two partitions are more distant, namely in the AD case, where they are separated by a distance $N/2$, the integrated autocorrelation time τ_W^{AD} is always smaller than the one corresponding to the other scenario τ_W^{AC}, where the distance between the partitions is $N/4$.

To further illustrate the origin of the above results, in Fig. 13.13, we show the behavior of the normalized autocorrelation function of the mutual information I for case BC. Figs. 13.13a, 13.13b and 13.13c correspond, respectively, to the Large D-XY, Haldane-Large D and Haldane-Néel transitions. Counterintuitively, we observe that despite the mutual information increasing with size (see Fig. 13.7), the autocorrelation of the Pauli-Markov chain remains constant.

These results demonstrate a remarkable unexpected efficiency of Pauli-Markov chains when dealing with long-range correlations: indeed, such Markov chains typically show a dynamical critical exponent between 0 and 1 for full state magic, while here, the exponent is actually negative - that is, sampling becomes simpler as volume increases, despite information not necessarily decaying. This feature makes Pauli-Markov chains potentially interesting to be used in experimental protocols.

13.3 Conclusions

We have investigated the relation between magic and bond dimension in the context of ground states of spin-1 systems, for which the resource theory of magic in terms of stabilizer Renyi entropies is well under control. We considered both the full-state magic, a global property, as well as the mutual magic, that characterizes the magic that resides in the correlations between subsystems. We mostly show results at critical points, since inside phases, convergence of magic with the bond dimension is so quick that is hard to characterize.

For full-state magic, we provide extensive numerical evidence that the stabilizer Renyi entropies converge rapidly with a scaling of $1/\chi^2$, significantly faster than that of entanglement. Then, for mutual magic, we again observed a very mild scaling

with respect to bond dimension, although we were not able to definitively determine the correct scaling form. These results lend credence to previous works that used small MPS bond dimension to study magic.

Additionally, a valuable byproduct of our investigation is the discovery that Pauli-Markov chains can efficiently estimate mutual information of disconnected subsystems, with the samples exhibiting small autocorrelations. This method - to the best of our knowledge - largely outperforms traditional methods utilizing exact TN contraction.

Overall, this work sheds light on the dependence of magic in MPS with the bond dimension; the latter is in turn directly linked to entanglement. Given the recent focus on the interplay between magic and entanglement, an interesting question is whether these results hold deeper significance, potentially hinting at a more fundamental connection between these two resource quantities. It would be intriguing to perform a similar analysis in the context of different classes of variational wave functions, such as projected entangled pair and tree tensor network states, where the bond dimension relation to entanglement is different than in MPSs. Finally, it could be interesting to investigate how some of the Pauli-based sampling methods might be suitably modified to measure magic and Renyi entropies experiments, relying on importance sampling.

Bibliography

1. Preskill, J. Quantum computing and the entanglement frontier. *arXiv preprint arXiv:1203.5813.* https://doi.org/10.48550/arXiv.1203.5813 (2012).
2. Shor, P. W. Polynomial-Time Algorithms for Prime Factorization and Discrete Logarithms on a Quantum Computer. *SIAM Journal on Computing* **26,** 1484–1509. https://doi.org/10.1137/s0097539795293172 (Oct. 1997).
3. Vidal, G. Efficient Classical Simulation of Slightly Entangled Quantum Computations. *Physical Review Letters* **91.** ISSN: 1079-7114. http://dx.doi.org/10.1103/PhysRevLett.91.147902 (Oct. 2003).
4. Nielsen, M. A. & Chuang, I. L. *Quantum Computation and Quantum Information* https://doi.org/10.1017/cbo9780511976667 (Cambridge University Press, June 2012).
5. Gottesman, D. Class of quantum error-correcting codes saturating the quantum Hamming bound. *Phys. Rev. A* **54,** 1862–1868. https://link.aps.org/doi/10.1103/PhysRevA.54.1862 (3 Sept. 1996).
6. Calderbank, A. R., Rains, E. M., Shor, P. W. & Sloane, N. J. A. Quantum Error Correction and Orthogonal Geometry. *Physical Review Letters* **78,** 405–408. ISSN: 1079-7114. http://dx.doi.org/10.1103/PhysRevLett.78.405 (Jan. 1997).
7. Bluvstein, D. *et al.* Logical quantum processor based on reconfigurable atom arrays. *Nature.* ISSN: 1476-4687. http://dx.doi.org/10.1038/s41586-023-06927-3 (Dec. 2023).
8. Kim, Y. *et al.* Evidence for the utility of quantum computing before fault tolerance. *Nature* **618,** 500–505. ISSN: 1476-4687. http://dx.doi.org/10.1038/s41586-023-06096-3 (June 2023).
9. Gottesman, D. *Stabilizer codes and quantum error correction* (California Institute of Technology, 1997).
10. Gottesman, D. *The Heisenberg representation of quantum computers* 1998. eprint: arXiv:quant-ph/9807006. https://doi.org/10.48550/arXiv.quant-ph/9807006.
11. Aaronson, S. & Gottesman, D. Improved simulation of stabilizer circuits. *Phys. Rev. A* **70,** 052328. https://link.aps.org/doi/10.1103/PhysRevA.70.052328 (5 Nov. 2004).
12. Bravyi, S. & Kitaev, A. Universal quantum computation with ideal Clifford gates and noisy ancillas. *Phys. Rev. A* **71,** 022316. https://link.aps.org/doi/10.1103/PhysRevA.71.022316 (2 Feb. 2005).
13. Campbell, E. T., Terhal, B. M. & Vuillot, C. Roads towards fault-tolerant universal quantum computation. *Nature* **549,** 172–179. https://doi.org/10.1038/nature23460 (Sept. 2017).

14. Dennis, E. Toward fault-tolerant quantum computation without concatenation. *Physical Review A* **63.** ISSN: 1094-1622. http://dx.doi.org/10.1103/PhysRevA.63.052314 (Apr. 2001).
15. Chitambar, E. & Gour, G. Quantum resource theories. *Reviews of Modern Physics* **91.** ISSN: 1539-0756. http://dx.doi.org/10.1103/RevModPhys.91.025001 (Apr. 2019).
16. Horodecki, R., Horodecki, P., Horodecki, M. & Horodecki, K. Quantum entanglement. *Reviews of Modern Physics* **81,** 865–942. ISSN: 1539-0756. http://dx.doi.org/10.1103/RevModPhys.81.865 (June 2009).
17. Veitch, V., Mousavian, S. A. H., Gottesman, D. & Emerson, J. The resource theory of stabilizer quantum computation. *New Journal of Physics* **16,** 013009. https://doi.org/10.1088/1367-2630/16/1/013009 (Jan. 2014).
18. Howard, M. & Campbell, E. Application of a Resource Theory for Magic States to Fault-Tolerant Quantum Computing. *Phys. Rev. Lett.* **118,** 090501. https://link.aps.org/doi/10.1103/PhysRevLett.118.090501 (9 Mar. 2017).
19. Leone, L., Oliviero, S. F. E. & Hamma, A. Stabilizer Rényi Entropy. *Phys. Rev. Lett.* **128,** 050402. https://link.aps.org/doi/10.1103/PhysRevLett.128.050402 (5 Feb. 2022).
20. Gross, D., Nezami, S. & Walter, M. Schur–Weyl Duality for the Clifford Group with Applications: Property Testing, a Robust Hudson Theorem, and de Finetti Representations. *Communications in Mathematical Physics* **385,** 1325–1393. https://doi.org/10.1007/s00220-021-04118-7 (June 2021).
21. Turkeshi, X., Dymarsky, A. & Sierant, P. *Pauli Spectrum and Magic of Typical Quantum Many-Body States* 2023. arXiv: 2312.11631 [quant-ph].
22. Leone, L. & Bittel, L. *Stabilizer entropies are monotones for magic-state resource theory* 2024. arXiv: 2404.11652 [quant-ph].
23. Haug, T. & Piroli, L. Stabilizer entropies and nonstabilizerness monotones. *Quantum* **7,** 1092. https://doi.org/10.22331/q-2023-08-28-1092 (Aug. 2023).
24. Haug, T., Lee, S. & Kim, M. S. Efficient Quantum Algorithms for Stabilizer Entropies. *Physical Review Letters* **132.** ISSN: 1079-7114. http://dx.doi.org/10.1103/PhysRevLett.132.240602 (June 2024).
25. Haug, T. & Piroli, L. Quantifying nonstabilizerness of matrix product states. *Phys. Rev. B* **107,** 035148. https://link.aps.org/doi/10.1103/PhysRevB.107.035148 (3 Jan. 2023).
26. Tarabunga, P. S., Tirrito, E., Bañuls, M. C. & Dalmonte, M. Nonstabilizerness via Matrix Product States in the Pauli Basis. *Physical Review Letters* **133.** ISSN: 1079-7114. http://dx.doi.org/10.1103/PhysRevLett.133.010601 (July 2024).
27. Lami, G. & Collura, M. Nonstabilizerness via Perfect Pauli Sampling of Matrix Product States. *Phys. Rev. Lett.* **131,** 180401. https://link.aps.org/doi/10.1103/PhysRevLett.131.180401 (18 Oct. 2023).
28. Tarabunga, P. S., Tirrito, E., Chanda, T. & Dalmonte, M. Many-Body Magic Via Pauli-Markov Chains—From Criticality to Gauge Theories. *PRX Quantum* **4,** 040317. https://link.aps.org/doi/10.1103/PRXQuantum.4.040317 (4 Oct. 2023).

29. Tarabunga, P. S. & Castelnovo, C. Magic in generalized Rokhsar-Kivelson wavefunctions. *Quantum* **8,** 1347. ISSN: 2521-327X. http://dx.doi.org/10.22331/q-2024-05-14-1347 (May 2024).
30. Liu, Z. & Clark, B. K. *Non-equilibrium Quantum Monte Carlo Algorithm for Stabilizer Rényi Entropy in Spin Systems* 2024. arXiv: 2405.19577 [quant-ph].
31. Chen, J., Yan, Y. & Zhou, Y. Magic of quantum hypergraph states. *Quantum* **8,** 1351. ISSN: 2521-327X. http://dx.doi.org/10.22331/q-2024-05-21-1351 (May 2024).
32. Passarelli, G., Fazio, R. & Lucignano, P. *Nonstabilizerness of permutationally invariant systems* 2024. arXiv: 2402.08551 [quant-ph].
33. López, J. A. M. & Kos, P. *Exact solution of long-range stabilizer Rényi entropy in the dual-unitary XXZ model* 2024. arXiv: 2405.04448 [quant-ph].
34. Beverland, M., Campbell, E., Howard, M. & Kliuchnikov, V. Lower bounds on the non-Clifford resources for quantum computations. *Quantum Science and Technology* **5,** 035009. ISSN: 2058-9565. http://dx.doi.org/10.1088/2058-9565/ab8963 (June 2020).
35. Grewal, S., Iyer, V., Kretschmer, W. & Liang, D. *Efficient Learning of Quantum States Prepared With Few Non-Clifford Gates* 2023. arXiv: 2305.13409 [quant-ph]. https://doi.org/10.48550/arXiv.2305.13409.
36. Hangleiter, D. & Gullans, M. J. Bell Sampling from Quantum Circuits. *Physical Review Letters* **133.** ISSN: 1079-7114. http://dx.doi.org/10.1103/PhysRevLett.133.020601 (July 2024).
37. Haug, T. & Kim, M. Scalable Measures of Magic Resource for Quantum Computers. *PRX Quantum* **4,** 010301. https://link.aps.org/doi/10.1103/PRXQuantum.4.010301 (1 Jan. 2023).
38. Oliviero, S. F. E., Leone, L., Hamma, A. & Lloyd, S. Measuring magic on a quantum processor. *npj Quantum Information* **8,** 148. https://doi.org/10.1038/s41534-022-00666-5 (Dec. 2022).
39. Leone, L., Oliviero, S. F. E. & Hamma, A. Nonstabilizerness determining the hardness of direct fidelity estimation. *Phys. Rev. A* **107,** 022429. https://link.aps.org/doi/10.1103/PhysRevA.107.022429 (2 Feb. 2023).
40. Odavić, J. *et al. Complexity of frustration: A new source of non-local non-stabilizerness* Oct. 2023. http://dx.doi.org/10.21468/SciPostPhys.15.4.131.
41. Gerster, M. *et al.* Unconstrained tree tensor network: An adaptive gauge picture for enhanced performance. *Phys. Rev. B* **90,** 125154. https://link.aps.org/doi/10.1103/PhysRevB.90.125154 (12 Sept. 2014).
42. Silvi, P. *et al.* The Tensor Networks Anthology: Simulation techniques for many-body quantum lattice systems. *SciPost Physics Lecture Notes.* https://doi.org/10.21468/scipostphyslectnotes.8 (Mar. 2019).
43. Oliviero, S. F. E., Leone, L. & Hamma, A. Magic-state resource theory for the ground state of the transverse-field Ising model. *Phys. Rev. A* **106,** 042426. https://link.aps.org/doi/10.1103/PhysRevA.106.042426 (4 Oct. 2022).
44. Vedral, V., Plenio, M. B., Rippin, M. A. & Knight, P. L. Quantifying Entanglement. *Phys. Rev. Lett.* **78,** 2275–2279. https://link.aps.org/doi/10.1103/PhysRevLett.78.2275 (12 Mar. 1997).

45. Gottesman, D. Theory of fault-tolerant quantum computation. *Phys. Rev. A* **57,** 127–137. https://link.aps.org/doi/10.1103/PhysRevA.57.127 (1 Jan. 1998).
46. Smith, G. & Leung, D. Typical entanglement of stabilizer states. *Phys. Rev. A* **74,** 062314. https://link.aps.org/doi/10.1103/PhysRevA.74.062314 (6 Dec. 2006).
47. Gütschow, J. Entanglement generation of Clifford quantum cellular automata. *Applied Physics B* **98,** 623–633. https://doi.org/10.1007/s00340-009-3840-1 (Dec. 2009).
48. Harrow, A. W. & Montanaro, A. Quantum computational supremacy. *Nature* **549,** 203–209. https://doi.org/10.1038/nature23458 (Sept. 2017).
49. Gheorghiu, V. Standard form of qudit stabilizer groups. *Physics Letters A* **378,** 505–509. https://doi.org/10.1016/j.physleta.2013.12.009 (Jan. 2014).
50. White, C. D., Cao, C. & Swingle, B. Conformal field theories are magical. *Phys. Rev. B* **103,** 075145. https://link.aps.org/doi/10.1103/PhysRevB.103.075145 (7 Feb. 2021).
51. Fliss, J. R. Knots, links, and long-range magic. *Journal of High Energy Physics* **2021.** https://doi.org/10.1007/jhep04(2021)090 (Apr. 2021).
52. Sarkar, S., Mukhopadhyay, C. & Bayat, A. Characterization of an operational quantum resource in a critical many-body system. *New Journal of Physics* **22,** 083077. https://doi.org/10.1088/1367-2630/aba919 (Aug. 2020).
53. Bao, N., Cao, C. & Su, V. P. Magic state distillation from entangled states. *Phys. Rev. A* **105,** 022602. https://link.aps.org/doi/10.1103/PhysRevA.105.022602 (2 Feb. 2022).
54. Matsuda, H., Kudo, K., Nakamura, R., Yamakawa, O. & Murata, T. Mutual information of Ising systems. *International Journal of Theoretical Physics* **35,** 839–845. https://doi.org/10.1007/BF02330576 (1996).
55. Melko, R. G., Kallin, A. B. & Hastings, M. B. Finite-size scaling of mutual information in Monte Carlo simulations: Application to the spin-$\frac{1}{2}$ XXZ model. *Phys. Rev. B* **82,** 100409. https://link.aps.org/doi/10.1103/PhysRevB.82.100409 (10 Sept. 2010).
56. Singh, R. R. P., Hastings, M. B., Kallin, A. B. & Melko, R. G. Finite-Temperature Critical Behavior of Mutual Information. *Phys. Rev. Lett.* **106,** 135701. https://link.aps.org/doi/10.1103/PhysRevLett.106.135701 (13 Mar. 2011).
57. Wilms, J., Troyer, M. & Verstraete, F. Mutual information in classical spin models. *Journal of Statistical Mechanics: Theory and Experiment* **2011,** P10011. https://iopscience.iop.org/article/10.1088/1742-5468/2011/10/P10011 (2011).
58. Wilms, J., Vidal, J., Verstraete, F. & Dusuel, S. Finite-temperature mutual information in a simple phase transition. *Journal of Statistical Mechanics: Theory and Experiment* **2012,** P01023. https://iopscience.iop.org/article/10.1088/1742-5468/2012/01/P01023/meta (2012).
59. Wolf, M. M., Verstraete, F., Hastings, M. B. & Cirac, J. I. Area Laws in Quantum Systems: Mutual Information and Correlations. *Phys. Rev. Lett.* **100,** 070502. https://link.aps.org/doi/10.1103/PhysRevLett.100.070502 (7 Feb. 2008).

60. Casini, H. Mutual information challenges entropy bounds. *Classical and Quantum Gravity* **24,** 1293. https://iopscience.iop.org/article/10.1088/0264-9381/24/5/013 (2007).
61. Lepori, L., Paganelli, S., Franchini, F. & Trombettoni, A. Mutual information for fermionic systems. *Phys. Rev. Res.* **4,** 033212. https://link.aps.org/doi/10.1103/PhysRevResearch.4.033212 (3 Sept. 2022).
62. Kudler-Flam, J. Rényi Mutual Information in Quantum Field Theory. *Phys. Rev. Lett.* **130,** 021603. https://link.aps.org/doi/10.1103/PhysRevLett.130.021603 (2 Jan. 2023).
63. Calabrese, P. & Cardy, J. Entanglement entropy and quantum field theory. *Journal of Statistical Mechanics: Theory and Experiment* **2004,** P06002. https://doi.org/10.1088/1742-5468/2004/06/p06002 (June 2004).
64. Caraglio, M. & Gliozzi, F. Entanglement entropy and twist fields. *Journal of High Energy Physics* **2008,** 076–076. ISSN: 1029-8479. http://dx.doi.org/10.1088/1126-6708/2008/11/076 (Nov. 2008).
65. Furukawa, S., Pasquier, V. & Shiraishi, J. Mutual information and boson radius in a c= 1 critical system in one dimension. *Physical Review Letters* **102.** ISSN: 1079-7114. http://dx.doi.org/10.1103/PhysRevLett.102.170602 (Apr. 2009).
66. Casini, H. & Huerta, M. A finite entanglement entropy and the c-theorem. *Physics Letters B* **600,** 142–150. ISSN: 0370-2693. http://dx.doi.org/10.1016/j.physletb.2004.08.072 (Oct. 2004).
67. De Boer, J., Järvelä, J. & Keski-Vakkuri, E. Aspects of capacity of entanglement. *Phys. Rev. D* **99,** 066012. https://link.aps.org/doi/10.1103/PhysRevD.99.066012 (6 Mar. 2019).
68. Zwanzig, R. W. High-Temperature Equation of State by a Perturbation Method. I. Nonpolar Gases. *The Journal of Chemical Physics* **22,** 1420–1426. https://doi.org/10.1063/1.1740409 (Aug. 1954).
69. Bennett, C. H. Efficient estimation of free energy differences from Monte Carlo data. *Journal of Computational Physics* **22,** 245–268. https://doi.org/10.1016/0021-9991(76)90078-4 (Oct. 1976).
70. Chib, S. Marginal Likelihood from the Gibbs Output. *Journal of the American Statistical Association* **90,** 1313–1321. https://doi.org/10.1080/01621459.1995.10476635 (Dec. 1995).
71. Gelfand, A. E. & Dey, D. K. Bayesian Model Choice: Asymptotics and Exact Calculations. *Journal of the Royal Statistical Society: Series B (Methodological)* **56,** 501–514. https://doi.org/10.1111/j.2517-6161.1994.tb01996.x (Sept. 1994).
72. Diciccio, T. J., Kass, R. E., Raftery, A. & Wasserman, L. Computing Bayes Factors by Combining Simulation and Asymptotic Approximations. *Journal of the American Statistical Association* **92,** 903–915. https://doi.org/10.1080/01621459.1997.10474045 (Sept. 1997).
73. Neal, R. M. *Statistics and Computing* **11,** 125–139. https://doi.org/10.1023/a:1008923215028 (2001).

74. Meng, X.-L. & Schilling, S. Fitting Full-Information Item Factor Models and an Empirical Investigation of Bridge Sampling. *Journal of the American Statistical Association* **91,** 1254–1267. https://doi.org/10.1080/01621459.1996.10476995 (Sept. 1996).

75. Gelman, A. & Meng, X.-L. Simulating normalizing constants: from importance sampling to bridge sampling to path sampling. *Statistical Science* **13.** https://doi.org/10.1214/ss/1028905934 (May 1998).

76. Chen, M.-H., Shao, Q.-M. & Ibrahim, J. G. *Monte Carlo Methods in Bayesian Computation* https://doi.org/10.1007/978-1-4612-1276-8 (Springer New York, 2000).

77. Wang, F. & Landau, D. P. Efficient, Multiple-Range Random Walk Algorithm to Calculate the Density of States. *Phys. Rev. Lett.* **86,** 2050–2053. https://link.aps.org/doi/10.1103/PhysRevLett.86.2050 (10 Mar. 2001).

78. Troyer, M., Wessel, S. & Alet, F. Flat Histogram Methods for Quantum Systems: Algorithms to Overcome Tunneling Problems and Calculate the Free Energy. *Phys. Rev. Lett.* **90,** 120201. https://link.aps.org/doi/10.1103/PhysRevLett.90.120201 (12 Mar. 2003).

79. Hastings, M. B., González, I., Kallin, A. B. & Melko, R. G. Measuring Renyi Entanglement Entropy in Quantum Monte Carlo Simulations. *Phys. Rev. Lett.* **104,** 157201. https://link.aps.org/doi/10.1103/PhysRevLett.104.157201 (15 Apr. 2010).

80. Humeniuk, S. & Roscilde, T. Quantum Monte Carlo calculation of entanglement Rényi entropies for generic quantum systems. *Phys. Rev. B* **86,** 235116. https://link.aps.org/doi/10.1103/PhysRevB.86.235116 (23 Dec. 2012).

81. Zhao, J. *et al.* Measuring Rényi entanglement entropy with high efficiency and precision in quantum Monte Carlo simulations. *npj Quantum Materials* **7.** https://doi.org/10.1038/s41535-022-00476-0 (June 2022).

82. Kitaev, A. & Preskill, J. Topological Entanglement Entropy. *Phys. Rev. Lett.* **96,** 110404. https://link.aps.org/doi/10.1103/PhysRevLett.96.110404 (11 Mar. 2006).

83. Levin, M. & Wen, X.-G. Detecting Topological Order in a Ground State Wave Function. *Phys. Rev. Lett.* **96,** 110405. https://link.aps.org/doi/10.1103/PhysRevLett.96.110405 (11 Mar. 2006).

84. Gerster, M., Rizzi, M., Silvi, P., Dalmonte, M. & Montangero, S. Fractional quantum Hall effect in the interacting Hofstadter model via tensor networks. *Phys. Rev. B* **96,** 195123. https://link.aps.org/doi/10.1103/PhysRevB.96.195123 (19 Nov. 2017).

85. Ferris, A. J. & Vidal, G. Perfect sampling with unitary tensor networks. *Phys. Rev. B* **85,** 165146. https://link.aps.org/doi/10.1103/PhysRevB.85.165146 (16 Apr. 2012).

86. Tagliacozzo, L., Evenbly, G. & Vidal, G. Simulation of two-dimensional quantum systems using a tree tensor network that exploits the entropic area law. *Phys. Rev. B* **80,** 235127. https://link.aps.org/doi/10.1103/PhysRevB.80.235127 (23 Dec. 2009).

87. Cataldi, G. *et al.* Hilbert curve vs Hilbert space: exploiting fractal 2D covering to increase tensor network efficiency. *Quantum* **5,** 556. https://doi.org/10.22331/q-2021-09-29-556 (Sept. 2021).

88. Felser, T., Silvi, P., Collura, M. & Montangero, S. Two-Dimensional Quantum-Link Lattice Quantum Electrodynamics at Finite Density. *Phys. Rev. X* **10,** 041040. https://link.aps.org/doi/10.1103/PhysRevX.10.041040 (4 Nov. 2020).

89. Magnifico, G., Felser, T., Silvi, P. & Montangero, S. Lattice quantum electrodynamics in (3+1)-dimensions at finite density with tensor networks. *Nature Communications* **12,** 3600. https://doi.org/10.1038/s41467-021-23646-3 (June 2021).

90. Felser, T., Notarnicola, S. & Montangero, S. Efficient Tensor Network Ansatz for High-Dimensional Quantum Many-Body Problems. *Phys. Rev. Lett.* **126,** 170603. https://link.aps.org/doi/10.1103/PhysRevLett.126.170603 (17 Apr. 2021).

91. Wu, F. Y. The Potts model. *Rev. Mod. Phys.* **54,** 235–268. https://link.aps.org/doi/10.1103/RevModPhys.54.235 (1 Jan. 1982).

92. Chen, W., Hida, K. & Sanctuary, B. C. Ground-state phase diagram of $S = 1$ XXZ chains with uniaxial single-ion-type anisotropy. *Phys. Rev. B* **67,** 104401. https://link.aps.org/doi/10.1103/PhysRevB.67.104401 (10 Mar. 2003).

93. Tzeng, Y.-C. & Yang, M.-F. Scaling properties of fidelity in the spin-1 anisotropic model. *Phys. Rev. A* **77,** 012311. https://link.aps.org/doi/10.1103/PhysRevA.77.012311 (1 Jan. 2008).

94. Hu, S., Normand, B., Wang, X. & Yu, L. Accurate determination of the Gaussian transition in spin-1 chains with single-ion anisotropy. *Phys. Rev. B* **84,** 220402. https://link.aps.org/doi/10.1103/PhysRevB.84.220402 (22 Dec. 2011).

95. Langari, A., Pollmann, F. & Siahatgar, M. Ground-state fidelity of the spin-1 Heisenberg chain with single ion anisotropy: quantum renormalization group and exact diagonalization approaches. *Journal of Physics: Condensed Matter* **25,** 406002. https://doi.org/10.1088/0953-8984/25/40/406002 (Sept. 2013).

96. Wolff, U. Critical slowing down. *Nuclear Physics B - Proceedings Supplements* **17,** 93–102. https://doi.org/10.1016/0920-5632(90)90224-i (Sept. 1990).

97. Wolff, U. Collective Monte Carlo Updating for Spin Systems. *Phys. Rev. Lett.* **62,** 361–364. https://link.aps.org/doi/10.1103/PhysRevLett.62.361 (4 Jan. 1989).

98. Wegner, F. J. Duality in generalized Ising models. *arXiv preprint arXiv:1411.5815.* https://arxiv.org/abs/1411.5815 (2014).

99. Blöte, H. W. J. & Deng, Y. Cluster Monte Carlo simulation of the transverse Ising model. *Phys. Rev. E* **66,** 066110. https://link.aps.org/doi/10.1103/PhysRevE.66.066110 (6 Dec. 2002).

100. Sandvik, A. W., Avella, A. & Mancini, F. *Computational Studies of Quantum Spin Systems* in *AIP Conference Proceedings* (AIP, 2010). https://doi.org/10.1063/1.3518900.

101. Montanaro, A. *Learning stabilizer states by Bell sampling* 2017. arXiv: 1707.04012 [quant-ph]. https://arxiv.org/abs/1707.04012.

102. Lu, T.-C. & Grover, T. Structure of quantum entanglement at a finite temperature critical point. *Phys. Rev. Res.* **2,** 043345. https://link.aps.org/doi/10.1103/PhysRevResearch.2.043345 (4 Dec. 2020).

103. Lu, T.-C. & Grover, T. Singularity in entanglement negativity across finite-temperature phase transitions. *Physical Review B* **99,** 075157. ISSN: 2469-9969. http://dx.doi.org/10.1103/PhysRevB.99.075157 (Feb. 2019).

104. Wald, S., Arias, R. & Alba, V. Entanglement and classical fluctuations at finite-temperature critical points. *Journal of Statistical Mechanics: Theory and Experiment* **2020,** 033105. https://doi.org/10.1088/1742-5468/ab6b19 (Mar. 2020).

105. Arceci, L., Silvi, P. & Montangero, S. Entanglement of Formation of Mixed Many-Body Quantum States via Tree Tensor Operators. *Phys. Rev. Lett.* **128,** 040501. https://link.aps.org/doi/10.1103/PhysRevLett.128.040501 (4 Jan. 2022).

106. Tarabunga, P. S., Mendes-Santos, T., Illuminati, F. & Dalmonte, M. Finite-temperature quantum discordant criticality. *Phys. Rev. B* **105,** 075104. https://link.aps.org/doi/10.1103/PhysRevB.105.075104 (7 Feb. 2022).

107. Frérot, I., Ran çon, A. & Roscilde, T. Thermal Critical Dynamics from Equilibrium Quantum Fluctuations. *Phys. Rev. Lett.* **128,** 130601. https://link.aps.org/doi/10.1103/PhysRevLett.128.130601 (13 Mar. 2022).

108. Niroula, P. *et al. Phase transition in magic with random quantum circuits* 2023. arXiv: 2304.10481 [quant-ph].

109. Rattacaso, D., Leone, L., Oliviero, S. F. E. & Hamma, A. Stabilizer entropy dynamics after a quantum quench. *Physical Review A* **108.** ISSN: 2469-9934. http://dx.doi.org/10.1103/PhysRevA.108.042407 (Oct. 2023).

110. Kadosawa, M., Nakamura, M., Ohta, Y. & Nishimoto, S. One-dimensional projection of two-dimensional systems using spiral boundary conditions. *Phys. Rev. B* **107,** L081104. https://link.aps.org/doi/10.1103/PhysRevB.107.L081104 (8 Feb. 2023).

111. Tirrito, E. *et al.* Quantifying nonstabilizerness through entanglement spectrum flatness. *Physical Review A* **109.** ISSN: 2469-9934. http://dx.doi.org/10.1103/PhysRevA.109.L040401 (Apr. 2024).

112. Turkeshi, X., Schirò, M. & Sierant, P. Measuring nonstabilizerness via multifractal flatness. *Phys. Rev. A* **108,** 042408. https://link.aps.org/doi/10.1103/PhysRevA.108.042408 (4 Oct. 2023).

113. Um, J., Park, H. & Hinrichsen, H. Entanglement versus mutual information in quantum spin chains. *Journal of Statistical Mechanics: Theory and Experiment* **2012,** P10026. https://doi.org/10.1088/1742-5468/2012/10/p10026 (Oct. 2012).

114. Alcaraz, F. C. & Rajabpour, M. A. Universal Behavior of the Shannon Mutual Information of Critical Quantum Chains. *Phys. Rev. Lett.* **111,** 017201. https://link.aps.org/doi/10.1103/PhysRevLett.111.017201 (1 July 2013).

115. Stéphan, J.-M. Shannon and Rényi mutual information in quantum critical spin chains. *Phys. Rev. B* **90,** 045424. https://link.aps.org/doi/10.1103/PhysRevB.90.045424 (4 July 2014).

116. Alcaraz, F. C. & Rajabpour, M. A. Generalized mutual information of quantum critical chains. *Phys. Rev. B* **91,** 155122. https://link.aps.org/doi/10.1103/PhysRevB.91.155122 (15 Apr. 2015).

117. Alcaraz, F. C. & Rajabpour, M. A. Universal behavior of the Shannon and Rényi mutual information of quantum critical chains. *Phys. Rev. B* **90,** 075132. https://link.aps.org/doi/10.1103/PhysRevB.90.075132 (7 Aug. 2014).

118. Alcaraz, F. C. Universal behavior of the Shannon mutual information in non-integrable self-dual quantum chains. *Phys. Rev. B* **94,** 115116. https://link.aps.org/doi/10.1103/PhysRevB.94.115116 (11 Sept. 2016).

119. Frau, M., Tarabunga, P. S., Collura, M., Dalmonte, M. & Tirrito, E. Nonstabilizerness versus entanglement in matrix product states. *Physical Review B* **110.** ISSN: 2469-9969. http://dx.doi.org/10.1103/PhysRevB.110.045101 (July 2024).

120. Veitch, V., Ferrie, C., Gross, D. & Emerson, J. Negative quasi-probability as a resource for quantum computation. *New Journal of Physics* **14,** 113011. https://doi.org/10.1088/1367-2630/14/11/113011 (Nov. 2012).

121. Sewell, T. J. & White, C. D. Mana and thermalization: Probing the feasibility of near-Clifford Hamiltonian simulation. *Phys. Rev. B* **106,** 125130. https://link.aps.org/doi/10.1103/PhysRevB.106.125130 (12 Sept. 2022).

122. Gross, D. Hudson's theorem for finite-dimensional quantum systems. *Journal of Mathematical Physics* **47,** 122107. https://doi.org/10.1063/1.2393152 (Dec. 2006).

123. Wootters, W. K. A Wigner-function formulation of finite-state quantum mechanics. *Annals of Physics* **176,** 1–21. https://doi.org/10.1016/0003-4916(87)90176-x (May 1987).

124. Wigner, E. On the Quantum Correction For Thermodynamic Equilibrium. *Phys. Rev.* **40,** 749–759. https://link.aps.org/doi/10.1103/PhysRev.40.749 (5 June 1932).

125. Pashayan, H., Wallman, J. J. & Bartlett, S. D. Estimating Outcome Probabilities of Quantum Circuits Using Quasiprobabilities. *Phys. Rev. Lett.* **115,** 070501. https://link.aps.org/doi/10.1103/PhysRevLett.115.070501 (7 Aug. 2015).

126. Yao, H. & Qi, X.-L. Entanglement Entropy and Entanglement Spectrum of the Kitaev Model. *Phys. Rev. Lett.* **105,** 080501. https://link.aps.org/doi/10.1103/PhysRevLett.105.080501 (8 Aug. 2010).

127. Schliemann, J. Entanglement spectrum and entanglement thermodynamics of quantum Hall bilayers at $\nu = 1$. *Phys. Rev. B* **83,** 115322. https://link.aps.org/doi/10.1103/PhysRevB.83.115322 (11 Mar. 2011).

128. Zaletel, M. P., Bardarson, J. H. & Moore, J. E. Logarithmic Terms in Entanglement Entropies of 2D Quantum Critical Points and Shannon Entropies of Spin Chains. *Phys. Rev. Lett.* **107,** 020402. https://link.aps.org/doi/10.1103/PhysRevLett.107.020402 (2 July 2011).

129. Isakov, S. V., Hastings, M. B. & Melko, R. G. Topological entanglement entropy of a Bose–Hubbard spin liquid. *Nature Physics* **7,** 772–775. https://doi.org/10.1038/nphys2036 (July 2011).

130. Block, M. S., D'Emidio, J. & Kaul, R. K. Kagome model for a $\mathbb{Z}_2$ quantum spin liquid. *Phys. Rev. B* **101,** 020402. https://link.aps.org/doi/10.1103/PhysRevB.101.020402 (2 Jan. 2020).

131. Affleck, I., Oshikawa, M. & Saleur, H. Boundary critical phenomena in the three-state Potts model. *Journal of Physics A: Mathematical and General* **31,** 5827–5842. https://doi.org/10.1088/0305-4470/31/28/003 (July 1998).

132. Di Francesco, P., Mathieu, P. & Sénéchal, D. *Conformal field theory* https://cds.cern.ch/record/639405 (Springer, New York, NY, 1997).

133. Lahtinen, V., Mansson, T. & Ardonne, E. Quantum criticality in many-body parafermion chains. *SciPost Physics Core* **4.** https://doi.org/10.21468/scipostphyscore.4.2.014 (May 2021).

134. Delfosse, N., Allard Guerin, P., Bian, J. & Raussendorf, R. Wigner Function Negativity and Contextuality in Quantum Computation on Rebits. *Phys. Rev. X* **5,** 021003. https://link.aps.org/doi/10.1103/PhysRevX.5.021003 (2 Apr. 2015).

135. Howard, M., Wallman, J., Veitch, V. & Emerson, J. Contextuality supplies the 'magic' for quantum computation. *Nature* **510,** 351–355. https://doi.org/10.1038/nature13460 (June 2014).

136. Bermejo-Vega, J., Delfosse, N., Browne, D. E., Okay, C. & Raussendorf, R. Contextuality as a Resource for Models of Quantum Computation with Qubits. *Phys. Rev. Lett.* **119,** 120505. https://link.aps.org/doi/10.1103/PhysRevLett.119.120505 (12 Sept. 2017).

137. Kocia, L. & Love, P. Discrete Wigner formalism for qubits and noncontextuality of Clifford gates on qubit stabilizer states. *Phys. Rev. A* **96,** 062134. https://link.aps.org/doi/10.1103/PhysRevA.96.062134 (6 Dec. 2017).

138. Raussendorf, R., Bermejo-Vega, J., Tyhurst, E., Okay, C. & Zurel, M. Phase-space-simulation method for quantum computation with magic states on qubits. *Phys. Rev. A* **101,** 012350. https://link.aps.org/doi/10.1103/PhysRevA.101.012350 (1 Jan. 2020).

139. Goto, K., Nosaka, T. & Nozaki, M. Probing chaos by magic monotones. *Phys. Rev. D* **106,** 126009. https://link.aps.org/doi/10.1103/PhysRevD.106.126009 (12 Dec. 2022).

140. Cirac, J. I., Pérez-García, D., Schuch, N. & Verstraete, F. Matrix product states and projected entangled pair states: Concepts, symmetries, theorems. *Reviews of Modern Physics* **93.** ISSN: 1539-0756. http://dx.doi.org/10.1103/RevModPhys.93.045003 (Dec. 2021).

141. Chen, J., Yan, Y. & Zhou, Y. Magic of quantum hypergraph states. *Quantum* **8,** 1351. ISSN: 2521-327X. http://dx.doi.org/10.22331/q-2024-05-21-1351 (May 2024).

142. Henley, C. L. From classical to quantum dynamics at Rokhsar–Kivelson points. *Journal of Physics: Condensed Matter* **16,** S891–S898. https://doi.org/10.1088/0953-8984/16/11/045 (Mar. 2004).

143. Ardonne, E., Fendley, P. & Fradkin, E. Topological order and conformal quantum critical points. *Annals of Physics* **310,** 493–551. https://doi.org/10.1016/j.aop.2004.01.004 (Apr. 2004).

144. Castelnovo, C., Chamon, C., Mudry, C. & Pujol, P. From quantum mechanics to classical statistical physics: Generalized Rokhsar–Kivelson Hamiltonians and the "Stochastic Matrix Form" decomposition. *Annals of Physics* **318,** 316–344. https://doi.org/10.1016/j.aop.2005.01.006 (Aug. 2005).

145. Piemontese, S., Roscilde, T. & Hamma, A. Entanglement complexity of the Rokhsar-Kivelson-sign wavefunctions. *Phys. Rev. B* **107,** 134202. https://link.aps.org/doi/10.1103/PhysRevB.107.134202 (13 Apr. 2023).

146. Rokhsar, D. S. & Kivelson, S. A. Superconductivity and the Quantum Hard-Core Dimer Gas. *Phys. Rev. Lett.* **61,** 2376–2379. https://link.aps.org/doi/10.1103/PhysRevLett.61.2376 (20 Nov. 1988).

147. Verstraete, F. & Cirac, J. I. Matrix product states represent ground states faithfully. *Physical Review B* **73.** ISSN: 1550-235X. http://dx.doi.org/10.1103/PhysRevB.73.094423 (Mar. 2006).

148. Schwarz, M., Temme, K. & Verstraete, F. Preparing Projected Entangled Pair States on a Quantum Computer. *Phys. Rev. Lett.* **108,** 110502. https://link.aps.org/doi/10.1103/PhysRevLett.108.110502 (11 Mar. 2012).

149. Zhu, G.-Y. & Zhang, G.-M. Gapless Coulomb State Emerging from a Self-Dual Topological Tensor-Network State. *Phys. Rev. Lett.* **122,** 176401. https://link.aps.org/doi/10.1103/PhysRevLett.122.176401 (17 Apr. 2019).

150. Lee, J. Y., Ji, W., Bi, Z. & Fisher, M. P. A. *Decoding Measurement-Prepared Quantum Phases and Transitions: from Ising model to gauge theory, and beyond* 2022. arXiv: 2208.11699 [cond-mat.str-el].

151. Zhu, G.-Y., Tantivasadakarn, N., Vishwanath, A., Trebst, S. & Verresen, R. Nishimori's Cat: Stable Long-Range Entanglement from Finite-Depth Unitaries and Weak Measurements. *Physical Review Letters* **131.** ISSN: 1079-7114. http://dx.doi.org/10.1103/PhysRevLett.131.200201 (Nov. 2023).

152. Chen, E. H. *et al. Realizing the Nishimori transition across the error threshold for constant-depth quantum circuits* 2023. arXiv: 2309.02863 [quant-ph].

153. Zhu, G.-Y., Chen, J.-Y., Ye, P. & Trebst, S. Topological Fracton Quantum Phase Transitions by Tuning Exact Tensor Network States. *Phys. Rev. Lett.* **130,** 216704. https://link.aps.org/doi/10.1103/PhysRevLett.130.216704 (21 May 2023).

154. Castelnovo, C., Trebst, S. & Troyer, M. in *Understanding Quantum Phase Transitions* 169–192 (CRC Press, Nov. 2010). https://doi.org/10.1201/b10273-10.

155. Hukushima, K. & Nemoto, K. Exchange Monte Carlo Method and Application to Spin Glass Simulations. *Journal of the Physical Society of Japan* **65,** 1604–1608. https://doi.org/10.1143/jpsj.65.1604 (June 1996).

156. Marinari, E., Parisi, G., Ruiz-Lorenzo, J. & Ritort, F. Numerical Evidence for Spontaneously Broken Replica Symmetry in 3D Spin Glasses. *Phys. Rev. Lett.* **76,** 843–846. https://link.aps.org/doi/10.1103/PhysRevLett.76.843 (5 Jan. 1996).

157. Castelnovo, C. & Chamon, C. Quantum topological phase transition at the microscopic level. *Phys. Rev. B* **77,** 054433. https://link.aps.org/doi/10.1103/PhysRevB.77.054433 (5 Feb. 2008).

158. Talapov, A. L. & Blöte, H. W. J. The magnetization of the 3D Ising model. *Journal of Physics A: Mathematical and General* **29,** 5727–5733. https://doi.org/10.1088/0305-4470/29/17/042 (Sept. 1996).

159. Nishimori, H. *Statistical Physics of Spin Glass and Information Processing: an Introduction* https://doi.org/10.1093/acprof:oso/9780198509417.001.0001 (Oxford University Press, July 2001).

160. Wannier, G. H. Antiferromagnetism. The Triangular Ising Net. *Phys. Rev.* **79,** 357–364. https://link.aps.org/doi/10.1103/PhysRev.79.357 (2 July 1950).

161. Houtappel, R. Order-disorder in hexagonal lattices. *Physica* **16,** 425–455. https://doi.org/10.1016/0031-8914(50)90130-3 (May 1950).

162. Blankschtein, D., Ma, M., Berker, A. N., Grest, G. S. & Soukoulis, C. M. Orderings of a stacked frustrated triangular system in three dimensions. *Phys. Rev. B* **29,** 5250–5252. https://link.aps.org/doi/10.1103/PhysRevB.29.5250 (9 May 1984).

163. Moessner, R. & Sondhi, S. L. Ising models of quantum frustration. *Phys. Rev. B* **63,** 224401. https://link.aps.org/doi/10.1103/PhysRevB.63.224401 (22 May 2001).

164. Isakov, S. V. & Moessner, R. Interplay of quantum and thermal fluctuations in a frustrated magnet. *Phys. Rev. B* **68,** 104409. https://link.aps.org/doi/10.1103/PhysRevB.68.104409 (10 Sept. 2003).

165. Wang, Y.-C., Qi, Y., Chen, S. & Meng, Z. Y. Caution on emergent continuous symmetry: A Monte Carlo investigation of the transverse-field frustrated Ising model on the triangular and honeycomb lattices. *Phys. Rev. B* **96,** 115160. https://link.aps.org/doi/10.1103/PhysRevB.96.115160 (11 Sept. 2017).

166. Katzgraber, H. G., Körner, M. & Young, A. P. Universality in three-dimensional Ising spin glasses: A Monte Carlo study. *Phys. Rev. B* **73,** 224432. https://link.aps.org/doi/10.1103/PhysRevB.73.224432 (22 June 2006).

167. Charfreitag, J., Jünger, M., Mallach, S. & Mutzel, P. *McSparse: Exact Solutions of Sparse Maximum Cut and Sparse Unconstrained Binary Quadratic Optimization Problems* in *2022 Proceedings of the Symposium on Algorithm Engineering and Experiments (ALENEX)* (eds Phillips, C. A. & Speckmann, B.) (2022), 54–66.

168. Kitaev, A. Anyons in an exactly solved model and beyond. *Annals of Physics* **321,** 2–111. https://doi.org/10.1016/j.aop.2005.10.005 (Jan. 2006).

169. Castelnovo, C., Chamon, C., Mudry, C. & Pujol, P. Zero-temperature Kosterlitz–Thouless transition in a two-dimensional quantum system. *Annals of Physics* **322,** 903–934. https://doi.org/10.1016/j.aop.2006.04.017 (Apr. 2007).

170. Moessner, R. & Sondhi, S. L. Three-dimensional resonating-valence-bond liquids and their excitations. *Phys. Rev. B* **68,** 184512. https://link.aps.org/doi/10.1103/PhysRevB.68.184512 (18 Nov. 2003).

171. Hermele, M., Fisher, M. P. A. & Balents, L. Pyrochlore photons: The $U(1)$ spin liquid in a $S = \frac{1}{2}$ three-dimensional frustrated magnet. *Phys. Rev. B* **69,** 064404. https://link.aps.org/doi/10.1103/PhysRevB.69.064404 (6 Feb. 2004).

172. Castro Neto, A. H., Pujol, P. & Fradkin, E. Ice: A strongly correlated proton system. *Phys. Rev. B* **74,** 024302. https://link.aps.org/doi/10.1103/PhysRevB.74.024302 (2 July 2006).

173. Benton, O., Sikora, O. & Shannon, N. Seeing the light: Experimental signatures of emergent electromagnetism in a quantum spin ice. *Phys. Rev. B* **86,** 075154. https://link.aps.org/doi/10.1103/PhysRevB.86.075154 (7 Aug. 2012).

174. Verstraete, F., Murg, V. & Cirac, J. Matrix product states, projected entangled pair states, and variational renormalization group methods for quantum spin systems. *Adv. Phys* **57,** 143–224. https://doi.org/10.1080/14789940801912366 (2008).

175. Schollwöck, U. The density-matrix renormalization group in the age of matrix product states. *Ann. Phys* **326,** 96–192. ISSN: 0003-4916. https://www.sciencedirect.com/science/article/pii/S0003491610001752 (2011).

176. Orús, R. A practical introduction to tensor networks: Matrix product states and projected entangled pair states. *Annals Phys.* **349,** 117–158. ISSN: 0003-4916. https://www.sciencedirect.com/science/article/pii/S0003491614001596 (2014).

177. Okunishi, K., Nishino, T. & Ueda, H. Developments in the Tensor Network — from Statistical Mechanics to Quantum Entanglement. *J. Phys. Soc. Jpn* **91,** 062001. https://doi.org/10.7566/JPSJ.91.062001 (2022).

178. Bañuls, M. C. Tensor Network Algorithms: A Route Map. *Annu. Rev. Condens. Matter Phys* **14,** null. https://doi.org/10.1146/annurev-conmatphys-040721-022705 (2023).

179. García-Ripoll, J. J. Time evolution of Matrix Product States. *New Journal of Physics* **8,** 305–305. ISSN: 1367-2630. http://dx.doi.org/10.1088/1367-2630/8/12/305 (Dec. 2006).

180. Schollwöck, U. The density-matrix renormalization group in the age of matrix product states. *Annals of Physics* **326,** 96–192. ISSN: 0003-4916. http://dx.doi.org/10.1016/j.aop.2010.09.012 (Jan. 2011).

181. Tarabunga, P. S. Critical behaviors of non-stabilizerness in quantum spin chains. *Quantum* **8,** 1413. ISSN: 2521-327X. http://dx.doi.org/10.22331/q-2024-07-17-1413 (July 2024).

182. Bañuls, M. C., Hastings, M. B., Verstraete, F. & Cirac, J. I. Matrix Product States for Dynamical Simulation of Infinite Chains. *Phys. Rev. Lett.* **102,** 240603. https://link.aps.org/doi/10.1103/PhysRevLett.102.240603 (24 June 2009).

183. Müller-Hermes, A., Cirac, J. I. & Banuls, M. C. Tensor network techniques for the computation of dynamical observables in one-dimensional quantum spin systems. *New Journal of Physics* **14,** 075003. http://dx.doi.org/10.1088/1367-2630/14/7/075003 (2012).

184. Hastings, M. & Mahajan, R. Connecting entanglement in time and space: Improving the folding algorithm. *Physical Review A* **91,** 032306. http://dx.doi.org/10.1103/PhysRevA.91.032306 (2015).

185. Hamaguchi, H., Hamada, K. & Yoshioka, N. *Handbook for Efficiently Quantifying Robustness of Magic* 2023. arXiv: 2311.01362 [quant-ph].

186. Wang, X., Wilde, M. M. & Su, Y. Quantifying the magic of quantum channels. *New Journal of Physics* **21,** 103002. https://doi.org/10.1088/1367-2630/ab451d (Oct. 2019).

187. Chen, B.-B., Chen, L., Chen, Z., Li, W. & Weichselbaum, A. Exponential Thermal Tensor Network Approach for Quantum Lattice Models. *Phys. Rev. X* **8,** 031082. https://link.aps.org/doi/10.1103/PhysRevX.8.031082 (3 Sept. 2018).

188. Bu, K., Gu, W. & Jaffe, A. Quantum entropy and central limit theorem. *Proceedings of the National Academy of Sciences* **120.** ISSN: 1091-6490. http://dx.doi.org/10.1073/pnas.2304589120 (June 2023).

189. Bu, K., Gu, W. & Jaffe, A. *Entropic Quantum Central Limit Theorem and Quantum Inverse Sumset Theorem* 2024. arXiv: 2401.14385 [quant-ph].

190. Ferris, A. J. & Vidal, G. Perfect sampling with unitary tensor networks. *Phys. Rev. B* **85,** 165146. https://link.aps.org/doi/10.1103/PhysRevB.85.165146 (16 Apr. 2012).

191. Heinrich, M. & Gross, D. Robustness of Magic and Symmetries of the Stabiliser Polytope. *Quantum* **3,** 132. https://doi.org/10.22331/q-2019-04-08-132 (Apr. 2019).

192. Leone, L., Oliviero, S. F. E. & Hamma, A. Learning t-doped stabilizer states. *Quantum* **8,** 1361. ISSN: 2521-327X. http://dx.doi.org/10.22331/q-2024-05-27-1361 (May 2024).

193. Leone, L., Oliviero, S. F. E., Lloyd, S. & Hamma, A. Learning efficient decoders for quasichaotic quantum scramblers. *Physical Review A* **109.** ISSN: 2469-9934. http://dx.doi.org/10.1103/PhysRevA.109.022429 (Feb. 2024).

194. Bejan, M., McLauchlan, C. & Béri, B. *Dynamical Magic Transitions in Monitored Clifford+T Circuits* 2023. arXiv: 2312.00132 [quant-ph].

195. Fux, G. E., Tirrito, E., Dalmonte, M. & Fazio, R. *Entanglement-magic separation in hybrid quantum circuits* 2023. arXiv: 2312.02039 [quant-ph].

196. Bravyi, S. *et al.* Simulation of quantum circuits by low-rank stabilizer decompositions. *Quantum* **3,** 181. https://doi.org/10.22331/q-2019-09-02-181 (Sept. 2019).

197. Leone, L., Oliviero, S. F. E., Esposito, G. & Hamma, A. Phase transition in stabilizer entropy and efficient purity estimation. *Physical Review A* **109.** ISSN: 2469-9934. http://dx.doi.org/10.1103/PhysRevA.109.032403 (Mar. 2024).

198. Bravyi, S., Smith, G. & Smolin, J. A. Trading Classical and Quantum Computational Resources. *Physical Review X* **6.** ISSN: 2160-3308. http://dx.doi.org/10.1103/PhysRevX.6.021043 (June 2016).

199. Zabalo, A. *et al.* Critical properties of the measurement-induced transition in random quantum circuits. *Physical Review B* **101.** ISSN: 2469-9969. http://dx.doi.org/10.1103/PhysRevB.101.060301 (Feb. 2020).

200. Lavasani, A., Alavirad, Y. & Barkeshli, M. Measurement-induced topological entanglement transitions in symmetric random quantum circuits. *Nature Physics* **17,** 342–347. ISSN: 1745-2481. http://dx.doi.org/10.1038/s41567-020-01112-z (Jan. 2021).

201. Lavasani, A., Alavirad, Y. & Barkeshli, M. Topological Order and Criticality in (2+1)D Monitored Random Quantum Circuits. *Physical Review Letters* **127.** ISSN: 1079-7114. http://dx.doi.org/10.1103/PhysRevLett.127.235701 (Dec. 2021).

202. Klocke, K. & Buchhold, M. Topological order and entanglement dynamics in the measurement-only XZZX quantum code. *Physical Review B* **106.** ISSN: 2469-9969. http://dx.doi.org/10.1103/PhysRevB.106.104307 (Sept. 2022).

203. Kells, G., Meidan, D. & Romito, A. Topological transitions in weakly monitored free fermions. *SciPost Physics* **14.** ISSN: 2542-4653. http://dx.doi.org/10.21468/SciPostPhys.14.3.031 (Mar. 2023).

204. Lang, N. & Büchler, H. P. Entanglement transition in the projective transverse field Ising model. *Physical Review B* **102.** ISSN: 2469-9969. http://dx.doi.org/10.1103/PhysRevB.102.094204 (Sept. 2020).

205. Nahum, A. & Skinner, B. Entanglement and dynamics of diffusion-annihilation processes with Majorana defects. *Physical Review Research* **2.** ISSN: 2643-1564. http://dx.doi.org/10.1103/PhysRevResearch.2.023288 (June 2020).

206. Seddon, J. R., Regula, B., Pashayan, H., Ouyang, Y. & Campbell, E. T. Quantifying Quantum Speedups: Improved Classical Simulation From Tighter Magic Monotones. *PRX Quantum* **2,** 010345. https://link.aps.org/doi/10.1103/PRXQuantum.2.010345 (1 Mar. 2021).

207. Rubboli, R., Takagi, R. & Tomamichel, M. *Mixed-state additivity properties of magic monotones based on quantum relative entropies for single-qubit states and beyond* 2023. arXiv: 2307.08258 [quant-ph]. https://arxiv.org/abs/2307.08258.

208. Zeng, B. & Wen, X.-G. Gapped quantum liquids and topological order, stochastic local transformations and emergence of unitarity. *Phys. Rev. B* **91,** 125121. https://link.aps.org/doi/10.1103/PhysRevB.91.125121 (12 Mar. 2015).

209. Zeng, B., Chen, X., Zhou, D.-L. & Wen, X.-G. *Quantum Information Meets Quantum Matter: From Quantum Entanglement to Topological Phases of Many-Body Systems* ISBN: 9781493990849. http://dx.doi.org/10.1007/978-1-4939-9084-9 (Springer New York, 2019).

210. Sykes, M. F. & Essam, J. W. Some Exact Critical Percolation Probabilities for Bond and Site Problems in Two Dimensions. *Physical Review Letters* **10,** 3–4. ISSN: 0031-9007. http://dx.doi.org/10.1103/PhysRevLett.10.3 (Jan. 1963).

211. Calabrese, P. & Cardy, J. Entanglement entropy and conformal field theory. *Journal of Physics A: Mathematical and Theoretical* **42,** 504005. ISSN: 1751-8121. http://dx.doi.org/10.1088/1751-8113/42/50/504005 (Dec. 2009).

212. Van der Marck, S. C. Percolation thresholds and universal formulas. *Physical Review E* **55,** 1514–1517. ISSN: 1095-3787. http://dx.doi.org/10.1103/PhysRevE.55.1514 (Feb. 1997).

213. Sierant, P. & Turkeshi, X. Universal Behavior beyond Multifractality of Wave Functions at Measurement-Induced Phase Transitions. *Physical Review Letters* **128.** ISSN: 1079-7114. http://dx.doi.org/10.1103/PhysRevLett.128.130605 (Apr. 2022).

214. Gu, A., Oliviero, S. F. E. & Leone, L. *Magic-induced computational separation in entanglement theory* 2024. arXiv: 2403.19610 [quant-ph]. https://arxiv.org/abs/2403.19610.

215. Zhu, H. Multiqubit Clifford groups are unitary 3-designs. *Phys. Rev. A* **96,** 062336. https://link.aps.org/doi/10.1103/PhysRevA.96.062336 (6 Dec. 2017).

216. Zhu, H., Kueng, R., Grassl, M. & Gross, D. *The Clifford group fails gracefully to be a unitary 4-design* 2016. arXiv: 1609.08172 [quant-ph]. https://arxiv.org/abs/1609.08172.

217. Leone, L., Oliviero, S. F. E., Zhou, Y. & Hamma, A. Quantum Chaos is Quantum. *Quantum* **5,** 453. https://doi.org/10.22331/q-2021-05-04-453 (May 2021).

218. Oliviero, S. F., Leone, L. & Hamma, A. Transitions in entanglement complexity in random quantum circuits by measurements. *Physics Letters A* **418,** 127721. https://doi.org/10.1016/j.physleta.2021.127721 (Dec. 2021).

219. Leone, L. *Mathematica script for Clifford Group and Beyond.* *https://github.com/lorenzoleone/Clifford-group-and-beyond* July 2023. https://github.com/lorenzoleone/Clifford-group-and-beyond (2023).

220. Elben, A. *et al.* The randomized measurement toolbox. *Nature Reviews Physics* **5,** 9–24. ISSN: 2522-5820. http://dx.doi.org/10.1038/s42254-022-00535-2 (Dec. 2022).

221. A thorough discussion of the finite-size scaling will be found in E. Tirrito et. al., in preparation.

222. Pichler, H., Zhu, G., Seif, A., Zoller, P. & Hafezi, M. Measurement Protocol for the Entanglement Spectrum of Cold Atoms. *Phys. Rev. X* **6,** 041033. https://link.aps.org/doi/10.1103/PhysRevX.6.041033 (4 Nov. 2016).

223. Johri, S., Steiger, D. S. & Troyer, M. Entanglement spectroscopy on a quantum computer. *Phys. Rev. B* **96,** 195136. https://link.aps.org/doi/10.1103/PhysRevB.96.195136 (19 Nov. 2017).

224. Choo, K., von Keyserlingk, C. W., Regnault, N. & Neupert, T. Measurement of the Entanglement Spectrum of a Symmetry-Protected Topological State Using the IBM Quantum Computer. *Phys. Rev. Lett.* **121,** 086808. https://link.aps.org/doi/10.1103/PhysRevLett.121.086808 (8 Aug. 2018).

225. Huang, H.-Y., Kueng, R. & Preskill, J. Predicting many properties of a quantum system from very few measurements. *Nature Physics* **16,** 1050–1057. ISSN: 1745-2481. http://dx.doi.org/10.1038/s41567-020-0932-7 (June 2020).

226. Kitaev, A. Fault-tolerant quantum computation by anyons. *Annals of Physics* **303,** 2–30. https://doi.org/10.1016/s0003-4916(02)00018-0 (Jan. 2003).

227. Dennis, E., Kitaev, A., Landahl, A. & Preskill, J. Topological quantum memory. *Journal of Mathematical Physics* **43,** 4452–4505. https://doi.org/10.1063/1.1499754 (Sept. 2002).

228. Raussendorf, R., Harrington, J. & Goyal, K. Topological fault-tolerance in cluster state quantum computation. *New Journal of Physics* **9,** 199–199. https://doi.org/10.1088/1367-2630/9/6/199 (June 2007).

229. Fowler, A. G., Mariantoni, M., Martinis, J. M. & Cleland, A. N. Surface codes: Towards practical large-scale quantum computation. *Phys. Rev. A* **86,** 032324. https://link.aps.org/doi/10.1103/PhysRevA.86.032324 (3 Sept. 2012).

230. Fishman, M., White, S. R. & Stoudenmire, E. M. The ITensor Software Library for Tensor Network Calculations. *SciPost Phys. Codebases*, 4. https://scipost.org/10.21468/SciPostPhysCodeb.4 (2022).

231. Fishman, M., White, S. R. & Stoudenmire, E. M. Codebase release 0.3 for ITensor. *SciPost Phys. Codebases*, 4–r0.3. https://scipost.org/10.21468/SciPostPhysCodeb.4-r0.3 (2022).

232. Calabrese, P. & Cardy, J. Entanglement entropy and quantum field theory. *Journal of Statistical Mechanics: Theory and Experiment* **2004,** P06002. ISSN: 1742-5468. http://dx.doi.org/10.1088/1742-5468/2004/06/P06002 (June 2004).

233. Vidal, G., Latorre, J. I., Rico, E. & Kitaev, A. Entanglement in Quantum Critical Phenomena. *Physical Review Letters* **90.** ISSN: 1079-7114. http://dx.doi.org/10.1103/PhysRevLett.90.227902 (June 2003).

234. Li, Y., Chen, X. & Fisher, M. P. A. Measurement-driven entanglement transition in hybrid quantum circuits. *Physical Review B* **100.** ISSN: 2469-9969. http://dx.doi.org/10.1103/PhysRevB.100.134306 (Oct. 2019).

235. Foreman-Mackey, D., Hogg, D. W., Lang, D. & Goodman, J. emcee: The MCMC Hammer. *PASP* **125,** 306–312. eprint: 1202.3665 (2013).

236. Sokal, A. in *Functional Integration: Basics and Applications* (eds DeWitt-Morette, C., Cartier, P. & Folacci, A.) 131–192 (Springer US, Boston, MA, 1997). ISBN: 978-1-4899-0319-8. https://doi.org/10.1007/978-1-4899-0319-8_6.

Conclusions and outlook

This thesis explores two different aspects of synthetic quantum matters: quantum simulation (Part I) and quantum information (Part II).

Part I explores the application of quantum simulation, particularly using Rydberg atom arrays, to investigate novel quantum phases of matter. In Chapter 3, we analyze the previously observed spin liquids [1, 2] by connecting it to a gauge theory. This connection directly shows that the observed spin liquid phase corresponds to the deconfined phase of the gauge theory itself, providing a clear-cut theoretical argument for its origin. Furthermore, in Chapter 4, we classify all possible chiral spin liquids in chiral Hamiltonians with $U(1)$ global symmetry, that is relevant in an experimental setup of Rydberg arrays. Such systems have been experimentally demonstrated in a minimal setup of three sites [3]. Importantly, our analysis using parton construction [4, 5] shows that chiral spin liquids emerge in physically realizable parameter regimes. Finally, in Chapter 5, we explore the emergence of exotic dipole symmetry and how it leads to interesting phenomena such as slow relaxation dynamics, in Rydberg arrays and cold atoms. In terms of future investigations, it would be interesting to investigate Rydberg models in various other lattice geometries, which are immediately available in tweezer arrays [6, 7], in order to look for more robust spin liquid states, and possibly even different classes of spin liquids than previously identified. This is particularly interesting as the symmetries of such synthetic materials are very different from those that arise in, e.g., solid state systems. Thus, understanding what types of spin liquids these synthetic materials can stabilize is crucial for future advancements in quantum simulation.

Part II explores the importance of magic, a key quantum information resource, in understanding complex quantum systems. We develop new techniques based on Markov chains and tensor networks to compute measures of magic such as the stabilizer Rényi entropy [8] and mana [9, 10], which are detailed in Chapters 7, 10 and 9. Additionally, we introduce the magic analogue of mutual information, dubbed mutual magic, which is free of boundary effects. Our numerical results reveal that full-state magic always scales extensively with size, and it does not appear to directly relate to critical points. However, its derivatives typically display singularities across the latter: this indicates that magic is strongly sensitive to criticality in a distinct way compared to entanglement. Furthermore, in Chapter 8, we show that mutual magic also exhibits signatures of criticality in (1+1)D conformal field theories in the form of logarithmic divergence, similarly to entanglement entropy [11]. In Chapter 11, we investigate magic transition in a measurement-only circuit model, which is efficiently simulable despite being tuned away from the Clifford limit. Our large-scale simulations further confirm the logarithmic scaling of mutual magic at the critical point. In Chapter 12, we further investigate the relationship between magic and entanglement, revealing a deep connection between the two. This connection can be leveraged to develop an experimental protocol to efficiently probe nonstabilizerness in cold atom and solid-state platforms. Finally, in Chapter 13, we study the dependence of magic with bond dimension, demonstrating that obtaining converged results for nonstabilizerness is easier than entanglement, making magic

a potentially more accessible quantity for practical applications. In perspective, a key next step is to develop other methods to calculate magic, possibly based on higher-dimensional tensor network such as PEPS or Quantum Monte Carlo. These advancements will allow us to explore the role of magic in diverse areas like gauge theory and topological phases of matter, thus providing deeper understanding on the role of magic in many-body phenomena. Furthermore, in view of the connection between entanglement and magic, it would be fascinating to explore the potential advantages in combining simulation techniques based on tensor networks and stabilizer formalism. Finally, while stabilizer Rényi entropies are good measures of magic [12], they lack the desirable property of strong monotonicity [13]. In light of this, it is desirable to construct a strong measure of magic, that is also computable in large systems.

Bibliography

1. Semeghini, G. *et al.* Probing topological spin liquids on a programmable quantum simulator. *Science* **374,** 1242–1247. https://www.science.org/doi/abs/10.1126/science.abi8794 (2021).
2. Verresen, R., Lukin, M. D. & Vishwanath, A. Prediction of Toric Code Topological Order from Rydberg Blockade. *Phys. Rev. X* **11,** 031005. https://link.aps.org/doi/10.1103/PhysRevX.11.031005 (3 July 2021).
3. Lienhard, V. *et al.* Realization of a Density-Dependent Peierls Phase in a Synthetic, Spin-Orbit Coupled Rydberg System. *Phys. Rev. X* **10,** 021031. https://link.aps.org/doi/10.1103/PhysRevX.10.021031 (2 May 2020).
4. Baskaran, G. & Anderson, P. W. Gauge theory of high-temperature superconductors and strongly correlated Fermi systems. *Phys. Rev. B* **37,** 580–583. https://link.aps.org/doi/10.1103/PhysRevB.37.580 (1 Jan. 1988).
5. Baskaran, G., Zou, Z. & Anderson, P. The resonating valence bond state and high-Tc superconductivity — A mean field theory. *Solid State Communications* **63,** 973–976. https://doi.org/10.1016/0038-1098(87)90642-9 (Sept. 1987).
6. Browaeys, A. & Lahaye, T. Many-body physics with individually controlled Rydberg atoms. *Nature Physics* **16,** 132–142. ISSN: 1745-2481. http://dx.doi.org/10.1038/s41567-019-0733-z (Jan. 2020).
7. Barredo, D., Lienhard, V., de Léséleuc, S., Lahaye, T. & Browaeys, A. Synthetic three-dimensional atomic structures assembled atom by atom. *Nature* **561,** 79–82. ISSN: 1476-4687. http://dx.doi.org/10.1038/s41586-018-0450-2 (Sept. 2018).
8. Leone, L., Oliviero, S. F. E. & Hamma, A. Stabilizer Rényi Entropy. *Phys. Rev. Lett.* **128,** 050402. https://link.aps.org/doi/10.1103/PhysRevLett.128.050402 (5 Feb. 2022).
9. Veitch, V., Ferrie, C., Gross, D. & Emerson, J. Negative quasi-probability as a resource for quantum computation. *New Journal of Physics* **14,** 113011. https://doi.org/10.1088/1367-2630/14/11/113011 (Nov. 2012).
10. Veitch, V., Mousavian, S. A. H., Gottesman, D. & Emerson, J. The resource theory of stabilizer quantum computation. *New Journal of Physics* **16,** 013009. https://doi.org/10.1088/1367-2630/16/1/013009 (Jan. 2014).
11. Calabrese, P. & Cardy, J. Entanglement entropy and quantum field theory. *Journal of Statistical Mechanics: Theory and Experiment* **2004,** P06002. https://doi.org/10.1088/1742-5468/2004/06/p06002 (June 2004).
12. Leone, L. & Bittel, L. *Stabilizer entropies are monotones for magic-state resource theory* 2024. arXiv: 2404.11652 [quant-ph].
13. Haug, T. & Piroli, L. Stabilizer entropies and nonstabilizerness monotones. *Quantum* **7,** 1092. https://doi.org/10.22331/q-2023-08-28-1092 (Aug. 2023).